

# Lawrence Berkeley National Laboratory

## Recent Work

### Title

RELATIVISTIC HEAVY ION COLLISIONS: EXPERIMENT

### Permalink

<https://escholarship.org/uc/item/4812s1bq>

### Authors

Friedlander, Erwin M.  
Heckman, Harry H.

### Publication Date

1982-04-01



# Lawrence Berkeley Laboratory

UNIVERSITY OF CALIFORNIA

RECEIVED  
LAWRENCE  
BERKELEY LABORATORY

JUN 2 1982

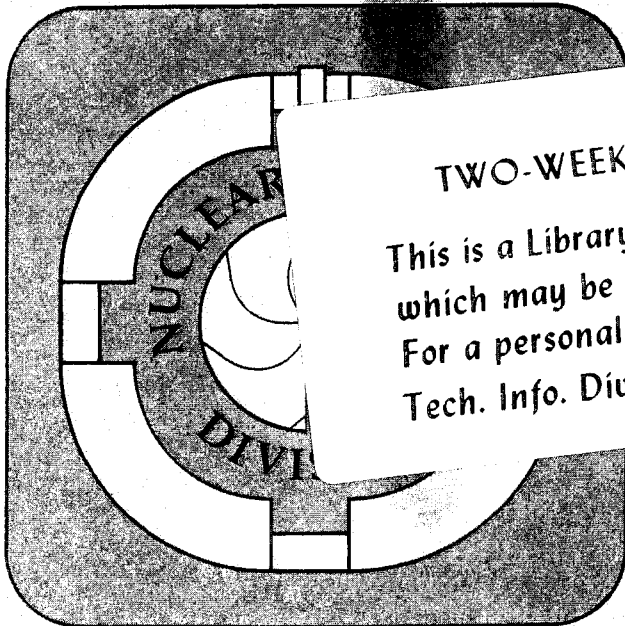
LIBRARY AND  
DOCUMENTS SECTION

To be published as a chapter in HEAVY ION SCIENCE,  
D. Allan Bromley, Ed., Plenum Press, 1982

RELATIVISTIC HEAVY ION COLLISIONS: EXPERIMENT

Erwin M. Friedlander and Harry H. Heckman

April 1982



TWO-WEEK LOAN COPY  
This is a Library Circulating Copy  
which may be borrowed for two weeks.  
For a personal retention copy, call  
Tech. Info. Division, Ext. ~~545~~ 6782

2.  
LBL-13864

RELATIVISTIC HEAVY ION COLLISIONS: EXPERIMENT

Erwin M. Friedlander and Harry H. Heckman

Nuclear Science Division  
Lawrence Berkeley Laboratory  
University of California  
Berkeley, CA 94720

This work was supported by the Director, Office of Energy Research,  
Division of Nuclear Physics of the Office of High Energy and Nuclear  
Physics of the U.S. Department of Energy under Contract DE-AC03-76SF00098.

Contents

1. INTRODUCTION
2. OBSERVABLES AND EXPERIMENTAL TECHNIQUES
  - 2.1. Definitions and Units
  - 2.2. Experimental Techniques and their Observables
    - 2.2.1 Time of Flight (TOF)
    - 2.2.2 Energy Loss and Calorimetry
    - 2.2.3 Magnetic Spectrometry
    - 2.2.4 Visual Techniques
  - 2.3. Pseudo-observables
3. NUCLEAR PHYSICS IN RHI COLLISIONS
  - 3.1. Limiting Fragmentation
    - 3.1.1. Projectile Fragmentation
    - 3.1.2. Interaction Properties of Projectile Fragments:  
Anomalons?
    - 3.1.3. Target Fragmentation
  - 3.2. Factorization
  - 3.3. Electromagnetic Dissociation
  - 3.4. Reaction Characteristics of the Mid-Rapidity Region
    - 3.4.1. Single Particle Spectra
      - 3.4.1a. Protons
      - 3.4.1b. Neutrons
      - 3.4.1c. Light Nuclei
    - 3.4.2. Associated Multiplicities and Topologically Biased  
Spectra

3.5 Source Sizes

3.5.1. Boson-Boson Correlations: Pion Interferometry

3.5.2. Two-Proton Correlations

3.5.3. Composite-Particle Emission

4. PARTICLE PRODUCTION IN RHI COLLISIONS

4.1 Proton-Proton Collisions

4.1.1. Multiplicities

4.1.2. Phase Space

4.1.3. Particle Composition

4.2. pA Collisions

4.2.1. Multiplicities

4.2.2. Multiplicity and Rapidity in pA Collisions

4.2.3. Transverse Momenta in pA Collisions

4.3. Particle Production in AA Collisions at Low and Moderate Energies

4.3.1. Pion Multiplicities

4.3.2. Rapidity Distributions

4.3.3. Transverse Momenta

4.3.4. Strange Particles

4.3.4a. Positive Kaons

4.3.4b. Negative Kaons

4.3.4c. Hyperons

4.3.4d. Hypernuclei

4.4. Very High Energy Nucleus-Nucleus Interactions

4.4.1. Cosmic Ray Interactions of VHE RHI

4.4.2.  $\alpha$ - $\alpha$  VHE Collisions

4.4.2a. Experimental

4.4.2b. Pion Multiplicities

4.4.2c. Large  $p_T$  Phenomena

4.5 The Centauro Puzzle

4.5.1. Experimental

4.5.2. Interpretation

4.6 RHI Interactions and Extensive Air Showers

4.6.1. Ultra High Energy Primary Cosmic Rays

4.6.2. Heavy Nuclei as EAS Primaries

5. CONCLUSIONS AND OUTLOOK

FOOTNOTES

REFERENCES

TABLES

FIGURE CAPTIONS

FIGURES

## 1. INTRODUCTION

Experimental studies of the interactions between nuclei at relativistic energies had their beginnings with the momentous discovery of the existence of the heavy ion component of the primary cosmic rays in 1948 by Freier, et al. (Fr 48, 48a). Because of the broad energy spectra of the cosmic rays, highly relativistic nucleus-nucleus collisions, with abundant particle production, were observed in these early experiments. Too, it was realized that complementary investigations on the elemental and isotopic abundances of the heavy ion component would have profound astrophysical implications.

In a series of brilliantly executed balloon-borne experiments by Bradt and Peters (Br 48, 49, 50, 50a), Kaplon (Ka 52); and Eisenberg (Ei 54), the fundamentals of experimental and theoretical approaches were established, the latter exemplified by Landau's hydrodynamical theory of nucleus-nucleus collisions (La 53), and have persisted throughout the development and maturation of the field of relativistic heavy ion physics.

It is without question that the decade of the 1970s witnessed a most significant technological advance in studies of relativistic heavy ion (RHI) interactions when beams of heavy nuclei accelerated to relativistic energies became available at the Lawrence Berkeley Laboratory Bevalac ( $T = 2.6 \text{ AGeV}^*$ , maximum), Princeton Particle Accelerator ( $T = 0.52 \text{ AGeV}$ , maximum), the JINR Synchrophasotron at Dubna ( $T = 4.5 \text{ AGeV}$ , maximum) and the Saturne at Saclay ( $T = 1.1 \text{ AGeV}$ , maximum). Within a span of less than one year, the kinetic energies of accelerated nuclei available in the laboratory increased by more than two orders of magnitude. This thrust forward was as traumatic for the field of traditional, i.e., low energy, nuclear physics as it was dramatic. The physics of heavy ions was

instantly propelled into the relativistic regime. The experimental techniques and theoretical concepts are necessarily those of high energy physics but with the additional complication that multi-nucleon systems having large dynamic ranges in particle multiplicities, charges, mass, excitation energies, and, possibly, nuclear temperatures and densities are the objects under investigation. RHI physics thus encompasses and demands much from the fields of nuclear physics, cosmic rays, and high energy physics. During the past decade, adventuresome experimentalists have accepted the challenge of this new frontier in physics with its inherent complications both in experimentation and in interpretation but with a great potential for revealing new properties of "nuclear matter".

Review articles that describe the early developments in RHI physics and complement well this chapter are those by Goldhaber and Heckman (Go 78), Stock (St 79), and Nix (Ni 79). Scott (Sc 80) has beautifully synthesized studies in heavy ion physics from the low energy region up to 100 AMeV, a regime where the limits of the traditional concepts of nuclear physics, and perhaps of nuclei themselves, begin to give way to particle physics and the onset of production of pions, kaons, hyperons, etc., in the relativistic region of 1-4 AGeV. Reviews that give specialized aspects of RHI are those on experiments by Schroeder (Sc 80a,80b) and Gutbrod (Gu 80) and on theory by Gyulassy (Gy 80), notable for its extensive list of references.

Experimental studies of RHI interactions have available the highly advanced technology of particle accelerators. Although the field is, figuratively, in transition from its adolescent to young adult stage in development, serious considerations are underway to design new accelerators that will enable heavy ion research to attack the virtually



unknown world of ultrarelativistic energies using beams of colliding nuclei as heavy as  $^{238}\text{U}$  at center-of-mass energies up to 40 AGeV.

The motivation for such a marriage of collisions of multibaryon systems with "elementary particle" physics is connected with the philosophy that nuclear forces cannot be divorced from their "sources", i.e., from the structure of nucleons and the behavior of their more or less hypothetical components. We cannot close our eyes to the fact that in spite of the progress in the understanding of hadron and lepton reactions, no consequent theory of nuclear forces has yet emerged. Nonetheless, the aspiration that elementary particle and nuclear physics can be unified, either by QCD or other theoretical concepts, is the ultimate goal of RHI interaction physics. With this in mind, this chapter, rather than attempting an exhausting review of the existing bibliography, will be concerned with a selection of experiments that either hinted at, or have the potential of revealing, aspects of nucleus-nucleus collisions that cannot be reduced to, or reconciled with, an incoherent superposition of colliding billiard balls.

Indeed a first generation of experiments amply proving this point has already been concluded in a closely related field, that of very high energy proton-nucleus collisions (see Sec. 4). The results of pA experiments have been in flagrant contradiction with the cascade predication based on the "billiard ball" concept and have necessitated the introduction of many-body approaches such as hydrodynamics (La 53, We 78), energy-flux cascade (Go 74), and the coherent tube model (Be 76, Af 77, Af 78).

Beyond the Berkeley and Dubna accelerators the only place to hunt for new effects (aside from burgeoning  $\alpha$ - $\alpha$  experiments at the CERN ISR)

is in the galactic cosmic radiation, which has a long history of pointing the way for experiments in energy realms accessible by new accelerators. An example from recent years are the Centauro events (Sec. 4.5), which still seem to defy any conventional interpretation.

This chapter will be structured as follows: In Section 2 we discuss observables and pseudo-observables in RHI collisions. Section 3 is a review of traditional nuclear physics in RHI collisions and lays the groundwork for Section 4 where particle production in RHI collisions is reviewed. Section 4 also scans the available evidence from ultrarelativistic collisions; beyond its intrinsic value, this information will also provide guidelines in choosing observables and experimental techniques for the new generation of envisaged heavy ion accelerators.

## 2. OBSERVABLES AND EXPERIMENTAL TECHNIQUES

In preparation for our review on experiments in RHI collisions, we give in this section definitions and units of the kinematic quantities to be used and a brief summary of the salient features of particle detectors and experimental techniques pertinent to the measurement of these quantities. We shall examine the advantages, as well as the limitations, of these techniques, being cognizant of the directly measurable "observables" as distinct from the operationally ambiguous "pseudo-observables" such as impact parameter, peripherality, centrality, etc. We comment on the latest developments in experimental facilities and the experimental problems that await us when very highly relativistic, very large-A nuclear beams from the next generation of accelerators confront experimenters with multiplicities of several hundreds of produced particles: pions, kaons, nucleons, hyperons, and fragment nuclei, conventional as well as exotic.

### 2.1. Definitions and Units

We follow the recommendations of Goldhaber and Heckman [Go 78] for the notations and units of kinematic quantities. These are:

- i) Momentum,  $p$  (GeV/c):  $p = \beta\gamma M$ , where  $\beta$  is the velocity,  $\gamma = (1 - \beta^2)^{-1/2}$  and  $M$  is the rest energy of the particle in GeV;  $c \equiv 1$  is assumed everywhere. Because of the conventional use in the literature of the notations  $p_{\parallel} \equiv p_L$  for longitudinal momentum and  $p_{\perp} \equiv p_T$  for transverse momentum, both notations for these quantities will be used in this chapter.
- ii) Rigidity  $R$ (GV):  $R = p/Zc$ , where  $Z$  is the number of units of charge carried by the ion.  $R$  is numerically equal to the momentum per unit charge,  $p/Z$ , and to  $0.02998 B\rho$ , where  $\rho$ (meter) is the radius

of curvature of the particle's trajectory in a magnetic field B (kilogauss).

iii) Total energy, E:  $E = \gamma M$  GeV. For nuclei we shall distinguish three energy regimes, which differ both in the experimental approach and in the range of physical phenomena open to investigation. These are the relativistic range,  $2 < \gamma < 10$ ; the very high energy (VHE) range,  $10 < \gamma < 10^3$ ; and the ultra high energy (UHE) range,  $\gamma \gg 10^3$ .

iv) Kinetic energy, T:  $T = (\gamma - 1)M$  GeV.

v) Kinetic energy per nucleon  $T/A = (\gamma - 1)M/A$  GeV, where A is the atomic mass number of the nucleus. Hence, T in units of T/A is  $T = [(\gamma - 1)M/A]$  AGeV. For clarity, T is often called "total" kinetic energy to avoid confusion with kinetic energy per nucleon, which is basically a measure of velocity. Similarly, momentum in units of momentum per nucleon is  $p = (\beta\gamma M/A)$  AGeV/c.

vi) Rapidity, y:  $y = \ln [(E + p_{\parallel})(E - p_{\parallel})^{-1}]^{1/2}$ , where  $p_{\parallel}$  is the longitudinal momentum.

vii) Pseudo-rapidity,  $\eta$ :  $\eta = \ln [(p + p_{\parallel})(p - p_{\parallel})^{-1}]^{1/2}$ , an approximation for y for highly relativistic particles,  $E \approx p$ .

Because  $p_{\parallel}/p = \cos\theta$ , it follows that  $\eta = -\ln(\tan \theta/2)$ , i.e.,  $\eta$  is a function of angle only.

The rapidity variable is of practical importance because (a) it expands the scale of the angular distribution of the narrow forward cone characteristic for high energy events so as to reveal shape and structure within and (b) it interrelates rapidity distributions in all longitudinally moving inertial frames by linear transformations along the rapidity axis. Specifically, the values  $y'$  and  $y$  in the two inertial frames moving at a

relative longitudinal velocity  $\beta_0$  are related by  $y' = y + \xi$ , where the shift  $\xi$  (called the boost parameter) is given by

$$\xi = -y(\beta_0) = -\frac{1}{2} \ln \frac{1+\beta_0}{1-\beta_0} \quad (2.1)$$

where  $\beta_0$  is positive for increasing rapidity. Since the mean rapidity in the CM system  $\langle y_{cm} \rangle = 0$ , we have

$$\langle y_{lab} \rangle = \langle y_{cm} \rangle + \xi = \xi \quad (2.2)$$

## 2.2. Experimental Techniques and Their Observables

RHI experiments are distinguished by their profusion of particles having wide ranges in charge and mass. In principle, the detection methods in RHI physics are a composite of low- and high-energy techniques. However, there are limitations to these techniques when they are applied to the detection of particles with high rates of energy loss. The copious production ( $\propto Z^2$ ) of  $\delta$  rays (electrons), for example, introduces technical problems that tend to limit the range of charge measurements, the accuracy of trajectory information in wire/drift chambers, and the application of bubble and streamer chambers to high-Z particles.

We summarize in Table 1 the quantities actually observed in electronic and visual techniques that suffice to determine directly, or indirectly, the characteristics of individual particles, i.e., the kinematical quantities and charge. The capability of each technique for detecting the decays of neutral particles is also described. The complete description of a particle, i.e. momentum (energy), charge and mass, requires measurement of three independent particle characteristics, a triad commonly used being time of flight for  $\beta$ ,  $dE/dx$  for  $Z$  (given  $\beta$ ), and

radius of curvature  $\rho$  of a trajectory (in a B field) for rest mass M (given  $\beta$  and Z).

### 2.2.1. Time of Flight (TOF)

The basic simplicity of the concept of measuring particle velocities by measurement of the TOF between two points is often not matched by the ~~electronic hardware required to achieve satisfactory particle~~

identification [Go 75]. If  $\Delta t$  is the error in the TOF for a particle of mass M and the velocity  $\beta$  is measured over a flight path  $\Delta L$ , the partial errors in  $\Delta M/M$  due to  $\Delta t$  alone are i) for magnetic spectrometers, where  $dE/dx$ , rigidity  $R \equiv B\rho$  and TOF are measured,

$$\frac{\Delta M}{M} = \beta \gamma^2 (\Delta L / \Delta t)^{-1} \quad (2.3)$$

~~and ii) for particle identifiers, where  $dE/dx$ , (total) kinetic energy T~~  
(particle identifiers are therefore appropriately classified as low-energy calorimeters) and TOF are measured

$$\frac{\Delta M}{M} = \beta \gamma (\gamma + 1) (\Delta L / \Delta t)^{-1} \quad (2.4)$$

Thus, at nonrelativistic energies, given equal values of  $\Delta L / \Delta t$ , the error  $\Delta M/M$  for the familiar  $\Delta E-E$  method (Eq. 2.4) is twice that for the  $dE/dx - R$  method (Eq. 2.3), whereas the errors  $\Delta M/M$  are equal when  $\gamma \gg 1$ , reflecting the equality of energy and momentum at relativistic energies.\*

### 2.2.2. Energy Loss and Calorimetry

Isotopic identification can be made by energy-loss measurements alone when one measures how the particle loses its kinetic energy in coming to rest [Po 59, Ba 63, Gr 72]. The "stopping signature" of a particle, i.e., the energy-loss  $\Delta E_n$  for each of n-sequential track segments required to stop the particle, can lead to isotopic identification, with

$\Delta A = 0.1-0.2$  mass units for A up to 56 [Gr 78, Al 78].

Furthermore, because the residual ranges of high-Z nuclei are comparable to their mean free paths (mfp) for interaction in matter at kinetic energies as high as  $\sim 1$  AGeV (e.g., the range and mfp of 1 AGeV  $^{238}\text{U}$  are both  $\approx 20$  gm/cm<sup>2</sup>), the use of multi-element particle identifiers under such experimental conditions will continue to be both effective and practical.

A contemporary and most heroic example of a large,  $4\pi$  multi-detector system is the "Plastic Ball", Fig. 1. This detector is, basically, a unique low-energy calorimeter. It is designed expressly to detect and identify stopped charged particles emitted from heavy ion collisions, primarily at low and intermediate Bevalac energies [Ma 79]. The Plastic Ball section is an assembly of 815  $\Delta E-E$  detector modules (two-element particle identifiers for ions  $Z \leq 5$ , with TOF measurements to remove the  $MZ^2$  ambiguity inherent in these detectors) and covers 94% of  $4\pi$  sr. Particles emitted in the forward  $9^\circ$  cone are detected by the  $4\text{m}^2$  Plastic Wall, a 150-element TOF apparatus. In addition to its function as a trigger device, the Plastic Wall combines  $dE/dx$  and TOF information to determine  $Z$  and  $\beta$  of high-energy particles. The new aspect of the Plastic Ball-Wall is its ability to select a variety of trigger modes (from "peripheral" to "central") based on the topology and TOF of the particles produced in the  $9^\circ$  forward cone.

Although a technique of wide application in particle and cosmic-ray physics, high-energy calorimetry has, to date, found only rudimentary applications in RHI experiments [Ch 74, St 81]. By high-energy calorimetry we refer to the process whereby the total energy of an incident particle is absorbed in a suitably designed detector (i.e., the

calorimeter) via the hadronic and electromagnetic cascades it produces. An output signal from the calorimeter is given that is, in principle, proportional to the total energy of the incident particle(s).

The role of calorimetry in RHI experiments is really one destined for the future, when ultra-relativistic, head-on collisions between massive nuclei,  $A \sim 200$ , can reasonably be expected to yield some  $10^3$  to  $10^4$  pions in a non-negligible fraction of all collisions. Under such conditions, the use of conventional procedures of identifying and measuring the momentum of each secondary particle to extract the physics of the interaction becomes unrealistic, if not impossible. Indeed, it is quite reasonable to expect that the important parameters that describe such high multiplicity events will not lie in the description of any particular set of particles, but may well depend on "energy flow", the multiplicity, and nature of the produced particles. Recently a prototype of such an energy flow detector has been successfully used to investigate  $p\bar{p}$ -collisions at the highest cms energy ever attained ( $\sqrt{s} = 540$  GeV, equivalent  $E_{lab} \approx 166$  TeV) [Ua 81].

A review of calorimetry, the existing technology, its limitations, and its potential applications to ultra-RHI experiments has been given by Willis [Wi 81]. This reference presents an intriguing exposé on how calorimetry can become a decisive experimental approach in the pursuit of new phenomena, unique to ultra-RHI collisions.

### 2.2.3. Magnetic Spectrometry

This widely used technique is based on the fact that the trajectory of an ion ( $M, Z$ ) through a configuration of magnetic fields depends only on



its rigidity. Under the condition that the velocity of the ion is high enough to ensure it is fully stripped of its electrons\*, a measure of a particle's rigidity,  $dE/dx$ , and  $\beta$  determines its mass, charge, and momentum. Representative of the magnetic spectrometer technique is the new and major facility at the Bevalac, the Heavy Ion Spectrometer System, HISS, Fig. 2 [Gr 81]. The heart of HISS is a 2 m diameter, 1 m gap superconducting magnet having a magnetic field of 30 kG (max). The HISS facility, with its full complement of detectors (drift chambers, ionization chambers, and TOF wall) and high dispersion beam line for the production and transfer of secondary beams of stable and unstable nuclei, will accommodate a comprehensive experimental program, using the entire range of heavy ion beams anticipated from the upgraded Bevalac (1982).

---

#### 2.2.4. Visual Techniques

Visual track detectors have found wide application in RHI experiments. They include nuclear emulsion, plastics, AgCl monocrystals, bubble and streamer chambers. Because of their  $\sim 4\pi$  solid-angle coverage, broad ranges in sensitivities to rates of ionization, excellent spatial resolution, and basic simplicity, visual methods are almost exclusively used for the detection and analysis of interactions on an event-by-event basis. The nature and amount of information extractable from visual techniques have traditionally been limited by the human element in scanning and measuring of events. However, recent advances in measurement systems that feature modern microscope-stage technology, interactive computer control, on-line data analysis, and, in the case of streamer chambers, digital analysis of film images (see chapter on Streamer Chambers for Heavy Ions by K. Van Bibber and A. Sandoval in this volume) have the potential to increase greatly the productivity of these methods.

The nuclear emulsion technique and its applications to particle detection are well documented in the works of Powell, et al. [Po 59] and Barkas [Ba 63], and references therein. The spatial resolution of emulsion, applicable to all ionizing tracks of charge  $Z \geq 1$ , ionization rates  $\geq dE/dx$  (min), is typically  $1 \mu\text{m}$  (angular resolution  $\sim 1 \text{ mrad}$  at relativistic energies), which surpasses all other particle detectors.

---

Quantities observable in emulsion are i)  $dE/dx$ , deduced from the  $dE/dx$ -dependent structure of the particle tracks, hence ii) charge  $Z$  when velocity  $\beta$  and/or residual range are known, iii) track range, which yields kinetic energy when the mass and charge of the particle are known, and iv) mean (absolute) angles of multiple scattering  $\langle |\alpha| \rangle$  and/or deflection in a magnetic field (which requires that emulsions be exposed in fields  $B \gtrsim 200 \text{ kG}$ ), giving rigidity  $p/Z$ .

---

Track images in single crystals of AgCl [Ch 62, Ch 63, Gr 72a, Sc 74, Sc 76, Ha 76] have visual properties similar to those observed in (de-sensitized) emulsions. Although the latent image in a AgCl crystal is unstable, with lifetimes  $\tau \approx 10^2$  to  $10^5 \text{ s}$ , a remarkable fact is that it can be made highly stable ( $\tau \gtrsim$  months) by simply exposing the detector to visible light,  $\lambda > 5000 \text{ \AA}$  during or immediately after the passage of the particle. Thus, the AgCl track detector can be switched "on and off". The methods of analysis of high- $dE/dx$  particle tracks in AgCl are essentially those used in the nuclear emulsion technique, with the added advantage of the absence of detector deformation and, hence, of track distortion.

Plastic detectors, of which Lexan (bisphenol A-polycarbonate) and CR-39 (allyl diglycol polycarbonate) are most widely known, are representative of a large class of dielectric solids that reveal the

passage of highly ionizing particles by chemical etching with a suitable reagent. The etching process preferentially removes the radiation-damaged material owing to its increased chemical reactivity, thereby producing a cone-shaped pit that is observable as a "track" under optical magnification [Fl 75, Ah 81]. An important feature of the dielectric detector is its complete insensitivity to ionization rates below some given threshold. Track-sensitive polymers have thresholds, defined by the quantity  $(Z/\beta)_{\min}$  (the minimum value of  $Z/\beta$  of a particle for which an etchable track is produced) in the range  $\sim 5$  to 100. Lexan, for example, has a value  $(Z/\beta)_{\min} \approx 60$ , whereas CR-39 (DOP) has  $(Z/\beta)_{\min} \approx 15$ .

Observable quantities in plastic detectors are the number, areas and cone angles of the etched pits. By measuring the rate of change of the cone angle  $\theta$  with range, both  $Z$  and  $\beta$  of the incident particle can be determined. At  $\beta \approx 1$  the charge resolution obtainable with CR-39 (DOP) is  $\sigma_Z \approx 0.23/\sqrt{n}$ , where  $n$  is the number of etch pits measured, for charges  $Z \gtrsim 18$ . In this charge range the resolution is superior to other visual detectors and is comparable to that attained by silicon detector telescopes for  $n$  as low as 4 [Ah 81].

Bubble chambers and streamer chambers have unique features that make them highly effective track detectors for specific applications in RHI [Sc 79a, Ba 80, Va 82]. The distinct advantage of the streamer chamber over all other visual detectors is that it can be triggered, usually by fast "downstream" scintillation or solid-state counters, to select events satisfying specific topological and/or energy-deposition constants in the trigger system. With sensitive times of 1-2  $\mu\text{s}$ , a streamer chamber can accept beam intensities  $10^5$ - $10^6$   $\text{s}^{-1}$ , making it an important tool for

extracting sub-samples of events having low (for visual detection) production cross sections.

Table 2 presents in succinct form the capabilities of different techniques used in RHI research, as far as measurements of more or less global characteristics of multiparticle events are concerned. In this respect the response of any given technique may differ considerably from the pattern presented in Table 1, where the response to single particle tracks was considered. Indeed, a highly accurate and statistically opulent technique may well be unable to handle either two tracks at a time or to disentangle them (which is equivalent).

A general remark: With a few exceptions, to be discussed below, purely electronic detectors lack the ability to analyze complex, multiparticle events. This is essentially the privilege of visual detectors, of which the nuclear emulsion gives probably the most comprehensive coverage (in that it detects with equal efficiency all particles in the whole rapidity range, including the target fragmentation region, largely inaccessible to other detectors, except with severe biases). Its only drawbacks are the relatively low rate of data gathering and its lack of "triggerability". With the advent of computer-driven microscope stages with on-line analysis, the first of these drawbacks is gradually overcome. Dealing with the second is obviously the task of hybrid systems, which employ electronic methods for locating the sites of selected interactions in the "vertex" (visual) detector, say to within  $1 \text{ mm}^3$ , by extrapolating the trajectories of emitted particles to a common origin. This technique has been used extensively, and successfully, during the past few years in high energy experiments in searches for the production and decay of charm/beauty particles, neutrino

interactions, etc. By applying hybrid methods to RHI experiments, detailed information on target-projectile correlations would become available. In particular, observations pertaining to the total target and projectile multiplicities, angular distributions, correlations, and jetting of fragments (quantities observed in the vertex detector) would be augmented by information on the momentum and isotopic identification of the emitted fragments (quantities supplied by the electronic detectors). Hybrid techniques thus can lead to "triggerable" topologies and, by means of multi-targeting, bring into effect a feature heretofore unavailable to passive (continuously sensitive) visual track detectors.

The streamer chamber, on the other hand, enjoys the advantage of magnetic rigidity analysis, "triggerability" and high rate of data acquisition. However, its poor charge and, to some extent also, spatial resolution require hybridization to ensure an efficient use in the study of multiparticle production in RHI collisions.

It should be noted that a new generation of electronic detection arrays tends to approximate "visual status". The most characteristic examples of this kind of array are the CERN Split Field Magnet (SFM) (a huge array of position and/or ionization sensitive detector arrays in a large-scale magnetic field), the HISS array, and the Plastic Ball/Wall. The SFM has already proved its capabilities not only in analyzing pp collisions occurring inside the CERN ISR, but recently has been used to analyze alpha-alpha collisions (see sec. 4.4.2). However, in spite of its mind-boggling complexity and advanced technology, even this instrument has proven incapable of providing directly and reliably such a simple characteristic of the  $\alpha\alpha$  collisions as their multiplicity distribution. It is illustrative to notice that one year after the data run has taken place

(a few hours of running yielding some 100,000 events) the puzzles connected with the geometrical corrections have yet to be solved.

Thus, it appears that unless quite new detection methods appear on the scene, the best prospects for the understanding of the physics of multiparticle final states from RHI collisions lie with hybrid detection systems in which the high resolving power and unambiguity of track identity of truly visual detectors is matched by the high selectivity and fast response of modern electronics.

The column labeled "spatial resolution" in Table 2 refers to the ability to identify multiple interactions occurring within the detector. The two distinct aspects here are the longitudinal and transverse resolutions. The first refers to the possibility of resolving two successive interactions if these are separated by, e.g., 100  $\mu\text{m}$ , which is not an uncommon occurrence for heavy projectiles in any target. Such successive interactions would be seen as distinct in nuclear emulsion but very probably counted as a single, high-multiplicity event in a bubble or streamer chamber. The second aspect of spatial resolution (transverse) refers to the possibility of assigning a secondary interaction (or decay vertex) to a given track. The "resolutions" indicated in Table 2 are actually the distances of confusion with neighboring tracks.

A final remark about cosmic-ray experiments. The main uncertainty in earlier studies of VHE RHI collisions was always connected with estimation of the primary energy of the event. Two recent advances are about to remove most of this uncertainty, viz.

- i) direct calibration of the angular distribution estimators for events recorded in nuclear emulsion at high energy accelerators like the FERMILAB machine and

ii) the increasing use of electronic calorimeters which sample ionization deposition by the whole nuclear plus electromagnetic cascade started by the primary interactions. Such calorimeters operated in conjunction with either emulsion stacks or extensive air-shower arrays have already yielded significant information, as discussed in Sec. 4.6.

### 2.3. Pseudo-observables

In interpreting the results of RHI experiments one is often faced with a more or less wide gap between what the experiment has actually measured and what it is supposed to have measured. We shall briefly examine a few examples of "pseudo-observable" quantities, indirectly connected with the real "observables" via assumptions and/or model representations with varying degrees of validity.

The examples of pseudo-observables discussed hereafter fall into three broad classes, viz.:

i) Quantities unmeasurable with a given experimental technique ("poor man's physics"). A look at Table 2 shows that in order to gain insight to important aspects of the interactions, one has to pay the price of not having access directly to certain quantities. A typical example is experiments on RHI collisions at energies exceeding those available at any existing accelerator by means of emulsion exposures to the galactic cosmic radiation. In spite of the excellent resolution available on angles and the  $dE/dx$  of all particles, the lack of accurate momentum measurements prohibits direct estimation of the mass of most fast particles, of the primary energy, and of the rapidity of the secondaries.

It is usually assumed that as soon as the charge of a RHI is known, its mass cannot lie very far from  $2Z$ . Although very accurate measurements

on heavy primaries at not too large energies have confirmed the validity of this assumption, it remains yet to be proven in the relativistic and especially in the ultra-relativistic energy range.

As attractive as the pseudo-rapidity  $\eta$  appears to be as an approximation for the rapidity  $y$  (indeed, in many cases the only estimate of  $y$  that can be made), the equating of  $y$  with  $\eta$  can lead to distorted, even erroneous, "pseudo"-conclusions about the underlying physics. The requirement for  $\eta$  to be a good approximation to  $y$  is that  $p_{\perp} \gg mc$  of the particle. This condition is most easily met in high-energy pion production but is generally unfulfilled for protons, since here  $\langle p_{\perp} \rangle < m_p c$ . This is demonstrated in Fig. 3, where the values of  $p_{\perp}$  and  $p_{\parallel}$  for pions and protons are plotted for several selected values of  $y$  and  $\eta$ . Illustrated in this figure is the fact that  $\eta \approx y$  for  $p_{\perp} \gtrsim 0.14$  and  $\gtrsim 0.94$  GeV/c for pions and protons, respectively, corresponding to the rest masses of these particles. Thus, for example, if  $\eta$  is applied to proton emission in projectile fragmentation reactions, where  $\langle p_{\perp} \rangle \approx 0.1$  GeV/c, one will obtain a mean value of the  $\eta$ -distribution that differs from the true mean of the  $y$ -distribution by about two rapidity units.

To convey how the identification of  $\eta$  with  $y$  can change the apparent rapidity spectra of highly relativistic protons at  $\gamma_{\text{lab}} = 1000$  ( $\gamma_{\text{cm}} \approx 22$ ), we show the results of a Monte Carlo calculation, Fig. 4, that i) generated a spectrum of protons by sampling from a uniform rapidity distribution in the center of mass in the interval  $-3 \leq y_{\text{cm}} \leq 3$ , assuming a proton  $p_{\perp}$ -distribution of the form  $N(p_{\perp}/p_0) = (p_{\perp}/p_0) e^{-p_{\perp}/p_0}$  with  $\langle p_{\perp} \rangle = 2 p_0 = 0.4$  GeV/c and ii) transformed the resultant  $y$ - and  $\eta$ -distributions to the lab frame. The generated  $y$ -distribution is shown in Fig. 4a. It is centered at  $\langle y \rangle = 3.80$  ( $= \ln 2 \gamma_{\text{cm}}$ ) with the



predicted standard deviation  $\sigma = 1.73 (= 6/\sqrt{12})$ . The distribution when plotted in terms of  $\eta$  is shown in Fig. 4b. The distortion of the parent  $y$ -distribution is clearly demonstrated, the mean value of the  $\eta$ -distribution being  $\langle \eta \rangle = 5.33$ , with  $\sigma = 2.1$  and  $\langle \eta \rangle - \langle y \rangle = 1.53$ . As expected, a similar illustrative calculation for pions at  $\gamma_{lab} = 1000$  shows smaller, but non-negligible, differences between the  $\eta$ - and  $y$ -distributions, with  $\langle \eta \rangle - \langle y \rangle = 0.52$ .

The point we stress here is that one must exercise extreme caution in assuming the equivalence of measured  $\eta$ -distributions and intrinsic  $y$ -distributions. This is particularly so for proton and light fragment production in heavy ion collisions, even at energies available at the ISR or envisioned for the proposed VENUS.

As to the primary energy, except for the (as yet very rare) cases when a calorimeter is available (i.e. excluding hybrid techniques!), it is estimated from angular measurements alone. Of the many methods used, four have gained wide acceptance and of these, three have been taken over from the field of  $pA$  interactions, while the fourth is specific to RHI only.

a) If the collisions are symmetric in some Lorentz frame in which mesons can be assumed to be ultra-relativistic, the velocity  $\beta_c$  of this frame can be estimated from the mean of the pseudo-rapidity  $\eta$ , i.e. from polar emission angles only

$$\xi \approx \langle \eta \rangle \tag{2.5}$$

If this particular Lorentz frame can be identified with the cms of a nucleon-nucleon collision (or, e.g., with the equal velocity system of relevance to hydrodynamical descriptions of RHI collisions), there appears a definite link between the mean pseudo-rapidity and the primary energy

per nucleon (i.e., its lab system Lorentz factor  $\gamma$ ). Typical for this method is the Castagnoli formula [Ca 53]

$$\ln \gamma_c \approx \langle \ln \cot \theta \rangle \quad (2.6)$$

with

$$\gamma \approx 2 \gamma_c^2 \quad (2.7)$$

It suffers from uncertainties due to both random and systematical fluctuations of the particle asymmetry in the assumed Lorentz frame. The latter are mainly caused by the nuclear contributions, i.e., by the nuclear enhancement of wide-angle (or low- $\eta$ ) particle emission known from pA reactions (see Sec. 4.2). Once this effect is corrected for, Castagnoli estimates for  $\gamma$  are good within a factor of  $\sim 2$ .

b) A systematically safer, but statistically poorer, method relies on the well-known constancy of the mean transverse momentum  $p_{\perp}$  (see Sec. 4.2). Assume all relativistic  $Z = 1$  secondaries to be mesons (an approximation certainly less justified for RHI than for proton primaries), and compensate for the unobserved neutral pions by a factor of  $3/2$  (isospin!); then:

$$E \approx \frac{3}{2} \langle p_T \rangle \sum \text{cosec } \theta_i \quad (2.8)$$

Both formulas have been tested with proton primaries around 200 GeV, and the general agreement is satisfactory, once the "nuclear" corrections are applied [Ot 80].

c) Whenever the events are detected in large emulsion stacks or, even better, in emulsion chambers in which electromagnetic cascades started by the decay photons of neutral pions are effectively developed, the primary energy can be estimated from the well-established transition curves of such cascades.\* The only assumption needed to connect  $\Sigma E_{\gamma}$  with

primary energy is that the coefficient of inelasticity be known or, more precisely, that the fraction of the primary energy going into electromagnetic radiation via  $\pi$ -mesons is known and energy independent.

d) Finally, whenever a RHI collision displays a well-identifiable cone of projectile fragments--either protons or, preferably, alphas whose identification is practically unambiguous--the rms opening angle of this cone is a good measure for the primary energy. Assuming isotropic evaporation of the fragments from a system moving with practically the primary's velocity one gets the well-known Bradt-Kaplan [Ka 52] formula:

$$\sqrt{\langle \theta_f^2 \rangle} \approx \frac{\sqrt{T/M}}{\beta\gamma} \quad (2.9)$$

where  $\theta_f$  are the emission angles of the fragments under consideration. Besides isotropy in the projectile frame one has also to assume a temperature  $T$  (which is usually taken as a standard 8 MeV\*) to apply the Bradt-Kaplan relation. However, recent results with Fe nuclei [Ba 81a] suggest that part of the collisions emit alphas with a considerably wider angular distribution, corresponding to temperatures of the order of 40 MeV. This may lead to systematic underestimation of the primary energy by this method.

ii) "Fuzzy" definitions, a typical example of which is the quantity (often casually) defined as multiplicity or "associated" multiplicity of a RHI collision. Here, even if the number of secondary particles is directly counted (albeit, in most electronic experiments only to the extent that sometimes quite important correction factors due to incomplete solid angle coverage and multiple hits must be applied) the physical meaning attached to the term "multiplicity" is often far from clear. Indeed, as soon as the production threshold for pions is exceeded, a wide

variety of mechanisms for 4-momentum transfer from primary to secondaries comes into play. The physics of target and/or projectile evaporation, meson production, baryon resonance excitation, and fast nucleon knock-out are so basically different from each other that correlation of any reaction parameter with a "global" multiplicity becomes meaningless; regularities observed, e.g., in the dependence of multiplicity defined in this undifferentiated way on primary energy may well be fortuitous and the result of superposition of several--possibly mutually canceling--effects.

iii) Model dependent pseudo-observables. A case overlapping the preceding as well as the present category is the paired concept of "centrality/peripherality". The geometrical concepts of an impact parameter and of the nucleus itself, with its constituent nucleons bound together by short-range forces within the nuclear volumes, and having intrinsic Fermi momenta  $p \approx \hbar/r_0 = 140 \text{ MeV}/c$ , have led to the important concepts of peripheral and central collisions between nuclei at relativistic energies.

Specifically, if  $R_T$  and  $R_p$  are the radii of the target and projectile nuclei, respectively, the limiting values of the impact parameter  $b$  give rise to the concepts of peripheral collisions, e.g., when  $|R_T - r_b| < b \leq R_T + R_b$ , and of central collisions, when  $0 \leq b \leq |R_T - R_b|$ . However, peripheral or grazing collisions are operationally characterized in the case of projectile fragmentation, by the emission of fragments, having velocities approximately equal to that of the incident projectile nucleus. Projectile fragments are supposed to be confined to a narrow forward cone whose angular width is determined by the Fermi-momentum distribution of the nucleons within the fragmenting nucleus. Similarly, peripheral collisions give rise to target

fragmentation, where the low energy, target related fragments are produced almost isotropically in angle, with small forward peaking.

The processes of projectile and target fragmentation are, of course, identical in their respective rest frames. In these rest frames fragments that have low velocities  $\beta \lesssim 0.3$  are deemed to be the "spectators" to the collision. On the other hand, the complete occultation of the projectile and target nuclei in central collisions can result in the catastrophic destruction of the interacting nuclei. Such collisions are assumed to involve high levels of excitation and the emission of a large number of particles, nuclear fragments (primarily nucleons and light nuclei), as well as of pions. Energetic fragments, e.g.,  $\beta \gtrsim 0.3$ , observed in the projectile and target rest frames, are visualized to come from the overlap of the nuclear volumes of the projectile and target nuclei and, hence, are denoted as "participants" in the collision.

It is, however, well known from pA collisions (see Sec. 5) that

a) single proton projectiles may transfer enough energy to a target nucleus to result in its complete breakup as well as in meson production and that

b) even such collisions conserve a remarkable degree of "peripherality" if by this term we understand that the projectile is seen as re-emerging with a sizeable fraction of its initial energy.

With this in mind a "high multiplicity RHI event", as seen by detectors looking at the target and mid-rapidity frames, may well be a "peripheral" collision in which the bulk of the projectile conserves its individuality (Fig. 5)(see also Sec. 4.4.1).

Thus, any "measurement" of an impact parameter, based on equating the probability of a given multiplicity class with the assumed cross-sectional area of a "central" nuclear region must be regarded with serious caution.

Finally, two examples of a different kind; here the quantity to be determined through measurement is clearly definable within the context of a given model but stays or falls with the model's validity and/or completeness:

- i) The size of the particle-emitting volume, viewed through two-particle boson-boson correlations at low relative momentum (see Sec. 3). The main uncertainty in this case comes from, as yet largely unknown, contributions from coherence effects of the kind already observed in pA collisions (see Sec. 4).
- ii) Thermodynamical notions, like temperature, entropy, and equation of state, can be rigorously defined within the context of given model representations. However, there is still a long way from the estimation of the slope of a (more or less) exponential spectrum to a "measurement" of temperature.

### 3. NUCLEAR PHYSICS IN RHI COLLISIONS

As an introduction to experiments in relativistic heavy ion physics, we give in this section a discourse on the "traditional" aspects of RHI physics--traditional in the context that the motivation for and the interpretation of a broad class of RHI experiments have their bases in traditional nuclear and high energy hadron physics.

That RHI physics be considered as a study of multibaryon systems (participants with  $B \geq 2$ ), hence an extension of elementary particle physics (participants with  $B = 0$  or  $1$ ), leads in a natural way to the introduction of high energy concepts (Ch 68, 72, 73). Indeed, the first experimental result from the Bevatron/Bevalac on the fragmentation reactions of 2.1-AGeV  $^{14}\text{N}$  (He 72) gave strong evidence that the hypothesis of limiting fragmentation, HLF (Be 69, Fr 72, Bo 74), developed to describe the single-particle inclusive spectra from high-energy "elementary" particle interactions, is surprisingly applicable to RHI in a completely different energy range. The extent to which the HLF is valid in such applications, particularly to the inclusive spectra of secondary fragments from RHI collisions, is being subjected to increasingly refined experiments (Gr 75, Li 75, An 77, Ol 81, Cu 74, Ka 80, and references therein).

The HLF states that for the inclusive reaction  $B + T \rightarrow F + X$ , where B and T represent the beam and target nuclei, F is the detected fragment nucleus, and X refers to all other (undetected) reaction products, the invariant cross section

$$E \frac{d^3 \sigma_{BT}^F (s, p_L, p_T)}{d^3 p} = f (s, p_L, p_T) \quad , \quad (3.1)$$

in the limit that fragment total energy  $E$ , or  $s = (p_B + p_T)^2 \rightarrow \infty$ , approaches a limiting form independent of energy  $E$  (or  $s$ ) for fixed  $p$ . Specifically,  $\lim_{p \rightarrow \infty} f(s, p_{\parallel}, p_{\perp}) = f(p_{\parallel}, p_{\perp})$ , hence the single-particle inclusive spectrum and cross sections become asymptotically energy independent. Related to the HLF is the factorization hypothesis for cross sections, which states that the cross section for the production of  $F$  at high energy may be expressed as a product,  $\sigma_{BT}^F = \sigma_B^F \gamma_T$ , where the cross section  $\sigma_B^F$  depends only on the beam and fragment and  $\gamma_T$ , the target factor, depends only on the target. A direct consequence of factorization in the region of limiting fragmentation is the prediction that the modes of fragmentation of the projectile (target) nucleus are independent of the target (projectile) nucleus. Hence, the production cross sections for  $F$ , for a given beam  $B$ , are expected to be energy independent and scaled in amplitude by the target factor  $\gamma_T$ . The practical consequence of the HLF and factorization is enormous, because the unlimited number of energy/target combinations one might conceivably measure for fragment production cross sections is now reduced to only one—once the asymptotic energy region is established.

### 3.1. Limiting Fragmentation

Experimental tests of the hypothesis of limiting fragmentation in RHI interactions have shown that the isotopic production cross sections and spectral distributions of "spectator" fragment nuclei are independent of energy for beam energies 1-2 AGeV. Observations that are relevant to the HLF come from experiments on projectile fragmentation [Li 75, Gr 75, Pa 75, An 77], where the fragments have velocities, hence rapidities, near that of the beam, and from experiments on target fragmentation [Cu 74, 76, 78, 78a, Ru 75, Po 79, Ka 80 (and references therein), Lo 80 (and



references therein)], where the low-velocity (-rapidity), target-related fragments are studied via radiochemical methods. Because of the equivalence of the projectile and target fragmentation in their respective rest frames, conclusions reached as to limiting fragmentation must be identical, as in fact, to the accuracy to which that projectile and target phenomena can be compared, they are.

### 3.1.1. Projectile Fragmentation

That limiting fragmentation is attained and established to within experimental errors of about 1% for beam energies  $T > 1$  AGeV was demonstrated by the results of Lindstrom, et al. (Li 75), who measured the 0-degree fragmentation cross sections for  $^{12}\text{C}$  and  $^{16}\text{O}$  beam nuclei in the energy interval  $T = 1.05\text{--}2.1$  AGeV. Measurements of about 470 cross sections for 35 isotopes of all nuclear fragments,  $1/3 \leq Z/A \leq 1$  for various targets H to Pb led to the conclusion that the cross sections  $\sigma_{\text{BT}}^{\text{F}}$  for the inclusive reaction  $B + T \rightarrow F + X$  are energy independent with  $\sigma_{\text{BT}}^{\text{F}}(2.1)/\sigma_{\text{BT}}^{\text{F}}(1.05) = 1.01 \pm 0.01$ . Limiting fragmentation is satisfied.

Implied, therefore, is that the momentum distributions for fragments of the projectile in the projectile frame, or, equivalently, their rapidity distributions, are also independent of beam energy and, except for target, i.e., scale factors, independent of the target nucleus. For fragment momenta limited to  $p \lesssim 400$  MeV/c (projectile frame) these limiting conditions are met to ~10% accuracy for fragment nuclei of  $^{12}\text{C}$  and  $^{16}\text{O}$  (Gr 75) and of  $^4\text{He}$  (Pa 75, An 77) for beam energies  $1.05 \leq T \leq 2.1$  AGeV. That energy-dependent changes are seen in the fragment spectra from  $^4\text{He}$  at 0.4 AGeV (An 77) indicates that the HLF is not met at this

energy; hence, the limiting fragment distribution are reached between  ${}^4\text{He}$ -beam energies 0.4 and 1.05 AGeV.

Figure 6 presents the rigidity spectrum of the carbon isotopes produced by the fragmentation of 2.1 AGeV  ${}^{16}\text{O}$  projectiles incident on a  $\text{CH}_2$  target. Typical of all such spectra, Fig. 6 demonstrates peaking of the rigidity distribution of each isotope near beam velocity (this is often referred to as the persistence of velocity) and the near equality of the widths of each isotope peak. When transformed to the projectile rest frame, the longitudinal momentum distributions show a Gaussian dependence on  $p_{\parallel}$ , defined by a central momentum  $\langle p_{\parallel} \rangle$  and standard deviation  $\sigma_{p_{\parallel}}$ . Figure 7 illustrates the Gaussian fit, with the fitted parameters indicated, for the isotope  ${}^{10}\text{Be}$  produced by the fragmentation of 2.1 AGeV  ${}^{12}\text{C}$  on a Be target.

The  $p_{\parallel}$  distributions of all projectile fragments, produced within the 12.5 mr acceptance cone, with the exception of protons, exhibit properties similar to those shown in Fig. 7. Specifically, irrespective of projectile, target, and beam energy (1.05 and 2.1 AGeV), the  $p_{\parallel}^{\text{proj}}$  distributions for all fragments  $A \geq 2$  from  ${}^{12}\text{C}$  and  ${}^{16}\text{O}$  are characterized by:

- i) a Gaussian shape, with rms widths  $\sigma_{p_{\parallel}} \approx 50$  to 200 MeV/c and values of  $\langle p_{\parallel} \rangle \approx -10$  to  $-130$  MeV/c. The negative values of  $\langle p_{\parallel} \rangle$  show that the mean velocities of the fragments are somewhat less than that of the projectile, a consequence of nuclear "friction" that one expects from the separation energy of the fragment from the projectile (Ge 78).

ii) rms deviations  $\sigma_{p_{\parallel}}$  and  $\sigma_{p_{\perp}}$  that are equal to within  $\sim 10\%$ , indicative of isotropic production of fragments in a frame that moves at  $\langle \beta_{\parallel} \rangle \approx -\langle p_{\parallel} \rangle / M_F$  in the projectile frame.

iii)  $\sigma_{p_{\parallel}}$  and  $\langle p_{\parallel} \rangle$  that are (a) independent of target mass and beam energy but (b) dependent on the masses of the beam B and fragment F.

These observations are consistent with the HLF.

Figure 8 shows the dependence of the rms deviation  $\sigma_{p_{\parallel}}$  on the mass of the fragment from  $^{16}\text{O}$  at 2.1 AGeV. The data are compared with a parabolic curve of the form  $\sigma_{p_{\parallel}}(x) = 2\sigma_0[x(1-x)]^{1/2}$ , where  $x = A_F/A_B$  and  $\sigma_0$  is taken here to be an adjustable parameter to best fit the data. Theoretical bases for the parabolic form of  $\sigma_{p_{\parallel}}$  [Le 74, Go 74a] are that, under the assumption of sudden shearing of the projectile:

i) the fragment momentum distributions are essentially those in the projectile nucleus, ii) there are no correlations between the momenta of different nucleons, and iii) momentum is conserved. The formulation of  $\sigma_{p_{\parallel}}$  by Goldhaber [Go 74a] relates  $\sigma_0$  with the Fermi momentum by  $P_F = 20 \sigma_0^2 (A_B - 1) / A_B^2$ . By assuming the projectile comes to thermal equilibrium, with an excitation temperature T, Goldhaber also relates T and  $\sigma_0$  by  $kT = 4 \sigma_0^2 / m_N B$ , where k is Boltzmann's constant and  $m_N$  is the nucleon mass. Thus introduced is a degeneracy in the interpretation of the inclusive spectra of fragments as to whether projectile fragmentation is a fast, shearing process or a slow one involving thermal equilibrium.

In Table 3 the experimentally determined quantities  $\sigma_0$  are compared with theory [Le 74, Fe 73, Go 74a]. Because the values of kT deduced from the data are close to the average binding energy/nucleon, complete disintegration of targets is possible. Unexplained is the question: why are bound fragments so abundantly produced?

The production of light nuclei from the fragmentation of  ${}^4\text{He}$  projectiles has been studied by Anderson (An 77) in the single-particle inclusive reactions  ${}^4\text{He} + (\text{C}, \text{CH}_2, \text{Cu}, \text{Pb}) \rightarrow (\text{p}, \text{d}, {}^3\text{H}, {}^3\text{He}) + \text{X}$  at beam energies 0.4, 1.05 and 2.1 AGeV. The experiment was expressly designed to address the applicability of the HLF to the fragmentation reactions of light nuclei and to relate the observed distributions to the internal structure of the projectile nucleus as an ultimate goal. Measured in Anderson's experiment were fragment momenta  $0.5 \leq p \leq 11.5$  GeV/c and production angles  $\theta_{\text{lab}} \leq 12^\circ$ , which allowed for measurement of transverse momenta  $p_{\perp} \leq 0.60$  GeV/c for protons.

Figure 9 presents the invariant cross sections  $E d^2\sigma/p^2 dp d\Omega$  vs rapidity for fragments  $A_F \leq 3$  produced at 0 deg in the reaction  ${}^4\text{He} + {}^{12}\text{C} \rightarrow \text{F} + \text{X}$  at 2.1 AGeV. As exhibited by the fragments from  ${}^{12}\text{C}$  and  ${}^{16}\text{O}$  described above, the dominant feature of the light fragment spectra is the persistence of the projectile velocity and the peaking of the cross section at  $y_{\text{proj}}$ . Clearly demonstrated is the separation between the rapidity regions of the projectile ( $y_B = 1.81$ ) and the target ( $y_T = 0$ ). Specific features of these results are the comparable cross sections for all the light nuclides at  $y = y_B$ , with the near equality of the  ${}^3\text{H}$  and  ${}^3\text{He}$  cross sections being in evidence over nearly five orders of magnitude. The proton cross sections exhibit a plateau in the mid-rapidity region; the d and  ${}^3\text{H}({}^3\text{He})$  cross sections show minima at  $y \approx 1.2$ , then begin to rise, reflecting the influence of target fragmentation.

Evidence that the HLF becomes invalid as the  ${}^4\text{He}$  beam momenta decrease from 1.75 to 0.93 AGeV/c (1.05 to 0.39 AGeV in energy) in the reaction  ${}^4\text{He} + \text{C} \rightarrow \text{p} + \text{X}$  is given in Fig. 10, where the longitudinal

momentum distributions of protons, having transverse momentum  $p_{\perp} = 0$ , are plotted in the projectile frame for three values of beam momentum. For momenta 2.88 and 1.75 AGeV/c, the spectra are in agreement within experimental errors out to  $p_{\parallel}(\text{proj}) = 0.40$  GeV/c. At 0.93 AGeV/c, the data begin to fall below those for the higher momenta at about  $p_{\parallel} = 0.20$  GeV/c. Note also that the proton spectra appear to consist of two regions; for  $p_{\parallel} < 0.2$  GeV/c, the spectra are Gaussian-like, whereas for  $p_{\parallel} > 0.2$  the spectra tend to be exponential.

The forward-transverse asymmetry of the  $p(\text{proj})$  distributions for protons from the reaction  $\alpha + C \rightarrow p + X$  at 2.88 AGeV/c, illustrated in Fig. 11, is representative of all such distributions for deuterons, tritons, and  $^3\text{He}$ . In each instance the  $p_{\perp}$  distributions at  $p_{\parallel}(\text{proj}) = 0$  is significantly broader than the  $p_{\parallel}(\text{proj})$  distributions at  $p_{\perp} = 0$ , with the forward-transverse symmetry violated for  $p_{\parallel}(\text{proj}) > 0.075$  AGeV/c. These results show that, for fragmentation reactions between light nuclei, the emission of fragments in the projectile frame is anisotropic, contradicting the sudden approximation (Le 74) and/or thermal models [Go 74a]. Implied by the broader  $p_{\perp}$  distributions is that hadronic scattering processes are important contributors to fragment production in collisions between light nuclei (An 77, Bi 77, Na 81 and references therein).

To summarize, the inclusive fragment production cross sections and spectra are found to be energy independent for beams  $4 \leq A_B \leq 16$  at energies  $\sim 1$ -2 AGeV, within the experimental errors of 1-10%. The hypothesis of limiting fragmentation is shown to be valid for beam energies  $> 1$  AGeV for fragment momenta  $p \leq 0.4$  GeV/c in the projectile frame. The cross sections and spectra become limiting at beam energies between 0.4 and 1 AGeV.

### 3.1.2. Interaction Properties of Projectile Fragments: Anomalons?

In 1954, six years after the discovery of the heavy ion component in cosmic rays, the first disquieting evidence emerged for projectile fragments from RHI collisions having, apparently, anomalously short reaction mean free paths ("anomalons"\*) [Mi 54]. Although subsequent cosmic-ray experiments through 1972 extended and supported such evidence [To 57, Ya 57, Fr 61, Ju 68, Cl 68, Ju 72], it was not until beams of accelerated nuclei became available that the technical and statistical limitations of the cosmic-ray experiments could effectively be eliminated and the problem systematically pursued. A Bevalac experiment that focused on the interaction properties of relativistic projectile fragments (PFs) in nuclear emulsions has been carried out with  $^{16}\text{O}$  and  $^{56}\text{Fe}$  projectiles at  $\sim 2$  AGeV [Fr 80, Ju 75].

In this LBL-NRC experiment, an interaction was defined to be one that involved the emission of at least one observable hadronic track. All relativistic PFs  $Z \geq 3$  emitted from the primary, secondary, tertiary, etc., interactions within a 100-mrad forward cone were followed until the topology of each event was completely determined, in other words, until each PF either interacted or left the stack. Charge measurements to  $|\Delta Z| \approx 1$  unit were carried out for all fragments, under the assumption that the PFs are produced at beam velocity.

Figure 12 is a microprojection drawing of a characteristic type of event observed in the experiment: a linear chain of successive PF interactions. In this event, a (first generation)  $^{56}\text{Fe}$  projectile initiates a succession of projectile fragmentations that gives rise to leading fragments of charge  $Z = 24, 20,$  and  $11$  in the second through fourth generations, respectively. Because no PF with  $Z \geq 3$  is emitted from the fourth generation, the chain terminates at this point. The longest chain of this type was observed at NRC

where the sequence was  $^{16}\text{O} \rightarrow \text{N} \rightarrow \text{C} \rightarrow \text{B} \rightarrow \text{B} \rightarrow \text{B} \rightarrow \text{Be} \rightarrow \text{He}$  (out stack), a 7-generation event. Note that the interactions in Fig. 12 are characteristic of high-energy, hadronic interactions, namely, the projectile fragments are confined to a narrow forward cone, with significant particle production and target excitation being evident.

The following quantities were measured for each PF: i) charge  $Z$ , ii) potential path  $T$  available for interaction in the emulsion detector, and, if it interacted, iii) the distance  $X$  to its interaction point. From these data, the estimated mean free path (mfp)  $\lambda^*$  for PFs of charge  $Z$  is given by

$$\lambda_Z^* = \Sigma S_i / N_Z \quad , \quad (3.2)$$

where  $\Sigma S_i$  is the total path length followed for both interacting and noninteracting tracks that leads to  $N_Z$  interactions. The estimate of the mfp by this procedure is independent of the stack size and/or potential path  $T$ . This is illustrated in Fig. 13, where the value of  $\lambda^*$  observed for primary  $^{16}\text{O}$  beam nuclei in 1 cm segments is plotted as a function of the distance  $D$  of that segment from the scan-line (pick-up point). The data are well accounted for by a constant value of  $\lambda^*$ .

The  $^{16}\text{O}$  data are representative of a series of mfp measurements of beam nuclei, varying from  $^4\text{He}$  to  $^{56}\text{Fe}$ , which, by definition, are taken to be the mfps of "normal" nuclei. A useful result of the mfp measurements of beam nuclei is that they can be parameterized as

$$\lambda_Z = \Lambda Z^{-b} \quad , \quad (3.3)$$

where the  $\Lambda$  for beam nuclei is  $\Lambda_{\text{beam}} = 30.4 \pm 1.6$  cm and  $b = 0.44 \pm 0.02$  [Fr 80]. This expression approximates well calculations of mfps in emulsion based on geometrical-overlap models. It also enables one to

reduce all measurements of  $\lambda_Z^*$  [Eq. (3.2)] of the PFs to a single parameter,  $\Lambda^*$ , estimated by the expression

$$\Lambda^* = \frac{\sum_Z \lambda_Z^* N_Z Z^b}{\sum_Z N_Z} \quad (3.4)$$

Figure 14 presents the ratio  $R_1$  of the mean-free-path parameter  $\Lambda^*$  for PFs (all generations combined), to the value  $\Lambda_{\text{beam}}$  measured on accelerator beams, plotted as a function of distance  $D$  from the origin of emission of the PF. In contrast to the  $^{16}\text{O}$  beam data, Fig. 13, the values for  $\Lambda^*$  are low for the first several centimeters, becoming compatible with  $\Lambda_{\text{beam}}$  for  $D \gtrsim 5$  cm. The short mfps at small distances  $D$  mean that there is an excess in the number of interactions at these distances. To obtain some insight as to the nature of this excess of interactions of PFs at short distances, a most elementary assumption can be made: In addition to normal nuclei, there is a component of "anomalous", PFs that are produced with probability  $\underline{a}$ , having a constant, "anomalously short" mfp,  $\lambda_a$ . Estimates of  $\underline{a}$  and  $\lambda_a$  from the data give  $\underline{a}^* \approx 6\%$  and  $\lambda_a \approx 2.5$  cm. (For comparison:  $\lambda(^{56}\text{Fe}) \approx 7.3$  cm,  $\lambda(^4\text{He}) \approx 22$  cm.) The solid curve through the data, Fig. 13 is the computed  $\Lambda^*$  vs  $D$  based on these parameters. Although this primitive model is compatible with the experimental data, it is quite clear that it is not necessarily unique.

An analysis of the mfp data that is independent of the approximate parameterization, Eq. 3.3, involves testing whether two estimates of  $\lambda$ , say  $\lambda_1^*$  and  $\lambda_2^*$ , are compatible with the assumption that they are the result of sampling from the same distribution. This is done by computing the ratio  $R_2 = \lambda_2^*/\lambda_1^*$ , which obeys the F-variance ratio distribution. The integral of the F-variance ratio distribution,  $P(<R_2)$  is uniformly distributed between 0 and 1, hence with  $\langle P \rangle = 1/2$ ,



provided  $\lambda_2^*$  and  $\lambda_1^*$  belong, in fact, to the same distribution. When this test was applied to the case where  $\lambda_2^*$  and  $\lambda_1^*$  are the values of  $\lambda_2^*$  of PFs for distances  $D \leq 2.5$  and  $>2.5$  cm, the observed distribution of  $P(<R_2)$  from the LBL-NRC experiment was not uniform, the mean  $\langle P \rangle$  being 3.4 SD below the expected value of 1/2. The conclusion drawn from this result is that the mfps of PFs at short distances  $D$  from their points of emission are significantly shorter than the mfps at longer distances, independent of any hypothesis as to the dependence of the mfp on  $Z$ , methods and efficiency of scanning.

The surprising result of the LBL-NRC experiment, namely that some small fraction of the PFs may have anomalously short mfps, up to nearly 10 times shorter than those observed for "normal" beam nuclei of the same charge, does not lend itself to an explanation within the framework of conventional physics. This observation sustains the early cosmic-ray evidence for a short mfp component among the PFs of relativistic nuclei. Because of the intrinsic limitation of these cosmic-ray experiments and the momentous revisions in our traditional concepts of the structure of nuclear matter they implied, the cosmic-ray results were given little recognition or credence.

The Bevalac experiment greatly alters the situation. Already independent confirmations of the LBL-NRC observations have been announced [Ja 82, Ba 81]. These later results are included in Table 4, which is a compilation of the world data on "anomalons" from both cosmic-ray and accelerator experiments. As quantitative measures for the short mfp effect we use, depending on the particular experiment, either:

- i) The ratio  $R_1$  of the mfp observed in projectile fragments to the mfp observed on "primary" nuclei that can be considered "normal",  
or

ii) the ratio  $R_2$  of the mfps of PFs measured at different distances from their points of emission (e.g., as above, for  $D \leq 2.5$  cm and  $>2.5$  cm).

The ratio  $R_1$  implies "external" calibration (or model calculations of the normal mfp), while  $R_2$  (the F-ratio defined previously) is an "internal" comparison, hence free of many real or imagined systematic effects. To assess the statistical significance of the deviations of  $R_1$  or  $R_2$  from unity (the null hypothesis), we utilize the facts that the quantity  $2NR_1$  is distributed like  $\chi^2$  with  $2N$  degrees of freedom (DOF), where  $N$  is the number of nuclear interactions observed. The ratio  $R_2$ , as noted above, obeys an F-distribution with  $2N_1$  and  $2N_2$  DOF, where  $N_1$  and  $N_2$  are the numbers of collisions observed at the two different distances from the origin. The appropriate integral probabilities,  $P_1(<R_1)$  or  $P_2(<R_2)$ , are given for each experiment, as are the combined global results for the measured ratios  $R_1$  and  $R_2$ . The confidence levels are also expressed in terms of equivalent Gaussian standard deviations (ESD) by which the observations deviate from the hypothesis of "normalcy", stating that  $\langle R_{1,2} \rangle = 1$ .

Table 4 tabulates the results of this type of analysis performed on:

- 1) Two cosmic-ray emulsion experiments measuring  $R_1$  [Cl 68, Ju 72]
- 2) Three emulsion experiments measuring  $R_2$ , two on 2 AGeV Bevalac beams [Fr 80, Ja 82] and one on cosmic-ray nuclei at higher energies [Ba 81], and
- 3) A propane bubble chamber (PBC) experiment [Ag 81] using 4 AGeV beams from the Dubna synchrophasotron, measuring  $R_1$ .

While all the emulsion experiments are directly comparable, the PBC experiment [Ag 81], as stated by its authors, had insufficient spatial resolution to identify uniquely interacting projectile fragments at distances less than 7 cm from the collision (equivalent to 2 cm of emulsion, if the amount of matter is relevant). For this reason the mfps close to the origin of the PFs, hence  $R_2$ , could not be measured. The larger deviations of the  $R_1$  ratios for the emulsion experiments reflect the inclusion of regions close to the points of emission of the PFs, where most of the anomalous effect is located. Nonetheless, in spite of the systematic weakening of any possible effect by the exclusion of distances  $D < 7$  cm, the value of  $R_1$  from the PBC data is systematically lower than unity for four different charges of fragments by (globally) 2.1 ESD.

All the deviations in Table 4 are in the same direction, that is, in the sense that all mfps of PFs are shorter than normal, or, shorter close to their point of emission. Thus, the data available consistently show that the mfps of relativistic PFs are anomalously short immediately after emission, e.g., at distances  $D \approx 2.5$  cm (corresponding to a proper time  $10^{-11}$  sec) by reason of time elapsed and/or amount of matter traversed; at greater distances, typically  $D \gtrsim 5$  cm, the mfps revert to "normal" beam values.

For the three emulsion experiments (Group 2 in Table 4), the overall probability that the observed deviation is due to a statistical fluctuation is  $\sim 10^{-7}$ . If the results of all the independent experiments tabulated in Table 4.5-1 are combined, the level of discrepancy increases to  $>6$  ESD, equivalent to an incomprehensibly small probability of  $10^{-11}$  for a chance fluctuation.

Barring this possibility, the observations are compatible with a (presumably) multibaryon state(s) that interacts with cross sections three to ten times larger than those of beam nuclei of the same charge. To affect a  $\lambda \approx 2.5$  cm in emulsion, such a multibaryon state would have to have an effective interaction radius about 3 fm larger than that of a uranium nucleus.

Such a conclusion is, obviously, a profound one, and new experimental approaches and interpretations are vital. Conventional explanations invoking excited states of nuclei, hyperfragment decay, background stars, and the superposition of particle tracks do not lead to mfps as short as  $\sim 2.5$  cm; especially they do not explain the very rapid increase of  $R_1$  in the first few cm from the origin. Others can be directly rejected by comparing the topologies of the interactions of PFs and beam nuclei. Future experimental directions must address questions pertaining to the lifetime of anomalons, production/reaction mechanisms, the property of "memory", whereby the anomalons tend to persist in subsequent generations of reactions [Fr 80], energy dependence, and, ultimately, masses and decay mechanisms.

The theoretical interpretations of the anomalon effect are as yet embryonic, like the experiment. Speculations have focused on the idea that 'quark bundles' in nuclei [Ro 79, Ka 79, Fr 81], or even pulsating blobs of quark matter [St 80c, St 80d] may be the key to the explanation. As provocative as the hint of what may be a new state of nuclear matter with a lifetime as long as  $10^{-11}$  sec is the fact that these unanticipated results have emerged from experiments on projectile fragmentation at energies as low as 2 AGeV, in relatively peripheral collisions deemed to involve low-momentum transfer.

### 3.1.3. Target Fragmentation

Because of the kinematic equivalence of the rest frames of the projectile and target, the phenomenon of target fragmentation should show independence of the beam nucleus and energy under the same kinematic limits as described for projectile fragmentation. Experimental tests of the HLF for target nuclei have been made, primarily, via radioanalytical studies of fragment residues of heavy target nuclei  $64 \leq A \leq 238$  under the bombardment of proton and heavy ion projectiles.

Cumming, et al. [Cu 78] demonstrated the approach to limiting fragmentation by examining the energy dependence of the slope of the mass-yield curve, which is taken to be an approximate measure of the excitation energy transferred to the target nucleus from the bombarding particle: a smaller slope corresponds to greater average mass loss, hence, higher average excitation energy. An example of such mass yield curves is given in Fig. 15, where the production cross sections are plotted versus the product mass for the fragmentation of Cu by  $\sim 2$  AGeV nuclei, namely 80 GeV  $^{40}\text{Ar}$  and 25 GeV  $^{12}\text{C}$  and by 28 GeV protons [Cu 78, 76]. Notable is that at these beam energies the mass yield curves for these beam nuclei are nearly the same in this target fragmentation region except for magnitude, which scale as  $\sigma_R$ , i.e.,  $\sigma_R^{40\text{Ar}}/\sigma_R^{1\text{H}} = 3.5$  ( $\approx A_{\text{proj}}^{1/3}$ ).

Presented in Fig. 16 is the energy dependence of the slopes of the exponential mass yield curves in the region  $37 \lesssim A \lesssim 57$  for the fragmentation of Cu by protons,  $0.35 \leq T_p \leq 28$  GeV,  $^4\text{He}$  at 0.41 and 0.72 GeV, 3.9 GeV  $^{14}\text{N}$ , 25 GeV  $^{12}\text{C}$ , and 80 GeV  $^{40}\text{Ar}$ . Illustrated here is that i) the data form a smooth curve when plotted in terms of total kinetic energy of the beam projectile, rather than velocity, i.e.

kinetic energy per nucleon or rapidity, ii) the onset of limiting fragmentation (energy independence) is evident for energies  $T \gtrsim 2$  GeV, and iii) there is striking similarity between protons and heavier beam nuclei in terms of their energy deposition. Support of these conclusions has come from similar experiments with a wide range of target-beam-energy combinations [Po 79, Mo 80, Lo 80, Ka 80, Lo 81, Ka 78].

Further insight to the applicability of the HLF comes from experiments on the recoil properties of target residues. Measured in such experiments are the fractions of each radionuclide that recoil out of a target in the forward (F) and backward (B) direction. Under a model that assumes the recoil target fragments arise from a two-step process [Al 68, Wi 78], the measured quantities can be related to  $\langle \beta_{\parallel} \rangle$ , the mean forward-directed velocity of the prefragment that results from the initial projectile-target interaction, and to  $\langle \beta \rangle$ , the mean Maxwellian-distributed velocity that arises from the de-excitation of the prefragment to produce the observed residue. The model assumes that  $\vec{\beta}$  is isotropically distributed in the moving frame ( $\beta_{\parallel}$ ) of the prefragment. Conceptually the two-step model is equivalent to the abrasion-ablation model [Ei 54, Bo 73, Go 77] that has been extensively used to interpret projectile fragmentation [Hü 75, 78, Ce 77, Ab 76, 76a]. Inherent in the two-step model is the assumption that the reaction occurs in two different time scales; first, the fast stage that results in an excited fragment having longitudinal velocity  $\beta_{\parallel}$  in the laboratory and second, the deexcitation stage that occurs on a much longer time scale.

The general characteristics of the mean velocities  $\langle \beta_{\parallel} \rangle$  of the first stage and  $\langle \beta \rangle$  of the second stage derived from experiment via the two-step model for a variety of beam nuclei and energies are shown in

Figs. 17 and 18. Figure 17 is a plot of the mean recoil velocity of the first step,  $\langle \beta_{\parallel} \rangle$ , versus the mass number of the detected fragment. The qualitative features illustrated here are: i) the recoil velocities  $\langle \beta_{\parallel} \rangle$  are small, typically  $\sim 1\%$  of the incident beam velocity, ii)  $\langle \beta_{\parallel} \rangle$  decreases with increasing  $A_F$  in the range  $24 \leq A_F < 100$ , with a leveling off or slight increase in  $\langle \beta_{\parallel} \rangle$  for  $A_F \gtrsim 100$  before it again decreases at fragment mass numbers  $\gtrsim 140$ , iii) the highest values of  $\langle \beta_{\parallel} \rangle$  are observed for  $^{12}\text{C}$  and  $^{20}\text{Ne}$  at  $\sim 0.4$  AGeV, where  $\langle \beta_{\parallel} \rangle$  vs  $A_F$  is independent of the beam particle, and iv) the recoil velocities  $\langle \beta_{\parallel} \rangle$  decrease with increasing beam energies, the observed  $\langle \beta_{\parallel} \rangle$  vs  $A_F$  becoming indistinguishable for protons at 28 GeV and  $^{12}\text{C}$  at 25 GeV. These results illustrate how the quantity  $\langle \beta_{\parallel} \rangle$  approaches the condition for limiting fragmentation, and that beam independence, e.g. protons and  $^{12}\text{C}$ , is virtually attained at kinetic energies  $T \gtrsim 25$  GeV.

The dependence of the mean velocity  $\langle \beta \rangle$  for several representative fragment nuclides in the second (deexcitation) stage of the reaction on the bombarding energy is shown in Fig. 18. The principal conclusion drawn from this figure is that the velocity  $\langle \beta \rangle$  for a given fragment is independent of the mass and kinetic energy of the projectile for beam energies  $T \gtrsim 3$  GeV, in support of the assumption of the two-step model that the deexcitation stage is slow and independent of the kinematics of its formation. The velocity  $\langle \beta \rangle$  thus is not particularly relevant to tests of the HLF. We therefore return to the recoil velocity  $\langle \beta_{\parallel} \rangle$  to extend our discussion of limiting fragmentation.

The key feature of Fig. 17 is that the loci of data points can be described, to good approximation, in terms of a mean momentum  $P_0 = 931 A_F \langle \beta_{\parallel} \rangle$  (MeV/c) that characterizes each plot of  $\langle \beta_{\parallel} \rangle$  vs  $A_F$ ,

especially for  $A_F \gtrsim 100$ . For the data shown, the values of  $P_0$  evaluated from the unweighted data for  $\langle \beta_{||} \rangle$  with  $A_F \leq 100$  are: curve a)  $420 \pm 7$  MeV/c, curve b)  $200 \pm 6$  MeV/c, and curve c)  $45 \pm 6$  MeV/c. The curves drawn through the data (extrapolated for  $A_F > 100$ ) are the expression  $\langle \beta_{||} \rangle = P_0 / 931 A_F$  using the above values for  $P_0$ . Although clearly an over-simplification, the data are represented well by  $A_F \langle \beta_{||} \rangle = \text{constant}$  over most of the range of fragment masses, with the largest deviations occurring at the highest beam energies (c) in the region of  $A_F = 60$  and, in all cases, for  $A_F \sim 140$ . That such deviations should occur is not unexpected owing to growing evidence that the general trend of angular distributions (lab frame) for fragment production in proton bombardment is to change from forward to sideward peaking at energies above 10 GeV. At a proton energy of 400 GeV, the distributions of some nuclides even show a backward enhancement [Po 79a]. Such changes may be indicative of changes in the reaction mechanisms.

Because the results of the foregoing radiochemical experiments on target fragmentation lend support to the two-step model and hence are the basis for deducing the variables  $\langle \beta_{||} \rangle$  and  $\langle p \rangle$ , it is informative to examine the actual kinematics of the two-step process. By doing so, an interpretation of the approximate invariance of  $P_0 \propto A_F \langle \beta_{||} \rangle$  is possible, which leads to a description of the asymptotic approach to limiting fragmentation in these experiments.

The two-step kinematic model we adopt [Ma 77] describes target fragmentation via the reactions a)  $B + T \rightarrow B^* + T^*$  and b)  $T^* \rightarrow F + X$  whereby the target nucleus T (beam nucleus B) is excited to the state  $T^*(B^*)$ , the decay of which leads to the observed target (projectile) fragment F. This model has been particularly successful in reproducing



the recoil momentum of projectile fragments from  $^{12}\text{C}$  and  $^{16}\text{O}$  at 2.1 AGeV [Ma 77, Ge 78] as well as for the fragments of  $^{16}\text{O}$  at the nonrelativistic energy of 0.02 AGeV [Ge 78]. Under the approximations that the recoil  $\ll$  excitation  $\ll$  nuclear rest energies, the conservation of energy and momentum leads to the following expression for the recoil velocity  $\langle \beta_{\parallel} \rangle$  of the excited target nucleus:\*

$$\langle \beta_{\parallel} \rangle \approx (\gamma E_T^* + E_B^*) / M_T \beta \gamma \quad , \quad (3.5)$$

where  $E_T^*$  and  $E_B^*$  are the excitation energies of the target and beam nuclei, respectively, and  $M_T$  is the target mass. Note that Eq. 3.5 exhibits the properties of limiting fragmentation, in that  $\langle \beta_{\parallel} \rangle$  becomes independent of beam energy and projectile mass (factorization) as  $\gamma \rightarrow \infty$ .

The constancy of the mean momentum  $P_O = M_F \langle \beta_{\parallel} \rangle$  MeV/c of the fragment recoils thus suggests that the quantity

$$P_O M_T = M_F \frac{\gamma E_T^* + E_B^*}{\beta \gamma} = k \text{ (a constant)}. \quad (3.6)$$

If we assume that, on the average, the excitation energies of the target and beam nuclei are equal (including proton beams), i.e.  $E_T^* = E_B^* (= E^*)$ , then

$$k = M_F E^* \sqrt{\frac{\gamma+1}{\gamma-1}} \quad . \quad (3.7)$$

Hence,

$$M_F E^* = k \sqrt{\frac{\gamma-1}{\gamma+1}} \quad , \text{ and} \quad (3.8a)$$

$$E^* = \langle \beta_{\parallel} \rangle M_T \sqrt{\frac{\gamma-1}{\gamma+1}} \quad . \quad (3.8b)$$

The kinematics of the two-step model thus lead to the prediction that the quantity  $M_F E^*$  is a constant for a given beam energy, with  $\gamma = E_B / M_B$ .

Furthermore, the excitation energy  $E^*$  is found to be linearly related to the mean recoil velocity  $\langle \beta_{\parallel} \rangle$  of fragment F. A linear correlation between  $E^*$  and  $\langle \beta_{\parallel} \rangle$  has also been demonstrated in a variety of intranuclear cascade calculations [Ka 78, Po 60], hence appears to be a model independent feature of the nuclear reaction.

In Fig. 19 the quantity  $M_F E^*$  (Eq. 3.8a) is plotted as a function of the beam kinetic energy for a variety of beam energies, beam and target nuclei.

The data show that  $E^*$  associated with each fragment mass reaches a maximum near 5 GeV, then decreases with beam energy, approaching an asymptotically limiting value for energies  $\gtrsim 25$  GeV. This dependence of  $E^*$  on kinetic energy is in qualitative agreement with the computational results from intranuclear cascade models [Ka 78]. Although the data are insufficient to establish the universality of the relationship between  $M_F E^*$  versus kinetic energy of the beam and the constancy of  $P_O M_T = k$ , the equality of the excitation energies  $E^*$  (as deduced from the two-step model) for the production of fragments  $24 \leq A_F \leq 100$  by 25-GeV  $^{12}\text{C}$  and 28-GeV protons incident on both  $^{64}\text{Cu}$  and  $^{197}\text{Au}$  targets appears to be well established. Within the experimental errors  $E^*(25 \text{ GeV}) \approx E^*(300 \text{ GeV})$ , from which we conclude that the HLF is valid for the variable  $M_F E^*$  for beam kinetic energies  $\gtrsim 25$  GeV. Since  $\langle \beta_{\parallel} \rangle \propto E^*$  (Eq. 3.8b), the implication is that the recoil velocity  $\langle \beta_{\parallel} \rangle$  (the kinematic quantity that controls the forward/backward ratio of the target fragments in the laboratory system) also attains a minimum, limiting value near 25-GeV beam energy. The fragment angular distributions therefore exhibit the smallest asymmetry at these energies, becoming more forward peaked as  $\langle \beta_{\parallel} \rangle$  increases with decreasing beam energy. One concludes from Fig. 19 that

limiting fragmentation is clearly not met for energies  $\gtrsim 10$  GeV, and that above this energy experiments of increased accuracy are necessary to establish the approach to the condition for limiting fragmentation.

That  $E^*(\beta_{\parallel})$  may attain a maximum in the vicinity of 5 GeV does not appear to be explainable by existing theories [Ka 78]. As mentioned above, changes in reaction mechanisms could lead to such effects. But, as stressed by Kaufman, et al. [Ka 80], an underlying problem in determining  $\langle\beta_{\parallel}\rangle$ , hence  $E^*$ , from target fragmentation data is that it is model dependent on the assumption that the angular distributions are isotropic in the frame moving at velocity  $\langle\beta_{\parallel}\rangle$  in the laboratory. Because this is known not to be the case for proton bombardment above  $\sim 10$  GeV, future experiments that have sufficient sensitivity to measure accurately the dependence of the angular distribution of fragments as a function of projectile mass and energy will be of key importance in confirming the hypotheses of limiting fragmentation and factorization in RHI interactions.

Thus, we learn from projectile and target fragmentation experiments that fragment production cross sections and momentum spectra of projectile fragments from light beam nuclei approach energy independence at beam energies between 0.4 and 1 AGeV, with energy independence being established for energies between 1.05 and 2 AGeV, i.e., above a few GeV kinetic energy. On the other hand, measurements of the recoil properties of target fragments, particularly the recoil velocity  $\langle\beta_{\parallel}\rangle$  and the related excitation energy  $E^*$ , as deduced via the two-step model, are shown to be more sensitive to energy variations than are the cross section measurements. Nonetheless, these kinematic quantities, after exhibiting large changes in the energy range 5.0 GeV (0.25 AGeV  $^{20}\text{Ne}$ ) to 25 GeV (2.1 AGeV  $^{12}\text{C}$ ), also show energy independence at energies 25 GeV and above, if we rely on the equivalency of protons and nuclei.

An important concept to come from the study of target fragmentation, attributable to the broad range of beam energies and masses that have been used, is that it is the kinetic energy of the projectile, rather than its velocity or rapidity, which is relevant to tests of the hypothesis of limiting fragmentation. We shall see similar conclusions when we discuss experiments on the multiplicity distributions of energetic, light target fragments produced in RHI collisions (Sec. 3.4.2).

### 3.2. Factorization

The observations that production cross sections and rapidity (velocity) distributions of fragment nuclei in the regions of target ( $y \approx 0$ ) and projectile ( $y \approx y_B$ ) rapidities have, within errors of measurement, attained energy independence for kinetic energies  $\gtrsim 25$  GeV ( $\gtrsim 2.1$  AGeV for  $A/Z = 2$  nuclei) intimates that the hypothesis of factorization is also valid in RHI collisions at these energies. Experimental tests of this hypothesis, namely, that the cross section for the production of fragment F in the inclusive reaction  $B + T \rightarrow F + X$

can be factored according to

$$\sigma_{BT}^F = \sigma_B^F \gamma_T, \quad (3.9)$$

where  $\gamma_T$  is dependent only on the target, have shown that the elemental and isotopic production cross sections can be factored according to Eq. 3.9 to high accuracy. As part of an experiment pertaining to the electromagnetic dissociation of relativistic  $^{18}\text{O}$  (see Sec. 3.3), Olson et al. [Ol 81] were able to demonstrate that the factorization of the isotopic cross sections for nuclear processes is valid to  $\sim 5\%$ --an rms accuracy that is essentially limited by systematic uncertainties in the experiment.

The property of factorization is illustrated in Figs. 20 and 21. Figure 20 presents the reduced cross section  $\sigma_{BT}^F/\gamma_T$  versus  $A_T$  for eight representative fragment nuclides from  $^{18}\text{O}$  incident on a variety of targets  $9 \leq A_T \leq 238$  at 1.7 AGeV. Figure 21 shows the corresponding target factors  $\gamma_T$  for  $^{18}\text{O}$  as well as the target factors for the isotopic production cross sections from the fragmentation of  $^{16}\text{O}$  at 2.1 AGeV [Li 75] and for element production from the fragmentation of  $^{56}\text{Fe}$  at 1.80 AGeV [We 79], obtained by least squares.

The excellent agreement of these data with the hypothesis of factorization is evident in Fig. 20, where the data are tightly distributed about the respective reduced cross sections  $\sigma_B^F$  indicated by the straight lines for each fragment. Drawn through the  $\gamma_T$  target factors in Fig. 21 are two analytical curves that have been conventionally used to represent the dependence of  $\gamma_T$  (normalized to  $\gamma_{12C}$ ) on the mass number  $A_T$  of the target; i)  $\gamma_T \propto A_T^n$  and ii)  $\gamma_T \propto A_T^{1/3} + A_B^{1/3} - d$ . The former expression is representative of "strict" factorization, whereas the latter, which has the form of a geometrical impact parameter and allows for a beam dependence, is representative of "weak" factorization [B1 79]. The data are satisfactorily described by either function, with the exponents  $n \approx 0.23$  for the  $^{16}\text{O}$  and  $^{18}\text{O}$  isotopic cross sections and  $n \approx 0.19$  for element production from  $^{56}\text{Fe}$ , indicated by the solid curves, Fig. 21. The dashed curves are a)  $A_T^{1/3} + 1.72$ , with  $d = 0.8$  and  $0.9$ , for  $^{16}\text{O}$  and  $^{18}\text{O}$ , respectively, and b)  $A_T^{1/3} + 2.63$ , with  $d = 1.2 \pm 0.3$ , for  $^{56}\text{Fe}$ . The geometrical character of the functional forms of  $\gamma_T$  supports the notion that the production of fragment nuclei is dominated by the geometry of peripherally colliding nuclei with radii  $\propto A^{1/3}$ . Not considered in such geometric

approximations are the effects of nuclear-form factors on  $\gamma_T$ . Such effects are evident in the data [Li 75]; a good example of this, shown in Fig. 21, is the equality of  $\gamma_{Be}$  and  $\gamma_C$ , which is observed in all the cited experiments.

Bleszynski and Sander [Bl 79] conceptually extended the geometrical aspects of RHI collisions by use of the abrasion-ablation model [Ei 54, Bo 73, Hü 75, 78, Ab 76, 76a]. They have proposed on the basis of this model a nonfactorable target factor of the form  $\gamma_T \propto (A_T^{1/3} + A_B^{1/3})^m$ , where  $m$  is related to the number  $n$  of participant nucleons knocked out of the projectile. For highly peripheral collisions  $n = 1$  and  $m \approx 0.85$ . For total reaction cross sections, the exponent reaches its maximum value  $m \approx 2$ , and  $\gamma_T$  becomes proportional to the geometric cross section.

To date, the range of projectile masses available for tests of the target- and projectile-mass number dependence of the fragmentation cross sections is not sufficient to establish whether factorization is "strict" or "weak". The indication that the exponent  $n$  decreases from  $\sim 0.23$  for  $^{16,18}O$  beams to  $\sim 0.19$  for  $^{56}Fe$  is compatible with the small target dependence expected for  $n$  from the abrasion-ablation model, but further enquiries with high-mass beams,  $A_B > 56$ , will be essential to clarify the basic features of factorization.

There are several important examples where the hypothesis of factorization clearly fails. The first is attributable to the enhancement of fragment production by the electromagnetic (Coulomb) dissociation of projectile nuclei by the virtual photon field of target nuclei via the Weizsäcker-Williams (WW) process. Because this electromagnetic effect is dependent on  $Z_T^2$ , the breakdown of factorization is most apparent for high- $Z$  target nuclei [see Sec. 3.4]. Although not yet observed, the

beam-energy dependence of the WW process will also lead to a breakdown in limiting fragmentation. The second case is that total nucleus-nucleus cross sections [Ja 75], as well as the inelastic (reaction) cross sections [Ja 75, He 78, We 79], are found to be "geometrical" and thus have a nonfactorable form  $\sigma = \pi r_0^2 (A_T^{1/3} + A_B^{1/3} - \delta)^2$ , where  $\delta$  is the overlap parameter. A third example is the observation of a special class of Fe-nucleus collisions in nuclear emulsions [Ba 81a] in which the momentum spectra of He-projectile fragments do not scale according to the HLF but change considerably in shape when going from light (CNa) to heavy (AgBr) target nuclei.

Target fragmentation experiments have also given evidence for the factorization of cross sections. In a series of investigations, Cumming et al. [Cu 74, Cu 76, Cu 78; see also Mo 78, Ka 80, Lo 81] found that the charge-dispersion curves of radionuclides produced from Cu bombarded by relativistic projectiles, including protons,  $^{12}\text{C}$ ,  $^{14}\text{N}$  and  $^{40}\text{Ar}$ , were indistinguishable within experimental errors. Furthermore, the relative production cross sections for products with mass greater than one-half that of the target were independent of projectile. Figure 22 shows the ratios of cross sections for the production of given nuclides from the bombardment of Cu by 80-GeV  $^{40}\text{Ar}$  and by 25 GeV  $^{12}\text{C}$  ions plotted as a function of the product mass. Although the data display a scatter suggestive of systematic sources of errors, no trend in the ratio  $\sigma_{\text{Ar}}/\sigma_{\text{C}}$  is evident, with 2/3 of the points lying within 10% of the (relative) mean value indicated.

Demonstrated in Fig. 23 is the extent to which factorization is apparent over a broad range of fragment masses [Ka 80]. The cross section ratios for  $^{14}\text{Na}$  through  $^{196}\text{Au}$  at 4.8 GeV have deviations from a

constant that probably lie within the experimental accuracy of the cross section measurements. At the highest energy, there is an enhancement in the production of the lightest nuclides by 25-GeV  $^{12}\text{C}$  relative to protons of the same energy. However, arguments are made that these fragments tend to be produced in collisions of small impact parameter, i.e. in "central" collisions, for which factorization fails. It should be pointed out, however, that although target fragmentation data lend support to the HLF, the experiments have predominantly been carried out at beam energies  $\lesssim 1$  AGeV, where limiting fragmentation is clearly not established (see Figs. 17 and 19), thus disallowing definitive tests of factorization. As pointed out by Morrissey et al. [Mo 79, 80], strongly divergent excitation energies can lead to similar final product distributions for (light) fragmenting nuclei. The dominating effect in establishing the mass distribution is the deexcitation process (at high excitation energies), with the consequence that the mass distributions may change little as the projectile energy increases from 8 to 25 GeV. Tests for factorization, as previously indicated, seem to make sense only in the energy regime for which limiting fragmentation is established, the latter being done most sensitively by studies of the recoil properties of the target residues.

### 3.3. Electromagnetic Dissociation

The most striking failure in the factorization of the isotopic production cross sections of RHIs arises from the coherent excitation of the projectile nucleus by photoabsorption in the nuclear Coulomb field of the target and its ultimate dissociation by particle emission.

Electromagnetic dissociation of RHI was predicted by Butler and Pearson [Bu 61] and observed in the collisions of cosmic ray RHI



( $10 < \gamma < 1000$ ) in nuclear emulsion by Rybicki [Ry 67].\* Evidence for the electromagnetic dissociation of beam nuclei at  $\gamma \approx 2-3$  has come from single-particle inclusive experiments with projectiles  $^{12}\text{C}$  and  $^{16}\text{O}$  [Li 75, He 76],  $^{56}\text{Fe}$  [We 79], and  $^{18}\text{O}$  [Ol 81], where significant enhancements in the one-nucleon- and (in the case of  $^{18}\text{O}$ ) two-nucleon-loss cross sections are observed for high-Z targets. Fig. 24 is representative of the experimental data that show the presence of a target ( $Z_T$ )-dependent cross section, indicative of an electromagnetic process [Ol 81]. Plotted in Fig. 24 are the beam-rapidity fragment-production cross sections for  $^{18}\text{O}$  projectiles at 1.7 AGeV as a function of the mass number of the target. The cross sections are normalized to unity at  $^9\text{Be}$ . The points labeled  $\gamma_T$  are the target factors for  $^{18}\text{O}$  discussed in Sec. 3.2 and shown in Fig. 21. A geometric approximation  $\gamma_T \approx A_B^{1/3} + A_T^{1/3} - 0.9$  for the target factors is shown by the solid curve. Except for the isotopes  $^{16,17}\text{O}$  and  $^{17}\text{N}$ , the target dependence of the isotopic production cross sections from  $^{18}\text{O}$  that exhibit factorization (Sec. 3.2), hence scale as the target factor  $\gamma_T$ , irrespective of the isotope. This factorable cross section defines the nuclear component,  $\sigma_{\text{nuc}} \equiv \sigma_B^F \gamma_T$ , of the total production cross section  $\sigma$ . In contrast, marked deviations in the cross section ratios from  $\gamma_T$ , up to  $\sim 150\%$  in U, are observed for  $^{16,17}\text{O}$  and  $^{17}\text{N}$ . The observation that the differences between the cross sections and  $\gamma_T$  for these nuclides increase approximately as  $Z^2$  of the target is strong evidence for an electromagnetic effect. Hence, the difference between the total and nuclear (factorable) cross sections is taken to be the electromagnetic cross section  $\sigma_{\text{EM}} \equiv \sigma_{\text{tot}} - \sigma_{\text{nuc}}$ , under the assumption that there is no interference between the nucleon and electromagnetic processes.

Interpretations of the observed enhancements of the 1-2 nucleon-removal cross sections in high-Z targets [He 76, We 79, Ol 81] have been based on the Weizsäcker-Williams (WW) method involving virtual photons [We 34, Wi 35]. In the WW theory, the cross section  $\sigma_{EM}$  for the electromagnetic dissociation of RHIs at velocity  $\beta$  in the nuclear Coulomb field of a target with atomic number  $Z_T$  is given by

$$\sigma_{EM} = \int_0^{\infty} \sigma(\omega) N(\omega) d\omega \quad . \quad (3.10)$$

In this expression  $\sigma(\omega)$  is the measured photonuclear cross section at photon energy  $\omega$ , e.g.  $\sigma(\gamma, n)$ ,  $\sigma(\gamma, 2n)$ , etc., and  $N(\omega)$  is the number density of virtual photons [Jä 75, Ja 75a] given by:

$$N(\omega) = (Z_T^2/\omega\beta^2) F(\beta, \omega b_{min}/\beta\gamma) \quad . \quad (3.11)$$

The only adjustable parameter in  $\sigma_{EM}$  is  $b_{min}$ , the minimum impact parameter, i.e. the impact parameter for which nuclear processes cease to dominate the interaction. Under the assumption that the WW process is dominated by transverse photons at relativistic energies, the virtual-photon spectrum  $N(\omega)$  is the same for all multipolarities. This justifies the use of the cross section  $\sigma(\omega)$  measured with real photons in Eq. 3.10.

The theoretical derivation of  $N(\omega)$  by Jackson [Ja 75a] is a classical development of the WW method for point charges moving at relativistic velocities. Jäckle and Pilkuhn [Jä 75] extended the WW theory to non-relativistic energies and incorporated nuclear absorption and Yukawa charge form factors into the theory. Although the shapes of the spectra  $N(\omega)$  given by these two theories are very similar, the intensities differ by 30-40%. The effect of this difference upon fitting Eq. 3.10 to

experimental cross sections is to yield estimates of the impact parameter  $b_{\min}$  that differ by about 3 fm, with  $b_{\min}(\text{J-P}) \approx b_{\min}(\text{Jackson}) + 3 \text{ fm.}^*$  The values of  $b_{\min}$  deduced from these experiments are closely approximated by the sum of the radii of the colliding nuclei. Hence,  $b_{\min}$  can be given by the expression

$$b_{\min} = r_{0.1}^B + r_{0.1}^T - d \quad (3.12)$$

where the  $r_{0.1}$ 's are the 10% charge density radii of the beam and target nuclei, and  $d$  is the radial-overlap distance.

The electromagnetic dissociation cross sections for  $^{18}\text{O}$  at 1.7 AGeV for various targets Ti through U are tabulated in Table 5. For  $^{16,17}\text{O}$  and  $^{17}\text{N}$ , where photodissociation cross sections are known, the calculated cross sections using the Jäckle-Pilkuhn (with  $d = 1.5 \pm 1.0 \text{ fm}$ ) and Jackson (with  $d = -1.5 \pm 1.0 \text{ fm}$ ) theories are given and compared with experiment. The appropriate photodissociation cross sections for  $^{16}\text{N}$ ,  $^{13,14}\text{C}$  from  $^{18}\text{O}$  have not been measured, hence only the experimental cross sections for these nuclides are given.

The model of electromagnetic dissociation accounts for the following aspects of the data given in Table 5:

i) it identifies those isotopic-production cross sections that are significantly enhanced by photoabsorption in the nuclear Coulomb field of the target.

ii) it yields the correct target dependence for the enhancements in the fragmentation cross sections, taken to be  $\sigma_{\text{EM}} = \sigma_{\text{tot}} - \sigma_{\text{nuc}}$ , and

iii) from the fits of the model to  $\sigma_{\text{EM}}$ , it establishes values of  $b_{\min}$  that limit the radial overlap distances  $d$  of the interacting nuclei to distances comparable to their charge-skin thicknesses,  $t \approx 2 \text{ fm}$ .

Furthermore, the results on the fragmentation of 1.7-A GeV  $^{18}\text{O}$  provide a rather definitive test of the electromagnetic dissociation process for the following reasons: First,  $^{18}\text{O}$  is the only nucleus for which the photonuclear  $(\gamma, n)$  and  $(\gamma, p)$  cross sections can both be measured by neutron counting only [Wo 79]; second,  $^{18}\text{O}$  has an abnormally large  $(\gamma, 2n)$  cross section, comparable to the  $(\gamma, n)$  cross section, the only light nucleus other than  $^{24}\text{Mg}$  with a large  $(\gamma, 2n)$  cross section. Because all three of the photonuclear cross sections have been measured simultaneously using a monoenergetic photon beam [Wo 79], measurements of the nuclear and electromagnetic production cross sections of  $^{16,17}\text{O}$  and  $^{17}\text{N}$  from relativistic  $^{18}\text{O}$  gives a strong basis for testing the electromagnetic dissociation hypothesis.

The observation that the cross section for the production of  $^{16}\text{O}$  (2-neutron removal) is enhanced in high-Z targets, whereas, for instance, 2-proton removal is not, is a unique result for  $^{18}\text{O}$  and essentially confirms the model of electromagnetic dissociation. Measurements of  $\sigma_{\text{EM}}$  for  $^{13,14}\text{C}$  and  $^{16}\text{N}$ , in addition to those predicted for  $^{16,17}\text{O}$  and  $^{17}\text{N}$ , clearly demonstrate that this technique allows one to study all the major photoreaction branchings simultaneously, which is an exceedingly difficult task by conventional techniques. Moreover, and perhaps more important for future experimentation, by the use of secondary heavy ion beams it will be possible to study the photoreactions of  $\beta$ -unstable nuclei, thereby extending photonuclear studies to realms unattainable by conventional techniques limited to stable targets. Experiments now in preparation [Be 79] will undertake coincidence measurements on two (or more) of the reaction products in order to deduce the invariant mass distributions of the daughter nucleus (to  $\Delta M \sim \pm 1$  MeV). This will permit

measurements of the excited-state branching ratios of charged-particle decay modes, which are, again, exceedingly difficult to obtain by conventional techniques.

Thus established by experiment is that the fragmentation reactions of RHIs with target nuclei involve both nuclear and electromagnetic processes. The fact that relativistic projectiles can undergo photodissociation by a "virtual-photon target" at rest in the laboratory portends new dimensions in studies of photonuclear spectroscopy.

#### 3.4. Reaction Characteristics of the Mid-Rapidity Region

From projectile-fragmentation experiments we have learned that for longitudinal and transverse momenta  $\geq 400$  MeV/c (projectile frame) nuclear fragments transform, conceptually, from "spectators" to "participants" in relativistic heavy ion collisions. Geometrically, this transition can be identified with collisions of diminishing impact parameters, the reaction products from which tend to become less and less identifiable with the rapidities of either the target or the projectile. In the limit, therefore, fragment nuclei (as well as produced particles) that populate the mid-rapidity region cannot be identified unambiguously with either the target or projectile. In this section we trace fragment production from momenta just above  $\sim 250$  MeV/c, i.e. near-target rapidities, to the realm of high momenta and large production angles that characterize the mid-rapidity region.

Perhaps the motivation for experimental studies of fragment production in the mid-rapidity region is stated most strongly by the artistic rendition of a collision between nuclei at relativistic energies given in Fig. 25. Illustrated here is the collision between two nuclei where the spectator/participant concept is depicted in its most

elementary, geometric form. From the left a projectile nucleus with velocity  $p_{inc}$  is incident upon a target nucleus at rest, with the collision about to take place at an impact parameter  $b$ . During the collision, the nucleons of the projectile and target within their respective overlapping volumes are cleanly cut away to form what is usually termed a "fireball" of participant nucleons. The remnants of the parent nuclei are the "spectators" to the collision, and they are the constituents of the target fragment and projectile fragment, the latter continuing forward at  $\approx \beta_{inc}$ . The fervent hope is that the blob of nuclear matter formed by the participants in RHI collisions will give rise to new reaction mechanisms and to novel states of nuclear matter produced under the most extreme conditions of matter and energy densities. The reaction products from such a nuclear system would be expected to be quite unrelated to target/projectile phenomena, hence deemed to be the dominant contributors to the mid-rapidity region. It is in this region that the quest for hints of extreme states of nuclear matter has been focused. As we shall see, it has been a difficult and, often, a confusing quest.

#### 3.4.1. Single-Particle Spectra

In contrast with projectile/target fragments, the single-particle inclusive spectra that comprise the bulk of our knowledge of the near-target and mid-rapidity regions are those associated with single- and few-nucleon systems. Although the production of low-baryon-number fragments appears to be a dominant feature of the mid-rapidity region, it is also true that the spectra are limited as to charge, mass, and energy by the experimental techniques employed.

Because the experimental data to be presented in this section are usually compared with one or more of a wide variety of theoretical models

advanced to interpret these data (for instance, the Fireball and its refined successor, the Firestreak, Relativistic Hydrodynamics, Row on Row, Cascade, Coherent tube, and CKO, i.e., clean knockout) we shall briefly describe the essence of the Fireball/Firestreak and CKO models as particular examples that represent the extremum in their assumptions as to the basic mechanisms in RHI collisions: the formation of a fully equilibrated thermodynamic system [Go 77, Go 78, My 78] versus single nucleon-nucleon scattering [Ha 79]. (For details, see J. Maruhn and W. Greiner, this Volume.)

The Fireball: The artistic concept of the collision between nuclei at high energy presented in Fig. 25 symbolizes the Fireball model [We 76, Go 77]. As illustrated, this model assumes that in a RHI collision, the "participating" nucleons in the overlapping volumes of the projectile and target aggregate into a nuclear fireball whose kinematic properties are determined by the condition that the projectile participants transfer all their momenta to the effective center-of-mass system of all nucleons that form the fireball. In this model, the fireball velocity  $\beta$  is equal to the velocity of the center-of-mass velocity  $\beta_{CM}$  of the participating nuclear subvolumes, its value depending only on the impact parameter  $b$  of the collision between the given pair of projectile and target nuclei. The lifetime of the fireball is assumed to be sufficiently long to establish an equilibrated, but nonrotating, ideal Fermi gas of nucleons that expands isotropically in its rest frame with a Maxwellian distribution in energy.

The elementary kinematics of the hypothetical fireball are:

- i)  $\beta_{CM}$ , the velocity of the center of mass of the  $N_P$  and  $N_T$  participant nucleons from the projectile and target nucleus, respectively, that form the fireball is

$$\begin{aligned} \beta_{CM} &= P_{lab}/E_{lab} \\ &= \frac{(\gamma^2 - 1)^{1/2}}{r + \gamma} \end{aligned} \quad (3.13)$$

$$\begin{aligned} \text{where } \gamma &= (1 - \beta_{inc}^2)^{-1/2}, \text{ and} \\ r &= N_T/N_P \end{aligned} \quad (3.14)$$

The ratio  $r$  is a function of the impact parameter  $b$  and of the relative sizes of the projectile and target nuclei, which can be estimated from the geometric volume defined by the intersections of a cylinder with a sphere [Go 77]. Note that when the collision takes place between nuclei of equal mass,  $r = 1$  and  $\beta_{CM} = \sqrt{\frac{\gamma-1}{\gamma+1}}$ , which is independent of  $b$  and equal to the nucleon-nucleon center-of-mass velocity.

ii)  $E_{CM}$ , the total energy in center of mass of the fireball is:

$$\begin{aligned} E_{CM} &= (E_{lab}^2 - P_{lab}^2)^{1/2} \\ &= m'(N_P^2 + N_T^2 + 2\gamma N_P N_T)^{1/2} \end{aligned} \quad (3.15)$$

where  $m'$  is taken to be the bound nucleon mass = 931 MeV.

iii)  $\epsilon$ , the available kinetic energy per nucleon in the center of mass is:

$$\begin{aligned} \epsilon &= \frac{E_{CM}}{N_T + N_P} - m \\ &= \frac{m'}{1+r} (1 + r^2 + 2r\gamma)^{1/2} - m \text{ (MeV)} \end{aligned} \quad (3.16)$$

where  $m$  is the mass of the free nucleon (939 MeV).

For equal mass nuclei,  $r = 1$ , and



$$\epsilon = m' \sqrt{\frac{1+\gamma}{2}} - m, \text{ a constant independent of } b. \quad (3.17)$$

iv)  $\tau$ , the temperature of the fireball corresponding to an equilibrated ideal gas of nucleons is

$$\tau = \frac{2}{3} E \quad (\text{nonrelativistic}) \quad (3.18)$$

From the above expressions, and assuming the momentum distributions of the nucleons in the center of mass is Maxwellian, the Fireball model yields a parameter-free calculation of the proton spectrum.

A refinement of the Fireball concept is found in the Firestreak model [Ha 65, My 78, Go 78a]. In this model the assumption is not that the entire overlap of the participant nucleons from the target and projectile fuse and equilibrate as a unit, but that the fusing and equilibration take place in imaginary, small tubes of nuclear matter, i.e. mini-fireballs, whose individual kinematic and thermodynamic properties follow from "fireball" kinematics appropriate for each tube. The improvement of the Firestreak over the Fireball model is mainly its ability to accommodate the diffuseness of the nuclear surfaces. Conceptually it suffers from the disadvantage that the assumed equilibration must take place over, ever smaller but independent, elements of nuclear volumes.

The CKO Model: The actual physical situation that develops during RHI collisions is certainly beyond the ability of any simple model to describe. The Clean-Knock-Out model [Ha 79] is representative of a class of models that specifically describes the single-scattering component of the inclusive spectrum [Ha 79, Ko 77, Sc 77], for only by an understanding of the "knock-out" component can questions relevant to local thermodynamic equilibrium and nuclear equation of state [Am 77, 77a] be

addressed experimentally. Under the assumption of straight-line trajectories, the average number of collisions experienced by incident high-energy nucleons increases from 2 to 3 for target nuclei of  $A = 20$ , to about 6 for  $A \approx 200$ . It is evident, therefore, that single-scatter mechanisms may well dominate in regions of high momentum transfer, particularly for the light nuclei and in the realm of high  $p_T$  associated with the mid-rapidity region of the inclusive spectrum.

The essential features of the Hatch and Koonin [Ha 79] model are the use of free nucleon-nucleon cross sections and the assumptions of an empirical nucleon momentum distribution in the nucleus of the form  $f(\underline{p}) \sim (p/p_0)/\sinh(p/p_0)$ , with  $p_0 = 90$  MeV/c. This parameterization of  $f(\underline{p})$  is compatible with  $180^\circ$  proton production in p-nucleus collisions [Fr 76, Fr 77, Am 76], and asymptotically approaches  $f(\underline{p}) \sim (p/p_0)\exp[-p/p_0]$ , a form that empirically accounts for the high-momentum behavior of the internal momentum distributions. Because the exponential distribution may also be consistent with the notion of nucleon interaction with "quasi-fragments" in the nucleus, it follows that the CKO model may implicitly include collective phenomena as well as simple nucleon-nucleon scattering.

The knock-out mechanism proceeds via the interaction between nucleons having off-shell four momenta, thereby overcoming an average binding potential to scatter to on-shell final states. By geometric normalization, the CKO model leads to parameter-free calculations of the cross sections for proton production and, by including the  $\Delta(1232)$  resonance in inelastic nucleon-nucleon collisions, for pion production.

3.4.1a. Protons. Figures 26-29 are several examples of the inclusive momentum and energy spectra of protons produced in RHI collisions for various combinations of projectile and target nuclei at

beam energies  $0.24 \leq T \leq 2.1$  AGeV. Figure 26, from the experiments of Nagamiya, et al. [Na 78], gives the proton inclusive spectra for 0.8 AGeV  $^{20}\text{Ne}$  on NaF, a target chosen in this case to simulate collisions between nuclei with equal mass. The proton spectra for  $15^\circ \leq \theta_{\text{lab}} \leq 130^\circ$ , presented as the Lorentz invariant production cross section versus the momentum in the laboratory, monotonically decrease with  $\theta_{\text{lab}}$  and approach an exponential form at high values of momentum. Well demonstrated in this figure is that the proton spectra from RHI collisions depart significantly from those of nucleon-nucleon collisions, in that production of protons with momenta up to twice the beam momentum per nucleon ( $p_{\text{beam}}/n = 1.45$  GeV/c) is observed at the forward angles in this experiment.

These data are remapped in the (rapidity)  $y$ -versus- $p_{\perp}/m_p c$  plane in Fig. 27a, on which the projections of the invariant cross sections  $\sigma_{\text{I}} = Ed^2\sigma/p^2 dp d\Omega$  for proton emission appear as contour plots of invariant cross section. Although the data are not comprehensive enough to populate fully the  $y$ - $p_{\perp}$  plane, they are sufficient to establish the general framework of the contours. On the basis of low- $p_{\perp}$  experiments, i.e., target and projectile fragmentation, and some artistic license, the contours are extended into the unmeasured regions of the  $y$ - $p_{\perp}$  plane in order to reveal the kinematic features of the 0.8 AGeV  $^{20}\text{Ne} + \text{NaF} \rightarrow p + X$  reaction. As anticipated, the contours of  $\sigma_{\text{I}}$  show symmetry about  $\bar{y} = (y_p + y_T)/2 = 0.62$ , the rapidity corresponding to  $90^\circ$  in the center-of-mass frame. For comparison with these data are the contours, shown in Fig. 27b, of an isotropic distribution centered at  $y_{\text{cm}} = 0$ , the rapidity of the center of mass. Strikingly evident, particularly at small  $v = |P|/m_p$ , is that proton emission is not isotropic in the CM frame but

peaks forward and backward from  $\bar{y}$  under the influence of emissions from the target and projectile. Note also that i) the contours for high momenta continue to be broader than those for isotropic emission in the CM and ii) the maximum values of  $P_{\perp}/m_p c$  approach  $v = 1.55$ , corresponding to beam velocity, indicative of multiple collisions and/or collective effects. These observations are incompatible with the production of a unique "fireball" source moving at the rapidity of the CM of two equal-mass participants. A spectrum of effective sources over a broad range of rapidities about  $\bar{y}$  is sufficient to account for the general shape of the contours. The Firestreak model, with its continuum of source velocities, therefore, appears to incorporate an essential refinement to the elementary fireball concept to accommodate experiment.

Proton emission from a heavy target bombarded by  $^{20}\text{Ne}$  as a function of beam energy is shown in Fig. 28 for the reaction  $\text{Ne} + \text{U} \rightarrow \text{protons}$  at  $0.24 \leq T \leq 2.1$  AGeV [Gu 80, Sa 80]. Superimposed on the data are the calculated spectra from the Firestreak model. The dominant disagreement between the experiment and the model calculations occurs at the  $30^\circ$  data, both in slope and magnitude, for all beam energies. Although the agreement is satisfactory at the larger angles and low beam energies, the agreement becomes progressively worse as the beam energy increases.

It has been suggested that the differences between the observed spectra and the Firestreak model at low proton energies could be attributable to Coulomb effects (neglected in the Firestreak model), an effect possibly enhanced by the uranium target in the above data. To address this problem, the  $Z_T$  dependence of the inclusive proton spectra from the 0.4 AGeV  $^{20}\text{Ne}$  bombardment of Al, Ag, Au and U (the latter data are shown in Fig. 28) were measured [Gu 80, Sa 80]. The experimental

result is that the proton spectra do not show significant Coulomb effects and that even for the Al target, where such effects are expected to be negligible, the disagreement between experiment and the Firestreak model persists essentially as illustrated for the uranium data shown in Fig. 28. The salient features of the proton inclusive spectra thus are not accounted for by the Fireball/Firestreak thermal models with their assumptions of straight-line longitudinal trajectories, clean-cut removal of the participant nucleons from the colliding nuclei, and negligible transverse communication between the participant and spectator regions. The lack of a strong  $Z_{\text{target}}$  dependence of the proton spectra is indicative of suppressed Coulomb barriers, and the inclusion of Coulomb effects into these models would not lead to improved agreement with experiment.

The inclusive proton spectra from the C + C and C + Pb reactions at 0.8 AGeV obtained by Nagamiya et al. [Na 78] have been interpreted by Hatch and Koonin [Ha 79] in terms of their single-collision (CKO) model, the antithesis of the thermal equilibrium models. The comparisons of the inclusive proton spectra for these systems with the CKO model are given in Fig. 29. For the C + C system, the data are well reproduced for large  $P_T$ , as one might intuitively expect. However, it is stressed by Hatch and Koonin that this agreement is crucially dependent on the asymptotically exponential internal momentum distribution, a sharper Fermi distribution, e.g.  $\exp[-p/p_0]^2$ , markedly underestimates the spectra at high momentum. In contrast, the proton spectra for the C + Pb reaction are not satisfactorily reproduced by the CKO model, either at the back angle or in most of the low-momentum regions. The spectra are suppressed for both systems at low momentum in the forward direction.

These deviations from the model indicate that multiple nucleon-nucleon scattering, but not necessarily equilibrium, processes are being observed.

That such divergent assumptions as thermal equilibrium and single-scattering mechanisms can lead to qualitative descriptions of the inclusive proton spectra only illustrates the insensitivity of inclusive excitations to the dynamics of the interaction between RHIs. Yet, by considering the typical time scales in RHI collisions and the minimum conditions for the establishment of an equilibrium state, one can mollify the apparently incompatible assumptions. For collisions between nuclei at energies  $\lesssim 1$  AGeV, the relevant time scales of a collision are [Sc 80]:

i) Collision time:

$$\tau_c \sim 2r_0 A^{1/3} / 0.8c \sim 10-20 \text{ fm}/c$$

ii) Relaxation time, the time between nucleon-nucleon collisions:

$$\tau_R \sim 2r_0 / 0.8c \sim 3-4 \text{ fm}/c$$

iii) Interaction time between nucleons:

$$\tau_I \sim r_0 \sim 1-2 \text{ fm}/c$$

Although the inequality  $\tau_I < \tau_R < \tau_c$  is evident, the differences between the characteristic times are not large. However, for the establishment of an equilibrated system described by an equation of state,  $\tau_R \ll \tau_c$ ; for direct, i.e., single-scattering mechanisms,  $\tau_I \ll \tau_R$ . Since neither of these conditions is met in fact, it follows that both mechanisms can be essential features of nuclear collisions, the relative importance of each dependent upon the geometry of the collision, the masses of the target and projectile, and the kinematic regions of the

emitted nuclei. Hüfner (Hü 78a), in addressing the question of "direct" versus "thermal" processes, has pointed out that the approximate number of nucleon-nucleon collisions within a cascade calculation to attain momentum of equilibration is only/the order of  $n_{\text{thermal}} \approx 4$ . He also noted that this is comparable to the calculated number of collisions (3) necessary for each of a system of 100 gas particles to reach equilibrium when emitted from a point in phase space (Ki 58). The implications are clearly that collisions between nuclei should exhibit direct as well as thermal behavior under these limitations. Intranuclear cascade codes, where components attributable to 1, ..., 4 and more collisions can be examined, also show that the attainment of equilibrium is rapid for four and more collisions as exhibited by their approach to Gaussian distributions in momentum [Ra 79].

The proton inclusive spectra thus involve reactions that embody the full range of direct to thermal mechanisms. The extent to which either, or any intermediate, mode is pertinent is subject to experiment. The observation that single-scattering does, in fact, take place in RHI collisions is well established in quasi-elastic, two-particle correlation measurements [Na 81]. The observations sufficient to establish, for example, the characteristic times for the formation, expansion, and the thermal and chemical equilibration of a nuclear fireball are clearly more difficult and less direct. It is for this reason that the experimental evidence for equilibration from the inclusive proton data is not conclusive.

In his summary of the 4th High Energy Heavy Ion Summer Study, Koonin (Ko 78) questioned the possibility that the answers to these problems may actually be attainable from inclusive experiments.

"... are we being fooled by some sort of implicit ergodic hypothesis? Namely, are we implicitly assuming that all particles in one event behave like an average particle in an average event? In other words, the inclusive measurements that we're performing do a gross averaging for us. Not only do they average over all the events we observe, but they also average over all the particles in a given event. I wonder if the dynamics in these collisions are being washed out by our inclusive averaging, and if all that we're really counting in the inclusive measurements is phase space. That is, in fact, a very nice explanation for why we can generate so many different models with so many different dynamic assumptions and still manage to fit the inclusive data. I think that there's a real need to prove the equilibrium event by event. That means rather complicated multiparticle coincidence measurements."

Toward this end, multiparticle coincidence measurements are routinely performed in visual detectors. A recent example of event by event analysis [Ba 81a] has indeed revealed at least two types of events characterized, e.g. in a thermal representation, by drastically different temperatures.

3.4.1b. Neutrons. Experimental information on inclusive neutron production in high-energy heavy ion collisions is presently limited to the measurement by Schimmerling, et al. [Sc 79] for the reaction  $^{20}\text{Ne} + \text{U} \rightarrow \text{n} + \text{X}$  at 0.3 AGeV. This experiment measured the double-differential cross sections for neutron emission in the energy range  $12 \lesssim T \lesssim 600$  MeV at laboratory angles  $30^\circ$  to  $90^\circ$ . These spectra are shown in Fig. 30. The physical content of these data is most conspicuously revealed when they are compared with the cross sections for proton emission from



0.4 AGeV  $^{20}\text{Ne} + \text{U} \rightarrow \text{p} + \text{X}$  [Sa80] and  $^{20}\text{Ne} + \text{Pb} \rightarrow \text{p} + \text{X}$  [Le 79, Na 81],

Fig. 31. Not only does the ratio of the neutron-to-proton cross sections differ significantly from the n/p ratio  $\sim 1.5$  for the Ne + U(Pb) system, but it varies monotonically with neutron energy, decreasing from n/p  $\approx 4$  at 20 MeV to  $\approx 0.3$  at 600 MeV.

The n/p cross section ratio versus particle energy at  $30^\circ$  in the laboratory as given in Fig. 31a is characteristic of the data at all angles. Shown as a dashed curve is the prediction from the firestreak model, which shows a moderate decrease in the n/p ratio, differing from n/p = 1.5 by  $\sim 0.2$  to  $\sim 0.9$  over the energy interval 20 to 600 MeV. The data deviate most strongly from the firestreak model calculation, which considers nucleon production only, with Coulomb effects neglected, at low energies.

Although Coulomb effects were suggested as a possible source of the differences between the neutron and proton spectrum, it was Stevenson [St 80] who pointed out, and was able to demonstrate, that the apparent discrepancy in the n/p ratio is attributable to the influence of the production of light nuclei upon the respective spectra of neutrons and protons. As will be discussed in the following section, copious production of light nuclei from the 0.4 AGeV  $^{20}\text{Ne} + \text{U}$  reaction is observed. As a result, this leads to the emission of more protons (up to 60%) bound in light nuclei,  $A \leq 4$ , from the  $^{20}\text{Ne} + \text{U}$  system than are emitted as free protons, especially at low fragment energies ( $T \lesssim 80$  A MeV) and at forward angles. Because the emitted fragments are predominantly  $T = 0$  ( $N = Z$ ) nuclei, their preferential removal from the neutron-excess system leads to an enhanced n/p ratio; in the limiting case, where all emitted protons are bound in nuclear clusters, the final

system will ultimately consist of neutrons only. By simply taking into account the number of protons and neutrons emitted as fragment nuclei, in addition to the measured yields of the nucleons, the apparent discrepancies between the production cross sections of neutrons and protons are removed. This is illustrated in Fig. 31b where the ratios of the cumulative sums of neutrons to protons (corrected for fragment emission) are shown not to exceed the n/p ratio of the U target nucleus equal to  $\sim 1.6$ . By incorporating the coalescence model for fragment production [Gu 76] into a cascade-model calculation (based on elastic "on-shell" nucleon-nucleon collisions), Stevenson was able to reproduce the essential features of the "pre-coalescence", i.e., corrected n/p ratio. The results of Stevenson's calculations are shown in Fig. 31b as a solid curve.

3.4.1c. Light Nuclei. Early experiments on energetic light nuclear fragments emitted from RHI collisions with heavy nuclei gave immediate evidence for clear-cut differences between heavy ion and proton-induced reactions. Sullivan, et al. [Su 73], by use of plastic detectors, compared the production of light nuclei with  $6 \leq Z \leq 15$  at energies  $1 \leq T_A \leq 5$  AMeV (momenta  $\approx 0.5$  to  $2.5$  GeV/c) from Au bombarded by 2.1-AGeV  $^{16}\text{O}$  and 2.1-GeV protons. They concluded that the  $^{16}\text{O}$  projectile deposits more energy in the nucleus than do protons, resulting in higher temperatures, further suppression of the effective Coulomb barrier, and increased nuclear distortion. The consequence of these effects is to lower both the mean charge and energy of the fragment nuclei (kinetic energies as low as 0.2 of that allowed by the spherical Au nuclear Coulomb barrier are observed), to increase the yield of these low-energy fragments by an order of magnitude, and to affect multiple emission of

heavy fragments  $Z \leq 6$ . For both proton and  $^{16}\text{O}$  projectiles, however, the angular distributions of the fragments were nearly isotropic, although increased forward peaking is observed for the higher energy fragments.

These observations were extended by Crawford, et al. [Cr 75] and Stevenson, et al. [St 77], who measured the energy,  $T \leq 75$  AMeV, and angular distributions for fragments  $Z \geq 3$  produced in the reactions  $2.1\text{-AGeV } ^{12}\text{C} + \text{Au} \rightarrow \text{Z}$  [Cr 75],  $0.5\text{-AGeV Ar} + \text{Au}$  and  $0.4\text{ AGeV Ne} + \text{U}$  [St 77]. Significant features of these data are: i) for fragment kinetic energies  $>150$  MeV, the cross sections deviate markedly from exponential (evaporation-like) distributions, tending to power-law distributions of the form  $T^{-n}$ , where  $n$  increases from  $\sim 2.7$  (boron) to  $\sim 5$  (oxygen); ii) the cross sections rapidly diminish with increasing charge of the fragment; and iii) the angular distributions are approximately isotropic but become increasingly anisotropic (forward peaked) with increasing fragment energies. The latter feature of the production of light nuclei derived from these experiments is illustrated in Fig. 32, which shows the correlation between  $\beta_0$ , the velocity of the moving frame parallel to the beam direction, in which the fragment distribution (taken to be Maxwellian, characterized by temperature parameter  $\tau$ ) is most nearly isotropic and  $\beta'$ , the velocity of the fragment in that particular frame. Evident from these data is that  $\beta_0$ , hence the anisotropy of the angular distribution in the laboratory frame, increases with  $\beta'$ , i.e. energy, of the fragment.

As illustrated in Fig. 32, the source velocities deduced by Stevenson, et al. from the spectra of light nuclei lie in the interval  $\sim 0.04 \leq \beta_0 \leq 0.11$ . These velocities are 5-10 times greater than those observed in target fragmentation studies by radioanalytical methods (Fig.

17), hence imply fundamental differences in their respective production mechanisms. The values of  $\beta_0$ , nonetheless, are significantly less than those expected from the Fireball model. Table 6 summarizes the average velocities  $\langle \beta_0 \rangle$  and thermal parameters  $\tau$  of the emitting sources obtained from thermodynamic fits to the composite fragment data of Stevenson et al. [St 77] and Gosset et al. [Go 77]. Included in Table 6 are the calculated values of these parameters from the kinematics of fireball production.

The salient points given in Table 6 are: i) the source velocities  $\beta_0$  are incompatible with those given by the Fireball model (calculated for the most probable impact parameter), while the experimental and calculated parameters  $\tau$  are in general agreement; ii) for projectile-target "explosion", i.e., the case when the target nucleus completely absorbs the total momentum of the incident projectile, the calculated values of  $\beta_0 \equiv \beta_{CM}$  and  $\tau$  are both reduced, bringing  $\beta_0(\tau)$  into better (poorer) agreement with experiment; and iii) the temperature parameters tend to increase as the mass of the fragment increases.

It was from this apparent incompatibility of the combination of high  $\tau$  and low  $\beta_0$  dictated by the thermodynamic fits to the light fragment data that led Stevenson et al. to conclude the experimental observations were inconsistent with the concept of thermal "fireball" sources, thus implicating the existence of nonthermal processes in fragment emission at intermediate energies  $\approx 0.1$  AGeV.

Recently, Randrup and Koonin (Ra 81) have addressed the problem of composite fragment formation at these energies by employing a statistical model developed to describe the multi-fragment disassembly of highly excited systems of nucleons. They find that a general consequence of

composite fragment formation is to produce temperatures that are substantially higher than expected for a gas of free nucleons at the same energy per nucleon (as was assumed in calculating the fireball parameters  $\tau$  given in Table 6). This comes about because the formation of composite fragments reduces the number of translational degrees of freedom, thereby increasing the effective temperature of the system. Randrup and Koonin show that temperature increases by factors of about two can be reasonably expected in such cases. This argument leads to the prediction of increasing  $\tau$  with fragment mass, which seems to be borne out in the data, Table 6.

These considerations thus allow the possibility that the temperatures given in Table 6, which correspond to a gas of free nucleons, be increased by factors of about two to describe fragment emission properly at the beam energies considered. Consequently, the higher temperatures observed in experiment are indicative of such a suppression in the degrees of freedom. The most striking consequence of this is that the "explosion" mechanism becomes an attractive, and distinctively unique nucleus-nucleus, hypothesis, which appears to account well for the observed low source velocities and high temperatures of light-fragment-emitting systems. The boron spectra from Ne + U at 0.4 AGeV [Go 77], Fig. 33 are representative of the thermodynamic fits that are characterized by  $\beta \approx \beta_{CM}$  of the fused projectile-target system and high  $\tau$ . In this particular example,  $\tau = 27$  MeV, about twice  $\tau_{calc} = 14$  MeV for an explosive collision.

Events observed in nuclear emulsions that could be considered as candidates for projectile-target explosions are shown in Fig. 34ab. In a) the interaction of a 2.1 AGeV  $^{14}\text{N}$  beam nucleus gives rise to 15  $Z = 1$

relativistic secondaries with no low-energy prongs associated with target fragmentation; could this represent the fusing of  $N_7 + O_8$ ? In this event, which was unique in a sample of 3000  $^{12}C$ ,  $^{14}N$ , and  $^{16}O$  interactions [He 78], all  $Z = 1$  fragments were emitted within a  $25^\circ$  forward cone. In b) a similar event is seen to occur, this time with an incident 1.9-AGeV Fe nucleus. This interaction involves the emission of 36  $Z = 1$  and one  $Z = 2$  relativistic particles, all within a  $35^\circ$  cone angle. Events with this topology occur in a small fraction of Fe interactions in emulsion. Such interactions have been subject to an analysis by Bhalla, et al. [Bh 79, Ot 78], who concluded that the angular distributions of charged particles from these types of collisions are incompatible with the clean-cut thermal participant-spectator model, in that too many "spectators" have become "participants".

This is demonstrated in Fig. 35 where the angular distribution of charged particles emitted from  $^{56}Fe$ -CNO interactions (selected on the basis  $N_h \leq 5$ ,  $N_s \geq 26$ ) show almost complete suppression of Fe projectile fragments at  $\eta \sim 1.6$  (indicated by arrow) where they are expected to occur, even for  $b = 0$  collisions. The predictions from a clean-cut fireball breakup, with spectator evaporation, are shown as curves, which emphasize the contradictions with experiment. Explanations of these data must certainly invoke  $p_\perp$  effects that effectively increase the transverse communication between the geometrically defined participant and spectator nucleons, a process that could give rise to the explosion of nuclear matter.

Complementary information on energetic multi-fragment production has come from studies on the emission of fast helium nuclei,  $10 \leq T \leq 250$  AMeV, from heavy ion collisions in nuclear emulsion. A key observation is

that the emission of fast He nuclei is predominantly associated with large stars, indicative of high-target (Ag Br) excitation energies [Ku 73, Ja 76]. The mean multiplicities and energies of He from reactions induced by heavy nuclei ( $12 \leq Z \leq 26$ ,  $T > 1$  AGeV) increase with  $\langle N_h \rangle$  (number of heavy prongs) and  $\langle N_{\pi^\pm} \rangle$ . Up to four to seven fast He nuclei have been observed, where the combined kinetic energies of the fast target-related He particles exceed 1 GeV [Ja 74]. In 2.1-AGeV  $^{16}\text{O}$  induced reactions, 60% of the He fragments having  $T \geq 10$  AMeV are emitted in events with multiplicities of three or more such He nuclei [Ja 76].

The angular distributions of He nuclei from emulsion (AgBr) nuclei are highly dependent on both fragment and beam energies. The distributions are nearly isotropic for He with energies  $\lesssim 10$  AMeV at relativistic beam energies (Ja 76, Ja 77) but become increasingly anisotropic (forward peaked) as fragment energy increases [Ja 77, Ku 73] and/or beam energy decreases [Ja 77]. Similar to heavier fragments, the energy spectrum of He,  $10 \leq T \leq 250$  AMeV, is of the form  $T^{-n}$ , where  $n = 2.5 \pm 0.3$  for 2.1-AGeV  $^{16}\text{O}$  projectiles [Ja 76], a result consistent with the general trend of increasing  $n$  values with increasing fragment mass [Cr 75].

These properties of He emission are exemplified in Fig. 36, which shows how the angular distribution of  $^3\text{He}$  fragments depends on beam energy, the target and projectile masses and the energy window of  $^3\text{He}$  fragment produced in the reactions  $^{20}\text{Ne} + \text{U} \rightarrow ^3\text{He} + \text{X}$  at beam energies  $T = 0.25, 0.4$  and  $2.1$  AGeV [Go 77]. Referring to the angular distributions for  $^3\text{He}$  in the energy interval 30-50 AMeV, the following qualitative conclusions can be made:

i) From curves a,b,c: As the energy of the  $^{20}\text{Ne}$  projectile decreases, the angular distribution of  $^3\text{He}$  becomes increasingly peaked forward.

ii) From curves a,d: The production of  $^3\text{He}$  is strongly dependent on the target, whereas

iii) From curves b,e: The production of  $^3\text{He}$  is virtually independent of the projectile.

Similar behavior is observed in the higher energy window, 50-100 A MeV, the notable difference being the increased forward-peaking of the  $^3\text{He}$  angular distribution.

Crucial to the interpretation of the differences between the energy spectra of neutrons and protons emitted in heavy ion interactions presented in the previous section was the fact that light-fragment production comprises a large fraction of the total baryonic cross section. This is illustrated in Fig. 37, which gives the percentage of the nucleonic charge emitted from 0.4 A GeV  $^{20}\text{Ne} + \text{U}$  in the form of p, d, t,  $^3\text{He}$ , and  $^4\text{He}$ . At fragment energies 30-50 A MeV, ~40 to 60% of the emitted charge is in the form of nuclear clusters, with protons becoming dominant at higher energies and laboratory angles. An impressive experimental observation is that the cross section in velocity space for the emission of a light fragment consisting of A nucleons is proportional to the  $A^{\text{th}}$  power of the cross section for the emission of single protons of the same velocity [Go 77]. This is elegantly demonstrated by the experiments of Nagamiya, et al. [Na 81] on the large-angle production of light nuclei  $1 \leq A \leq 3$  in RHI collisions.

Fig. 38 exemplifies the accuracy to which the  $A^{\text{th}}$  power relationship is satisfied for the spectra of deuterons, tritons, and  $^3\text{He}$  from C + C



interactions at 0.8 AGeV at all momenta and angles. Superimposed on the deuteron spectra is the (normalized) square, and on those for  $^3\text{H}$  and  $^3\text{He}$  the cube of the observed proton spectra, evaluated at equal velocities.

Models that interrelate the production of light nuclei and nucleons in velocity space in this manner are the coalescence [Bu 63, Sc 63, Gu 76, Go 77, Ka 80a] and thermodynamic [Me 80, Me 78, 78a, Me 77, Me 77a, Al 75] models. In the coalescence model, nucleons are assumed to coalesce into a fragment nucleus of mass A when A neutrons and protons are emitted in a reaction with momenta/nucleon that terminate within a coalescence sphere of radius  $p_0$ . The production cross section for fragment A at  $p/A$  (Mev/c) is given by

$$\frac{d^2\sigma}{p^2 dp d\Omega} = \frac{1}{A!} \left( \frac{4\pi p_0^3 \gamma}{3\sigma_0} \right)^{A-1} \left( \frac{d^2\sigma(n)}{p^2 dp d\Omega} \right)^A, \quad (3.19)$$

where  $\sigma(n)$  is the cross section for single nucleon production at momentum  $p = m_n \beta \gamma$  and  $\sigma_0$  is the total reaction cross section. The only adjustable parameter is  $p_0$ . The Ath power relation follows immediately from thermodynamic models that characterize the thermalization of particles at kinetic energy T as  $\propto \exp(-T/\tau)$ , since this expression in terms of  $T/A = f(\beta)$  is  $\exp(-T/A\tau)^A$ . The thermodynamic model leads formally to the same expression as Eq. (3.19).

Nagamiya et al. [Na 81] have expressed Eq. (3.19) in terms of the invariant differential cross sections for the production of the composite fragment A at momentum  $p_A = A p_p$  with  $p_p$  the proton momentum, i.e.,

$$E_A (d^3\sigma_A / dp_A^3) = C_A [E_p (d^3\sigma_p / dp_p^3)]^A \quad (3.20)$$

where  $C_A$  is a constant appropriate for each fragment. The coalescence coefficients observed by Nagamiya, et al. for deuteron production,  $C_2$ , in Ne + NaF collisions at bombarding energies 0.4, 0.8 and 2.1 AGeV are plotted versus deuteron momentum in Fig. 39. Clearly evident from this figure is that  $C_2$ , within the errors of measurement, is independent of the momentum and angle of emission of the deuteron. Furthermore,  $C_2$  is compatible with energy independence; by varying projectile-target combinations,  $C_2$  is found to be dependent on the masses of the projectile and target. Similar conclusions are drawn for  $C_A$  from the  $^3\text{H}$ ,  $^3\text{He}$ , and  $^4\text{He}$  spectra as well.

The predictions for  $C_2$  from the Firestreak model are given in Fig. 39 and are in disagreement with the data. Because of the spectrum of excitation energies (temperatures) that are hypothesized for nuclear collisions in this model, it inherently cannot satisfy Eq. (3.20). But more fundamental than this is the experimental observation that it is the observed proton spectra, rather than the "primordial" proton spectra that exist before the formation of the composite particles, that are pertinent to the coalescence concept. This, in addition to the practical invariance of  $C_A$  to kinematic variables, immediately suggests a form of equilibration is established in the formation and dissociation of composite fragments; hence they are products of final-state interactions. Thus, while the fundamental mechanisms involved in the coalescence model still needs clarification, experiment has yielded evidence for what is, overtly, a most compelling example of an equilibrium-like phenomenon in light fragment production.

### 3.4.2. Associated Multiplicities and Topologically Biased Spectra

That the first generation of RHI experiments on single-particle inclusive spectra has not led to a rigorous theoretical framework to describe them is attributable to the general insensitivity of single-particle data to details of the interaction mechanisms, to the implicit averaging over impact parameters, and to particle correlations in the multiparticle final state. This is manifest in collision events such as that illustrated in Fig. 40, where there can be little doubt that much of the information content in such an event is irretrievably lost when only a single particle of a particular species, selected from among the maze of typically 50-100 secondary fragments, is detected.

The most obvious (and in visual detectors, the most visually obvious) feature of an RHI interaction is the multiplicity of the emitted fragments. Under the plausible assumption that fragment multiplicities are correlated with excitation energies, hence, via cascade model calculations, correlated with impact parameters of the collisions [Sm 77, Ya 79], single-particle spectra from events selected on the basis of their associated multiplicities have been subjected to experimental studies as a means to sharpen the quest for collective phenomena, effects of multiple nucleon-nucleon collisions, etc. in relativistic nuclear collisions.

By associated multiplicity is meant the multiplicity of particles that is associated with the coincident detection of a given fragment in a single-particle inclusive experiment. Associated multiplicities, historically, have been habitually measured in  $4\pi$ -nuclear emulsion detectors by recording the number of target-related fragments,  $n_b$ , having kinetic energies  $\leq 30$  AMeV,  $n_g$ , the number of tracks in the interval 30-500 MeV ( $dE/dx \sim 1.5 dEdx|_{\min}$ ) and  $n_s$ , the number of  $Z = 1$

relativistic (shower) particles with  $dE/dx < 1.5 dE/dx|_{\min}$ . Associated multiplicities in electronic experiments have come to mean the number of fragments deduced from the  $m$ -fold coincidences in azimuthal arrays of detectors. A cutaway drawing of such an array of detectors, used by Sandoval, et al. [Sa 80], is shown in Fig. 41. By this technique, one observes how the multiplicities depend on masses and kinematics of the interacting nuclei and the detected coincident fragment (incident on the movable detector telescope, Fig. 41). It allows one to select, on an event-by-event basis, interactions that satisfy topologies deemed to be characteristic of peripheral and central collisions (e.g., large  $m$  with azimuthal symmetry), asymmetric interactions, coplanarity, etc.

Measurements of associated multiplicities by the techniques described are basically counting devices, hence, except for minimum-energy cutoffs and detector thresholds, contain no information as to energy, charge or mass of the incident particle. Resolving the associated multiplicities into nuclear ("pre-existing") and mesonic ("produced") components is therefore not possible; as a result, the fundamental, if not crucial, role of associated pion emission in heavy ion collisions cannot be addressed. Another technical difficulty with the detector arrays used to date (and which the large plastic-ball, plastic-wall device is being designed to overcome ([Ma 79]) is to estimate reliably the true multiplicity from the  $m$ -fold associated multiplicity detected for a given event. "True" average multiplicities,  $\langle M \rangle$ , however, can be estimated by Monte Carlo techniques and/or by corrections for missing solid angle, coincidence summing, and accidental and dead time probabilities under the simplest assumptions of uniform azimuthal distributions and no correlations in particle emission [Sa 80, Na 80].

Figure 42 presents the average associated multiplicities emitted from a U target, associated with a coincident proton  $40 < T < 200$  MeV detected in the detector telescope at  $90^\circ$  to the beam direction, plotted as a function of the total kinetic energy for projectiles of different mass. To first approximation  $\langle M \rangle$  depends only on the total kinetic energy,  $T$ , of the projectile and not, for example, on the kinetic energy per nucleon,  $T/A$ . The  $\langle M \rangle$  vs  $T$  relation does not exhibit any structure attributable to the threshold for pion production. Furthermore, the scaling of  $\langle M \rangle$  with total kinetic energy has been observed to be independent of the charge of the detected fragment  $4 \leq Z \leq 33$  in the reactions  $8\text{-AGeV } {}^{20}\text{Ne} + \text{Au [Me } 80\text{q}]$ .

That the total kinetic energy of the projectile is the relevant kinematic variable in ordering the mass yield curves obtained in radioanalytical experiments on target fragmentation for a wide variety of targets, projectile masses and energies has been stressed in Sec. 3.1.3. Because the associated multiplicities are predominantly those of light, energetic fragments from the target, they are the complements of the residues of the target nuclei, hence related to the mass yield curves.

The straight line in Fig. 42 is a power law fit ( $\langle M \rangle = 3.7 T^{0.72}$ ). The dashed line on the same figure is the dependence of the mean number  $\langle A' \rangle$  of nucleons of the projectile involved in a collision with a  ${}^{238}\text{U}$  target\* on the projectile mass  $A_p$  ( $\langle A' \rangle = 0.75 A_p^{0.8}$ ). The fact that these lines are almost parallel makes it difficult to interpret the "T-scaling" in terms of collective effects. Indeed, if the multiplicity in a nucleon-nucleon collision would depend more or less linearly on primary energy, i.e., on the Lorentz factor  $\gamma$  of the projectile, an independent nucleon model of AA collisions would lead to  $\langle M \rangle \sim A' \gamma$ , which is borne out by the data. Thus, if any cooperative effects would be

present at these (still relatively low) primary energies they are of more subtle magnitude and their detection would require experiments of higher accuracy.

Intriguing events of the type  $^{20}\text{Ne} + \text{Ag} \rightarrow Z = 26 + X$  at beam energy 0.4 AGeV have been observed by Meyer et al. [Me 80a], where the transverse momenta of the  $Z = 26$  fragments, detected at  $90^\circ$  in the laboratory, have  $p_\perp$  up to  $\sim 2$  GeV/c, and where the associated fragments are highly asymmetric in azimuth indicative of momentum conservation. At beam energy per nucleon of 0.4 GeV ( $p = 0.94$  GeV/c), the impossibility of transferring  $p_\perp \sim 2$  GeV/c in a single nucleon-nucleus interaction clearly dictates that such events involve cooperative interactions between the nucleons of the colliding nuclei.

The dependence of single-particle inclusive spectra on the associated multiplicities has been examined as a means to interrelate spectral features and associated emission patterns with impact parameter [Na 80, St 80]. Because the associated multiplicities cannot lead to quantitative estimates of the true multiplicities nor of the limits in impact parameter, "low" and "high" cuts in the associated multiplicities of charged particles have been made to classify the multiplicity-biased spectra as representative of peripheral-like and central-like collisions, respectively [St 80a]. The spectrometer system employed by Nagamiya et al. [Na 78, 79] included a 9-set array of tag counters placed approximately symmetric in azimuth at  $40^\circ$  with respect to the beam direction. The tag counters, each of which subtended  $\Delta\theta = 10^\circ$  and  $\Delta\phi = 22^\circ$ , recorded energetic particles equivalent to  $T_{\text{proton}} \gtrsim 100$  MeV. The angular and momentum distributions of protons in the reaction  $0.8\text{-AGeV Ar} + \text{Pb} \rightarrow p + X$  as a function of the observed associated tag-counter multiplicities

measured by Nagamiya, et al., are shown in Figs. 43 and 44. By Monte Carlo calculations,  $M_{\text{tag}} \geq 5$  corresponds to  $\langle M_{\text{true}} \rangle \approx 49$  for the Ar + Pb system under the assumption all particles are protons. Because the total yield of  $\pi^{\pm}$  mesons is about 20% at this energy, refinements in the estimates for  $M_{\text{true}}$  are possible but not essential for the comparisons made in these figures.

Figure 43 illustrates how the angular distributions of protons,  $T \geq 100$  MeV, vary with  $M_{\text{tag}}$ . The inclusive data (i.e., no multiplicity tag) show a strong forward peaking, which becomes increasingly suppressed as the multiplicity  $M_{\text{tag}}$  increases. The forward suppression of spectra associated with high multiplicities, i.e. "central" collisions, as we shall see, is also characteristic of particle emission at lower energies [He 78, St 80]. A graphically more informative presentation of these data is shown in Fig. 44. Here the invariant cross sections are plotted as contours in the rapidity  $y$  versus  $p_{\perp}/m_{\text{p}}c$  plane, where the high multiplicity-biased spectra and the unbiased inclusive spectra can be compared. Whereas the inclusive data are highly influenced by fragments of the target ( $y_{\text{T}}$ ) and projectile ( $y_{\text{p}}$ ) at small  $p_{\text{T}}$ , contributions from projectile fragments to the proton spectrum associated with high multiplicities,  $M_{\text{tag}} \geq 5$ , have essentially disappeared. The reason for the suppression of proton emission at forward angles noted previously is thus apparent.

The contours of the invariant cross sections in Fig. 44 show that the angular distributions of high energy protons tend to symmetry about  $y_0 = 0.43 \pm 0.03$ , which corresponds to an effective  $\beta_{\text{CM}} = 0.405 \pm 0.025$ . Assuming "fireball" kinematics (Sec. 3.4.1), this value of  $\beta_{\text{CM}}$  is that expected when  $A' = 80 \pm 10$  nucleons of the Pb target effectively absorb

the full momentum of the incident 0.8 AGeV  $^{40}\text{Ar}^-$  nucleus, forming a fireball of  $\sim 120$  nucleons. The  $80 \pm 10$  participant nucleons of the target is compatible with the number of nucleons of a Pb nucleus that is geometrically overlapped by a  $^{40}\text{Ar}$  nucleus at an impact parameter  $b = 0$ , which, following Swiatecki [Go 77], is  $A_T'(b = 0) = 95$ .

The qualitative features of the high multiplicity-biased inclusive proton spectra, e.g., the increased suppression of the projectile fragments as  $M_{\text{tag}}$  increases and, for the highest proton energies, the approach to an isotropic distribution in a frame moving with rapidity  $y_0 \approx y(\text{CM})$ , indicate that these spectra are predominantly attributable to collisions involving the highest levels of excitation (hence, indicative of small  $b$ ), with strong collective effects and/or multiple nucleon-nucleon collisions.

---

Similar conclusions have been presented by Stock, et al. [St 80], who compared the emission patterns of protons,  $12 \leq T \leq 210$  MeV for "low" and "high" associated multiplicities, i.e. associated multiplicities that comprised the lower and upper 15% of the integral distribution of multiplicities. In terms of the  $y$  vs  $p_{\perp}/m_p c$  plane (see Fig. 44), the emitted protons considered by Stock, et al. were kinematically confined to the region bounded by  $y \approx \pm 0.5$  and  $p_{\perp}/m_p c \gtrsim 0.7$ , i.e., to near-target rapidities. Salient features of these proton spectra associated with high and low multiplicities are

For heavy targets (Ag to U):

- i) The invariant proton cross sections at low momenta are compatible with isotropy, the centers of which indicate source velocities that increase monotonically with transverse momentum. No unique source for proton emission is observed.



ii) For high multiplicities, the (central) collisions tend to form highly excited systems with relatively low source velocities. This indicates a transverse spreading of the incident energy throughout the heavy nucleus in contradistinction to longitudinal localization of energy deposition assumed in geometrical models. This leads to a suppression in the forward emission and, in addition, to new evidence for a momentum-dependent sideward peaking of the protons in the angular region  $30^\circ$  (at  $p \sim 625$  MeV/c) to  $\sim 90^\circ$  (at  $p \sim 150$  MeV/c). Similar peaking has previously been reported by Schopper et al. [Sc 78, Ba 75] in the angular distribution of low energy  $Z = 1, 2$  fragments emitted from high-multiplicity stars in AgCl (visual) detectors irradiated by high energy  $^4\text{He}$  and  $^{12}\text{C}$  nuclei.

For the case when the projectiles and targets are of equal mass ( $^{40}\text{Ar} + ^{40}\text{Ca}$ ), the contours of the invariant cross section associated with high-multiplicity events are mainly dominated by the apparent decay of a mid-rapidity source, consistent with  $y_{\text{CM}} = (y_{\text{P}} + y_{\text{T}})/2$  of the nucleon-nucleon system. No sideward peaking in the protons is observed in the collisions between equal-mass nuclei.

Rather than on the basis of high associated multiplicities, interactions deemed characteristic of small impact parameters have also been selected on the criterion that they exhibit the absence of beam-velocity fragments within the forward projectile-fragmentation cone [He 78, Ba 80]. In the nuclear emulsion experiment of Heckman, et al., this criterion was used to select "central" collisions initiated by 2 AGeV beam nuclei, where a  $5^\circ$ -fragmentation cone was adopted. This established an angular void several times greater than the measured standard deviation of the angular distribution of projectile fragments [He 78a], thereby

insuring that all (or nearly all) of the nucleons of the projectile interacted strongly in the target nucleus.

Track ranges and angles were measured over  $4\pi$  steradians for fragments with residual ranges  $0.01 \leq R \leq 4$  mm. This range interval corresponds to protons and  ${}^4\text{He}$  with kinetic energies  $1 \leq T \leq 31$  AMeV, thus extending "central-collision" emission spectra to energies and rapidities below the cut-off thresholds of the previously discussed experiments.

By evaluating for each fragment range,  $R$ , the equivalent proton (or  ${}^4\text{He}$ ) velocity,  $\beta$ , through the power-law expression

$$\beta = 0.174 (R Z^2/A)^{0.29} , \quad (3.21)$$

where  $Z^2/A = 1$  for protons and  ${}^4\text{He}$ , the range-angle data can be presented in terms of the rapidity variable. This is done in Fig. 45, where the measured rapidity distributions of the low-energy fragments emitted from "central" collisions between  $\sim 2$  AGeV  ${}^4\text{He}$ ,  ${}^{16}\text{O}$ , and  ${}^{40}\text{Ar}$  and emulsion nuclei are shown. The mean values  $\langle y \rangle \approx \langle \beta_L \rangle = \beta_{||}$  give source velocities of the three distributions in the interval  $\beta_{||} = 0.014 \pm 0.02$ , and the mean standard deviation  $\langle \sigma \rangle = 0.082 \pm 0.001$ , with no evidence for dependence on the projectile. The curves fitted to the data are covariant, nonrelativistic Maxwell-Boltzmann distributions, where  $\beta_{||} = \langle y \rangle$  and  $\sigma = \sqrt{\tau/M_n}$ . With  $M_n$  the nucleon mass, the distributions correspond to Maxwellian temperatures  $\tau \approx 6-7$  MeV. These data continue the trend of decreasing excitation energies and source velocities with decreasing fragment energies. Note that the longitudinal source velocities are comparable to those observed in radiochemical experiments and that the  $\tau$  derived from these data is characteristic of temperatures associated with

the binding energies of nuclei and with projectile fragmentation [Gr 75, Go 74].

The angular distributions observed for fragments with energies  $T < 31$  AMeV are shown in Fig. 46. The distributions are presented as functions of both  $\theta$  and  $\cos\theta$ . Drawn through the data are curves derived from the fitted Maxwell-Boltzmann distributions; the fitted parameters  $\beta_{\parallel}$  and  $\beta_{\circ} = \sqrt{2T/M_n}$  apply to the solid curves. The distributions of  $dN/d\cos\theta$  consistently show greater isotropy in the forward, relative to the backward, hemisphere. In the case of  $^{16}\text{O}$ , the fits to the data in the backward and forward hemispheres illustrate these differences. It is clear that the angular distributions can be accounted for by a general suppression of particle emission in the forward direction and/or an enhanced emission near  $90^\circ$ . Both effects have been found to be characteristic of the high-multiplicity data at higher proton fragment energies, and it is rather surprising that similar behavior still persists in the very low energy fragment data.

In summary, we have seen that experiments on charged-particle multiplicities and multiplicity-(or topologically) biased single-particle spectra have revealed new aspects of RHI collisions not deduced from inclusive experiments. The overriding conclusion to be drawn from these experiments is the importance of transverse communication between the nucleons of the target and projectile, whether manifest in

- i) the total kinetic-energy dependent multiplicities, or
- ii) the production of high- $p_{\perp}$  heavy clusters, or
- iii) the apparent stopping of the interacting nucleons of the target and projectile in their CM systems, or

- iv) the complete eradication of beam-velocity fragments from the projectile-fragmentation cone, which may be related to
- v) the increased suppression of particle emission in the forward hemisphere with increased associated multiplicities, and
- vi) the systematic observations of sideward peaking of  $Z = 1$  and 2 fragments at laboratory angles  $30-90^\circ$ .

Although hydrodynamical calculations tend to give overall agreement with these data [St 80, St 79a, 80b], it is evident that these phenomena are not solely due to kinematic effects alone. There can be little argument that hints of new, and perhaps unconventional, reaction mechanisms are present in these data. The tasks at hand are to ferret them out with improved and imaginative experiments and, obviously, theory.

### 3.5 Source Sizes

#### 3.5.1. Boson-Boson Correlations: Pion Interferometry

Cocconi [Co 74] and, independently, Kopylov, Podgoretsky and co-workers [Ko 74, Ko 74a] pointed out that the principle of intensity interferometry, an astronomical technique developed and used by Hanbury-Brown and Twiss [Ha 56] to measure the apparent angular diameter of optical and radio sources, can also be applied equally well to systems of hadronic dimensions. In analogy to the Hanbury-Brown-Twiss (HBT) effect, the correlations between simultaneously emitted identical bosons, i.e. pions, can, in fact, be used to determine the space-time dimensions of the interaction region from which they are emitted.

The basic concepts of intensity interferometry or, in the present context, pion interferometry are illustrated in Fig. 47. Schematically represented in this figure is an event in which a pion,  $\pi_1$ , with four-momentum  $p_1$  is detected at space-time  $x_1$ , in coincidence with a

second pion  $\pi_2$  with  $p_2$  at  $x_2$ . Under the assumption that the source of the pions extends over space and time, the coincident event can occur in two ways; either  $\pi_1$  is emitted from  $r_1$  and  $\pi_2$  from  $r_2$  (solid lines) or  $\pi_2$  is emitted from  $r_1$  and  $\pi_1$  from  $r_2$  (dashed lines). Because the two possible configurations are indistinguishable in producing a coincidence, the total amplitude  $\psi$  of the event is, for pions, the sum of the partial amplitudes. Assuming plane-waves, the coincidence rate is proportional to the probability

$$|\psi(p_1 \text{ at } x_1, p_2 \text{ at } x_2)|^2 \propto 1 + \cos[(p_1 - p_2) \cdot (r_1 - r_2)] \quad (3.22)$$

with  $p = (E, \vec{p})$  and  $r = (t, \vec{r})$ , we have

$$|\psi|^2 \propto 1 + \cos[q_0(t_1 - t_2) - \vec{q} \cdot (\vec{r}_1 - \vec{r}_2)], \text{ where} \quad (3.23)$$

$$q_0 = E_1 - E_2 \text{ and } \vec{q} = \vec{p}_1 - \vec{p}_2.$$

Thus, the coincidence rate measured as functions of  $q_0$  and  $\vec{q}$  for pairs of like pions will exhibit a modulation, i.e., a second-order interference effect, from which the characteristic dimensions and lifetimes of pion-emitting sources can be determined.

Because  $r_1$  and  $r_2$  represent only two distinct emitters that make up the entire source, the observed coincidence rate,  $R$ , is obtained by integrating  $|\psi|^2$  over the space-time distribution function  $\rho(r)$  of the source, i.e.,

$$R = \int |\psi|^2 \rho(r_1) \rho(r_2) d^4 r_1 d^4 r_2 \sim 1 + |\rho(q_0, \vec{q})|^2, \quad (3.24)$$

where  $\rho(q_0, \vec{q})$  is the Fourier transform of the assumed pion source function.

Analytic expressions of R commonly employed to extract the characteristic space-time parameters of the source from experimental data are based on i) a uniform emission of pions from the surface of a sphere [Co 74, Ko 74, Ko 74a] and ii) a Gaussian distribution of the form  $\rho(t,r) \sim \exp\{-r^2/r_0^2 + t^2/\tau^2\}$ , which results in a coincidence rate given by

$$R(q, q_0) = K \left[ 1 + \exp\left(-\frac{\tau^2 q_0^2}{2} - \frac{r_0^2 q^2}{2}\right) \right], \quad (3.25)$$

where K is an arbitrary normalization constant and  $r_0$  and  $\tau$  are the characteristic space-time parameters [Ya 78]. The properties of the above expression for R are quite general, irrespective of the assumptions about the intrinsic distribution of the source, although the physical interpretations of  $r_0$  and  $\tau$  will tend to be model dependent. Several qualitative features of  $R(q, q_0)$  that should be noted are:

- i) For like pions there is constructive interference, an effect of Bose-Einstein statistics, as  $\vec{q} \rightarrow 0$ , i.e. the pions have equal momentum vectors, and as  $q_0 \rightarrow 0$ , i.e. the pions have equal energy.
- ii) As either  $q_0$  or  $\vec{q}$  increases,  $R(q, q_0)$  decreases from a maximum value of 2 at the origin, monotonically approaching a plateau value of 1 for  $q_0 \gg \tau^{-1}$  and/or  $|q| \gg r_0^{-1}$ .
- iii) As discussed by Deutschmann et al. [De 76], the angular dependence of the second-order interference effect allows for the possibility that, by examining pion pairs emitted in appropriately chosen solid angles, the shape of the source can be determined.
- iv) Although the parameter  $\tau$  can be identified with the lifetime of the source as a whole, Cocconi [Co 74] has suggested that the characteristic length  $\delta = c\tau$  might well represent the depth of the

"photosphere" of the pion-emitting source, analogous to an astronomical interpretation. The value of  $\delta$ , although conceivably dependent on direction of emission, would necessarily be  $\lesssim r_0$  in this case.

The most critical aspect of an experimental measurement of the two-particle correlation function is the determination of the background distribution in the absence of Bose-Einstein correlations. Two procedures have been adopted to deduce this background. The first is to normalize (bin by bin) the distributions of like-pions (e.g.  $\pi^-\pi^-$ ) by the corresponding distributions of unlike-pions ( $\pi^+\pi^-$ ). The second procedure, suggested by Kopylov [Ko 74], is to carry out this normalization by selecting each like-pion from different events. The former technique has been used almost exclusively in particle physics experiments [De 76, Gr 76, Ca 76]. However, owing to low pion multiplicities, differential Coulomb effects for the  $\pi^+$  and  $\pi^-$  in the nuclear Coulomb field, and experimental limitations [Bi 80], the latter (Kopylov) method for establishing the noncorrelated background has been employed in RHI experiments [Fu 78, Bi 80, Lu 81]. Although the selection of pions from different events clearly establishes them to be uncorrelated, there are inherent difficulties that must be considered. Momentum conservation, for instance, is not satisfied in this method. However, it is generally assumed that the large number of final-state particles (nucleons, light nuclei, and pions) associated with heavy ion reactions tend to minimize any possible distortions to the background spectra so derived. Indeed, the procedures by which one actually fabricates a noncorrelated background spectrum from the  $N$  uncorrelated pions [which can yield anywhere from  $N/2$  to  $N(N-1)/2$  simulated pairs] are not standard, are dependent on each

experiment, and, hence, can lead to ill-defined statistical and systematic errors. The uncertainty thereby introduced into the background spectrum that is adopted in an experiment to extract a two-particle correlation function and, hence, the resultant parameters  $r_0$  and  $\tau$  of the source derived therefrom has yet to be fully assessed. It is with these reservations in mind that we consider the following experiments, which have given us the first tantalizing glimpses of the sizes and lifetimes of the sources of pion emission in high-energy baryonic collisions.

Experimentally, the Gaussian  $2\pi^-$ -correlation function that explicitly includes the background distribution  $R_D^{--}(q, q_0)$ , a notation that indicates the two  $\pi^-$  are from different events ( $R_S^{--}$  indicates they are from the same event) is defined as

$$R^{--} = \frac{R_S^{--}(q, q_0)}{R_D^{--}(q, q)} = K \left[ 1 + \lambda \exp \left( -\frac{\tau^2 q_0^2}{2} - \frac{r_0^2 q^2}{2} \right) \right] . \quad (3.26)$$

Here, the parameter  $\lambda$  is included to represent the degree to which the pion emitters are statistically independent, thus indicative of the degree of coherence of the emitting system [Fo 77]. In the "chaotic" limit,  $\lambda \equiv 1$  [Gy 79].

The first application of pion interferometry to RHI collisions was by Fung et al. [Fu 78], who used the LBL streamer chamber to study  $2\pi^-$  correlations in the reactions of 1.8-AGeV  $^{40}\text{Ar}$  beams with heavy nuclei. Representative of these data is Fig. 48, which shows the ratio  $R^{--}$  versus  $q(\text{MeV}/c)$  for events from a  $\text{Pb}_3\text{O}_4$  target triggered in a "central collision" mode that selected high-multiplicity events, accounting for  $\sim 15\%$  of the total number of interactions. The data show a clear enhancement at low values of  $q$ . The parameters extracted from this



interference pattern by maximum likelihood, given Eq. (3.26), are listed in Table 7. The multiplicities of  $\pi^-$  observed in these collisions were  $2 \leq N_{\pi^-} \leq 15$ . Subsequently, pion-interferometry analyses of these data were made for subgroups of events having different pion multiplicities [Lu 81]. Referring to Table 7, the pion source radius  $r_0$  is seen to increase from about 3 to 6 fm as the pion multiplicity increases from the lowest (2-4) to highest (13-15) values. (Because of the insensitivity of the value of  $r_0$  to the lifetime parameter,  $c\tau$  is set to 1.5 fm in the analyses of the  $\pi^-$ -multiplicity subgroups.)

A salient feature of the  $r_0$  parameter is that it is comparable to the radius of the  $^{40}\text{Ar}$  projectile nucleus  $\approx 1.2 A^{1/3} = 4.1$  fm, incompatible with the values of  $r_0 \approx 1$  fm deduced from pp [Ez 77] and  $\pi\pi$  [De 76] collisions. The monotonic increase in  $r_0$  with pion multiplicity indicates a direct correlation between the size of the pion source with the degree of excitation energy in the collision. Geometrically, this can be associated with diminishing impact parameters and greater overlap of the interacting nucleon volumes. Although the errors in the values of  $r_0$  are large, it is of interest to point out that the multiplicity  $N_{\pi^-}$  appears to be proportional to  $r_0^3$ , hence to the volume of the pion-emitting source. Lu et al. compared their observations with the predictions of the thermodynamic fireball model of Gyulassy and Kaufmann [Gy 78] for the dependence of the pion multiplicity upon  $r_0$ , the mean fireball radius. The relationship between  $N_{\pi^-}$  and  $r_0$  is a function of the assumed freezeout density  $\rho_c$ , i.e., the critical nuclear density of the expanding fireball below which further pion production and absorption ceases. They conclude that the  $r_0$  data are more compatible with  $\rho_c \approx \rho_0$  (normal nuclear density) than with the typically assumed values of

$\approx \rho_0/3$  [Go 78]. As mentioned by Lu et al., however, the experimental values of  $r_0$  follow directly from Eq. 3.26, devoid of corrections for the relative Coulomb interactions between the pions (in their center-of-mass), Coulomb effects owing to the nuclear charges and possible final-state interactions.

That such corrections may be significant comes from the analysis by Bistirlich et al. [Bi 80] of their experiment on  $2\pi^-$  and  $2\pi^+$  correlations in the (equal projectile-target mass) reaction  $^{40}\text{Ar} + \text{KCl} \rightarrow 2\pi + X$  at 1.8 AGeV. This experiment employed a magnetic spectrometer system to measure the momenta of the like-pions in the momentum range  $200 \leq p \leq 800$  MeV/c emitted within a solid angle  $\sim 0.1$  msr at laboratory angles  $40-50^\circ$ . Bistirlich et al. incorporated into their analysis the Coulomb corrections cited above, finding that the  $2\pi$  relative Coulomb interaction between the pion pair is dominant. For low relative momentum in the 2-pion center-of-mass,  $q_{\text{rel}}$ , Coulomb repulsion between the pions suppresses the number of events in the observed ratio  $R(q, q_0)$  at low values of  $q$ . The correction for this effect is given by the expression  $n_{\text{corr}}(q) = G(\eta)^{-1} n_{\text{obs}}(q)$ , where  $n(q)$  denotes the density of events at  $q$  and  $G(\eta)$  is the Gamov function given by [Gy 78]

$$G(\eta) = \frac{2\pi\eta}{e^{2\pi\eta} - 1}, \quad \text{with } \eta = \frac{m_\pi c}{137 q_{\text{rel}}}. \quad (3.27)$$

At  $q_{\text{rel}} = 5$  MeV/c, for example,  $G(\eta) = 0.5$ , which means the suppression of events by the Coulomb repulsion between the pions at this relative momentum suffices to cancel any Bose-Einstein enhancement. Because of the sensitivity of  $G(\eta)$  on  $q_{\text{rel}}$ , the Gamov correction is applied on an event-by-event basis. The effect of the Gamov correction on the correlation function is illustrated in Fig. 49 and, hence, on the

estimates of  $r_0$ , given in Table 7, where the corrected values of  $r_0$  (with  $c\tau \equiv 1.5$  fm) obtained by Bistirlich et al. are roughly twice as large as the uncorrected values of  $r_0$ . Allowing the parameter  $\lambda$  to vary does not significantly change  $r_0$ , but the Ar + KCl data do indicate that  $\lambda < 1$ , implying that some coherent processes of pion emission may be present (Sec. 4.2).

To compare the heavy ion results with those from hadronic ( $B = 0,1$ ) collisions, the representative data of Ezell et al. [Ez 77] (pp) and Deutschmann et al. [De 76] ( $\pi^\pm p$ ) are included in Table 7. The qualitative trend is that the size of the pion source in these more "elementary" collisions are  $\sim 1$  fm  $\approx \hbar/m_\pi c$ , with transverse radii  $r_\perp$  apparently larger than radii  $r_\parallel$  characteristic of the longitudinal (beam) direction. The pionic fireball thus seems to be "pancake" shaped. Within the accuracies of all measurements, the lifetime parameter  $c\tau$  is less than  $r_0$ , and it may even depend on the direction of emission, compatible with the "photosphere" interpretation.

Demonstrated by these initial experiments on pion interferometry in RHI collisions is that the space-time structure, and even coherence, of the pion-radiating sources are amenable to experimental study. Not only have they shown that the lifetime and radius parameters can be extracted from two-pion events, they also have shown them to be sensitive to the relative ( $\pi\pi$ ) Coulomb effects, but less so to the external (nuclear) Coulomb interactions [Bi 80]. In parallel with the obvious need for improved experiments and statistical accuracies necessary to reveal the actual shapes of the sources must come refinements in the methods analysis (particularly relevant to procedures for evaluating the non-Bose-Einstein background and the distorting influence of coherent sources). The

observed correlation of  $\pi^-$  multiplicities with  $r_0$  would seem to give great impetus to these studies.

### 3.5.2. Two Proton Correlations

Recently the problem of the size of the source of secondaries in RHI collisions has been approached in a manner similar to the HBT-type experiments described in the previous section but with a different physical content. Instead of looking at newly produced particles, this experiment [Za 81] measured correlations between two protons emitted from 1.8 AGeV Ar + KCl collisions. A magnetic spectrometer was tuned to record either a bite of phase space near mid-rapidity or one near beam rapidity (Fig. 50). A set of "multiplicity" counters, used to select "impact parameters", looked at a quite different region of phase space, close to target rapidity.

The correlation function  $R$  defined via the one- and two-particle differential cross sections

$$\frac{d^2\sigma}{d^3p_1 d^3p_2} = \frac{1}{\sigma_T} \frac{\langle n(n-1) \rangle}{\langle n \rangle^2} \frac{d\sigma}{d^3p_1} \frac{d\sigma}{d^3p_2} (1 + R) \quad (3.28)$$

is plotted in Fig. 51 against the momentum difference between the two protons. A comparison with theoretical predictions [Ko 77] leads to estimates for the radius of the source volume of  $\sim 3.5$  fm in the beam-rapidity measurement and to  $\sim 2.8$  fm at mid-rapidity. The former result is comparable to the radius of the incoming Ar nucleus. However, the latter value is too small to be easily interpretable in terms of a fireball comprising a sizeable fraction of the participating nucleons; it is also at variance with the estimate for the same radius derived from

two-pion correlations with the same projectile-target combination at the same primary energy [Fu 78].

In interpreting this result one must bear in mind the fact that, whereas in boson-boson correlations quantum interference (i.e. HBT-) effects are the determining factor, proton-proton correlations are dominated by nuclear (attractive) and Coulomb (repulsive) forces. It is the interplay of these two effects that gives rise to the maximum in the curves of Fig. 51 and to the fact that the source radius is related to the height rather than to the width of the maxima.

A word of caution is also in order concerning the statistical factor  $\langle n(n-1) \rangle / \langle n \rangle^2$  in Eq. 3.28. Indeed, the moments of the proton multiplicity distribution as sampled by this experiment are a priori unknown (the multiplicity counters sampled a different region in phase space) and setting the factor equal to unity amounts to assuming that the proton multiplicity distribution is Poissonian, a fact still to be confirmed.

### 3.5.3 Composite-Particle Emission

Under the assumption that thermodynamic equilibrium is established in a source volume  $V$ , a thermal model for composite-particle emission leads to a relation between  $V$  and  $C_A$ , the proportionality constant in Eq. 3.20 [Le 79, Na 81, Me 77, 78, 78a];

$$V \propto \left( \frac{1}{C_A} \right)^{\frac{1}{A-1}} \quad (3.29)$$

The volume  $V$  evaluated for 0.8-AGeV C, Ne, and Ar beams by Nagamiya, et al. can be expressed in terms of the equivalent radius  $R$  by the empirical expression

$$R = r_1 + r_2 (A_T^{1/3} + A_P^{1/3}) \text{ fm} \quad (3.30)$$

with

$$r_1 = 2.0 \pm 0.2 \text{ fm } ({}^2\text{H})$$
$$= 1.6 \pm 0.2 \quad ({}^3\text{H} \text{ and } {}^3\text{He})$$
$$= 1.0 \pm 0.4 \quad ({}^4\text{He})$$

and  $r_2 = 0.24 \pm 0.08 \text{ fm}$

Of particular interest is that  $r_1$  decreases with fragment mass, which implies that heavier fragments may be emitted from smaller source volumes.

For the Ar + Pb system, for example, the values of R, Eq. 3.30, vary from 3.2 to 4.2 fm depending on the fragment mass ( $R_{\text{exp}} = 3.0$  to 4.3 fm). These values are remarkably similar to values of R obtained in pion-interferometry experiments for this system at 1.8 AGeV [Fu 78, Lu 81] (see Sec. 3.5.1). This raises the question of how to interpret such similarities in the apparent source volumes for so dissimilar reaction mechanisms; the thermodynamic (coalescence) mechanism being characteristically a low-energy phenomenon whereas pion interferometry involves high-energy, multi-pion production processes. Although the near equality of the source volumes may be fortuitous, an understanding of the apparent redundancy of low- and high-energy effects in terms of reaction volumes is fundamental to any theoretical treatment of correlated emission in high-energy heavy ion collisions.

#### 4. Particle Production in RHI Collisions

Very high energy (VHE) "nuclear" collisions, in which target and/or projectile are multibaryon systems and the projectile kinetic energy greatly exceeds its rest mass\* have been observed and been available for investigation for a long time in the galactic cosmic radiation. The advent of VHE particle accelerators, especially the proton synchrotrons at Serpukhov, Fermilab, and CERN, has opened up also the field of VHE proton-nucleus (pA) collisions and has afforded the first glimpses of reaction mechanisms that clearly cannot be reduced to a superposition of independent "billiard-ball-like" baryon-baryon collisions. A characteristic feature of collisions in this energy range is that low-energy baryon-baryon interactions, the so-called nuclear structure effects, which overshadow the interpretation of some of the RHI experiments at lower energies, play a minor role, if any. This is due to the facts that i) the nuclear binding energies pale in comparison to the kinetic energies involved, ii) the associated de Broglie wavelengths of the projectiles become minuscule not only in comparison with nuclear size but also with internuclear distances and nucleon "size", and iii) the collisions are essentially inelastic with a major part of the available energy going into the production of new particles (pions, kaons, baryon-antibaryon pairs). The relatively large multiplicities of these newly produced particles put their specific stamp on the methods of analysis (e.g., with rare exceptions, selection of a given and completely defined final state becomes practically impossible).

Naturally, any discussion of the new evidence coming from VHE pA collisions requires a brief review of the relevant features of VHE pp collisions.

#### 4.1 Proton-Proton Collisions

##### 4.1.1 Multiplicities

The most immediate indicator of particle production is the multiplicity  $n$  of produced particles. It is interesting to note that already at its very birth the notion of multiple particle production was entangled in "pA effects". Indeed, before the relatively large value of the strong coupling constant was established, Yukawa's epigones predicted that meson (like photon) emission would be "single", and that only "repeat performances" in nuclei (i.e., cascading, in modern terms) could produce bunches of mesons. It was Heisenberg (He 53) who predicted "explosive" processes, accompanied by shock-wave phenomena, in which many ( $\langle n \rangle \sim \sqrt{s}$ ) mesons would be emitted in a single act. A more plausible version of the multiple theory was soon given by Fermi (Fe 50) who derived from "first", i.e., thermodynamic principles a  $\langle n \rangle \sim s^{1/4}$  dependence. The differences between Fermi's approach and that of Landau (La 53), who included relativistic hydrodynamics in the description of the process, will play an important role in the understanding of pA collisions discussed in Sec. 4.2.

The controversy of "single" vs "multiple" was resolved by the observation of a single p-p event in a balloon-flown nuclear emulsion plate by the Chicago Group (Lo 50), which showed the production of over 20 mesons in a "single act" (i.e., in one nucleon-nucleon collision).

Figure 52 shows the dependence on primary energy of both  $\langle n^- \rangle$  and  $\langle n_{ch} \rangle$ , where  $n^-$  is the number of negatively charged secondaries\* and  $n_{ch}$  is the total number of charged secondaries ( $n_{ch} = 2n^- + 2$ ). The straight lines are power law fits to the (most reliable) hydrogen bubble chamber data from 50 to 400 GeV:

$$\langle n \rangle = A s^\delta$$



with A, the factor of interest, as the only fitted parameter. The  $\delta$ -values were imposed to be 1/4 for  $n_{ch}$  and 3/8 for  $n^-$ . Since theoretical predictions were for created particles only, it appears that early "confirmations" of the Fermi-Landau  $s^{1/4}$  law were fortuitous. The value 3/8, which fits the created ( $n^-$ ) particles quite satisfactorily, belongs to a more refined version of the thermodynamic theory [Kr 54].

A deeper insight into the dynamics of the particle production process is provided by analyzing not just the mean number of produced particles but the actual shape of the statistical distribution law of that number, i.e. the multiplicity distribution.

Early results in the 20-50 GeV region seemed to suggest that the distribution of  $n_{ch}$  is close to a Poisson law. However, reliable bubble chamber data [Ch 72a] taken at 200 GeV in the Fermilab proton beam showed brutal departures from the Poisson distribution. Figure 53 displays the multiplicity distributions of negative secondaries observed at 50 GeV and 200 GeV in hydrogen bubble chambers. The curves are Poisson distributions with the same mean as the experimental data. As can be seen, the 50 GeV data provide a good fit, whereas the 200 GeV data do not. Quantitatively such differences are measured by the so-called second Mueller parameter\* [Mu 71]

$$f_2 \equiv \langle n^2 \rangle - \langle n \rangle^2 - \langle n \rangle$$

which must be zero for a Poisson law and positive if the distribution is "wider". Figure 54 shows a plot of  $f_2$  vs  $\langle n^- \rangle$  for all pp data from 20 GeV (CERN PS) to 2000 GeV (CERN ISR). The full line shows the prediction of the so-called KNO-scaling [Ko 72] based on the concept of Feynman scaling [Fe 69]. It is seen that except for  $\langle n^- \rangle \sim 2$ , i.e. primary energies close to 50 GeV (see Fig. 52),  $f_2$  is positive and increases

strongly with  $\langle n \rangle$ , i.e., with primary energy. It is also obvious that in spite of its initial apparent success (in a limited energy range), KNO scaling also provides a poor fit.

The issue of presence or absence of "Poissonicity" in pp collisions is hardly of academic interest either by itself or, especially, in the (RHI) context discussed here (i.e. within the context of particle production in multibaryon collisions, be it pA or AA). Indeed, whereas one is used to take the Poisson law for granted in measurements, e.g., counting statistics, etc., its appearance in such a fundamental process as meson emission is far from trivial. It is sufficient to mention that e.g. thermodynamic models implying a totally chaotic source do not predict a Poisson distribution whereas a purely coherent source is expected to be poissonian [Gl 67, Fo 78]. This property could be reconciled with  $f_2 \neq 0$  (Fig. 54) if more than one type of poissonian collision were involved. Figure 55 shows a comparison of all bubble chamber data from 50 to 400 GeV with the assumption [Fr 78] that pp collisions are a mixture of just two components with different mean multiplicities but each, by itself, obeying the Poisson law. The good fit argues in favor of a sizable coherent component among the produced particles and has its implication in specific features of the HBT experiments [Fo 78].

#### 4.1.2. Phase Space

The next characteristic of p-p collisions whose reflection in p-A collisions reveals unexpected phenomena is the population of phase space. The bulk of the produced particles have a narrow transverse momentum ( $p_T$ ) distribution (exponential in invariant cross section) with a relatively low mean, close to twice the pion rest mass; this mean does not depend on primary energy nor on the particle's momentum, as shown in Fig. 56. Most

of the energy-momentum flux is thus concentrated along the reaction axis\*, leading to a rapidity distribution that is roughly gaussian at the lower end of the VHE primary energy range and increasingly develops a flat plateau at really high energies ( $>1000$  GeV). A minute fraction (less than  $10^{-3}$ ) of all produced secondaries have a quite different behavior, with transverse momenta ranging as high as 20 GeV/c and a much flatter  $p_T$  distribution the parameters of which strongly depend on primary energy. Figure 57 shows the first observation of this effect. This "high- $p_T$ " region, discovered first in ISR experiments [Bü 73] (i.e., at 500-2000 GeV equivalent lab energy), is thought to reflect deeper features of collision dynamics, either in terms of parton effects [Fi 78] or in terms of early, high-temperature stages of thermo-hydrodynamical models [Fr 79].

#### 4.1.3. Particle Composition

Finally, whereas at lower energies pions dominate the produced particles and heavier objects (kaons, baryon-antibaryon pairs) constitute exotic occurrences, kaon production in VHE collisions saturates around 10% and NN production rises steeply to about  $\sim 7\%$  around 1000 GeV [Bo 72, Be 72].

## 4.2 pA Collisions

### 4.2.1 Multiplicities

We turn now to particle production in proton-nucleus (pA) collisions in the VHE range, which is the prototype for any projections of p-p results to RHI collisions. The obvious first candidate for comparison is the particle multiplicity  $n$ . From the beginning it must be stressed that any expectation for p-A when extrapolated from pp is strongly model-dependent. Indeed, because of the smallness of inter-nucleon

distances in nuclear matter ( $\sim 1$  fm) the traversal time of which is comparable to the lifetimes of most known resonances,\* the ulterior fate of particles produced in the first p-nucleon encounter inside the nucleus will critically depend on the spatio-temporal development of the state produced. If, e.g., one adopts Fermi's [Fe 50] original idea that statistical equilibrium is established practically instantaneously and that from there on the number of real particles in the system is "frozen", one would expect a naive tree-like cascade to develop, leading in a heavy nucleus to an enormous number of secondaries emitted. If, however, Pomeranchuk's idea [Po 51], developed by Landau in his hydrodynamical theory, were true, i.e., if the system takes a long time to cool down to a temperature  $\sim m_{\pi}$ , so that the real number of particles is undefined until the system finally disintegrates, the glob of hot hadronic matter formed in the first p-nucleon encounter will collide with another nucleon long before one could speak of "free" particles and hence no cascade (in the naive sense of the word) has a chance to develop.

An important consequence of the naive, tree-like cascade picture is that the fragmentation of the target nucleus is due to a large extent to the collisions of the cascading mesons with nucleons lying in their path. Since the meson multiplicity rises with primary energy, one would expect the multiplicity  $N_h$  of nonrelativistic target fragments to be energy dependent, too.

The differences implied in the multiplicity increase for produced particles, i.e., in the ratio  $R \equiv \langle n \rangle_{pA} / \langle n \rangle_{pp}$ , in going from pp to pA collisions by the two above-mentioned extreme assumptions are quite dramatic. In the naive cascade picture, if the target nucleus is large enough to allow for just one more cascade step for the produced particles

(this is certainly the case e.g. for silver nuclei) and if only this much cascading is taken into account, the increase, e.g. at 200 GeV, is expected to be by a factor of  $R \sim 5$ .

The qualitative predictions of the naive cascade models were contradicted by a series of careful nuclear emulsion experiments where the emulsion served both as target (H, CNO and Ag Br, the latter representing 3/4 of the effective cross section) and as a high spatial resolution  $4\pi$  detector.

This resolving power yields, on one hand, unambiguous counts of the multiplicity  $n_s$  of relativistic secondaries (predominantly pions, with the surviving baryon projectile emerging charged in  $\sim 1/2$  of the events) and, on the other, an accurate count of the number  $N_h$  of target related fragments (mostly protons) with nonrelativistic and often very low kinetic energies.

The first evidence contradicting the tree-like cascade picture came just from the energy dependence (or rather the lack thereof) of the distribution law of  $N_h$ . From such low primary proton energies as 6 GeV [Wi 65] and up to the energies of cosmic-ray jets, i.e.  $\sim 1$  TeV [Fr 67] the parameters of the  $N_h$  distribution were found rigorously energy independent.

The first hints for low pA meson multiplicities came from cosmic-ray exposures [Ab 67]; quantitative results with high statistics from Fermilab beams at 200 GeV [He 74, Co 74a, Ba 75a] established that, for the "average" emulsion target equivalent to  $\sim 2.5$  nuclear mean free paths in nuclear matter,  $R$  is close to 1.7, i.e., much less than even the "tamest" cascade prediction.

The next surprise provided by these emulsion experiments and confirmed by later counter experiments [Bu 75] is the energy dependence of  $\langle n \rangle$ . The "tame" "first generation only" cascade model considered above implies that, if  $\langle n \rangle_{pp}$  increases like  $E_0^\delta$ ,  $\langle n \rangle_{pA}$  should increase much faster, at least like  $E_0^{2\delta}$ .

Figure 58 shows that this is certainly not the case. This figure shows again (full points) the  $\langle n_{ch} \rangle$  data of Fig. 52 plotted against beam energy together with pA data on  $\bar{n}_s$  (relativistic secondaries) from nuclear emulsions. Open circles, triangles, and squares refer to subsets of data selected by the number  $N_h$  of target-related slow fragments associated with the relativistic secondaries. While the first group selects to some extent collisions in light targets, the last one is due to "central" collisions with the Ag Br target component. All these sets of data points run parallel to each other; on a log-log plot, this means that they show the same value of  $\delta$  as the p-p data, in flagrant contradiction to cascade predictions. In other words, once the VHE region is reached, R is independent of primary energy and depends only on target size and/or involvement.

The full squares in Fig. 58 represent data from an electronic counter experiment [Bu 75] with p-Cu collisions\* averaged over all impact parameters. They show the same pattern as the emulsion results.

#### 4.2.2 Multiplicity and Rapidity in pA Collisions

We have seen that the increase of the mean multiplicity, i.e., the value of R, is much less than expected from the assumption of "free" particles suffering independent collisions inside the nucleus. Another unexpected result of pA emulsion studies [Co 74a] confirmed later by electronic methods [Bu 75] is the location in phase space of this increase.

In the picture of independent collisions one would expect a sizable increase to occur in the forward rapidity region. Indeed it is well known that pp collisions are on the average  $\sim 50\%$  inelastic, i.e., that the incoming baryon re-emerges as a leading particle carrying  $\sim 1/2$  the primary energy, the rest being carried away essentially by the created particles\*. Because the multiplicity depends only weakly on energy and because the opening angle of the forward cone goes only as  $\gamma_c^{-1} \sim (\sqrt{E})^{-1}$  ( $\gamma_c$  is the cms Lorentz factor), any subsequent collision of the leading baryon should roughly double the primary multiplicity in this cone.

Figure 59a shows for 200 GeV pA interactions the dependence of the mean multiplicity in the forward  $5^\circ$  cone (circles) (which corresponds to  $90^\circ$  in the pp cms) on  $N_h$ , along with (squares) the mean multiplicity outside this cone. One must remember that  $N_h \leq 8$  corresponds mainly to collisions with light (CNO) targets whereas  $N_h \geq 9$  tags collisions with the heavy (Ag Br) target component with increasing "centrality" as  $N_h$  increases beyond 9.

As can be seen, the whole increase in multiplicity due to "nuclear" effects is localized in the wide cone (corresponding to backward cms rapidities) whereas the "forward" multiplicity practically does not depend on target size. This conclusion is strengthened by the data of Fig. 59b, which shows the same multiplicities plotted against  $A_T^{1/3}$ \*\* for electronic counter data taken with pure targets and integrated over impact parameters.

These results, which prove beyond any remaining doubt the inability of the independent particle model to describe the collision mechanism, have triggered a plethora of theoretical speculations (e.g. coherent tube [Da 72], nova cascade [Fr 74], energy flux cascade [Go 74], and a modern,

sophisticated version of Landau's hydrodynamics [We 78]). All these models have in common the unavoidable assumption that, far from real secondaries interacting independently, the bulk of the energy flux resulting from the first p-nucleon encounter in the nucleus hits, as a whole, the next nucleon(s). Irrespective of the details of these models they all predict the low value of R, its independence on primary energy, and the similarity of the pA forward cone to that produced in pp collisions. However, they all fail to predict certain recently observed statistical properties of the meson distributions, which will be discussed at the end of this section.

A good way to visualize the behavior of the "excess" radiation produced by the nuclear environment of the first p-nucleon encounter is to consider "difference distributions". Let

$$\rho(\eta) \equiv \frac{d\bar{n}}{d\eta} \quad (4.1)$$

be the mean density of relativistic particles (per event) at pseudorapidity  $\eta$ . Define

$$\Delta_{ab} \equiv \rho_a - \rho_b \quad (4.2)$$

as the difference between particle densities  $\rho_a(\eta)$  and  $\rho_b(\eta)$  produced in two classes of collisions, say, a and b, differing by target size and/or involvement.

Figure 60 shows as circles  $\rho(\eta)$  as a function of  $\eta$  for p-carbon collisions. The crosses and square symbols represent  $\Delta_{ab}$  where a refers to collisions with the heavier target and b to collisions with carbon. It is obvious that the excess particles are shifted towards low rapidities (roughly 1/2 the c.m.s. rapidity) and hence do not appear to be emitted



from a system at rest in the lab frame. The integral excess multiplicities (i.e., the areas under curves similar to the ones on Fig. 60) for different targets are plotted in Fig. 61 against  $\Delta\bar{v}$  for the different target pairs,

$$\Delta\bar{v} = \bar{v}_a - \bar{v}_b \quad . \quad (4.3)$$

$\bar{v}$  is the "equivalent nuclear matter slab thickness" defined [Bi 77a] as

$$\bar{v} = A_T \frac{\sigma_{pp}}{\sigma_{pA}} \approx 0.71 A_T^{0.31} \quad . \quad (4.4)$$

The straight line in Fig. 61 is not a fit, but the dependence

$$\Delta\rho(\Delta\bar{v}) = \frac{1}{2} (\bar{n}_{ch})_{pp} \Delta\bar{v} \quad (4.5)$$

expected if each unit of nuclear slab thickness would contribute one-half of the multiplicity of a pp collision at the same beam energy (in this case 200 GeV).

The physical picture that these results suggest [Co 74a, Fr 74] is that of i) propagation of the forward cone of the first p-nucleon collision through nuclear matter without visible absorption or multiplication (e.g., by successive absorption and re-emission of the energy flux) and ii) a constant contribution of  $\bar{v}$  "backward" cones by nucleons lying on the projectile's path, and only by these.

It has been shown recently [Fo 81] that two effects discussed in previous paragraphs, viz. i) the dominant Poisson character of pp multiplicity distributions and ii) the unaltered persistence of the forward meson cone in pA collisions, allow a common interpretation in analogy to quantum optics. Indeed, if the first pp-collision in a nucleus behaves like a coherent source, the radiation in the forward direction leads to the phenomenon known in optics as self-induced transparency [McC 67]. This is the successive absorption and re-emission of a narrow pulse

of coherent radiation by target components with at least two energy levels (in our case this means baryons). An immediate consequence of this interpretation is that a nuclear target acts as a filter selecting a purely coherent beam in the forward direction. Hence the multiplicity distribution of the forward cone (treated as a mini-jet) should approach a Poisson shape. Figure 62 shows the distribution of multiplicities in four bins of pseudo-rapidity in p-emulsion collisions at 200 GeV [Fo 81]. It is seen that whereas the "backward region" shows a complex (akin to chaotic) character, the forward rapidity bins are almost purely Poisson, as expected for a coherent beam.

The observation of a sizeable coherent component in meson-producing nuclear collisions has a direct bearing on the determination of source sizes in AA collisions, because its presence may considerably distort the correlation function for pion pairs [Fu 78].

#### 4.2.3. Transverse Momenta in pA Collisions

The results of the preceding paragraph show that production of the bulk of the mesons is related to a linear geometrical picture in which a narrow tube of nucleons contributes collectively to the final state.

What about the--very infrequent but even more important--particles emitted with very large transverse momenta? We know they do occur in pp collisions (Sec. 4.1.2) but do they occur in pA collisions, too? Another puzzle was brought up by VHE pA experiments [Cr 75a, An 77a], in which a magnetic spectrometer recorded identified secondaries of  $p_T > 0.7$  GeV/c [i.e., beyond the "normal" exponential (Fig. 56)] from collisions of 200 to 400 GeV proton beams with different nuclear targets ranging from  $^2\text{H}$  up to W. Fitting the target mass dependence of the Lorentz invariant cross sections by a power law

$$E \frac{d^3\sigma}{dp^3} \sim A_T^{\alpha(p_T)}, \quad (4.6)$$

they obtain for different types of secondaries the dependences of  $\alpha$  on the (large)  $p_T$  shown in Fig. 63. The puzzling fact emerging from these graphs is that  $\alpha$  increases with  $p$  beyond unity! Now a linear trajectory effect ( $A^{1/3}$ ) weighted with a geometric cross section ( $A^{2/3}$ ) could at most lead to  $\alpha = 1$ . It looks as if high- $p_T$  secondaries would be produced either "in volume" (which would contradict the conclusions drawn from the bulk of the secondaries) or that strong "cooperative" effects are present in the nuclear tube [Af 78, Fr 78a].

#### 4.3. Particle Production in AA Collisions at Low and Moderate Energies

##### 4.3.1. Pion Multiplicities

Before considering VHE multiple pion production we take a look at the information provided to date by the two RHI accelerators in use, viz. the Berkeley Bevalac and the Dubna Synchrophasotron.

One open question is, as already noted (see Sec. 3.4.2), whether the energy per nucleon or the total energy is relevant for the hadronic production process. If the latter were true, a 1.8 AGeV Ar beam (as currently provided by the Bevalac) might be considered as a  $\sim 70$  GeV beam and typical VHE phenomena could be expected. The same would be valid for a 4.5 AGeV  $^{16}\text{O}$ -beam from the Dubna machine. Unfortunately, the experiments on pion production performed to this day at the Bevalac have not justified this kind of approach.

At the lower end of the energy range (just above threshold) counter experiments were carried out [Na 78] to measure inclusive pion spectra in 0.8 AGeV Ne-NaF collisions. Figure 64 displays an energy spectrum taken at zero cms rapidity. It is seen to be exponential, i.e., the  $p_T$

spectrum is exponential in transverse mass; the corresponding temperature is very low by pp or pA standards, i.e.  $\sim 50$  MeV ( $\sim 1/3$  the freeze-out temperature of all high-energy reactions). The angular distributions appear to be consistent with isotropy in the cms; as can be seen from Fig. 65 the pion yield at all angles is consistent with an  $A^{2/3}$  dependence on the target mass. Hence, no "linear effects" of the kind discussed earlier for pA collision have yet set in.

The most complete information on pion production at the Bevalac has come from a streamer chamber experiment [Sa 80a] with 1.8 AGeV  $^{40}\text{Ar}$  incident on a KCl target. The mean negative pion multiplicity\* is plotted in Fig. 66 against the cms energy per nucleon. A linear increase is evident, again at variance with the  $s^{1/4}$  dependence observed in pp and pA collisions.

The shape of the multiplicity distribution is rather reminding of that observed in  $\lesssim 10$  GeV proton interactions. At a fixed number of participant nucleons the partial multiplicity distributions are well consistent with a Poisson shape; however, because the pp multiplicity distributions in this energy range are narrower than predicted by the Poisson law ( $f_2 < 0$ ) it seems likely that the Poisson-like shape is accidental and due mainly to the fluctuations in the number of meson-producing collisions.

The two-fold increase in beam energy provided by the Dubna machine seems to change the pattern towards greater similitude with the multiple production processes observed at higher energies in pp and pA.

Here again streamer chamber experiments have yielded the most pertinent results. Negative pion production has been studied with

4.5 AGeV  $^4\text{He}$  beams [Ab 80] and  $^{12}\text{C}$  beams [Ak 80], on different targets ranging from Li to Pb.

Figure 67 displays a few multiplicity distributions from events induced by the He beam. The squares and triangles show results from pp collisions chosen to match more or less the He-beam results. The resemblance is striking. In Fig. 68 we plot the available energy in the pp-cms  $E'_{\text{CM}}(\text{pp})$  against the energy  $E'_{\text{CM}}(\alpha\text{A})$  available in the cms of a 4.5 AGeV alpha particle and of a tube of nuclear matter cut out in the target by the alpha cross section. Within the large errors of the matching\*, there appears to be a linear relationship between the two energies

$$E'_{\text{CM}}(\text{pp}) \sim 0.4 E'_{\text{CM}}(\alpha\text{A}) \quad (4.7)$$

---

which means that, even if the linear dependence (Fig. 66) observed at 1.8 AGeV still holds at 4.5 AGeV, the effective nucleon-nucleon production is only half as effective as in a free pp collision. Conversely one might invoke collective effects to explain an inhibition of the production process; but in view of the evidence (to be discussed in Sec. 4.5) from VHE RHI induced cosmic ray jets such an interpretation seems rather unlikely.

Figure 69 illustrates the deviation of the multiplicity distributions at this energy from the Poisson shape. The  $f_2$  vs  $\langle n \rangle$  plot is very different for the He and the C exposures with much larger widths in the latter case. (An equivalent description is the statement that the  $D \sim \langle n \rangle / 2$  relationship [Wr 70] is violated by the C-induced events.) It is interesting that it has not been possible to find pp-multiplicity distributions to match the C events. Figure 70 shows a comparison of 50 GeV pp events with 4.5 AGeV C-C events, which have approximately the same mean multiplicity. The distributions are quite different, the C

events having an excess of very low multiplicities. This may be understood in terms of the much higher geometrical probability of very peripheral C-C collisions, involving only one nucleon of each colliding nucleus; such a collision would be indistinguishable from a low-energy (4.5 GeV!) pp collision.

In an attempt to see whether some sort of "linear regime" is established, we have plotted the mean multiplicities of both He and C interactions on various nuclei at 4.5 AGeV in Fig. 71 against the product

$$N_{\text{eff}} = A_P^{2/3} A_T^{1/3} \quad (4.8)$$

i.e. against the mass of a tube with the projectile cross section cut out from the target. With the exception of a single point (due to He-Pb collisions), the data from both beams fit surprisingly well a straight line

$$\langle n \rangle \sim 0.25 + 0.125 N_{\text{eff}} \quad (4.9)$$

In other words, at this energy only about one out of eight participating nucleons is responsible for the creation of a negative pion.

#### 4.3.2. Rapidity Distributions

No explicit rapidity distributions have yet been measured for AA collisions at the Bevalac. However, the He-A experiment at 4.5 AGeV [Ab 80] has produced such results for five different targets. The pattern observed in VHE pA collisions is already apparent here, with nuclear transparency present at  $y > 2$  (Fig. 72) and all the increase in multiplicity localized at low rapidities. This fits in well with the "linear" i.e.  $A_T^{1/3}$  dependence of  $\langle n \rangle$  discussed above. It would be very interesting to know whether heavier projectiles show similar effects, but unfortunately no such data are available as yet. Still, it is somewhat surprising to see the "VHE behavior" of rapidity distributions

set in so early (it is noticeably absent [Fr 74] at 6...20 GeV in pA collisions). This may be the first indication for a cooperative effect simulating >50 GeV pp physics with  $\sim 5$  AGeV nuclei.

#### 4.3.3. Transverse Momenta

Figure 73 shows the  $p_T$  spectra recorded at 4.5 AGeV [Ab 80] with the He-beam on different targets. The spectra display the familiar shape known from pp collisions with means around 0.2-0.25 GeV/c, corresponding to "temperatures" of the order of the pion rest mass. This is by itself another indicator for the fact that an energy regime much exceeding  $\sim 5$  AGeV has been reached (compare the soft  $p_T$  spectra at 0.8 AGeV, in Fig. 64). However, the correlation between  $\langle n \rangle$  and  $A_T$  shown in Fig. 74 is opposite to that observed at higher energies (the A dependence is stronger at low  $p_T$ !).

Also  $\langle p_T \rangle$  shows a consistent, if slow, decrease with target mass. Unfortunately (probably because of the relatively low fluxes available to the RHI accelerators), no data exist as yet concerning  $p_T$  spectra in the "high- $p_T$ " region, i.e., beyond 1-2 GeV/c. Such data are urgently needed to confirm (or disprove, as the case may be) a contribution of cooperative effects to the pion producing processes in the lower energy range.

#### 4.3.4. Strange Particles

Experimental information on strange-particle production in RHI collisions is, at this writing, just beginning to become available. The production of strange particles and nuclei, i.e., kaons, hyperons and hypernuclei at beam energies  $\sim 2$  AGeV is either below or slightly above the nucleon-nucleon center-of-mass threshold energies. Thus, relative to nuclear fragments and pions, the cross sections for strange-particle production are small, the kaon/pion ratio being typically  $10^{-3}$ .

Although the important and unique aspects of strange-particle production to RHI collisions have long been recognized, the inherent experimental difficulties in resolving strange particles from the prolific background of nucleons and pions had first to be surmounted.

The attractive feature of studying strangeness-producing reactions is that they proceed via strangeness (quantum number S)-conserving nucleon-nucleon reactions, the most important of which, in the present context, are:



---

Thus, not only is direct particle production observed (kaons) in these reactions, but the participant nucleon involved in the reaction may also be observed as the resultant hyperon ( $\Lambda, \Sigma$ ). The threshold energies  $\sqrt{s}_{th}$  for the above free NN reactions are 2.55, 2.62, and 2.86 GeV, respectively. To place these in proper perspective, the value of  $\sqrt{s}$  is 2.73 GeV for a nucleon-nucleon collision at 2.1 AGeV, the maximum beam energy available for RHI experiments at the Bevalac. At such energies, the production mechanisms may reasonably be expected to be modified by the effects of Fermi motion and, possibly, collective phenomena. Because the  $(S = +1)K^+$  can only undergo elastic scattering with nucleons, and perhaps pions, after its production and before its escape from the interacting volume of the colliding nuclei (no absorption channels are available at the energies we shall be considering), experiments on  $K^+$  production have the potential for gaining information on the "primordial" nucleon-nucleon interaction and/or the properties of the surrounding



nuclear matter traversed by the  $K^+$  meson. The first kaon-production experiments have begun to bear on this problem but with some rather unexpected results.

4.3.4a. Positive Kaons. The single-particle inclusive spectra for  $K^+$  have been measured in the momentum range  $0.35 \leq p_K \leq 0.75$  GeV/c by Schnetzer [Sc 81c] at beam energy 2.1 AGeV for p, d, and Ne incident on a variety of targets: C, NaF, NaCl, Cu, and Pb. The  $K^+$ -production cross sections were measured at laboratory angles  $15^\circ$  to  $80^\circ$ , using the magnetic spectrometer described by Nagamiya [Na 78, Na 81]. Representative of the  $K^+$  data are those shown in Fig. 75. Presented here are the measured differential production cross sections for  $K^+$  mesons, plotted versus the kinetic energy of the  $K^+$  in the center of mass of the nucleon-nucleon system, for both AA and pA collisions. Included in this figure are the cross sections for  $p + p \rightarrow K^+ + X$  at  $T_p = 2.54$  GeV [Ho 68]. The notable characteristics of the data are:

- i) For both AA and pA, the  $K^+$  cross sections decrease exponentially with  $T_{K^+}^{cm}$ .
- ii) Although the range of  $K^+$  momenta measured at each angle was insufficient to give significant overlap in  $T_{K^+}^{cm}$ , the fact that the pA and AA cross sections are apparently ordered to yield a single curve means that the  $K^+$  production cross sections are isotropic in angle and depend only on  $T_{K^+}^{cm}$  in the nucleon-nucleon system.
- iii) A major change in the spectral shape of  $K^+$  occurs as one goes from the pp to pA reactions; except for a slight change in exponential slope, there are no differences between the pA and AA spectra.

and iv) To within a factor of about two, the pA and AA  $K^+$  cross sections scale as  $A_p A_T$ , i.e. independent behavior of particles with no shadowing effects.

That exponentially shaped spectra are observed suggests the possibility that the  $K^+$  mesons may be produced by a thermal process. Asai, et al. [As 81] addressed this hypothesis by calculating the  $K^+$  spectra expected from the fireball model when the nucleons,  $\pi$ 's,  $K$ 's,  $\Delta$ 's,  $\Sigma$ 's, and  $\Lambda$ 's are in thermal and chemical equilibrium. Although the calculated spectral shape is compatible with that observed, the absolute value of the cross sections is about 20X too large. This result definitely rules out the assumption that the kaons achieve chemical equilibrium before emission. This is quite reasonable because the small inelastic cross section of  $K^+$  would intuitively lead one to expect that there is insufficient time for the  $K^+$  to attain chemical equilibrium.

The data shown in Fig. 75 exhibit other contradictions with the thermal hypothesis and with the assumption that the exponential slopes are representative of temperatures of thermalized systems. First, the exponential fits to the Ne + Pb and Ne + NaF data correspond to temperatures 160 and 122 MeV, respectively. This variation of temperature with target mass is opposite to that predicted from the fireball model because the excitation energy available to the fireball is maximum when the target and projectile masses are equal. Second, because the emission of all particles in the fireball model is isotropic in the rest frame of the fireball, the observation of apparent isotropy of the  $K^+$  in the nucleon-nucleon system (rather than a system nearer to the laboratory frame) in the p + NaF reaction would be, in itself, an indication of a

nonthermal mechanism for  $K^+$  production in RHI as long as hydrodynamical effects do not come into play.

Randrup [Ra 81a] has pointed out that, although the average kaon-nucleon (nearly totally elastic) cross section is small,  $\sigma_{KN} \sim 9$  mb, it is not small enough to allow the kaons to escape the interaction volume unscathed. In fact, a kaon, after its production, suffers on the average about one collision in traversing the adjacent nuclear matter. Randrup treated the multi-collision problem of kaons, produced in baryon-baryon collisions, by use of the "row-on-row" linear cascade model [Ra 80a, Kn 79]. He concluded that the scattering mechanism significantly alters the predicted kaon spectra.

This is shown in Fig. 76, where the invariant production cross sections versus laboratory momenta, measured at angles  $15^\circ$  to  $80^\circ$ , for the reaction  $Ne + NaF \rightarrow K^+ + X$  are compared with the row-on-row model, without (dashed curves) and with (solid curves) scattering of the kaons. The calculated values have been increased by a factor of two to aid in the comparison with the data. The effect of scattering of the kaons on the angular distribution is clearly evident. At forward angles the effect is small, but at the larger angles the effect is striking. In the region of  $p_K \sim 500$  MeV/c the kaon yield is effectively increased by an order of magnitude, and the slopes of the spectra are decreased by about one-half in order to fit the data. These calculations demonstrate how scattering of the kaons substantially alters their initial spectral distributions. Studies of kaon production in RHI collisions thus may not reveal directly the nature of the early stages of the reaction between nuclei.

An intriguing result from the  $K^+$  experiment of Schnetzer is that the  $A_T$ -dependence of the kaon yield, as indicated by the exponent  $\alpha$  in

the expression  $\sigma \propto A_T^\alpha$ , is greater for heavy projectiles (Ne) than for light (deuteron) projectiles. Similarly, the  $A_p$ -dependence of the kaon yield for heavy targets is greater than for light targets. Such behavior does not follow from simple geometry and independent nucleon-nucleon collisions and thus may indicate a collective effect.

4.3.4b. Negative Kaons. A recent Bevalac experiment carried out by Shor, et al. [Sh 81] was a search for subthreshold production of  $K^-$  and  $\bar{p}$  in the reaction  $^{28}\text{Si} + ^{28}\text{Si}$  at 2.1 AGeV. At this beam energy the center-of-mass energy available for particle production in nucleon-nucleon collisions is 850 MeV. The center of mass threshold energies for the production of  $K^-$  and  $\bar{p}$  in nucleon-nucleon collisions are 990 MeV and 1876 MeV, respectively. The production of these particles thus requires more energy than is available in individual nucleon-nucleon collisions by 140 MeV for  $K^-$ , 1026 MeV for  $\bar{p}$ . The production of either of these particles in the experiment would therefore be a clear signature of a multi-nucleon collective effect.

Principal features of the experiment were the production of a 0-deg. secondary beam of negative particles from a symmetric target-projectile system that established a unique center of mass frame. The secondary beam was analyzed by a three-magnet beam-transport system set to transmit  $Z = -1$  particles of momentum 0.99 GeV/c, the momentum of anti-protons produced at rest in the nucleon-nucleon center of mass system. Kaons at this momentum have center-of-mass energies  $T^{\text{cm}} = 70$  MeV.

The result of the experiment was that no  $\bar{p}$  signal was detected above background, but that an unexpectedly large yield of  $K^-$  (based on 52 events) was observed, well resolved from the dominant pions.

The preliminary value of the measured differential cross section at  $0^\circ$  for  $K^-$ ,  $p_K = 0.99$  GeV/c is  $d^2\sigma/dPd\Omega = 1.3$  mb (srGeV/c) $^{-1}$  (with  $\sim 50\%$  error).

To ascertain whether this result is compatible with  $K^-$  production by nucleon-nucleon collisions only, Shor et al. i) measured  $K^-$  production for 4.8-GeV protons on Cu under the same conditions and then ii) compared the observed ratio of the production cross sections,  $\sigma(\text{Si,Si})/\sigma(\text{p,Cu})$ , with the result of model calculations assuming nucleon-nucleon interactions only. The calculations incorporated a Fermi-momentum distribution parameterized as a superposition of two Gaussians ( $\sigma_1 = 90$  MeV/c and  $\sigma_2 = 190$  MeV/c). This distribution has given good agreement with experiments on the backward scattering of protons [Ge 80] and the subthreshold production of  $\bar{p}$  in p-nucleon collisions [Do 65]. The conclusion reached by Shor et al. is that the experimentally observed ratio is 40 times greater than can be accommodated by, what is believed to be, a conservative theoretical estimate for this ratio. Thus the surprisingly high rate of  $K^-$  production observed in the experiment apparently cannot be explained by Fermi-momentum effects, and the possibility of collective phenomena is perhaps unattractive owing to the fact that the de-Broglie wavelength at 2 AGeV is smaller than the internucleon distances. Equilibration of the  $^{28}\text{Si} + ^{28}\text{Si}$  system appears unlikely [Za 81], although under such conditions the rate of  $K^-$  production would be increased. Unexplored are the notions of pre-existing clusters and/or collective tubes that could be invoked to diminish the  $K^-$  threshold energies.

4.3.4c. Hyperons. In contrast to kaons, which must be individually identified by mass measurements, or to hypernuclei, which are a rare

occurrence to begin with and furthermore require tagging by means of (again identified) kaons (see 4.3.4d), lambda-hyperons are both relatively frequent and easily identifiable via their  $p-\pi^-$  decay in flight.

Recently, the LBL streamer chamber facility at the Bevalac was used to investigate  $\Lambda^0$  production in a subset of  $^{40}\text{Ar-KCl}$  collisions at 1.8 AGeV [Ha 81]. The selected subset of events was defined by the absence of large projectile-fragment charges (veto counter) and represents  $\sim 10\%$  of the total reaction cross section. The authors expect this selection to favor small nuclear impact parameters and hence to bias the events towards "central" collisions. The primary beam velocity sets the energy of a nucleon-nucleon collision just above the threshold for  $NN \rightarrow \Lambda^0 KN$  production.

As usual, the lambdas were identified by the specific kinematics of the  $p-\pi^-$  decay as shown in Fig. 77. The small  $K^0$  population of the invariant mass plot is due mainly to the poor spatial resolution of the streamer chamber, which necessitated rejection of any decay within a distance where most  $K^0$  decays were located.

The interesting information provided by this experiment is illustrated by Fig. 78, which displays the identified lambdas on a Peyrou plot. The circle centered at  $P_{||} = 0$  gives the kinematic limit for lambda production in pp collisions; as can be seen, it is practically empty of events. The lower two-thirds of this figure illustrate attempts to explain the large  $p_T$  values of the lambdas by means of conventional effects (Fermi motion of the nucleon sources and rescattering of the lambdas in the nuclear matter surrounding the primordial collision). Although inclusion of these effects changes the prediction towards better qualitative agreement with experiment, it fails when a quantitative

comparison is made; the average transverse momentum is at least twice larger than any model prediction. Thus some form of collective interaction and/or high densities must be present.

In any case, the hope that strangeness would provide "unadulterated" information about the early stages of the AA interactions has, once again, not been fulfilled. The conclusion that the kinematic parameters of the lambdas reflect rather their ulterior history is reinforced by a measurement of their polarization, which is found close to zero, as would be expected from significant rescattering.

4.3.4d. Hypernuclei. The first strange-particle production experiment using a beam of RHIs was the pioneering effort by the University of Arizona, Tucson, under T. Bowen, who used the 2.1 AGeV  $^{16}\text{O}$  beam from the Bevatron to produce relativistic mass 16 hypernuclei [Ni 76]. The hypernuclei, and their decay products, were studied with large-gap spark chambers that were triggered by the low-momentum  $\text{K}^+$  meson produced in association. The experiment demonstrated several important technical advantages gained by use of RHIs in hypernuclear studies. The principal one is that hypernuclei associated with the projectile are produced near beam rapidity. In such cases, the relativistically dilated lifetime (e.g.,  $\tau \sim 3$ ) of the hypernuclei allow for several centimeters of flight path before their decay takes place well outside the target. At relativistic velocities, charge and momentum measurements are facilitated for both the hypernucleus and its decay products. The latter are also relativistic and are confined to a small solid angle about the direction of the hypernucleus. Above all, the ability to trigger on the  $\text{K}^+$  in associated production greatly enhances the efficiency in selecting hypernuclear events of interest.

By requiring that no charged secondaries other than a high-Z ion exited the target (in association with the  $K^+$ ), Nield et al. [Ni 76] effectively selected in their experiment the reactions



Restricting the decay vertices to 2-4 prongs, a mean decay length of  $\lambda = 7.7^{+3.0}_{-2.2}$  cm, based on 22 events, was obtained. Assuming beam rapidity, i.e.  $\beta\gamma = 3.01$ , this value of  $\lambda$  corresponds to a proper lifetime of  $\tau({}^{16}_Z_A) = 0.86^{+0.33}_{-0.26} \times 10^{-10}$  sec. Before this experiment,  ${}^5_1H_1$  was the heaviest hypernucleus for which a lifetime had been measured [Ni 76].

---

~~The approximate cross section per target nucleon for the production~~  
of  ${}^{16}_Z_A$  in the above reactions observed in the experiment is  $2 \pm 1$   $\mu\text{b}$ /target nucleus. This can be compared with the production of free  $\Lambda^0$ s in 2.8-GeV  $p + {}^{12}_6C$  collisions, which is  $440 \pm 200$   $\mu\text{b}$ /incident proton [Bo 60]. From these data one may conclude that only about 1% of the  $\Lambda$ s produced are bound in nuclear fragments to form hypernuclei.

Povh [Po 78] has called attention to the intriguing possibility that intense RHI beams could be used to produce multiple hypernuclei, where two or more nucleons within a nucleus are converted to  $\Lambda$  hyperons [Ke 73]. Such experiments would necessarily rely on the detection of multiple  $K^+$  in associated production to make the experiment feasible.



#### 4.4. Very High Energy Nucleus-Nucleus Interactions

Ever since the discovery of heavy relativistic nuclei in the galactic cosmic radiation [Fr 48] the nuclear emulsion detectors flown in balloons at high altitudes (>30 km) have revealed collisions of such nuclei with targets in the composition of the detector [Ka 52]. At these altitudes the primary flux is little if at all degraded by collisions with nuclei in the residual atmosphere, and we are looking at a "pseudo accelerator" for very high energy heavy ions, albeit of very low intensity. The great experimental effort implied when trying to collect data in the face of such adversities as low flux, a priori unknown energy and "beam" charge and mass is, however, richly repaid by the broad (if steeply falling) energy spectrum, which provides us with a unique window to the world of multibaryon interactions in the range of, say, >100 AGeV, with isolated events going up to factors of  $10^4$  higher in energy. Furthermore, the charge spectrum of these heavy nuclei, although peaked around C,N,O, extends with still acceptable intensity up to Fe.

Recently, the accelerator competition to cosmic rays has again perked up by the acceleration of He-nuclei in the CERN Proton Synchrotron (PS) and their storage for beam-beam collisions in the Intersecting Storage Rings (ISR) where alpha-alpha collisions at an equivalent laboratory (fixed target) energy of 500 AGeV have been studied. However, the He nucleus is still a relatively simple multibaryon system, and it is hard to predict whether new, specific phenomena expected in this field will show up at  $A = 4$ . Thus, until heavier nuclei can be accelerated and stored (ISR and, hopefully the new generation of High Energy RHI accelerators like VENUS), cosmic rays are still for a long time the only way of access to suspected "extreme" nuclear states.

In the following these two, quite different, types of evidence will be reviewed separately.

#### 4.4.1. Cosmic Ray Interactions of VHE RHI

In trying to cope with the inherent uncertainties of reactions of VHE cosmic RHI the following tools and/or assumptions deserve a brief mention.

The charge of the RHI can quite accurately be estimated from the density of  $\delta$  rays along their tracks, which (as has been checked experimentally up to Fe) increases like the square of the nuclear charge. The mass (i.e., the isotopic composition of the RHI cosmic "beam") is, however, unknown in individual events and in most cases one has to live with the assumption that the primaries under consideration are not too far away from the valley of stability (i.e. from  $A \approx 2Z$ ).

Estimation of the primary energy of each individual event is another matter altogether. Most methods used up till now rely on certain properties of relativistic kinematics together with simplifying assumptions about the dynamics of the collision (See Sec. 2.3, Eqs. (2.6), (2.8), and (2.9)).

Figure 79 shows an example of VHE RHI interaction in a balloon-flown nuclear emulsion [Po 59]. A primary carbon nucleus of energy  $>1000$  AGeV collides with an emulsion nucleus (presumably of the C,N,O group since  $N_h < 8$ ) to produce  $>100$  mesons, most of which lie inside a narrow cone. The opening of this very cone provides a rough Castagnoli type estimate for the primary energy. In the right half of the figure this cone is seen farther away from the collision vertex. A narrow core of  $Z = 1$  tracks can be seen, which is due to the fragmentation of the primary nucleus. In many cases of this kind, comparison of the narrow (meson) and "very narrow" (proton) cones allows one to cross-check the Castagnoli and

Bradt-Kaplan estimates for the primary energy, the former being derived from the produced mesons whereas the latter is derived from projectile fragments (see Sec. 2.3, Eqs. (2.6) and (2.9), respectively). The meson multiplicity appears to be quite high; if one remembers that at ISR energies ( $\sim 1000$ - $2000$  GeV equivalent laboratory energy) the multiplicity is close to 12, it looks as if all nucleons of the primary nucleus would have interacted and produced comparable numbers of mesons. This simplistic interpretation conflicts, however, with the persisting "very narrow" fragmentation cone, which indicates that most protons of the primary escaped the relatively large momentum transfer interactions needed to produce the mesons.

Figure 80 shows a schematic drawing of a "family" of VHE RHI collisions started by the incidence of a phosphorus nucleus of  $\sim 1300$  AGeV on a large emulsion stack [Ab 67]. A total of 28 interactions are produced by the primary and the products of its successive fragmentations. The event codes next to the interactions should be read: " $(N_h + n_s + \text{heavier fragments})$  primary". One fact illustrated by this family is the wide range of multiplicities induced by apparently similar collisions, if the conventional criteria for "peripherality" or lack thereof are applied. Event #1 where a Mg fragment survives from the primary produces at most 7 mesons, whereas event #2 with a Na surviving from Mg produces 42 relativistic secondaries, mostly mesons. Still, by the same criterion as in event #1 (namely survival of a sizable "spectator" part of the incident nucleus), this second event would have been classified as "peripheral", too. The last event in the RHI chain (#20) has  $N_h = 0$  but a multiplicity of 44 with complete destruction of the incoming Li nucleus. Such events are illustrative of the pitfalls

connected with "estimation" of impact parameters via the absence of high-Z projectile fragments (see Sec. 2.3,iii) and Fig. 5).

The pseudorapidity distribution of the RHI-induced events from this family is shown in Fig. 81 (events are identified by their codes in Fig. 80). The rightmost vertical arrows show the  $\eta$ -value where one would expect particles at "beam-rapidity", i.e. the surviving  $Z = 1$  fragments of the "primaries". Such a well-defined projectile fragment cone can be seen in event d (#6). The vertical line indicates the rapidity of a pp cms at the same energy. While events f (#2) and e (#20) are clearly symmetric with respect to this line, d (#6) obviously has a large number of particles produced at mid-rapidity. This kind of angular distribution can hardly be predicted from what is known in pp and pA collisions.

Historically, this family is important also because it provides one of the first examples of "applied VHE RHI research." Indeed, the 20 events produced by protons and neutrons surviving the RHI interactions can be treated as a kind of monokinetic beam (see Sec. 3.1). This allowed the first reliable estimation of the mean meson multiplicity at  $\sim 1000$  GeV in pp collisions, long before this number was confirmed with high statistics at the ISR [Ab 67].

An obvious question raised by the sometimes very large multiplicities of RHI-induced jets is whether they fit into any "reasonable" extrapolation from pA results at comparable energies. Since we are dealing with a triple manifold of variability (E and Z for the primary,  $N_h$  for the target) we will attempt to scale the multiplicity in three steps, viz.:

a) account for target size by using the linear dependence between  $n_s$  and  $N_h$ , i.e. scale  $n_s$  to

$$X_1 = n_s / (1 + a N_h) \quad (4.12)$$

b) use the constancy of

$$R = \langle n_s \rangle_{pA} / \langle n_s \rangle_{pp} \quad (4.13)$$

i.e. scale

$$X_2 = X_1 / E^\delta. \quad (4.14)$$

Figure 82 shows the multiplicity distribution of ~2000 events from p-emulsion collisions at 69, 200, and 300 GeV, in the scaling variable  $X_2$ . The dashed histogram gives the distribution of  $X_2$  for 32 alpha-induced jets at >200 AGeV collected in Otterlund's compilation [Ot 81]. The full-line histogram is obtained from RHI  $Z \geq 3$  collisions above 200 AGeV (same compilation);

c) we try to account for the complexity of the projectile by scaling  $X_2$  down by a factor of

$$\left( \frac{A_Z}{A_{He}} \right)^{2/3} \approx \left( \frac{Z}{2} \right)^{2/3}. \quad (4.15)$$

As can be seen, the distribution obtained from RHI is considerably wider, reflecting the frequent occurrence of jets of ~200 mesons in collisions of moderate primary energy/nucleon (200 AGeV or so).

Before drawing the rather tantalizing conclusion that new, cooperative phenomena are responsible for the very high multiplicities produced by VHE RHI, one must, however, bear in mind the possibility that the energy scaling may be at fault because of a systematic underestimation of the true energy of the incident cosmic nuclei.

#### 4.4.2. Alpha-Alpha VHE Collisions

4.4.2a. Experimental. As noted earlier,  $\alpha$ - $\alpha$  collisions, while lacking the complexity of collisions of heavier nuclei, are accessible to accelerator-type, i.e. high intensity experiments, at really high energies. The tool that makes such experiments possible is the CERN accelerator complex, which among others comprises the PS-ISR facility.

In the summer of 1980 alpha particles were accelerated in the Proton Synchrotron and successfully stored in the Intersecting Storage Rings at an energy of 15 AGeV, achieving a total center-of-mass energy of 126 GeV,\* with a luminosity of  $2.8 \cdot 10^{28} \text{ cm}^{-2} \text{ s}^{-1}$  corresponding to  $\sim 3$  A of alpha current in each of the two beams.

Figure 83 portrays one of the experimental arrangements used in the study of  $\alpha$ - $\alpha$  collisions, namely the so-called split-field magnet (SFM). The intersection region is viewed by three arrays of MWPCs covering almost 4 pi steradians. This is the best approximation to date of a multi-cubic-meter visual detector, capable of handling trajectories and momenta of up to 40 charged particles at a time. One must, however, bear in mind that the data are subject to considerable geometric corrections because of the finite solid angle covered by the different chamber arrays as well as because of the finite resolving power of the chambers themselves. The additional errors brought in by these corrections may often lower the realistic equivalent statistics of a, say, 100000 events run to those of a 2-4000 events bubble-chamber run.

4.4.2b. Pion Multiplicities. Both "traditional" and large four-momentum transfer experiments have been performed with the  $\alpha$ - $\alpha$  facility. As an example of the former, Table 8 [A1 81] shows the results of a fragmentation experiment, in terms of the dispersions of the  $p_T$

distributions of different light nuclear projectile fragments. As might have been expected, no dramatic effects can be seen; one might as well have been looking at a Bevalac experiment! It is in the inelastic channels, with abundant pion production, that the interesting features of VHE  $\alpha$ - $\alpha$  interactions are revealed.

Figure 84 shows a comparison between the multiplicity distribution of negative particles (even at this energy, mostly pions!) in  $\alpha$ - $\alpha$  collisions and pp collisions recorded at the same energy per nucleon [Be 81]. Table 9 lists the means as well as the  $f_2$  values for the two distributions. The last column in this table shows the normalized second factorial cumulants of the multiplicity distributions.

As can be seen, there is a marked increase in the mean multiplicity of produced particles. Again, like in pA collisions, the increase is small, with  $R = 1.60 \pm 0.01$ . The width of the multiplicity distribution is much larger in  $\alpha\alpha$  collisions than in pp, with a much larger departure from poissonicity. If this increased width is taken to reflect the effect of a large variety of  $\nu$ -values, i.e. of multiple collisions, one is once more forced to conclude from the low R value that the meson-producing efficiency of these collisions is inhibited by collective processes like coherent tubes, self-induced transparency, etc.

Figure 85 shows the location in rapidity of the multiplicity increase. This figure also includes results from a p $\alpha$  run with the protons stored at 31 GeV. The pattern known from pA interactions is visible as a strong increase of R at large positive  $y$ -values (the "alpha target region"). The  $\alpha\alpha$  collisions are, of course, symmetric but R shows an enhancement near  $y=0$  with a central R of  $1.74 \pm 0.09$ . This may well be just the effect of superposition of the two symmetric fall-offs towards  $R = 1$  similar to that seen in the p-alpha curves.

4.4.2.c. Large  $p_T$  phenomena. A much awaited result was the distribution of  $p_T$  beyond, say, 2 GeV/c where new features had been seen in both pp and pA interactions. If one interprets the A dependence of the large  $p_T$  spectra [Cr 75a] as a cooperative "volume" effect ( $\alpha > 1$  in Eq. 4.6) it would be tempting to check whether  $\alpha\alpha$  collisions would exhibit a 16-fold increase ( $4 \times 4!$ ) over pp collisions at the same energy.\*

Figure 86 shows a comparison of  $p_T$  spectra (in invariant cross sections) from  $\alpha\alpha$  and pp collisions [Fa 81]. The slopes of the  $\alpha\alpha$  and of the pp spectra are comparable, but the intensity of the  $\alpha\alpha$  spectrum lies well above the 16-fold pp curve. The enhancement is by a factor of  $\sim 24$  at  $p_T = 4$  GeV/c and reaches  $\sim 40$  at  $p_T = 6$  GeV/c. This is perhaps the most striking example of "non-billiard-ball" behavior seen to date and justifies interest in an extended VHE nucleus-nucleus investigation program.

#### 4.5. The Centauro Puzzle

##### 4.5.1. Experimental

In looking for RHI interactions at energies still higher than those reached by the ISR, or even observable in balloon or satellite-flown emulsion stacks, one cannot overlook a few highly unusual cosmic-ray events, which may possibly involve an even more unusual specie of VHE "nuclei". The events were recorded in large area ( $\sim 100 \text{ m}^2$ ) and long duration ( $\sim 1$  year) exposures of emulsion and (Pb+X-ray film) chambers to the cosmic radiation on Mt. Chacaltaya (5220 m above sea level,  $\sim 500 \text{ g/cm}^2$  atmospheric depth) by a Brazil-Japan Collaboration [La 80].

The detector consisted of an upper chamber capable of detecting electron-photon cascades with  $E > 0.2$  TeV, a production layer (essentially C), and a lower chamber geared to the detection of VHE hadrons through the



electromagnetic cascades induced by neutral pion decay. The five events dubbed "Centauros" were outstanding from the run-of-the-mill events by a high hadron multiplicity ( $\sim 100$ ) recorded in the lower chamber, i.e. the Centauro's "body" produced in an interaction 50-500 m above the apparatus, without any perceptible  $\pi^0$  production recorded in the upper chamber, i.e. the Centauro's "head". The few gamma rays observed in the upper chamber can be completely accounted for by nuclear interactions in the intervening air layer of the hadrons produced in the main event, which occurred in the air. A further unusual feature of these events is the apparently very high mean  $p_T$  of the hadrons, viz.  $\sim 1.7$  GeV/c, almost an order of magnitude higher than that of the hadrons from pp or pA collisions as seen both at the ISR at  $\sim 1$  TeV and in cosmic-ray events at comparable energies, i.e.  $\sim 200$  TeV.

A group of similar events (as far as  $\pi^0$  paucity is concerned) but with considerably lower hadron multiplicity ( $\sim 15$ ) has been dubbed "Mini-Centauros"; the statistical significance of their "degree of ununusality" is, however, much lower than that of the Centauro-type events.

#### 4.5.2. Interpretation

If the Centauro events are assumed to be produced by the collision of a single hadron with an air nucleus, their interpretation in terms of the information available from lower energies meets with considerable difficulties. The suppression of pion production (suppression of  $\pi^0$  production only would imply isospin violation!) suggests predominant production of baryon-antibaryon pairs. As already mentioned (See Sec. 4.1.3) even at 1 TeV such pairs account for only  $\sim 7\%$  of the produced particles. Even if this fraction would rise dramatically as energy increases towards  $\sim 1000$  TeV, this would conflict with the high  $\pi^0$

multiplicities observed (at even higher energies) in Extensive Air Showers (EAS). Furthermore, because of the large  $\langle p_T \rangle$ , such events would have to be entirely of the "large  $p_T$ " type. In thermodynamical terms [Fr 79] this would imply no cooling stage from the initial temperature to the pion-mass decay level, i.e. a fast decay of the kind envisaged by Fermi [Fe 50].

An easy way out of these difficulties would seem to lie in replacing the primary hadron by a primary nucleus and assigning the hadrons observed in the detector to the fragmentation products of this nucleus. In other words, circumvent the difficulty of overabundant baryon production by assuming the baryons to preexist.

However, it is very difficult to explain the Centauro observations in terms of normal nuclei. Indeed the mean free path in air of, say, an iron nucleus is only  $\sim 30 \text{ g/cm}^2$  and its survival down to  $\sim 500 \text{ g/cm}^2$  is highly unlikely. McCusker [McC 79] has argued that most of the collisions suffered would be peripheral, leaving a heavy fragment ( $Z \sim 20$ ) surviving at the observation level with a probability barely consistent with the Centauro rate. Still this would not explain why: a) the  $\pi^0$ s from the (unavoidable) interactions in air of the  $\sim 12$  nucleons stripped off are not observed and, mainly, b) the transverse momenta of the projectile fragments are an order of magnitude too high (see Fig. 79, where the nucleon fragmentation cone is well compatible with the Bradt-Kaplan formula and hence with  $\langle p_T \rangle \lesssim 150 \text{ MeV}/c$ ).

Furthermore, streamer chamber observations at the Bevalac [Sa 80a] have shown that collisions with total fragmentation of the primary RHI ("central trigger"), which would simulate the Centauros, are associated with abundant pion production. There is no apparent reason why this should change at higher energies.

A different type of "nucleus" has been considered as a candidate for the Centauro primary by Bjorken [Bj 79], namely a glob of nuclear matter of very high density held together by an extra quark. This system may have a much longer mean free path than a normal nucleus and penetrate even up to 1000 m of rock in the absence of a catastrophic central collision in which the nucleons would be released from the meta-stable glob. A difficulty encountered by this interpretation is that the high  $\langle p_T \rangle$  implies a temperature at which deltas (and other resonances) must be in equilibrium with ordinary nucleons. The  $\pi^0$ s from the decay of these resonances should then have been detected in the upper emulsion chamber.

Whatever their interpretation at this moment, the Centauro events remain a puzzle that must be addressed by experiments at any new VHE RHI accelerators.

#### 4.6. RHI Interactions and Extensive Air Showers

##### 4.6.1. Ultra High Energy (UHE) Primary Cosmic Rays

The highest energies of RHI interactions discussed hitherto were limited to  $\sim 10^2$  TeV. As can be seen in Fig. 87, the cosmic-ray spectrum extends, albeit with very low intensities, up to energies nine orders of magnitude higher than that. How low these intensities can be is best illustrated by the fact that the observations at energies exceeding  $10^{20}$  eV are limited to  $\sim 0.1$  incident nuclei per year over one square kilometer of the earth's surface [Ga 80].

Obviously with such low intensities the chance of observing an individual collision in a detector of reasonable size becomes despairingly low, to say nothing of the fact that even in nuclear emulsion (the detector with the highest transverse resolving power) it would become impossible to resolve some 500 mesons lying within  $10^{-3}$  mrad from the unavoidable electromagnetic cascades due to pi-zero decay.

It becomes evident that reactions at such high energies necessitate a calorimetric type of approach, the calorimeter material being supplied in this case by the earth's atmosphere. An extra-nuclear cascade of the type depicted in Fig. 80 but with a primary energy lying in the  $\sim 10^3$  TeV region (rather than in the TeV region as is the case in this figure) would initiate what is called an Extensive Air Shower (EAS). The nucleonic component (be it free primary protons or fragmentation products of heavier nuclei) transfer in successive collisions occurring in the air layer (equivalent down to the earth's surface to  $\sim 10$  nucleon or pion mean free paths) more and more of their energy to pions. One-third of this energy is turned over by the two-photon decay of the  $\pi^0$ 's to electromagnetic cascades; even after passing their maximum these cascades manage to spray large areas of the earth's surface with showers of up to  $10^9$  electrons covering many square kilometers.

It is this property that makes such rare events easily detectable by widespread arrays of electronic counting systems or by their global energy deposition in the atmosphere via Cherenkov light and/or scintillation [Je 53, Ca 79].

Embedded in these showers are the high energy muons resulting from  $\pi$  (and also K) -decay, which occurs with high probability because of the low density of the calorimetric material. The core of the showers is populated by the VHE hadrons, either surviving nucleons, or mesons of such high energies that their Lorentz factors turn them into quasi-stable particles at the distances involved (typically kilometers). Since the majority of interactions in the EAS occur at relatively low energies, either already reached by VHE accelerators or accessible to conservative extrapolations from accelerator data, the consequences of various

assumptions about the UHE collisions in the first few steps of the cascade can be tested by detailed extra-nuclear cascade calculations. Such calculations are being currently performed both by analytical and (mainly!) by Monte Carlo techniques (see e.g. [E1 79]).

The significance of EAS for the study of RHI interactions becomes apparent if one notices in Fig. 87 that the primary spectrum (explored beyond 100 TeV by means of the EAS only!) undergoes a change of slope beyond  $\sim 10^{15}$  eV. For many years it has been debated whether

- i) new physical processes set in around this threshold, thus changing the basic characteristics (momentum transfer, multiplicity, etc.) of elementary pp interactions as we know them even from our biggest accelerators;
- ii) there is a real change in primary spectrum shape (such a conclusion would have profound astrophysical implications); or
- iii) the composition of the primary "beam" changes drastically at UHE with a definite tilt towards heavy nuclei. It is this latter possibility that has lately received strong experimental support and that we will concentrate upon in the following.

#### 4.6.2. Heavy Nuclei as EAS Primaries

At low energies nuclei with  $Z > 2$  constitute less than 1% of all primaries. The integral energy spectrum of all primaries is well described locally by a power law

$$F(>E) \sim E^{-\gamma} . \quad (4.16)$$

If  $\gamma$  would not depend on the  $Z$  of the primary the composition would remain unchanged up to the highest energies. This brings up the obvious question of how to distinguish events with RHI primaries when, basically, detection

of an EAS is based on the late stages of the extra-nuclear cascade and the primordial UHE collision (and hence its originating particle) is not directly observed. Of the various solutions proposed and also tried, we shall discuss only a recent experiment by the Maryland group [Go 79]. It involves recording by means of a hadron calorimeter the arrival times of high energy ( $>35$  GeV) hadrons near the core of an EAS with respect to the arrival time of the shower front (a relatively thin and slightly curved electron disc). In a proton-induced EAS the surviving baryon loses  $\sim 1/2$  of its energy in each nuclear collision and still retains  $\sim 10^{-3}$  of its initial energy after a 10-step cascade through the atmosphere (at, say,  $10^{15}$  eV this is still an impressive  $\sim 1$  TeV). Hence its time delay is hardly noticeable even with the best electronic time resolution available at present. If, however, the EAS is induced by, say, a Fe-primary then at the same total energy (as measured by the total number of electrons in the shower) the projectile fragment nucleons from the first encounter(s) may be delayed by as much as tens of nanoseconds with respect to the shower front. Figure 88 shows a sample of such delays from the Maryland experiment. Barring the copious production of new, quasi-stable very massive particles (the rare occurrence of which was possibly observed in the same experiment) this is probably the most direct evidence for the increased role of RHI among EAS primaries. Figure 89 shows the result of one of the model calculations performed in order to interpret these data. The curves are contours of constant exponent  $\gamma$  (in Eq. 4.16) taken to be different for Fe and p-primaries. As can be seen the experimental point requires a difference of  $\sim 0.3$  in the exponents with a "harder" spectrum for the Fe primaries. This apparently small difference in  $\gamma$  is in fact large enough to increase the proportion of Fe by about one order

of magnitude for every 1000-fold increase in primary energy. As a result, very heavy nuclei (mainly Fe) constitute  $\sim 40\%$  of the EAS primaries around  $10^6$  GeV per nucleus, and the characteristics of AA interactions dominate the early history of the EAS development.

The "global calorimetric" measurements of EAS development by the atmospheric scintillation technique (e.g. the "Fly's Eye" device of the Utah group) have just begun to provide information as to the position of the shower maximum and its fluctuations at very high energies ( $> 10^6$  GeV/nucleus). Figure 90 shows a few examples of the early stages of EAS development as seen in a high altitude experiment on Mt. Chacaltaya [Ag 73]. Dashed curves superimposed on the data are calculated for proton primaries and are in obvious contradiction with experiment. Fe primaries (full curves) fit much better but still fail to match the very fast initial rise. Thus there appears the suspicion that some new effects set in at UHE.

For proton primaries the rise of the EAS transition curve is determined by the electromagnetic cascading of the photon component (which is, at present, thought to be thoroughly understood), the collision inelasticity, and the collision cross section. For heavy, especially iron, primaries, which seem to be dominant, an additional factor is the fragmentation pattern of the primary nucleus and of its remnants. However, even extreme models, which assume complete destruction of the primary into individual nucleons, fail in eliminating the discrepancies [Ga 80] so the fault must lie either with the reaction mechanism (huge four-momentum transfers) or with the collision cross section (very short mean free paths). Involuntarily, one is led to think of the observations at low energies, described in Sec. 3.1.2. If the explanation would be

sought in terms of copious anomalon production the lifetimes would be required to be rather long, in view of the very rarefied atmosphere layer in which the first collisions take place. Thus a new element of interest is added to the much awaited data from the Fly's Eye experiment and others of its kind.



## 5. CONCLUSIONS AND OUTLOOK

Relativistic heavy ion physics began as a "no man's land" between particle and nuclear physics, with both sides frowning upon it as "unclean", because on one hand, hadronic interactions and particle production cloud nuclear structure effects, while on the other, the baryonic environment complicates the interpretation of production experiments.

We have attempted to review here the experimental evidence on RHI collisions from the point of view that it represents a new endeavor in the understanding of strong interaction physics.

Such an approach appears increasingly justified; first, by the accumulation of data and observations of new features of hadronic interactions that could not have been detected outside a baryonic environment; second, by the maturation of the field owing to the advances made over the past several years in experimental inquiries on particle production by RHI, including pions, kaons, hyperons, and searches for antiprotons; and third, by the steady and progressive increase in the energy and mass ranges of light nuclear beams that have become available to the experimenter; indeed the energy range has widened from the  $\sim 0.2$  to 2 AGeV at the Bevalac to  $\sim 4$  AGeV at Dubna and recently, to the quantum jump in energies to  $\sim 1000$  equivalent AGeV at the CERN PS-ISR. Accompanying these expansions in the energy frontier are the immediate prospects for very heavy ion beams at the Bevalac up to, and including, 1 AGeV  $^{238}\text{U}$ , thereby extending the "mass frontier" to its ultimate extent.

It is with this increasing arsenal of beams and beam energies that the field of RHI interaction physics is being shaped. Obviously this ultimately influences the fundamental concepts and objectives as well as the trends in the physics under experimental investigation.

The revolution of RHI physics properly began in cosmic ray studies. The early Bevalac experiments on projectile fragmentation were an initial response to address some of the needs of the cosmic ray community for fragmentation cross sections that are vital to the understanding of cosmic ray sources and propagation of heavy nuclei in the interstellar medium. Although projectile fragmentation has been the most extensively studied and applied aspect of RHI at energies  $\sim 2$  AGeV, where the fragmentation of beam nuclei gives rise to a virtually unlimited variety of isotopically pure beams for experiments on, e.g., nuclear structure, searches for new neutron-rich nuclides and medical applications, a systematic program on measurements of fragmentation cross sections of essential importance to the astrophysical problems approached via cosmic rays has yet to materialize--an obvious void in a vital interdisciplinary program.

Complementary to projectile fragmentation have been the experiments on target fragmentation that have focused on light fragment production from heavy targets, primarily in the target and near-target regions of rapidity, but with brief excursions into the mid-rapidities.

Experiments in this latter field, performed mainly at the Bevalac (i.e. at energies not exceeding 2 AGeV) have hardly justified the hopes that they would provide evidence for new states of nuclear matter. A multitude of theoretical and/or phenomenological models, widely differing in their initial assumptions, have fitted these data, especially the innumerable single-particle inclusive spectra, equally well. Neither have

the investigations of particle multiplicities and of (trigger-biased) strange particle production revealed any new, unexpected features of the interactions.

Conversely, it appears reasonable to ask the question: Were these hopes justified in the first place? In other words, was it reasonable to expect at 1-2 AGeV essentially new phenomena, when the pp c.m.s. energy was slightly above pion production threshold and rather in the delta-resonance region?

Still, a few results seem to have presented us with puzzles. The Lambda production [Ha 81], while failing to yield information on the "early" stages of the reaction, has produced a too wide  $p_T$ -distribution difficult to interpret in terms of "conventional" Fermi motion and rescattering. The discrepancies between the size estimates for the interaction volume obtained via two-particle correlations on bosons [Fu 78, Bi 80, Lu 81] and fermions [Za 81] may indicate that unconventional mechanisms are at play.

One instance where RHI collisions clearly have "paid off" is the (predictable!) observation of isotopes far from stability [We 79a]. However, here we are still in the realm of "peripheral" collisions.

If one were to select experiments that have produced results directly comparable to the exciting new information available from p-nucleus collisions (Sec. 4.) one is left with the streamer chamber data from the JINR 4.5 AGeV machine [Ak 80, Ab 80], where both multiplicity and (especially) rapidity distributions of pions suggest that a sort of high-energy regime has been reached, in spite of the still very low beam rapidity. It is a pity that no comparable data have been obtained at the Bevalac, be it only for comparison purposes.

Obviously, the most tantalizing result prompted by previous knowledge from p-A is the behavior of "high- $p_T$ " pion spectra in alpha-alpha collisions at the ISR [Fa 81]. The enormous excess of differential cross sections above even an A\*A prediction strongly hints at cooperative mechanisms of a kind not envisaged in currently fashionable models of the interaction.

As to the observations of "short" mean free paths of projectile fragments at the Bevalac [Fr 80, Ja 82] and in cosmic rays [Ba 81] they are, in a peculiar way, in a class by themselves; they came as a surprise only to those either unfamiliar with, or unwarrantedly wary of, the cosmic-ray evidence accumulating over the years; from a theoretical point of view, they are as unexpected and intriguing now as they were at the time of their first observation, twenty-eight years ago.

The role of RHI physics is to close the gaping crevasse of knowledge that still exists between  $B = 0,1$  and  $B > 1$  phenomena. In the authors' view, the message that all the results discussed in this chapter appear to convey is that there is a definite need for a new generation of RHI experiments conducted at considerably higher energies and, if possible, higher intensities than have been available up to this day.

With increasing energy, especially for colliding beams and increasing nuclear sizes involved, the large number of reaction channels opening up as well as the high multiplicities of produced particles may well render inadequate the most sophisticated tools of investigation available at present at the largest high-energy accelerators.

Implicitly the choice of variables becomes critical, because selection of very well-defined final states becomes meaningless.

While conventional counting techniques may well cope with the low-intensity tails of some distributions, e.g. the  $p_T$  spectra, more global techniques like high-resolution calorimetry seem more apt to handle such variables as energy--and momentum--flow.

It is not a priori clear that a considerable increase in projectile mass will necessarily lead to new insight as long as the beam rapidity remains low. Still scientific research may remain a sterile endeavor as long as one restricts experimentation to subjects for which either our common sense (so often proved faulty!) or the theoretical court astrologers have predicted a favorable constellation.

This work was supported by the Director, Office of Energy Research, Division of Nuclear Physics of the Office of High Energy and Nuclear Physics of the U.S. Department of Energy under Contract DE-AC03-76SF00098.

FOOTNOTES

- p. 5 \*Following the recommendations of Goldhaber and Heckman (Go 78) we denote the total kinetic energy  $T(\text{GeV})$  of a particle of mass number  $A$  to be the kinetic energy per nucleon  $\tau \equiv T/A$  (GeV) times  $A$ , i.e.,  $T = \tau A\text{GeV}$ . See Sec. 2.1.
- p. 12 \*To the extent that TOF measurements belie their inherent simplicity, the identification of the uranium isotopes ( $\Delta M \sim 0.25$  amu) by measurements of rigidity,  $dE/dx$  and TOF (given  $\Delta t \approx \pm 50$  psec) at an energy of 20 AGeV (as proposed for VENUS) will require a flight path of 7.2 kilometers! -- in Berkeley??
- p. 15 \*This condition is not met when  $\beta \lesssim Z/137 \approx \beta_K$ , the velocity of the ion's K electron. A significant complication to momentum measurements of highly charged nuclear fragments, having  $Z$  up to 92, will thus occur when the condition  $\beta \gg \beta_K$  is not met. From the results of Crawford [Cr 79] on the attachment/loss cross sections of atomic electrons at relativistic beam energies, one arrives at the prediction that the relative abundances (at equilibrium) of one electron carrying to fully stripped U ions at 1 AGeV will vary from  $r = N(+91)/N(+92) = 1.8$  in hydrogen, to 0.5 in carbon. The ambiguity of atomic charge states thus diminishes the applicability of magnetic spectrometers for high- $Z$  nuclei at energies  $\gtrsim 1$  AGeV.
- p. 24 This method works best if  $\Sigma E_\gamma \gtrsim 1$  TeV.

- p. 25 \*This numerical assumption has been checked until recently only for light primary nuclei [He 78, Bh 79].
- p. 36 \*Credit for the term "anomalons" goes to Marsha Kuntz, Univ. of Cal., Irvine, who propitiously mistyped the word "anomalous" in an announcement of a talk on this subject.
- p. 47 \*Derived from relativistic energy conservation with the approximation that neglects all quadratic terms of the recoil momentum and excitation energies. The nonrelativistic expression for the recoil momentum is also used.
- p. 55 \*The photo-effect of Doppler-shifted sunlight on ultra high energy cosmic nuclei responsible for extensive showers (Sec. 4.6) was discussed as early as 1951 by Zatsepin [Za 51].
- p. 57 \*The  $N(\omega)$  spectrum given by Jäckle and Pilkuhn for a point source should be equivalent to that given by Jackson; however, it is not [O1 81]. The significance of interpretations of experiments would increase markedly with improved treatments of the virtual-photon theory, at least until such time as the virtual photon spectrum can be determined by experiment [Be 79].
- p. 83 \*Computed under the simplified geometry of colliding disks (Lorentz-contracted spheres).

- p. 101. \*as compared to "relativistic" collisions where these quantities are just comparable
- p. 102. \*Because of a net incident charge of +2, newly created secondaries must be created in pairs and  $n^-$  reflects 1/2 of that number!
- p. 103. \*and higher factorial cumulants, too!
- p. 105. \*i.e., the projectile momentum vector
- p. 106. \*especially in view of the large Lorentz time-dilatation factors involved
- p. 108. \*Cu is approximately equal to the "average" emulsion target nucleus.
- p. 109. \*Target excitation and evaporation accounts for  $\lesssim 2\%$  of the primary energy!
- p. 109. \*\*To first order this is proportional to the average path length of the proton through the target nucleus of mass  $A_T$ .
- p. 114. \*Hereafter only negative pion multiplicity data are discussed, since they are the only unequivocally produced particles detected and isospin arguments can be used to extrapolate to all pions. Such an analysis tacitly implies ignoring the (albeit very small) production rate of strange particles and baryon-antibaryon pairs.



p. 115 \*Obviously the pp results were taken from energies just available in the literature and thus they can only be expected to match the He data loosely!

p. 132 \*Equivalent in terms of cms energy to collisions of 512 AGeV alphas on a stationary He target.

p. 134 \*This factor remains unchanged if quark content, rather than nucleon content, of the two colliding objects is considered.

---

REFERENCES

- Ab 67 F. Abraham, J. Gierula, R. Levi Setti, K. Rybicki, C.H. Tsao, W. Wolter, R.L. Fricker, and R.W. Huggett, Phys. Rev. 159:1110 (1967).
- 
- Ab 76 A. Abdul-Magd, J. Hüfner, and B. Schürmann, Phys. Lett. 60B:327 (1976).
- Ab 76a A. Abdul-Magd and J. Hüfner, Z. Phys. A277:379 (1976).
- Ab 80 A. Kh. Abdurakhimov, et al. [Dubna-Tbilisi-Warsaw-Alma Ata-Moscow (FIAN) Collaboration] Warsaw Univ. Preprint IFD/2/80.
- Af 77 Y. Afek, G. Berland, G. Eilam, and A. Dar, Phys. Rev. D15:2622 (1977).
- 
- Af 78 Y. Afek, G. Berlad, G. Eilam, and A. Dar, Nuovo Cimento 43:485 (1978).
- Ag 73 C. Aguirre, et al. Proc. 13th Int. Cosmic Ray Conference. Denver, U.S.A. (1973) vol. 4, 2598. Quoted in G.B. Yodh, Composition of Cosmic Rays at High Energies, invited talk, Baltimore APS Meeting 1981, U. of Maryland, PT-81-099.
- Ag 81 G.N. Agakishew, N. Ahababian, T. Baatar, A.M. Baldin, E. Bartke, E. Bogdanovich, V.A. Vartunian, A.P. Gasparian, N.S. Grigalashvilli, V.A. Grishin, G.R. Gulkanian, L.D. Didenko, I.A. Ivanovskaia, T. Kanarek, R.A. Kvatadze, E.N. Kladnitzkaya, M. Kowalsky, S.K. Kopylova, V.B. Lyubimov, R.R. Mehtiev, V.F. Nikitina, V.M. Popova, L. Sinuc, M.J. Soloviev, A.N. Solemin, M.K. Suleimanov, G.P. Toneeva, A.P. Cheplakov, L.M. Shcheglovo, J.I.N.R. Preprint P1-81-79 Dubna 1981

- Ah 81 S.P. Ahlen, P.B. Price, and G. Tarle, Physics Today 34:32 (1981).
- Ak 80 V.D. Aksinenko, et al. (Dubna-Tbilisi-Alma Ata-Warsaw Collaboration) Nucl. Phys. A348:518 (1980)
- Al 68 J.M. Alexander, in Nuclear Chemistry Vol. I (L. Yaffe, ed.), Academic, New York (1968), p. 273.
- Al 75 J.P. Alard, A. Baldit, R. Brun, J.P. Costilhes, J. Dhermain, J. Fargeik, L. Fraysse, J. Pellet, G. Roche, and J.C. Tamain, Nuovo Cimento 30A:320 (1975).
- Al 78 W.E. Althouse, A.C. Cummings, T.L. Garrard, R.A. Mewaldt, E.C. Stone, and R.E. Vogt, IEEE Trans. on Geoscience Electronics GE-16:204 (1978).
- Al 81 M.G. Albrow and M. Jacob, Physics with  $\alpha$ -Particles, CERN 5.2.81, series 2 Number 2 (1981)
- Am 72 V. Ammosov, V.N. Boitsov, P.F. Ermolov, A.B. Fenyuk, P.A. Gorichev, E.P. Kistener, S.V. Klimenko, B.A. Manyokov, A.M. Moiseev, R.M. Sulyaev, S.V. Tarasevich, A.P. Vorobjev, H. Blumenfeld, J. Derre, P. Granet, M.A. Jabiol, A. Leveque, M. Loret, E. Pauli, Y. Pons, J. Prevost, J.C. Scherer, M. Boratav, J. Laberrigue, H.K. Nguyen, and S. Orenstein, Phys. Lett. 42B:579 (1972).
- Am 76 R.D. Amado and R.M. Woloshyn, Phys. Rev. Lett. 36:1435 (1976).
- Am 77 A.A. Amsden, F.H. Harlow, and J.R. Nix, Phys. Rev. C15:2059 (1977).
- Am 77a A.A. Amsden, J.N. Ginocchio, F.H. Harlow, J.R. Nix, M. Danos, E.C. Halbert, and R.K. Smith, Phys. Rev. Lett. 38:1055 (1977).
- An 77 L.M. Anderson, thesis, Lawrence Berkeley Laboratory Report LBL-6769, 133 pp.(1977).

- An 77a D. Antreasyan, J.W. Cronin, H.J. Frisch, M.J. Shochet, L. Kluberg, P.A. Piroué, and R.L. Sumner, Phys. Rev. Lett. 38:115 (1977).
- As 81 F. Asai, H. Sato, and M. Sano, Phys. Lett. 98B:19 (1981).
- Ba 63 W.H. Barkas, Nuclear Research Emulsions, Academic Press, New York (1963), 518 pp.
- Ba 74 S. Baush, Y. Cho, D.C. Colley, M. Derrick, R. Engelmann, L.G. Hyman, K. Jaeger, B. Musgrave, J.J. Phelan, J. Rest, P. Schreiner, P.F. Schultz, R. Singer, H. Yuta, L. Voyvodic, R. Walker, and J. Whitmore, Phys. Rev. D9:9 (1974).
- Ba 74a S. Barish, Y. Cho, D.C. Colley, M. Derrick, R. Engelmann, L.G. Hyman, K. Jaeger, B. Musgrave, J.J. Phelan, J. Rest, P. Schreiner, P.F. Schultz, R. Singer, H. Yuta, L. Voyvodic, R. Walker, and J. Whitmore, Phys. Rev. D9:2689 (1974).
- Ba 75 H.G. Baumgardt, J.U. Schott, Y. Sakamoto, E. Schopper, H. Stöcker, J. Hofmann, W. Scheid, and W. Greiner, Z. Phys. A237:359 (1975).
- Ba 75a J. Babecki, Acta Phys. Polonica B6:443 (1975).
- Ba 80 J. Bartke, Nucl. Phys. A335:481 (1980). (Proc. of the Eighth Intern. Conf. on High Energy Physics and Nuclear Structure, Vancouver, August 1979).
- Ba 81 H.B. Barker, P.S. Freier, and C.J. Waddington, Proceedings of the Seventeenth International Conference on Cosmic Rays, Versailles, France, July 13-25, Abstract HE 3.1-6, Vol. 5:75 (1981).
- Ba 81a H.G. Baumgardt, E.M. Friedlander, and E. Schopper, J. Phys. G7:L175 (1981).

- Be 69 J. Benecke, T.T. Chou, C.N. Yang, and E. Yen, Phys. Rev. 188:2159 (1969).
- Be 72 A. Bertin, P. Capiluppi, M. D'Agostino-Bruno, R.J. Ellis, G. Giacomelli, A.M. Rossi, G. Vannini, A. Bussiére, and R.T. Poe, Phys. Lett. 41B:201 (1972).
- Be 76 G. Berlad, A. Dar, and G. Eilam, Phys. Rev. D13:161 (1976).
- Be 79 B.L. Berman, H.J. Crawford, D.E. Greiner, H.H. Heckman, P.J. Lindstrom, D.L. Olson, and T.J.M. Symons, Bevalac Proposal 517 H, 17 pp. (1979).
- Be 81 W. Bell, et al., [CERN-MPI Heidelberg-Lund-PI Heidelberg-Virginia-Dortmund-Berkeley-Warsaw Collaboration] CERN EP/81/61.
- Bh 79 K.B. Bhalla, S. Hertzman, A. Oskarsson, and I. Otterlund, Phys. Lett. 82B:216 (1979).
- Bi 77 G. Bizard, C. LeBrun, J. Berger, J. Duflo, L. Goldzahl, F. Plouin, J. Oostens, M. Van Den Bossche, L. Vu Hai, F.L. Fabbri, P.L. Picozza, and L. Satta, Nucl. Phys. A285:461 (1977).
- Bi 77a J. Bialas, Acta Phys. Polonica B8:585 (1977).
- Bi 80 J.A. Bistirlich, R.J. Bossingham, H.R. Bowman, C.W. Clawson, K.M. Crowe, K.A. Frankel, O. Hashimoto, J.G. Ingersoll, M. Koike, J.P. Kurck, C.J. Martoff, J.P. Miller, D. Murphy, J.O. Rasmussen, J.P. Sullivan, P. Truöl, E. Yoo, and W.A. Zajc, Proceedings of the Hakone Seminar, Vol. 1:393 (1980); also private communication, W.A. Zajc.
- Bj 79 J.D. Bjorken and L.D. McLerran, Cosmic Rays and Particles Physics--1978, AIP Conf. Proc. Nr. 49, New York (1979) p. 509.
- Bl 79 M. Bleszynski and C. Sander, Nucl. Phys. A326:525 (1979).

- Bo 60 T. Bowen, J. Hardy, Jr., G.T. Reynolds, G. Tagliaferri, A.E. Werbrouck, and W.H. Moore, Phys. Rev. 119:2041 (1960).
- Bo 72 B. Bogdan, I. Cincheza, J. Cohen, E.M. Friedländer, M. Haiduc, M. Marcu, A. Marin, S. Neagu, R. Nitu, T. Visky, H. Annoni, C. Busi, A. Cordaillat, A. Gurtu, and A.J. Herz, Phys. Lett. 41B:221 (1972).
- Bo 73 J.D. Bowman, W.J. Swiatecki, and C.F. Tsang, Lawrence Berkeley Laboratory Report LBL-2903, 22 pp. (1973).
- Bo 74 H. Boggild and T. Ferber, Ann. Rev. Nucl. Sci. 24:451 (1974).
- Br 48 H.L. Bradt and B. Peters, Phys. Rev. 74:1828 (1948).
- Br 49 H.L. Bradt and B. Peters, Phys. Rev. 75:1779 (1949).
- Br 50 H.L. Bradt and B. Peters, Phys. Rev. 77:54 (1950).
- Br 50a H.L. Bradt and B. Peters, Phys. Rev. 80:943 (1950).
- Br 73 W. Bromberg, D. Chaney, D. Cohen, T. Ferbel, P. Slattery, D. Underwood, J.W. Chapman, J.W. Cooper, N. Green, B.P. Roe, A.A. Seidl, and J.C. VanderVelde, Phys. Rev. Lett. 31:1565 (1973).
- Bu 61 S.T. Butler and C.A. Pearson, Nuovo Cimento 19:1266 (1961).
- Bu 63 S.T. Butler and C.A. Pearson, Phys. Rev. 129:836 (1963).
- Bü 73 F.W. Büsser, L. Camilleri, L. DiLella, G. Gladding, A. Placci, B.G. Pope, A.M. Smith, J.K. Yoh, E. Zavattina, B.J. Blumenfeld, L.M. Lederman, R.L. Cool, L. Litt, and S.L. Segler, Phys. Lett. 46B:471 (1973)
- Bu 75 W. Busza, J.E. Elias, D.F. Jacobs, P.A. Swartz, C.C. Young, and M.R. Sogard, Phys. Rev. Lett. 34:836 (1975).
- Ca 53 C. Castagnoli, G. Cortini, C. Franzinetti, A. Manfredini, and D. Moreno, Nuovo Cimento 10:1539 (1953).

- Ca 76 E. Calligarich, G. Cecchet, R. Dolfini, A. Giovannini, S. Ratti, M. Tirelli, R. Gessaroli, G. Parrini, S. Squarcia, G. Costa, L. Perini, J.L. Lloyd, and R.G. Thompson, Lett. al Nuovo Cimento 16:129 (1976).
- Ca 79 G.L. Cassiday, H.E. Bergeson, E.C. Loh, J.W. Elbert, and D. Steck, Cosmic Rays and Particle Physics--1978, AIP Conf. Proc. Nr. 49 New York (1979) p. 417.
- Ce 77 L.S. Celenza, J. Hüfner, and C. Sander, Nucl. Phys. A276:509 (1977).
- Ch 62 C.B. Childs and L. Slifkin, Phys. Rev. Lett. 9:354 (1962).
- Ch 63 C.B. Childs and L. Slifkin, Rev. Sci. Inst. 34:101 (1963).
- Ch 68 G.F. Chew, Comments Nucl. Part. 2:107 (1968).
- Ch 72 G.F. Chew, "High Energy Heavy Ion Beams as Tests of Nuclear Democracy and as a Tool to Clarify Regge Asymptotic Behavior," LBL Internal Report (1972), unpublished.
- Ch 72a J.W. Chapman, N. Green, B.P. Roe, A.A. Seidl, D. Sinclair, J.C. VanderVelde, C.M. Bromberg, D. Cohen, T. Ferbel, P. Slattery, S. Stone, and B. Werner, Phys. Rev. Lett. 29:1686 (1972).
- Ch 73 G.F. Chew, "Large and Small Baryon Numbers in High Energy Collision Theory," LBL Internal Report (1973), unpublished.
- Ch 74 D.L. Cheshire, R.W. Huggett, D.P. Johnson, W.V. Jones, S.P. Rountree, S.D. Verma, W.K.H. Schmidt, R.J. Kurz, T. Bowen, and E.P. Krider, Phys. Rev. D10:25 (1974).
- Ch 79 M. Chemtob, Nucl. Phys. A314:387 (1979).
- Cl 68 T.F. Cleghorn, P.S. Freier, and C.J. Waddington, Can. J. Phys. Suppl. 46:572 (1968).
- Co 74 G. Cocconi, Phys. Lett. 49B:459 (1974).

- Co 74a J.I. Cohen, E.M. Friedländer, M. Marcu, A.A. Marin, and R. Nitu, Nuovo Cim. Lett. 9:337 (1974).
- Cr 75 H.J. Crawford, P.B. Price, J. Stevenson, and L.W. Wilson, Phys. Rev. Lett. 34:329 (1975).
- Cr 75a J.W. Cronin, H.J. Frisch, M.J. Shochet, J.P. Boymond, P.A. Piroue, and R.L. Sumner, Phys. Rev. D11:3105 (1975).
- Cr 79 H.J. Crawford, Lawrence Berkeley Laboratory Report LBL-8807, Ph.D. Thesis: 84 pp. (1979).
- Cu 74 J.C. Cumming, P.E. Haustein, R.W. Stoenner, L. Mausner, and R.A. Naumann, Phys. Rev. C10:739 (1974).
- Cu 76 J.C. Cumming, R.W. Stoenner, and P.E. Haustein, Phys. Rev. C14:1554 (1976).
- Cu 78 J.C. Cumming, P.E. Haustein, T.J. Ruth, and G.J. Virtes, Phys. Rev. C17:1632 (1978).
- Cu 78a J.C. Cumming, P.E. Haustein, and H.C. Hseuh, Phys. Rev. C18:1372 (1978).
- Da 72 A. Dar and J. Vary, Phys. Rev. D6:2412 (1972).
- De 76 M. Deutschmann, R. Honecker, H. Kirk, M. Klein, R. Nahnauer, R. Hartmann, H. Plothow, V.T. Cocconi, M.J. Coughlin, S. Humble, G. Kellner, D.R.O. Morrison, D. Smid, R. Stroynowski, L. Aniola, T. Coghén, K. Dziunikowska, J. Figiel, A. Zalewska, E. Leitner, J. Stiewe, J. Krolikowski, A. Para, and A.K. Wroblewski, Nucl. Phys. B103:198 (1976).
- Do 65 D.E. Dorfan, J. Eades, L.M. Lederman, W. Lee, C.C. Ting, P. Piroue, S. Smith, J.L. Brown, J.A. Kadyk, and G.H. Trilling, Phys. Rev. Lett. 14:995 (1965).
- Ei 54 Y. Eisenberg, Phys. Rev. 96:1378 (1954).



- E1 79 R.W. Ellsworth, G.B. Yodh, and T.K. Gaisser, Cosmic Rays and Particle Physics--1978 AIP Conf. Proc. Nr. 49, New York (1979) p. 111.
- Ez 77 Ezell, L.F. Gutay, A.T. Laasanen, F.T. Dao, P. Schübelin, and F. Turkot, Phys. Rev. Lett. 38:873 (1977).
- Fa 81 M.A. Faessler, CERN-EP/81-103 (1981).
- Fe 50 E. Fermi, Prog. Theor. Phys. 5:270 (1950).
- Fe 69 R. Feynmann, Phys. Rev. Lett. 23:1415 (1969).
- Fe 73 H. Feshbach and K. Huang, Phys. Lett. 47B:300 (1973).
- Fi 74 A. Firestone, V. Davidson, D. Lam, F. Nagy, C. Peck, A. Sheng, F.T. Dao, R. Hanft, E. Malamud, F. Nezirick, A. Dzierba, R. Poster, P. Schlein, and W. Slater, Phys. Rev. D10:2080 (1974).
- Fi 78 R.D. Field, Phys. Rev. Lett. 40:997 (1978).
- Fl 75 F.L. Fleischer, P.B. Price, and R.M. Walker, Nuclear Tracks in Solids, University of California Press, Berkeley (1975).
- Fo 77 G.N. Fowler and R.M. Weiner, Phys. Lett. 70B:201 (1977).
- Fo 78 G.N. Fowler and R. Weiner, Phys. Rev. D17:3118 (1978).
- Fo 81 G.N. Fowler, E.M. Friedlander, and R. Weiner, LBL-12279 (1981) Phys. Lett., in press.
- Fr 48 P. Freier, E.J. Lofgren, E.P. Ney, F. Oppenheimer, H.L. Bradt, and B. Peters, Phys. Rev. 74:213 (1948).
- Fr 48a P. Freier, E.J. Lofgren, E.P. Ney, and F. Oppenheimer, Phys. Rev. 74:1818 (1948).
- Fr 61 E.M. Friedlander and M. Spirchez, Nucl. Sci. Abstr. 15:3457 (1961).
- Fr 67 E.M. Friedlander and A. Friedman, Nuovo Cimento 52A:912 (1967).

- Fr 72 W.R. Frazer, L. Ingber, C.H. Mehta, C.H. Poon, D. Silverman, K. Stowe, P.D. Ting, and H.J. Yesian, Rev. Mod. Phys. 44:284 (1972).
- Fr 74 E.M. Friedlander, M. Marcu, and R. Nitu, Lett. Nuovo Cimento 9:341 (1974).
- Fr 74a E.M. Friedlander, Nuovo Cimento Lett. 9:337 (1974).
- Fr 76 S. Frankel, W. Frati, O. Van Dyck, R. Werbeck, and V. Highland, Phys. Rev. Lett. 36:642 (1976).
- Fr 77 S. Frankel, Phys. Rev. Lett. 38:1338 (1977).
- Fr 78 E. Friedlander, AIP Conference Proceedings No. 49, Particles and Fields, subvolume 16, p. 157 (1978).
- Fr 78a E. Friedlander and R.M. Weiner, Lawrence Berkeley Laboratory Report LBL-7724 (1978).
- Fr 79 E. Friedlander and R.M. Weiner, Phys. Rev. Lett. 43:15 (1979).
- Fr 80 E.M. Friedlander, R.W. Gimpel, H.H. Heckman, Y.J. Karant, B. Judek, and E. Ganssauge, Phys. Rev. Lett. 45:1084 (1980).
- Fr 81 S. Fredriksson and J. Jändel, Royal Institute of Technology, Stockholm, Sweden Report TRITA-TFY-81-11, 8 pp. (1981).
- Fr 82 E.M. Friedlander and Y.J. Karant, LBL Nuclear Science Annual Report, to be published (1982).
- Fu 78 S.Y. Fung, W. Gorn, G.P. Kiernan, J.J. Lu, Y.T. Oh, and R.T. Poe, Phys. Rev. Lett. 41:1592 (1978).
- Ga 80 T.K. Gaisser and G.B. Yodh, Ann. Rev. Nucl. Part. Sci. 30:475 (1980).
- Ge 78 C.K. Gelbke, C. Olmer, M. Buenerd, D.L. Hendrie, J. Mahoney, M.C. Mermaz, and D.K. Scott, Phys. Rep. 42:312 (1978).
- Ge 80 J.V. Geaga, S.A. Chessin, J.Y. Groissard, J.W. Harris, D.L. Hendrie, L.S. Schroeder, R.N. Treuhaft, and K. Van Bibber, Phys. Rev. Lett. 45:1993 (1980).

- Gl 67 R. Glauber and B. Mollow, Phys. Rev. 160:1076 (1967).
- Go 74 K. Gottfried, Phys. Rev. Lett. 32:957 (1974).
- Go 74a A.S. Goldhaber, Phys. Lett. 53B:306 (1974).
- Go 75 F.S. Goulding and B.G. Harvey, Ann. Rev. Nucl. Sci. 25:167 (1975).
- Go 77 J. Gosset, H.H. Gutbrod, W.G. Meyer, A.M. Poskanzer, A. Sandoval, R. Stock, and G.D. Westfall, Phys. Rev. C16:629 (1977).
- Go 78 A.S. Goldhaber and H.H. Heckman, Ann. Rev. Nucl. Part. Sci. 28:161 (1978).
- Go 78a J. Gosset, J.I. Kapusta, and G.D. Westfall, Phys. Rev. C18:844 (1978).
- Go 79 J.A. Goodman, R.W. Ellsworth, A.S. Ito, J.R. McFall, F. Siohan, R.E. Streitmatter, S.C. Tonwar, P.R. Vishwanath, and G.B. Yodh, Cosmic Rays and Particle Physics--1978 AIP Conf. Proc. Nr. 49, New York (1979) p. 207.
- Gr 72 D.E. Greiner, Nucl. Inst. and Methods 103:291 (1972).
- Gr 72a F. Granzer, E. Schopper, K. Dardat, G. Henig, J.U. Schott, G. Haase, and F. Zörgiebel, Proc. of the 8th International Conference on Nuclear Photography and Solid State Track Detectors, Vol. 1:365 (1972).
- Gr 75 D.E. Greiner, P.J. Lindstrom, H.H. Heckman, B. Cork, and F.S. Bieser, Phys. Rev. Lett. 35:152 (1975).
- Gr 76 F. Grard, V.P. Henri, J. Schlesinger, R. Windmolders, E. DeWolf, F. Verbeure, D. Drijard, Y. Goldschmidt-Clermont, A. Grant, and A. Stergiou, Nucl. Phys. B102:221 (1976).
- Gr 78 D.E. Greiner, F.S. Bieser, and H.H. Heckman, IEEE Trans. on Geoscience Electronics GE-16:163 (1978).

- Gr 81 D.E. Greiner, Proceedings of the Workshop on Future Relativistic Heavy ion Experiments, GSI Darmstadt, October 7-10, 1980, R. Bock and R. Stock, Editors, GSI 81-6:470 (1981).
- Gu 76 H.H. Gutbrod, A. Sandoval, P.J. Johansen, A.M. Poskanzer, J. Gosset, W.G. Meyer, G.D. Westfall, and R. Stock, Phys. Rev. Lett. 37:667 (1976).
- Gu 80 H.H. Gutbrod, Conf. on High Energy Nuclear Interactions and Properties of Dense Nuclear Matter (Hakone) Japan, 7-11 July 1980. Also Lawrence Berkeley Laboratory Report LBL-11123, 49 pp. (1980).
- Gy 78 M. Gyulassy and S.K. Kauffmann, Phys. Rev. Lett. 40:298 (1978).
- Gy 79 M. Gyulassy, S.K. Kauffmann, and L.W. Wilson, Phys. Rev. C20:2267 (1979).
- Gy 80 M. Gyulassy, 1980 Inst. of Nuclear Studies, Kikuchi Summer School on Nuclear Physics at High Energy, Fuji-Yoshida, Japan, 1-4 July 1980. Also Lawrence Berkeley Laboratory Report LBL-11040, 58 pp. (1980), and references therein.
- Ha 56 R. Hanbury-Brown and R.Q. Twiss, Nature 178:1046 (1956).
- Ha 65 R. Hagedorn, Nuovo Cim. Suppl. 3:147 (1965).
- Ha 76 G. Haase, E. Schopper, and F. Granzer, Proc. of the 9th International Conference on Solid State Nuclear Track Detectors, Vol. 1:199 (1976).
- Ha 79 R.L. Hatch and S.E. Koonin, Phys. Lett. 81B:1 (1979).
- Ha 81 J.W. Harris, A. Sandoval, R. Stock, H. Stroebele, R.E. Renfordt, J.V. Geaga, H.G. Pugh, L.S. Schroeder, K.L. Wolf, and A. Dacal, Phys. Rev. Lett. 47:229 (1981).
- He 53 W. Heisenberg, Kosmische Strahlung, Springer, Berlin (1953) p. 148 ff.

- He 72 H.H. Heckman, D.E. Greiner, P.J. Lindstrom, and F.S. Bieser, Phys. Rev. Lett. 28:926 (1972).
- He 74 J. Hebert, C.J.D. Hebert, H. Areti, P.M. Patel, G. Hartner, M.-A. Vincent, G. Baumann, R. Devienne, J. Lory, C. Meton, D. Schune, B. Willot, Tsai-Chü, M. Morand, P. Cüer, R. Kaiser, J.P. Massue, R. Pfohl, G. Baroni, S. diLiberto, S. Petrara, G. Romano, J. Cohen, E.M. Friedlander, A. Marin, M. Marcu, R. Nitu, I.O. Herlund, A. van Ginneken, M. Juric, R. Schmitt, J.M. Bolta, J. Pellicer, G. Rey, F. Tejerina, F. Fernandez, J. Medina, A. Dura, and V. Gandia, Phys. Lett. 48B:467 (1974).
- He 76 H.H. Heckman and P.J. Lindstrom, Phys. Rev. Lett. 37:56 (1976).
- He 78 H.H. Heckman, H.J. Crawford, D.E. Greiner, P.J. Lindstrom, and L.W. Wilson, Phys. Rev. C17:1651 (1978).
- He 78a H.H. Heckman, D.E. Greiner, P.J. Lindstrom, and H. Shwe, Phys. Rev. C17:1735 (1978).
- Ho 68 W.J. Hogan, P.A. Piroué, and A.J.S. Smith, Phys. Rev. 166:1472 (1968).
- Hü 75 J. Hüfner, K. Schäfer, and B. Schürmann, Phys. Rev. C12:1888 (1975).
- Hü 78 J. Hüfner, C. Sander, and G. Wolschin, Phys. Lett. 73B:289 (1978).
- Hü 78a J. Hüfner, Proceedings of 4th High Energy Heavy Ion Summer Study, Lawrence Berkeley Laboratory (24-28 July 1978), LBL-7766, p. 135.
- Ja 72 J.D. Jackson and R.L. McCarthy, Phys. Rev. B6:4131 (1972).
- Ja 74 B. Jakobsson, R. Kulberg, and I. Otterlund, Z. Physik 268:1 (1974).

- Ja 75 J. Jaros, Thesis, Lawrence Berkeley Laboratory Report LBL-3849, 166 pp. (1975).
- Ja 75a J.D. Jackson, Classical Electrodynamics, Wiley, New York (1975) 2nd ed., p. 719.
- Jä 75 R. Jäckle and H. Pilkuhn, Nucl. Phys. A247:521 (1975).
- Ja 76 B. Jakobsson and R. Kulberg, Physica Scripta 13:327 (1976).
- Ja 77 B. Jakobsson, R. Kulberg, and I. Otterlund, Nucl. Phys. A276:523 (1977).
- Ja 82 P.L. Jain and G. Das, Phys. Rev. Lett. 48:305 (1982).
- Je 53 J.V. Jelley and W. Galleraith, Phil. Mag. 44:619 (1953).
- Ju 68 B. Judek, Can. J. Phys. 46:343 (1968).
- Ju 72 B. Judek, Can. J. Phys. 50:2082 (1972).
- Ju 75 B. Judek, Proceedings of the Fourteenth International Conference on Cosmic Rays, Munich, West Germany, 1975 (Max-Planck-Institut für Extraterrestrische Physik, Garching, West Germany, 1975) Vol. 7, p. 2342.
- Ka 52 M.F. Kaplon, B. Peters, H.L. Reynolds, and D.M. Ritson, Phys. Rev. 85:295 (1952).
- Ka 78 S.B. Kaufman, E.P. Steinberg, and M.W. Weisfield, Phys. Rev. C18:1349 (1978).
- Ka 79 Y.K. Karant, Lawrence Berkeley Laboratory Report LBL-9171, 8 pp. (1979).
- Ka 80 S.B. Kaufman, E.P. Steinberg, B.D. Wilkins, and D.J. Henderson, Phys. Rev. C22:1897 (1980).
- Ka 80a J.I. Kapusta, Phys. Rev. C21:1301 (1980).
- Ke 73 A.K. Kerman and M.S. Weiss, Phys. Rev. C8:408 (1973).
- Ki 58 C. Kittel, Elementary Statistical Physics Wiley and Sons (New York), p. 219 (1958).

- Kn 79 J. Knoll and J. Randrup, Nucl. Phys. A324:445 (1979).
- Ko 72 Z. Koba, H. Nielsen, P. Olesen, Nucl. Phys. B40:317 (1972).
- Ko 74 G.I. Kopylov, Phys. Lett. 50B:472 (1974).
- Ko 74a G.I. Kopylov and M.I. Podgoretsky, Yad. Fiz. 18:656 (1973) [Sov. J. Nucl. Phys. 18:336 (1974)].
- Ko 77 S.E. Koonin, Phys. Rev. Lett. 39:680 (1977).
- Ko 78 S. Koonin, Proceedings of 4th High Energy Heavy Ion Summer Study, Lawrence Berkeley Laboratory (24-28 July 1978), LBL-7766, p. 379.
- Kr 54 W.L. Kranshaar and L.J. Marks, Phys. Rev. 93:326 (1954).
- Ku 73 R. Kullberg and I. Otterlund, Z. Phys. 259:245 (1973).
- La 53 L. Landau, IZV. Akad. Nauk SSSR 17:51 (1953).
- La 80 C.M.G. Lattes, Phys. Reports 65:151 (1980).
- Le 74 J.V. Lepore and R.J. Riddell, Jr., Lawrence Berkeley Laboratory LBL-3086, 24 pp. (1974).
- Le 79 M.-C. Lemaire, S. Nagamiya, S. Schnetzer, H. Steiner, and I. Tanihata, Phys. Lett. 85B:38 (1979).
- Li 75 P.J. Lindstrom, D.E. Greiner, H.H. Heckman, B. Cork, and F.S. Bieser, Lawrence Berkeley Laboratory Report LBL-3650, 10 pp. (1975).
- Lo 50 J. Lord, J. Fainberg, and M. Schein, Phys. Rev. 80:970 (1950).
- Lo 80 W. Loveland, Cheng-Luo, P.L. McGaughey, D.L. Morrissey, and G.T. Seaborg, Lawrence Berkeley Laboratory LBL-11658, pp. 38 (1980), submitted to Phys. Rev. C.
- Lo 81 W. Loveland, D.L. Morrissey, K. Aleklett, G.T. Seaborg, S.B. Kaufman, E.P. Steinberg, B.D. Wilkins, J. Cumming, P.E. Haustein, and H.C. Hseuh, Phys. Rev. C23:253 (1981).

- Lu 81 J.J. Lu, D. Beavis, S.Y. Fung, W. Gorn, H. Huie, G.P. Kiernan, R.T. Poe, and G. VanDalen, Phys. Rev. Lett. 46:898 (1981).
- Ma 77 N. Masuda and F. Uchiyama, Phys. Rev. C15:1598 (1977).
- Ma 79 M.R. Maier, H.G. Ritter, and H.H. Gutbrod, Proceedings of the IEEE Transactions in Nuclear Science, San Francisco, CA, 17-20 October 1979; also Lawrence Berkeley Laboratory Report LBL-10062, 4 pp. (1979).
- Me 77 A. Mekjian, Phys. Rev. Lett. 38:640 (1977).
- Me 77a A. Mekjian, R. Bond, P.J. Johansen, S.E. Koonin, and S.I.A. Garpman, Phys. Lett. 71B:43 (1977).
- Me 78 A. Mekjian, Phys. Rev. C17:1051 (1978).
- Me 78a A. Mekjian, Nucl. Phys. A312:491 (1978).
- Me 80 A. Mekjian, Phys. Lett. 89B:177 (1980).
- Me 80a W.G. Meyer, H.H. Gutbrod, Ch. Lukner, and A. Sandoval, Phys. Rev. C22:179 (1980).
- Mi 54 A. Milone, Nuovo Cimento Suppl. 12:353 (1954).
- Mo 71 E.J. Moniz, I. Sick, R.R. Whitney, J.R. Ficenec, R.D. Kephart, and W.P. Trower, Phys. Rev. Lett. 26:445 (1971).
- Mo 78 D.J. Morrissey, W. Loveland, and G.T. Seaborg, Z. Phys. A289:123 (1978).
- Mo 79 D.J. Morrissey, L.F. Oliveira, J.O. Rasmussen, G.T. Seaborg, Y. Yariv, and Z. Fraenkel, Phys. Rev. Lett. 43:1139 (1979).
- Mo 80 D.J. Morrissey, W. Loveland, M. de Saint Simon, and G.T. Seaborg, Phys. Rev. C21:1783 (1980).
- Mu 71 A.H. Muller, Phys. Rev. D4:150 (1971).
- My 78 W.D. Myers, Nucl. Phys. A296:177 (1978).
- McC 67 S.L. McCall and E.L. Hahn, Phys. Rev. Lett. 18:908 (1967).



- McC 79 C.B.A. McCusker, 16th ICRC, Kyoto (1979) p. 365.
- Na 78 S. Nagamiya, I. Tanihata, S. Schnetzer, L. Anderson, W. Brückner, O. Chamberlain, G. Shapiro, and H. Steiner, J. Phys. Soc. Japan 44 Suppl.:378 (1978).
- Na 79 S. Nagamiya, L. Anderson, W. Brückner, O. Chamberlain, M.-C. Lemaire, S. Schnetzer, G. Shapiro, H. Steiner, and I. Tanihata, Phys. Lett. 81B:147 (1979).
- Na 80 S. Nagamiya, M.-C. Lemaire, S. Schnetzer, H. Steiner, and I. Tanihata, Phys. Rev. Lett. 45:602 (1980).
- Na 81 S. Nagamiya, M.-C. Lemaire, E. Moeller, S. Schnetzer, G. Shapiro, H. Steiner, and I. Tanihata, Lawrence Berkeley Laboratory Report LBL-12123, 116 pp. (1981), submitted to Phys. Rev. C.
- 
- Ni 76 K.J. Nield, T. Bowen, G.D. Cable, D.A. DeLise, E.W. Jenkins, R.M. Kalbach, R.C. Noggle, A.E. Pifer, Phys. Rev. C13:1263 (1976).
- Ni 79 J.R. Nix, Prog. Nucl. Phys. 2:237 (1979).
- O1 81 D.L. Olson, B.L. Berman, D.E. Greiner, H.H. Heckman, P.J. Lindstrom, G.D. Westfall, and H.J. Crawford, Phys. Rev. C24:1529 (1981).
- Ot 67 I. Otterlund, Arkiv Fysik 38:467 (1967).
- Ot 78 I. Otterlund, Proceedings of 4th High Energy Heavy Ion Summer Study, Lawrence Berkeley Laboratory (24-28 July 1978), LBL-7766 p. 289.
- Ot 81 I. Otterlund, Proc. Workshop on Future Relativistic Heavy Ion Experiments, GSI Darmstadt GSI 81-6/1981, p. 185.

- Pa 75 J. Papp, J. Jaros, L. Schroeder, J. Staples, H. Steiner, A. Wagner, and J. Wiss, Phys. Rev. Lett. 10:601 (1975).
- Po 51 I. Ya. Pomeranchuk, Dokl. Akad. Nauk. SSSR, 78:884 (1951).
- Po 59 C.F. Powell, P.H. Fowler, and D.H. Perkins, The Study of Elementary Particles by the Photographic Method, Pergamon, London: 669 pp. (1959).
- 
- Po 60 N.T. Porile, Phys. Rev. 120:572 (1960).
- Po 78 B. Povh, Ann. Rev. Nucl. Part. Sci. 28:1 (1978).
- Po 79 N.T. Porile, G.D. Cole, and C.R. Rudy, Phys. Rev. C19:2288 (1979).
- Po 79a N.T. Porile, D.R. Fortney, S. Pandian, R.A. Johns, T. Kaiser, K. Wielgoz, T.S.K. Chang, N. Sugarman, J.A. Urbon, D.J. Henderson, S.B. Kaufman, and E.P. Steinberg, Phys. Rev. Lett. 43:918 (1979).
- 
- Ra 79 J. Randrup, Nucl. Phys. A314:429 (1979).
- Ra 80 J. Randrup and C.M. Ko, Nucl. Phys. A343:590 (1980).
- Ra 81 J. Randrup and S.E. Koonin, Nucl. Phys. A356:223 (1981).
- Ra 81a J. Randrup, Phys. Lett. 99B:9 (1981).
- Ro 79 W.J. Romo and P.J. Watson, Phys. Lett. 88B:354 (1979).
- Ru 75 C.R. Rudy and N.T. Porile, Phys. Lett. 59B:240 (1975).
- Ry 67 K. Rybicki, Nuovo Cim. Ser. 10, 49B:203 (1967).
- Sa 80 A. Sandoval, H.H. Gutbrod, W.G. Meyer, R. Stock, Ch. Lukner, A.M. Poskanzer, J. Gosset, J.-C. Jourdain, C.H. King, G. King, Nguyen Van Sen, G.D. Westfall, and K.L. Wolf, Phys. Rev. C21:1321 (1980).
- Sa 80a A. Sandoval, R. Stock, H. Stelzer, R. Renfordt, J. Harris, J. Brannigan, J. Geaga, L. Rosenberg, L. Schroeder, and K.L. Wolf, Phys. Rev. Lett. 45,874 (1980).

- Sc 63 A. Schwarzschild and C. Zupancic, Phys. Rev. 129:854 (1963).
- Sc 74 J.U. Schott, Dissertation, Institut für Kernphysik der J.W. Goethe-Universität, Frankfurt/M (IKF-33) 1974.
- Sc 76 J.U. Schott, E. Schopper, and R. Staudt, Proceedings of the 9th International Conference on solid State Nuclear Track Detectors, Vol. I:615 (1976).
- Sc 77 I.A. Schmidt and R. Blankenbecler, Phys. Rev. D15:3321 (1977).
- Sc 78 E. Schopper and H.G. Baumgardt in Proceedings of the Symposium on Relativistic Heavy Ion Research, GSI Darmstadt (March 7-10, 1978) p. 104.
- Sc 79 W. Schimmerling, J.W. Kast, D. Ortendahl, R. Madey, R.A. Cecil, B.O. Anderson, and A.R. Baldwin, Phys. Rev. Lett. 43:1985 (1979).
- Sc 79a L.S. Schroeder, Nucl. Inst. and Methods 162:395 (1979).
- Sc 80 D.K. Scott, Prog. in Part. and Nucl. Phys. 4:5 (1980).
- Sc 80a L.S. Schroeder, 1980 Inst. of Nuclear Studies, Kikuchi Summer School on Nuclear Physics at High Energy, Fuji-Yoshida, Japan, 1-4 July 1980. Also Lawrence Berkeley Laboratory Report LBL-11102, 63 pp. (1980).
- Sc 80b L.S. Schroeder, Seminar on High Energy Nuclear Interactions and Properties of Dense Nuclear Matter (Hakone) Japan, 7-11 July 1980. Also Lawrence Berkeley Laboratory Report LBL-10899, 75 pp. (1980).
- Sc 81 S.R. Schnetzer, Thesis, Meson Production in Relativistic Heavy Ion Collisions, Lawrence Berkeley Laboratory Report LBL-13727, 124 pp. (August 1981).

- Sh 81 A. Shor, K. Ganezer, J. Carroll, G. Igo, J. Geaga, S. Abachi, A. Sagle, T. Mulera, V. Perez-Mendez, P. Lindstrom, F. Zarbakhsh, and D. Woodward, Proc. of 5th High Energy Heavy Ion Summer Study, Lawrence Berkeley Laboratory Report LBL-12652 (1981) p. 470.
- Sk 59 P. Skeggestad and S.O. Sörensen, Phys. Rev. 113:1115 (1959).
- Sm 77 R.K. Smith and M. Danos, Proceedings of the Topical Conference on Heavy Ion Collisions, Fall Creek Falls Park, Tennessee (1977), p. 363.
- St 77 J. Stevenson, P.B. Price, and K. Frankel, Phys. Rev. Lett. 38:1125 (1977).
- St 79 R. Stock, in Heavy Ion Collisions Vol. 1 (R. Bock, ed.) North Holland, Amsterdam (1979), p. 607.
- St 79a H. Stöcker, J.A. Maruhn, and W. Greiner, Z. Phys. A293:173 (1979).
- 
- St 80 J.D. Stevenson, Phys. Rev. Lett. 45:1773 (1980).
- St 80a R. Stock, H.H. Gutbrod, W.G. Meyer, A.M. Poskanzer, A. Sandoval, J. Gosset, C.H. King, G. King, Ch. Lukner, Nguyen Van Sen, G.D. Westfall, and K.L. Wolf, Phys. Rev. Lett. 44:1243 (1980).
- St 80b H. Stöcker, J.A. Maruhn, and W. Greiner, Phys. Rev. Lett. 44:1725 (1980).
- St 80c H. Stöcker, G. Graebner, J.A. Maruhn, and W. Greiner, Z. Physik A295:401 (1980).
- St 80d H. Stöcker, G. Graebner, J.A. Maruhn, and W. Greiner, Phys. Lett. 95B:192 (1980).
- St 81 J.D. Stevenson, J. Martinis, and P.B. Price, Phys. Rev. Lett. 47:990 (1981).

- Su 73 J.D. Sullivan, P.B. Price, H.J. Crawford, and M. Whitehead, Phys. Rev. Lett. 30:136 (1973).
- Th 77 W. Thome, K. Eggert, K. Giboni, H. Lisken, P. Darriulat, P. Dittmann, M. Holder, K.T. McDonald, H. Albrecht, T. Modis, K. Tittel, H. Preissner, P. Allen, I. Derado, V. Eckardt, H.-J. Gebauer, R. Meinke, P. Seyboth, and S. Uhlig, Nucl. Phys. B129:365 (1977).
- To 57 S. Tokunaga, T. Ishii, K. Nishikawa, Nuovo Cimento 5:517 (1957).
- Ua 81 UA-1 Collaboration, Phys. Lett. 107B:320 (1981).
- Va 82 K. Van Bibber and A. Sandoval in Heavy Ion Science (D.A. Bromley, ed.) Plenum Press, New York (1982).
- We 34 C.F. von Weizsäcker, Z. Phys. 88:612 (1934).
- 
- We 76 G.D. Westfall, J. Gosset, P.J. Johansen, A.M. Poskanzer, W.G. Meyer, H.H. Gutbrod, A. Sandoval, and R. Stock, Phys. Rev. Lett. 37:1202 (1976).
- We 78 R.M. Weiner and A. Masuda, Phys. Rev. D18:1515 (1978).
- We 79 G.D. Westfall, L.W. Wilson, P.J. Lindstrom, H.J. Crawford, D.E. Greiner, and H.H. Heckman, Phys. Rev. Lett. C19:1309 (1979).
- We 79a G.D. Westfall, T.J.M. Symons, D.E. Greiner, H.H. Heckman, P.J. Lindstrom, J. Mahoney, A.C. Shotter, D.K. Scott, H.J. Crawford, C. McParland, T.C. Awes, C.K. Gelbke, and J.M. Kidd, Phys. Rev. Lett. 43:1859 (1979).
- We 79a G.D. Westfall, T.J.M. Symons, D.E. Greiner, H.H. Heckman, P.J. Lindstrom, J. Mahoney, A.C. Shotter, and D.K. Scott, H.J. Crawford, C. McParland, T.C. Awes, C.K. Gelbke, and J.M. Kidd, Phys. Rev. Lett. 43:1859 (1979).
- Wi 35 E.J. Williams, Mat. Fys. Medd. Dan. Vid. Selsk. 13:no. 4 (1935).

- Wi 65 H. Winzeler, Nucl. Phys. 69:661 (1965).
- Wi 78 L. Winsberg, Nucl. Instr. Methods 150:465 (1978).
- Wi 81 W.J. Willis, Proceedings of the Workshop on Future Relativistic Heavy Ion Experiments, GSI Darmstadt, October 7-10, 1980, R. Bock and R. Stock, Eds., GSI 81-6, p. 499 (May 1981).
- Wo 78 V. Wosiek, Acta Phys. Pol. B9:191 (1978).
- 
- Wo 79 J.G. Woodworth, K.G. McNeill, J.W. Jury, R.A. Alvarez, B.L. Berman, D.D. Faul, and D. Meyer, Phys. Rev. C19:1667 (1979).
- Wr 70 A. Wroblewski, Proc. Colloquium on High Multiplicity Hadronic Interactions. Paris: Ecole Polytechnique (1970) pp. 11-57.
- Ya 57 H. Yagoda, Nuovo Cimento 6:559 (1957).
- Ya 78 F.B. Yano and S.E. Koonin, Phys. Lett. 78B:556 (1978).
- 
- Ya 79 Y. Yariv and Z. Fraenkel, Weizmann Institute Report No. WIS-79/15-Ph (1979).
- Za 51 G.T. Zatsepin, Doklady Akad. Nauk SSSR 80:577 (1951).
- Za 81 F. Zarbakhsh, A.L. Sagle, F. Bouchard, T.A. Mulera, V. Perez-Mendez, R. Talaga, I. Tanihata, J.B. Carrol, K.S. Ganezev, G. Igo, J. Oostens, D. Woodward, and R. Sutter, Phys. Rev. Lett. 46:1268 (1981).

Table 1. Response of different techniques to the characteristics of single particle events.<sup>a</sup>

Technique	$\beta$	$ p $	$\theta$	$Z \geq 1$	E	Capability for detection of neutral decays
TOF	$\frac{\Delta L}{\Delta t}$					
Cerenkov	$\beta$ , thresh.					
Scintillators, solid-state detectors	$\frac{dE}{dx}$ , given Z			$\frac{dE}{dx}$ , given $\beta$		
Calorimetry						
a) low E			Target-detector angle, e.g. plastic ball	$\frac{dE}{dx}$ , given $\beta$	Kinetic energy of non-interacting, stopping particles, e.g. particle identifiers.	
b) high E					Total energy of interacting particles via nuclear and E.M. cascades	
Magnetic Spectrometry		$p \propto Z\rho$	Trajectory fitting (helix)			
Nuclear emulsion	<u>grain density</u> , given Z	$p \propto Z/\beta$ $p \propto Z\rho$	Trajectory fitting (straight line)	$\frac{dE}{dx}$ , given $\beta$	Kinetic energy by range given $M/Z^2$	For $\tau \lesssim 10^{-12}$ s e.g. Dalitz pairs, charmed particles
Plastics	<u>etch rate</u> , given Z	b	b	b	"	
Bubble/streamer chambers	<u>bubble/streamer densities</u> , given Z	$p \propto Z\rho$	Trajectory fitting (helix)			For $10^{-10} \lesssim \tau \lesssim 10^{-9}$ s e.g. $K^0$ , $\Lambda^0$

<sup>a</sup>Underlined quantities are those actually measured.

<sup>b</sup>Possible, but not yet demonstrated.

Electronics Techniques

Visual Techniques

Table 2. Response of different techniques to joint characteristics of multiparticle events.

Technique	Primary energy	Multiplicities		Semi-inclusive Studies	Triggering (event selection)	Spatial resolution	
		Pre-existing	Created				
TOF		If hodoscoped, proj. frame only			Yes		
Electronic Techniques	Cerenkov Scintillators, solid-state detectors				Yes		
	Calorimetry				Yes		
	a) low E		yes, but only for large arrays, e.g. the Plastic Ball	Yes, for large arrays	Yes	low	
	b) high E	Total energy deposition via nuclear and E.M. cascades			Yes		
Magnetic spectrometry		mainly in proj. frame	mainly for central and projectile rapidities	Yes, for large arrays	Yes		
Visual Techniques	Nuclear emulsion	Via angular distributions of projectile fragments &/or mesons	$\sim 4\pi$ sr, incl. target fragments of range $> 5 \mu\text{m}$	$\sim 4\pi$ sr, complete coverage down to $\sim 0.5$ AMeV	Yes, rapidity for target and pseudo-rapidity for proj. frame	(AgCl only) hybrid systems only for emulsion proper	0.5- $5 \mu\text{m}$
	Plastics						
	Bubble chambers		$\sim 4\pi$ sr, low-energy target fragments lost if range $< \text{few } 100 \mu\text{m}$	$\sim 4\pi$ sr	Yes, mainly in central and proj. rapidity regions	hybrid systems only	$> 1-10$ mm
	Streamer chambers		$\sim 4\pi$ sr, low-energy target fragments lost in targets	$\sim 4\pi$ sr, mainly negative secondaries	"	Yes	$> 10$ cm



Table 3. Comparison of theory and experiment for parameters related to a  $\sigma_{P_{\parallel}}$  mass dependence of the form  $\sigma_{P_{\parallel}}^2 = 4\sigma_o^2 F(B-F)/B^2$ .  
 Derived quantities are Fermi momentum  $P_f = 20\sigma_o^2(B-1)B^2$   
 and average excitation energy  $kT = 4\sigma_o^2/m_n B$ .

Parameter	Reference	Projectile		
		Energy		
		$^{16}_O$	$^{12}_C$	$^{12}_C$
		2.1 AGeV	2.1 AGeV	1.05 AGeV
$\sigma_o$ (MeV/c)	expt. [Gr 75]	171 ± 3	147 ± 4	141 ± 5
"	sudden			
	approximation [Le 74]	162	145	145
"	virtual			
	clusters [Fe 73]	212	179	179
$P_f$ (MeV/c)	expt. [Gr 75]	185 ± 3	182 ± 5	174 ± 6
"	electron			
	scattering [Mo 71]	230	221	221
kT (AMeV)	expt. [Gr 75]	7.8 ± 0.3	7.7 ± 0.4	7.1 ± 0.5
average binding energy (MeV)		8.0	7.7	7.7

Table 4. Compilation of Data on Short MFP of Projectile Fragments

Group	Detector	Primary	"Beam"	Ratio Measured	ESD <sup>a</sup>	Probability P(<R)	Ref.
1)	Emulsion	cosmic rays		R <sub>1</sub>	2.8 <sup>b</sup>		C1 68
	"	"	"	R <sub>1</sub>	3.1		Ju 72
2)	"	2 AGeV	Fe,O	R <sub>2</sub>	3.4	3.4 x 10 <sup>-4</sup>	Fr 80
	"	2 AGeV	Fe,Ar	R <sub>2</sub>	3.2	6.9 x 10 <sup>-4</sup>	Ja 82
	"	Cosmic rays		R <sub>2</sub>	<u>2.8<sup>b</sup></u>	<u>2.5 x 10<sup>-3</sup></u>	Ba 81
				Global:	5.1	1.5 x 10 <sup>-7</sup>	
	Propane						
3)	Bubble Chamber	4 AGeV	C	R <sub>1</sub>	2.1 <sup>c,d</sup>		Ag 81

<sup>a</sup>Equivalent standard deviations from the hypothesis that R is unity.

<sup>b</sup>Experiments share, in part, a common data base.

<sup>c</sup>Excludes first 7 cm of track after collision.

<sup>d</sup>This number was derived in Ref. Fr 82 from the observed deviations between secondary cross sections and the beam values (all positive). Although not significant by itself, this deviation points in the same direction as the rest of the available experimental data.

Table 5. Electromagnetic dissociation cross sections (mb).

Fragment	Target	Measured	Calculated	
		$\sigma_{em}$	JPE1 <sup>a</sup>	WW <sup>b</sup>
(a)				
<sup>17</sup> O	Ti	8.7 ± 2.7	13.4	12.5
	Pb	136.0 ± 2.9	132.	135.
	U	140.8 ± 4.1	162.	167.
<sup>16</sup> O	Ti	6.3 ± 2.5	5.8	5.4
	Cu	9.0 ± 3.5	9.4	9.0
	Sn	27.5 ± 4.0	24.0	23.7
	W	50.0 ± 4.3	46.1	46.8
	Pb	65.2 ± 2.3	53.9	55.2
	U	74.3 ± 1.7	66.1	68.1
<sup>17</sup> N	Ti	-0.5 ± 1.0	2.9	2.4
	Pb	20.2 ± 1.8	23.3	23.8
	U	25.1 ± 1.6	28.5	29.2
(b)				
<sup>16</sup> N	Ti	2.7 ± 2.1		
	Pb	12.7 ± 4.4		
	U	11.3 ± 5.1		
<sup>14</sup> C	Ti	8.8 ± 1.1		
	Pb	33.7 ± 4.0		
	U	35.1 ± 2.7		
<sup>13</sup> C	Ti	-1.6 ± 1.5		
	Pb	21.9 ± 2.4		
	U	17.6 ± 2.6		

<sup>a</sup>For d = 1.5 fm<sup>b</sup>For d = -1.5 fm

Table 6. Average velocities and thermal parameters of emitting Maxwellian sources.

Fragment	0.4 AGeV $^{20}\text{Ne} + \text{U}$				0.5 AGeV $^{40}\text{Ar} + \text{Au}$	
	Ref. St 77		Ref. Go 77		Ref. St 77	
	$\beta_0$	$\tau(\text{MeV})$	$\beta_0$	$\tau(\text{MeV})$	$\beta_0$	$\tau(\text{MeV})$
$^8\text{Li}$	0.060	37			0.059	56
B	0.091	62	0.06	27	0.070	61
C	0.087	61			0.087	61
N					0.100	61
O					0.082	69
F					0.087	74
Weighted Ave.	0.076 $\pm$ 0.017 52				0.085 $\pm$ 0.006 65	
Calc.: fireball <sup>a</sup>	0.27	49			0.38	63
Calc.: "explosion" <sup>b</sup>	0.077	14			0.18	40

<sup>a</sup>Ref. Go 77, Table VII

<sup>b</sup>Eqs. 3.13-3.18

Table 7. Results of pion interferometry analysis in RHI experiments, based on parametric fits to a Gaussian source density distribution, Eq. 3.26. Lifetime parameter  $c\tau$  is either estimated or, because of its insensitivity to the value of  $r_0$  is set to 1.5 fm. The parameters  $r_0$  and  $c\tau$  from representative pp and  $\pi p$  experiments, based largely on a uniform source density distribution are included for comparative purposes.

Pair	Beam	Target	Pion Multiplicity	$r_0$ (fm)	$c\tau$ (fm)	$\lambda$	$\chi^2/NDF$	Ref.
$2\pi^-$	1.8 A GeV	$Pb_3O_4$	2-15 ( $\pi^-$ )	$3.98 \pm 0.78$	$0.6^{+1.2}_{-0.5}$	$\cong 1$	14.69/7	Fu 78
		$^{40}Ar$						
$2\pi^-$	"	"	2-4	$3.12 \pm 1.10$	$\cong 1.5$	"	8.56/7	Lu 81
			5-8	$4.00 \pm 0.72$		"	15.15/7	
			9-12	$4.82 \pm 0.65$		"	7.23/7	
			13-15	$5.57 \pm 1.17$		"	3.59/7	
$2\pi^-$	"	KCl	-	$1.84^{+0.27}_{-0.25}$	"	"		Bi 80
				$2.98 \pm 0.30^a$	"	"		
				$3.18 \pm 0.33^a$	"	$0.86 \pm 0.07$		
$2\pi^+$	"	"	-	$1.60^{+0.55}_{-0.40}$	"	$\cong 1$		
				$3.85 \pm 0.45^*$	"	"		
				$3.92 \pm 0.43^a$	"	$0.78 \pm 0.07$		
$2\pi^-$	p	p		$r_{  } = 0.73^{+0.10}_{-0.11}$	$0.59 \ 0.17^b$	$\cong 1$		Ez 77
	28.5 GeV/c			$r_{\perp} = 1.65^{+3.56}_{-0.99}$				
$2\pi^+$	$\pi^{\pm}$	p	5 & 7	$r_{  } = 0.9^{+1.10^b}_{-0.3}$	$0.4^{+0.6^b}_{-0.4}$	"		
	4-25 GeV/c	( $\pi^{\pm}$ )		$r_{\perp} = 1.8^{+0.3^b}_{-0.5}$	$1.6^{+0.4^b}_{-0.6}$	"		

<sup>a</sup>Corrected for  $2\pi$  relative Coulomb interaction: Gamov correction

<sup>b</sup>based on uniform radiating spherical source

Table 8. Abundance and dispersion of transverse momentum distribution for nuclear fragments produced in  $\alpha\alpha$  collisions at the ISR

---

Fragment	Abundance %	$\sigma_{P_T}$ (MeV/c)
p	64	176 $\pm$ 20
d	18	250 $\pm$ 10
t	2	310 $\pm$ 20
He <sup>3</sup>	3	320 $\pm$ 30
$\alpha$	13	285 $\pm$ 15

---

Table 9. Comparison of parameters of the negative pion multiplicity distribution from pp and  $\alpha\alpha$  collisions at the ISR

---

	$\langle n^- \rangle$	$f_2$	$\phi_2 = f_2 / \langle n^- \rangle^2$
pp	$4.44 \pm 0.05$	$4.20 \pm 0.10$	$0.213 \pm 0.005$
$\alpha\alpha$	$7.15 \pm 0.07$	$16.28 \pm 0.48$	$0.318 \pm 0.009$

---

FIGURE CAPTIONS

- Fig. 1. Schematic drawing of the "Plastic Ball-Wall" detector system. Details of the scintillator modules are shown.
- Fig. 2. Schematic drawing of the HISS facility at the Bevalac, showing direct and high-dispersion beam lines to the 2 m dia, 30 kG superconducting HISS magnet.
- Fig. 3. Values of transverse and longitudinal momenta for pions and protons for selected values of rapidity  $y$  and pseudo-rapidity  $\eta$ .
- Fig. 4. a) Rapidity and b) pseudo-rapidity distributions for protons at  $\gamma_{\text{lab}} = 1000$  in the laboratory frame that result from the transformation of the same (Monte Carlo generated) center of mass rapidity distributions, assumed to be uniform between  $-3 \leq y_{\text{cm}} \leq 3$ .
- Fig. 5. A nuclear collision of a 1.9-AGeV  $^{56}\text{Fe}$  (enters left) observed in nuclear emulsion. This collision produces a high multiplicity of target fragments, which, on this evidence alone, would serve to identify the event as a candidate for a central collision, yet exhibits the characteristics of a peripheral collision where the bulk of the incident Fe nucleus maintains its identity as a fragment of  $Z \approx 22$ , accompanied by (2) He fragments.
- Fig. 6. Rigidity spectrum of the carbon isotopes produced by the fragmentation of 2.1 AGeV  $^{16}\text{O}$  projectiles. Arrows indicate the rigidities of each isotope at beam velocity.
- Fig. 7. Longitudinal momentum distribution in the projectile frame for  $^{10}\text{Be}$  fragments from 2.1 AGeV  $^{12}\text{C}$  incident on a Be target. Solid curve is a Gaussian fit to the data, with  $\langle P_{\parallel} \rangle = -35 \pm 7$  MeV/c and  $\sigma_{P_{\parallel}} = 134 \pm 3$  MeV/c.



- Fig. 8. RMS deviation of the longitudinal momentum distribution in the projectile frame versus mass of the fragment from  $^{16}\text{O}$  at 2.1 AGeV.
- Fig. 9. Invariant production cross section versus rapidity for nuclei  $A_F \leq 3$  produced at 0-deg by the fragmentation of  $^4\text{He}$  at 2.1 AGeV.
- Fig. 10. Longitudinal momentum distributions of protons in the projectile frame, with  $p_{\perp} = 0$  from  $^4\text{He}$  projectiles at momenta 0.93, 1.75, and 2.88 AGeV/c incident on a  $^{12}\text{C}$  target.
- Fig. 11. Forward-transverse asymmetry of the momentum distributions of protons in the projectile frame from 2.88 AGeV/c  $^4\text{He}$  incident on a  $^{12}\text{C}$  target.
- Fig. 12. A succession of (4) fragmentation reactions initiated by a 1.9 AGeV  $^{56}\text{Fe}$  that enters from the left. Actual distance between first and final interactions is 5.7 cm.
- Fig. 13. Measured values of MFP in nuclear emulsion for  $^{16}\text{O}$  beam nuclei at 2.1 AGeV as a function of the distance from the scan-line (pick-up point) of the incident  $^{16}\text{O}$ .
- Fig. 14. The ratio  $R_1$  of the mean-free-path parameter  $\Lambda^*$  for PFs to  $\Lambda_{\text{beam}}$  plotted as a function of distance from the origins of emission of the PFs.
- Fig. 15. Mass yield curves for the fragmentation products of Cu bombarded by 80 GeV  $^{40}\text{Ar}$ , 25 GeV  $^{12}\text{C}$ , and 28 GeV  $^1\text{H}$  [Cu 78].
- Fig. 16. Slope of mass yield curve versus kinetic energy of beam. Proton beams are indicated by solid points, heavy ion beams by open points [Cu 78].

Fig. 17. Longitudinal recoil velocity versus fragment mass number  $A_F$  for selected targets, beams, and beam energy. Solid curves are  $\langle \beta_{||} \rangle = P_0 / 931 A_F$  for the values of  $P_0$  indicated. Dashed lines delineate data points. Data are from refs. Ka 78, Ka 80, and Lo 81.

Fig. 18. Mean velocity of selected fragments from the deexcitation stage as a function of the kinetic energy of P,  $^{12}\text{C}$ , and  $^{20}\text{Ne}$  projectiles. Symbols are: i) for Au target;  $\uparrow$ : protons [Ka 78];  $\bullet$ :  $^{12}\text{C}$  [Ka 80];  $\blacksquare$ :  $^{20}\text{Ne}$  [Ka 80] and ii) for Ta target;  $\square$ :  $^{20}\text{Ne}$  [Lo 81].

Fig. 19. The product of the fragment mass and excitation energy as a function of beam energy and mass. Symbols are: i) for Au target,  $\circ$ : protons;  $\bullet$ :  $^{12}\text{C}$ ;  $\blacksquare$ :  $^{20}\text{Ne}$  and ii) for U target;  $\diamond$ :  $^{12}\text{C}$  and  $\blacklozenge$ :  $^{20}\text{Ne}$ . Data are compiled from references Lo 81, Ka 80, Lo 80, and Ka 78.

Fig. 20. Reduced cross sections for the production of eight representative fragment nuclides from 1.7 AGeV  $^{18}\text{O}$  versus mass number of target.

Fig. 21. Target factors, normalized to  $\gamma_T(^{12}\text{C})$ , plotted versus mass number of target. See text for the description of the solid and dashed curves.

Fig. 22. Ratio of production cross sections of various nuclides from the bombardment of Cu by 80 GeV  $^{40}\text{Ar}$  and by 25 GeV  $^{12}\text{C}$  plotted as a function of the product mass number. Dashed line is the mean ratio for  $37 \leq A_F \leq 64$  [Cu 78].

Fig. 23. Production cross sections of target fragments,  $14 \leq A_F \leq 196$ , from the bombardment of  $^{197}\text{Au}$  by heavy-ion projectiles, relative to those by protons at the same kinetic energies, plotted as a function of mass number of the fragment. Dashed lines indicate the calculated ratios of the total reaction cross sections [Ka 80].

Fig. 24. Beam-rapidity fragment production cross section ratios (normalized to the  $^9\text{Be}$  cross sections) for  $^{18}\text{O}$  at 1.7 AGeV plotted versus mass number of the target.

Fig. 25. An artist's view of a collision between nuclei at relativistic energies, depicting the spectator/participant concept and the formation of a nuclear "fireball" by the participating (overlapping) nucleons in the collision.

---

Fig. 26. Lorentz invariant cross section for the production of protons by 0.8 AGeV  $^{20}\text{Ne}$  on NaF. The laboratory beam momentum per nucleon is indicated by an arrow [Na 78].

Fig. 27. a) Contour plot of the invariant cross sections for proton emission in the  $P_{\perp}/m_p c$  versus rapidity plane. Dotted lines are not based on measurements but are drawn to illustrate the general features of a complete contour map, based on present knowledge.

b) Calculated contours of invariant cross sections in the  $P_{\perp}/m_p c$  versus rapidity plane for isotropic particle emission in the center of mass frame [Na 78].

Fig. 28. Double differential cross sections for protons from  $^{20}\text{Ne}$  incident on U at four different beam energies. Firestreak model calculations for proton emission are indicated by the curves drawn at each laboratory angle.

Fig. 29. Comparison of the knock-out model [Ha 79] with experiments for the inclusive proton and pion spectra for 0.8 AGeV  $^{12}\text{C}$  incident on C and Pb targets [Na 78]. Shown are the double differential cross sections plotted versus laboratory momentum observed at various laboratory angles.

Fig. 30. Double differential cross sections for neutron emission in the reaction  $^{20}\text{Ne} + \text{U} \rightarrow \text{n} + \text{X}$  at 337 AMeV plotted as a function of neutron energy. The spectra are shown for laboratory angles  $30^\circ$ :  $\circ$ ;  $45^\circ$ :  $\triangle$ ;  $60^\circ$ :  $\square$ ; and  $90^\circ$ :  $\diamond$ . Solid curves are the results of firestreak model calculations [Sc 79].

Fig. 31. Neutron to proton cross-section ratios as a function of neutron energy at  $30^\circ$  laboratory angle. a) Ratios of the measured neutron and proton cross sections for Ne + Pb(U) collisions at 0.4 AGeV beam energy. Proton data are based on refs. Sa 80 (solid points) and Le 79, Na 81 (open points). Firestreak calculations for each set of ratios are shown. b) Neutron to proton ratio corrected to the time before coalescence, i.e. fragment emission, takes place. The solid line is the calculated ratio for a U target given by a cascade model [St 80].

Fig. 32. Velocity of frame for which the angular distribution, evaluated in that frame, is most nearly isotropic.

Fig. 33. Boron spectra from Ne + U at 0.4 AGeV, with thermodynamic fits characterized by  $\beta = 0.06 \approx \beta_{\text{cm}}$  of the fused projectile-target system [Go 77].

Fig. 34. Microprojection drawings of emulsion events exhibiting characteristics of projectile-target explosions. Top) a 2.1 AGeV  $^{14}\text{N}$  beam nucleus gives rise to 15 high velocity  $Z = 1$  fragments within a forward  $25^\circ$  cone. Bottom) a 1.9 AGeV  $^{56}\text{Fe}$  interaction in emulsion that produces 36  $Z = 1$  and one  $Z = 2$  relativistic fragments within a forward  $35^\circ$  cone.

Fig. 35. Pseudo-rapidity distribution of charged particles emitted from central Fe + CNO reactions in emulsion detectors. The curves show predictions from the fireball model plus spectator evaporation [Bh 79, Ot 80].

Fig. 36. Dependence of the angular distribution of  $^3\text{He}$  fragments on beam energy, target and projectile masses and energy window of the  $^3\text{He}$  fragment: (a)-(c) Ne on U at 2.1, 0.4, and 0.25 AGeV, respectively; (d) Ne on Al at 2.1 AGeV; and (e)  $^4\text{He}$  on U at 0.4 AGeV [Go 77].

Fig 37. Percentages of protons bound in clusters of  $^4\text{He}$ ,  $^3\text{He}$ ,  $^3\text{H}$ , and  $^2\text{H}$  produced in the Ne + U reaction at 0.4 AGeV at  $30^\circ$  and  $90^\circ$  in the laboratory, as a function of energy per nucleon. Percentage of free protons is given on right scale [Sa 80].

Fig. 38. Spectra of deuterons,  $^3\text{H}$  and  $^3\text{He}$  from 0.8 AGeV C + C collisions are shown by the solid data points. Open points are the spectra deduced from the squares (for deuterons) and cubes (for  $^3\text{H}$  and  $^3\text{He}$ ) of the observed proton spectra in the same collisions [Na 81].

Fig. 39. Ratios  $E_d(d^3\sigma/d^3P_d)/[E_p(d^3\sigma/dP_p^3)]$  at  $p_d = 2p_p$  for Ne + NaF collisions at beam energies 0.4, 0.8, and 2.1 AGeV. The data are compared with firestreak model calculations [Na 81].

- Fig. 40. A high-multiplicity event produced by the collision of a 1.8 AGeV  $^{40}\text{Ar}$  with an Ag(Br) nucleus in nuclear emulsion. Approximately 63 secondary particles are emitted in this interaction. A 50  $\mu\text{m}$  scale is shown.
- Fig. 41. Schematic diagram of an azimuthal array of detectors surrounding a scattering chamber, containing targets and detector telescope, used in experiments on target fragmentation [Sa 80].
- Fig. 42. Average associated multiplicities  $\langle M \rangle$  plotted versus the total kinetic T of the projectile indicated, incident on uranium [Sa 80]. Dashed line: mean number of participating projectile nucleons  $A'$  plotted vs the projectile mass  $A_p$ .
- Fig. 43. Proton angular distributions in collisions of 0.8 AGeV Ar + Pb, plotted as a function of the tag-counter multiplicity M.
- 
- Protons with energies more than 100 MeV were detected [Na 80].
- Fig. 44. Proton spectra from 0.8 AGeV Ar + Pb collisions for inclusive (above) and high-multiplicity (below) events. Projectile and target rapidities are indicated by  $y_p$  and  $y_T$ , respectively [Na 80].
- Fig. 45. Rapidity distributions of low-energy fragments emitted from central collisions between 2 AGeV  $^4\text{He}$ ,  $^{16}\text{O}$ , and  $^{40}\text{Ar}$  and emulsion nuclei [He 78].
- Fig. 46. Angular distributions of target fragments  $T < 31$  AMeV observed in emulsions produced by  $^4\text{He}$ ,  $^{16}\text{O}$ , and  $^{40}\text{Ar}$  projectiles at 2.1 (1.8) AGeV. Curves are fitted Maxwell-Boltzmann distributions;  $\beta_{||}$  is the mean longitudinal source velocity,  $\beta_{\perp} = [2\tau/M_n]^{1/2}$  where  $\tau$  is the characteristic temperature.
- Fig. 47. Possible configurations of a two-pion coincident event.

- Fig. 48. Kopylov ratio  $R^{\bar{m}}$  versus relative pion momentum  $q$ . 1.8-AGeV  $^{40}\text{Ar}$  beam incident on  $\text{Pb}_3\text{O}_4$ , events selected by "central" trigger [Fu 78].
- Fig. 49. Kopylov ratio versus relative pion momentum. 1.8-AGeV  $^{40}\text{Ar}$  incident on KCl. Gamov-corrected data with fitted (solid) curve are shown. Dashed curve is fit to uncorrected data [Bi 80].
- Fig. 50. Acceptance of the spectrometer + multiplicity counter array used in ref. [Za 81]:  $S$  denotes the spectrometer acceptance,  $M$  that of the multiplicity counters.
- Fig. 51. Plot of the correlation function  $R$  (Eq. 3.28) for proton pairs with low relative momentum from 1.8 AGeV Ar + KCl collisions. Full circles: data taken near beam rapidity; crosses: data taken at mid-rapidity without multiplicity selection; open circles: the same with a multiplicity cut (in the target rapidity region) corresponding to an estimated mean multiplicity of  $\sim 25$ .
- Fig. 52. Dependence of multiplicity in pp collisions on primary energy. Upper curve: total charged multiplicity; lower curve: multiplicity of negative secondaries. The straight lines are power law fits constrained to given exponents.
- Fig. 53. Multiplicity distributions in VHE pp collisions: Circles: 50 GeV; crosses: 200 GeV.
- Fig. 54. Energy dependence of the deviation from poissonicity of pp multiplicity distributions. The second factorial cumulant  $f_2$  is plotted against the mean multiplicity (negative secondaries). Circles: HBC-data; crosses: ISR-data.

Fig. 55. Comparison of multiplicity distributions from pp collisions with a mixture of two Poisson distributions: the ratio of the observed probability for emitting  $n^-$  negative secondaries to the expectation (computed from the fitted parameters) is plotted against the reduced multiplicity. Different symbols refer to HBC (50-400 GeV) and ISR (500-2000 GeV) experiments [Am 72, Br 73, Ch 72a, Fi 74, Ba 74a, Th 77].

---

Fig. 56. Transverse momentum spectra (invariant cross sections) of secondaries from pp collisions in the "low  $p_T$ " range ( $\lesssim 1$  GeV/c). 1: HBC data ( $\pi^-$ ) at 22 GeV; the rest of the curves are from ISR experiments, viz. 2: 300 GeV  $\pi^-$ ; 3: 1400 GeV  $\pi^-$ ; 4: 1400 GeV p; 5: 1400 GeV  $\bar{p}$ .

Fig. 57. Same as Fig. 56 in the "high  $p_T$ " range ( $p_T > 1$  GeV/c). ISR data for neutral pions. 1: 300 GeV; 2: 500 GeV; 3: 1000 GeV; 4: 1400 GeV; 5: 2000 GeV) approximate equivalent laboratory energy; except for curve 5, the scales are shifted by one order of magnitude (in invariant cross section) with respect to each other. To offer a comparison of slopes, the dashed line, labeled L, is the extrapolation of the universal "low  $p_T$ " spectrum (not normalized).

---

Fig. 58. Energy dependence of charged particle multiplicity in pA collisions. Circles, crosses and triangles: Emulsion data at different degrees of target excitation (AgBr); squares: counter data on Cu target. Full circles: pp data from HBC redrawn from Fig. 52.



- Fig. 59. Target size dependence of charged particle multiplicities from pA collisions in two rapidity bins: circles: forward cms hemisphere; squares: backward cms hemisphere (for a pp collision at the same energy, viz. 200 GeV). a) emulsion data; b) counter data.
- Fig. 60. Comparison of the pseudo-rapidity distribution of charged secondaries from p-C collisions (circles) with the same distribution for excess particles ( $\Delta_{ab}$ 's) produced in p-Cu and p-Pb collisions; arrow shows cms rapidity.
- Fig. 61. The mean multiplicity of excess particles from different target nuclei (normalized to that of the forward cms hemisphere in pp collisions at the same energy) plotted against the average target thickness.
- 
- Fig. 62. Correlation between nuclear transparency and poissonicity in different rapidity bins (200 GeV emulsion data). a)  $N_h$  dependence; b) multiplicity distribution of the corresponding rapidity bin. Straight lines: predictions for a chaotic source; curves: for a coherent source;  $Y_m$  is the maximum rapidity kinematically allowed.
- Fig. 63. Transverse momentum dependence (in the "high  $p_T$ " range) of the exponent  $\alpha$  in the power-law approximation for the target-size dependence of particle production cross sections in pA collisions.
- Fig. 64. Transverse momentum spectra of pions from low-energy AA collisions.
- Fig. 65. Target mass dependence of pion production at different emission angles in low-energy AA collisions.

Fig. 66. Energy dependence of negative pion production in AA collisions in the Bevalac energy range (streamer chamber data).

Fig. 67. Multiplicity distributions of negative pions from He nucleus collisions at 4.5 AGeV (streamer chamber). Circles: C target; crosses: Al target; squares and triangles: "matching" pp collisions (HBC data) at 28 and 42 GeV, respectively.

Fig. 68. Plot of cms available energy in alpha-nucleus collisions vs the same energy in "matching" pp collisions.

Fig. 69. Same as Fig. 54 for AA collisions at 4.5 AGeV: circles: He beam; squares: C beam.

Fig. 70. Comparison of negative pion multiplicity distributions from: circles: CC collisions at 4.5 AGeV (i.e.  $\sim 50$  GeV total projectile energy) with that from 50 GeV pp collisions, triangles.

---

Fig. 71. Dependence of negative pion multiplicity from 4.5 AGeV AA collisions on projectile and target sizes.

Fig. 72. Rapidity distributions of negative secondaries from 4.5 AGeV He collisions with different targets.

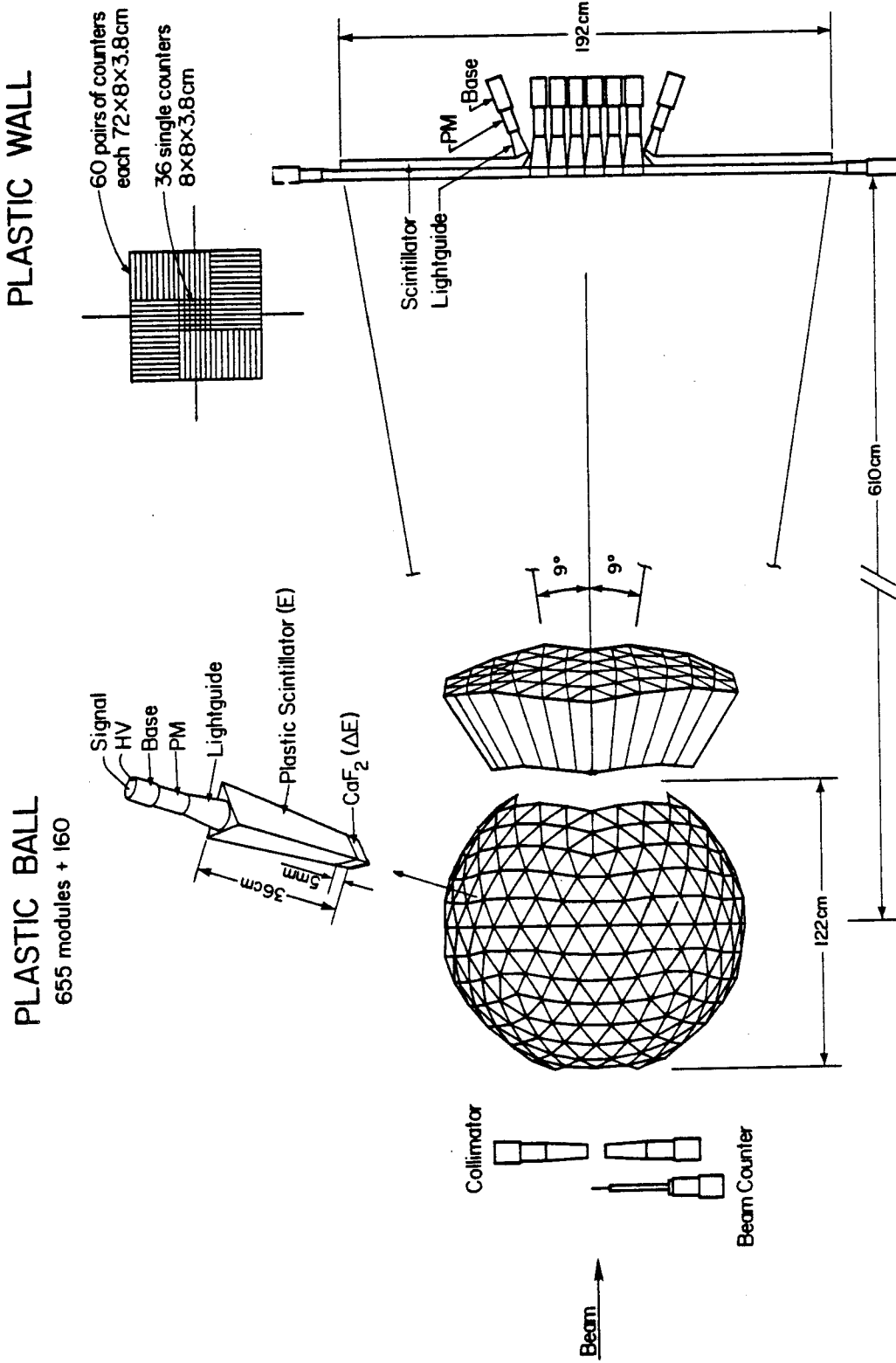
Fig. 73. Transverse momentum distributions of negative secondaries from 4.5 AGeV He collisions with different targets.

Fig. 74. Dependence of the mean charged particle multiplicity from 4.5 AGeV He collisions with different targets on the average target thickness, for low and high transverse momenta.

Fig. 75. Differential cross sections for the production of  $K^+$  mesons plotted as a function of kinetic energy of the  $K^+$  in the nucleon-nucleon center of mass system for both AA and pA collisions. Beam energies for proton and  $^{20}\text{Ne}$  projectiles are 2.1 AGeV [Sc 81c]. The trend of the cross sections for  $p + p \rightarrow K^+ + x$  at 2.54 GeV is also shown [Ho 68].

- Fig. 76. Invariant cross sections for the production of  $K^+$  mesons versus laboratory momenta of the  $K^+$  measured at angles  $15^\circ$  to  $80^\circ$  in the laboratory for the reaction  $Ne + NaF \rightarrow K^+ + x$  at 2.1 AGeV. The data are compared with the row-on-row model, without (dashed curves) and with (solid curves) scattering of the kaons [Sc 81c, Ra 80a].
- Fig. 77. Results of kinematic fits to the observed neutral strange particle decays,  $\Lambda \rightarrow p\pi^-$  and  $K^0 \rightarrow \pi^+\pi^-$ , plotted in the invariant mass plane  $m(p\pi^-)$  vs  $m(\pi^+\pi^-)$  [Ha 81].
- Fig. 78.  $^{40}\text{Ar} + \text{KCl} \rightarrow \Lambda$  events as a function of  $p_\perp$  and  $p_\parallel$  in the nucleus-nucleus c.m. at 1.8 AGeV. a) Scatterplot of the data. The hatched curve shows the region where events were excluded because of poor spatial resolution. The solid curve corresponds to the  $NN \rightarrow \Lambda KN$  kinematic limit. b) Linear contour plot of the results for the Monte Carlo calculation (Fermi motion only). c) Linear contour plot for Monte Carlo results with subsequent rescattering included [Ha 81].
- Fig. 79. Microphotograph of a VHE AA collision. Production of  $\geq 100$  pions by a  $> 1$  ATeV cosmic-ray carbon nucleus; in b) the narrow meson cone has spread out and the even narrower cone of  $Z = 1$  projectile fragments can be clearly distinguished from the meson jet [from Po 59].
- Fig. 80. An example of extra-nuclear cascade induced in an emulsion stack by a 1.3 ATeV (cosmic-ray) P nucleus.
- Fig. 81. Pseudo-rapidity distributions of secondaries from the 6 RHI collisions among the family portrayed in Fig. 80.

- Fig. 82. Multiplicity distributions from cosmic-ray jets induced by RHI, compared to those from (accelerator) pA collisions. The variable is the reduced multiplicity, i.e. the multiplicity of relativistic secondaries normalized to the same energy and target thickness (Eq. 4.14); circles: accelerator p-emulsion data (69, 200, and 300 GeV); dashed histogram: cosmic-ray He primaries; solid histogram: cosmic ray  $Z > 3$  primaries, scaled via Eq. 4.15.
- Fig. 83. Schematic view of the Split Field Magnet detector array at the CERN ISR.
- Fig. 84. Comparison of multiplicity distributions of negative pions from  $\alpha$ - $\alpha$  collisions at 15 + 15 AGeV and pp collisions at 15 + 15 GeV in the CERN ISR.
- Fig. 85. Rapidity dependence of the relative negative pion yield in: a)  $\alpha$ -p and pp, and b)  $\alpha$ - $\alpha$  and pp collisions at the same energy per nucleon.
- Fig. 86. Transverse momentum distribution of secondaries from (15 + 15) AGeV  $\alpha$ - $\alpha$  collisions in the "high- $p_T$ " range, compared to 16 times the corresponding yield from pp collisions.
- Fig. 87. The primary cosmic ray spectrum.
- Fig. 88. Distribution of time delays between VHE hadrons detected in the Maryland calorimeter, with respect to the shower front of associated EAS [Go 78].
- Fig. 89. Estimation of the exponent of the primary Fe energy spectrum from the data of Fig. 88.
- Fig. 90. Evolution of the electron component of EAS compared to predictions for proton primaries (dashed curves) and Fe primaries (solid curves).



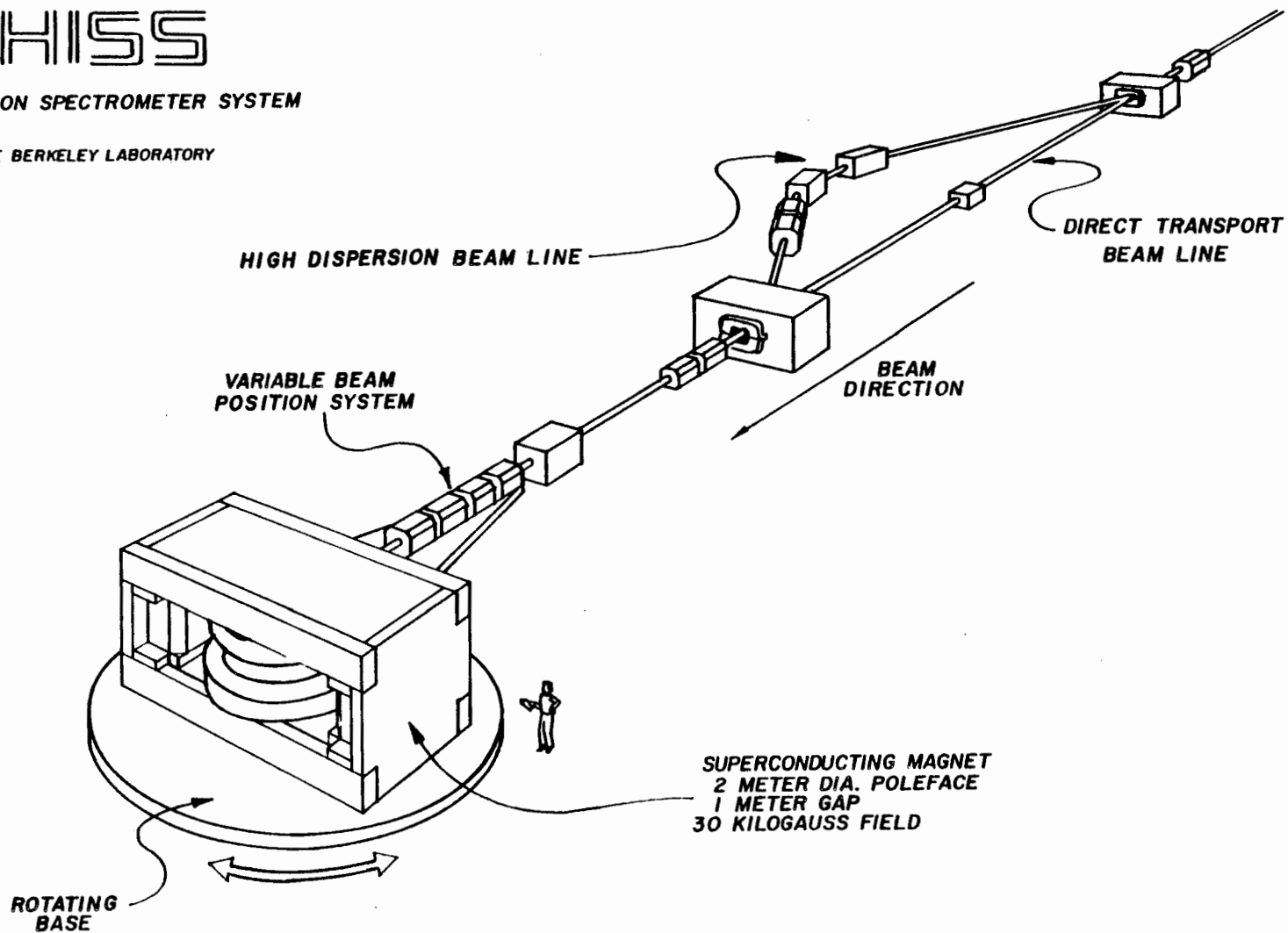
XBL 792-329

Fig. 1

# HISS

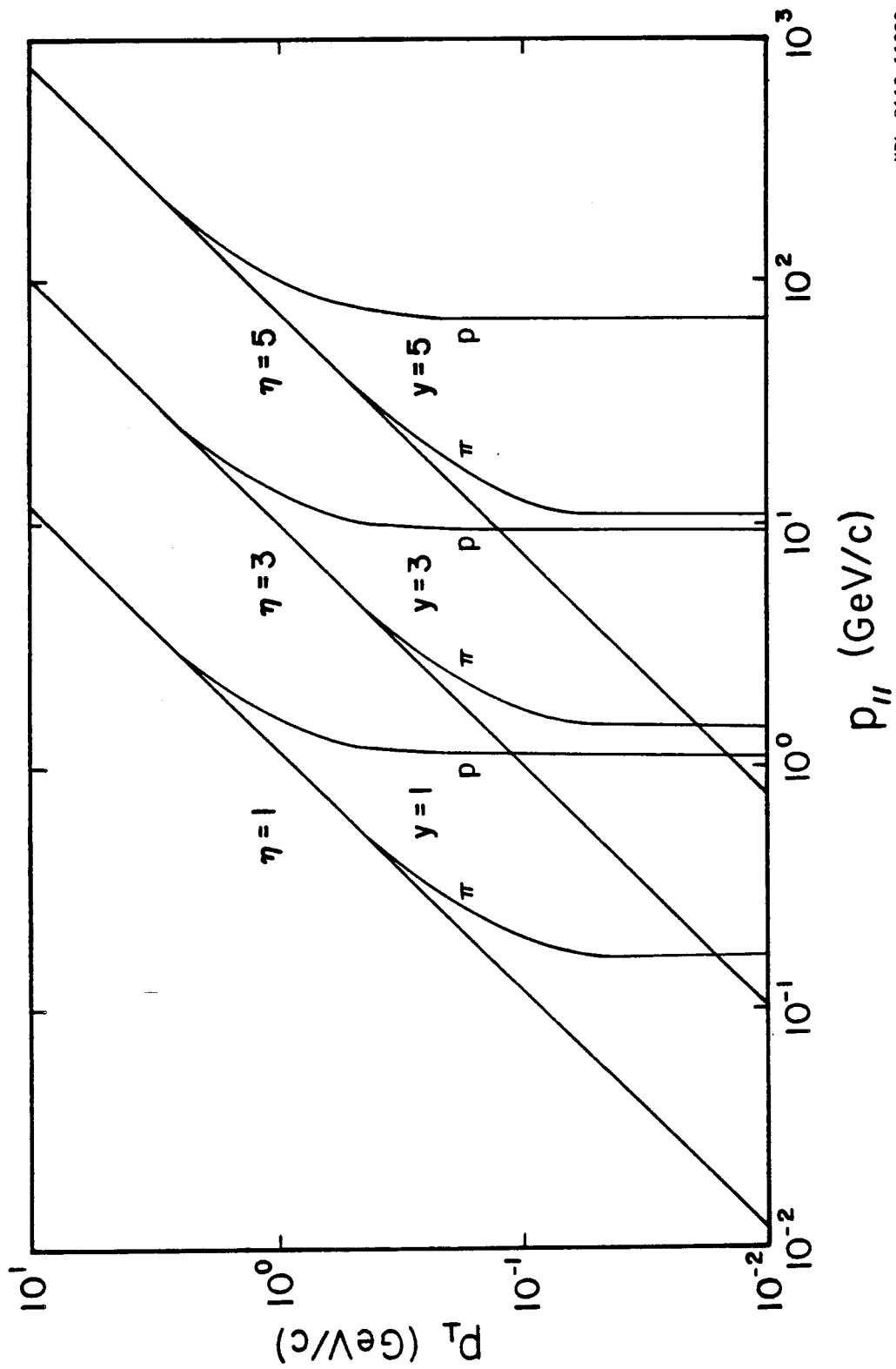
HEAVY ION SPECTROMETER SYSTEM

LAWRENCE BERKELEY LABORATORY



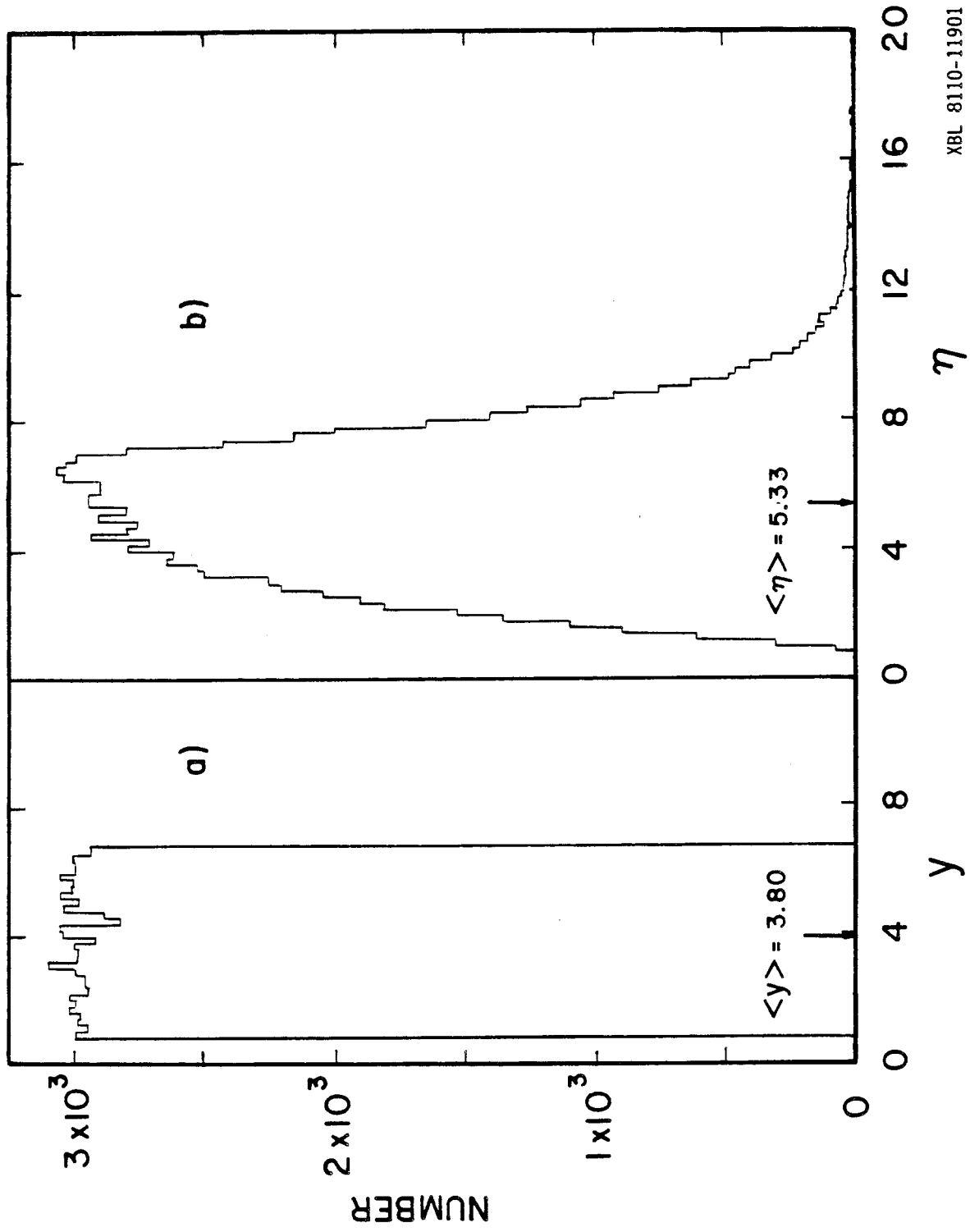
XBL 799-12037

Fig. 2



XBL 8110-11900

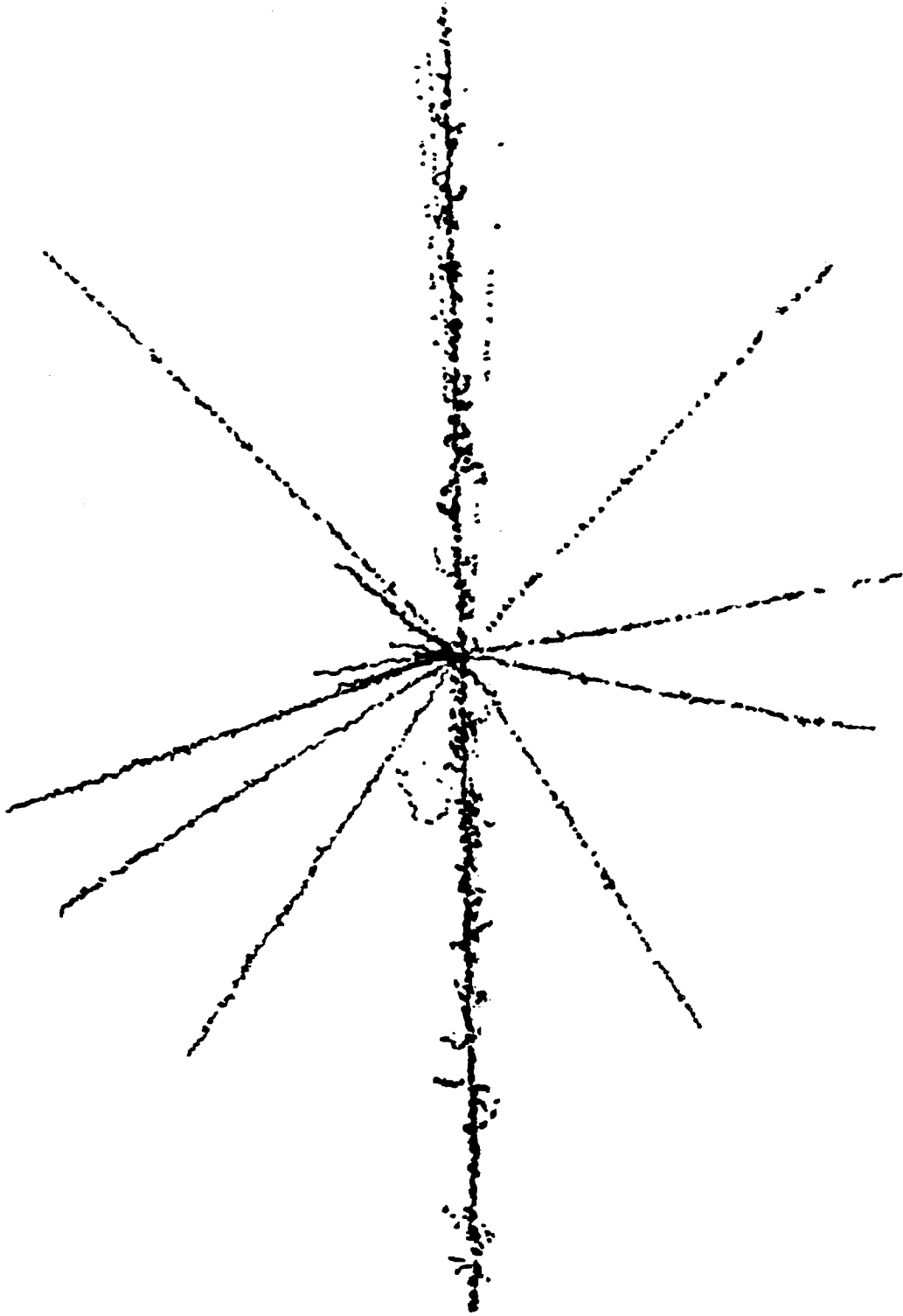
Fig. 3



XBL 8110-11901

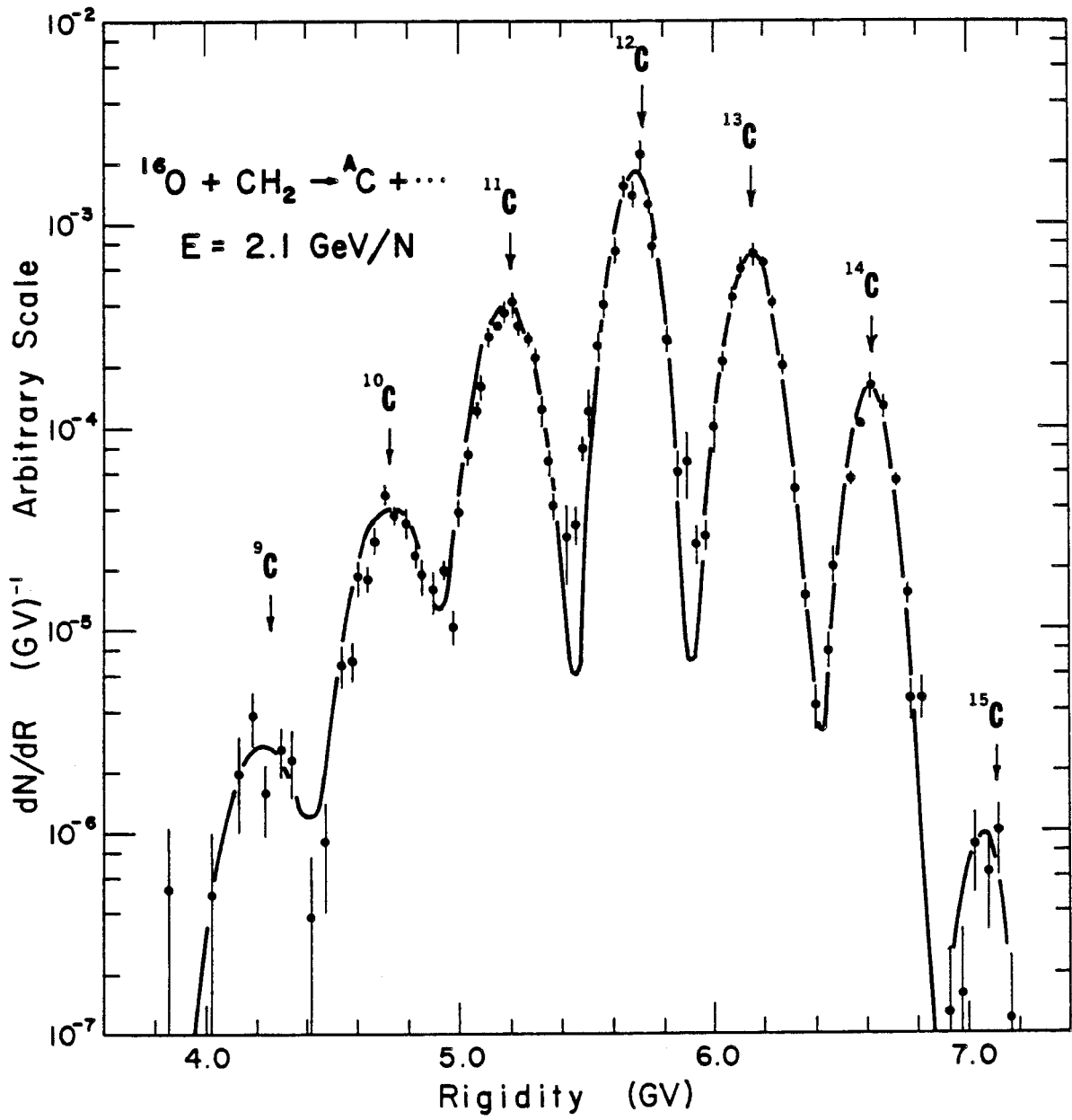
Fig. 4





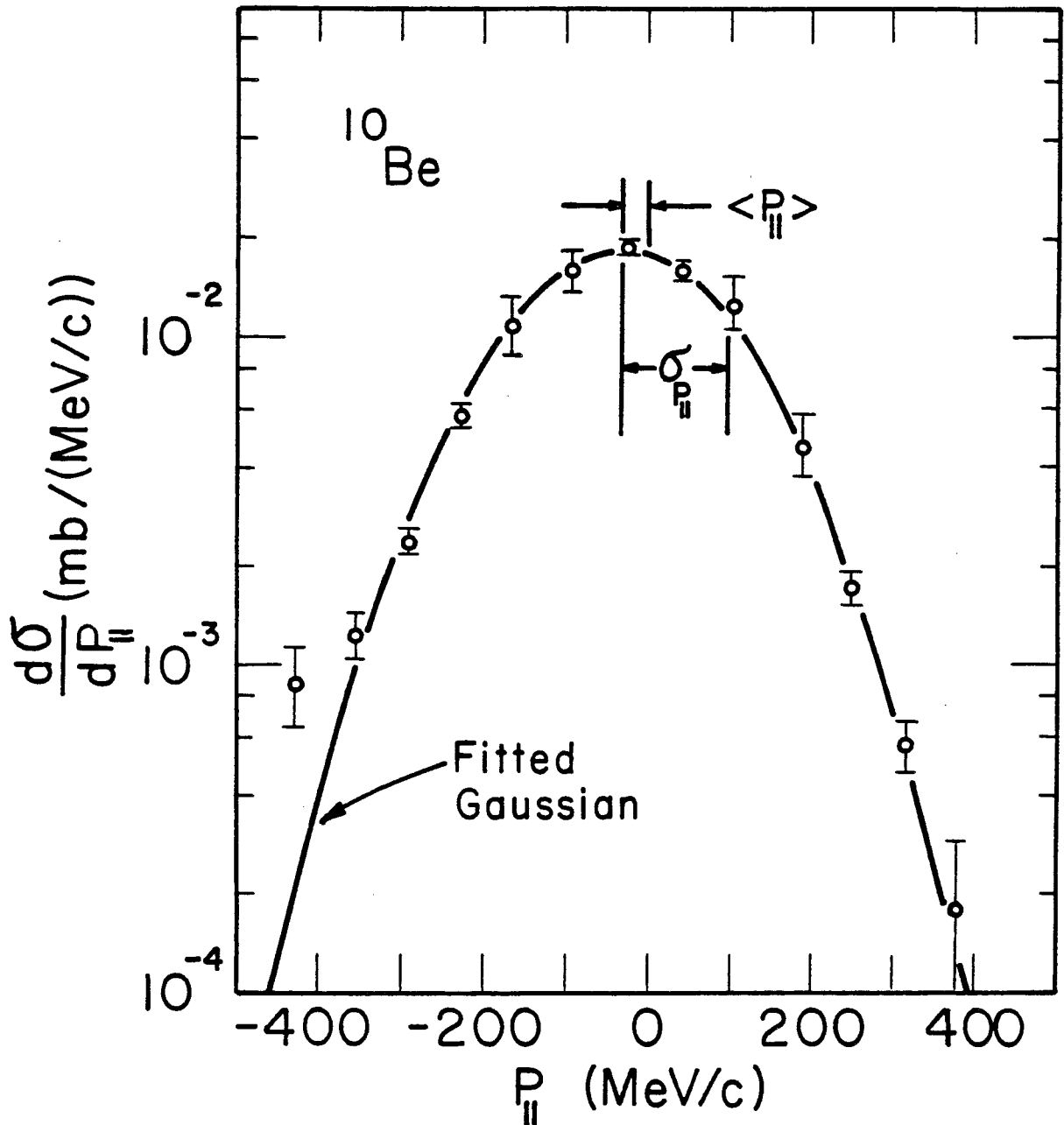
XBL 8111-12549

Fig. 5



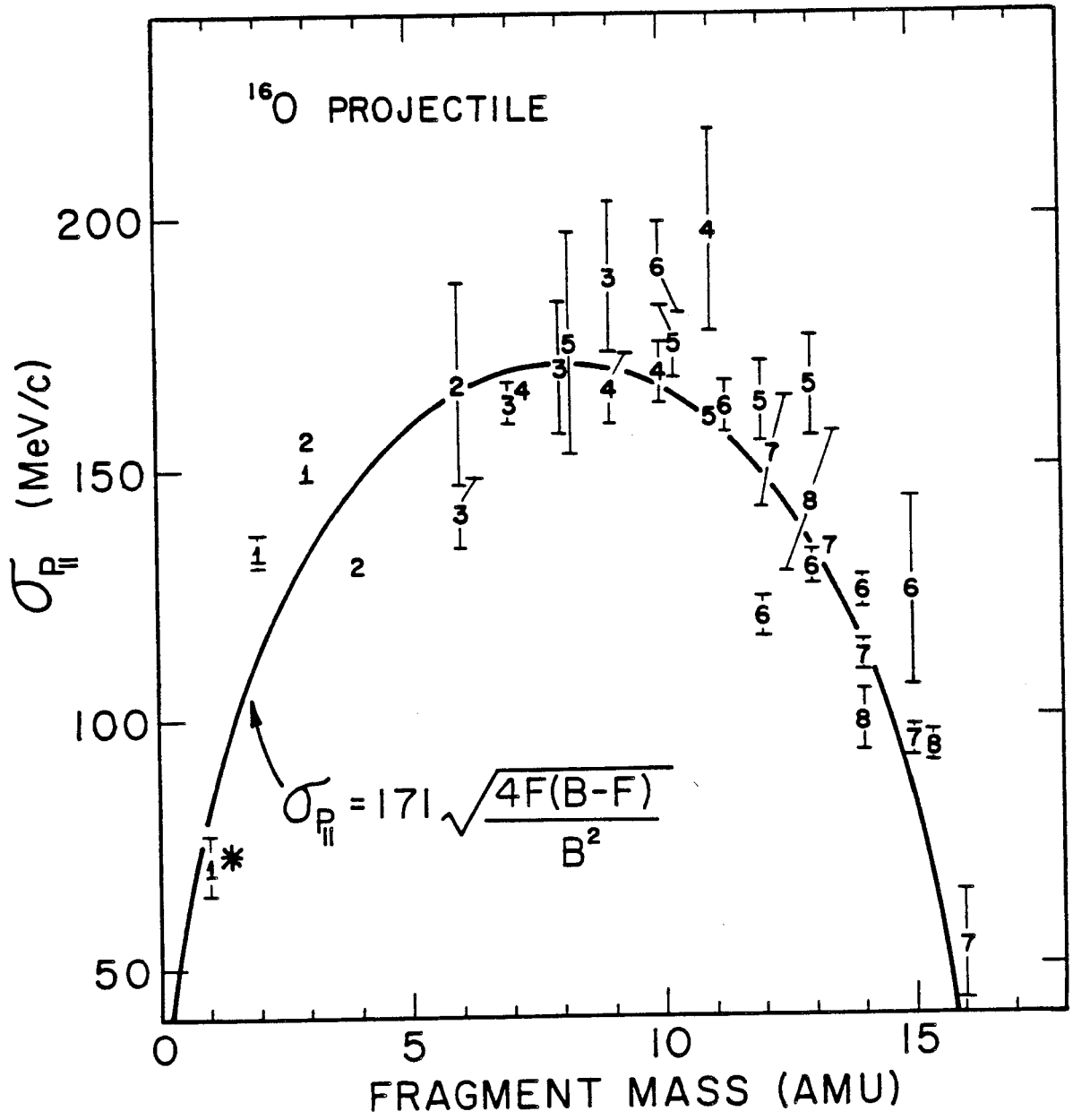
XBL 753-410A

Fig. 6



XBL 753-454

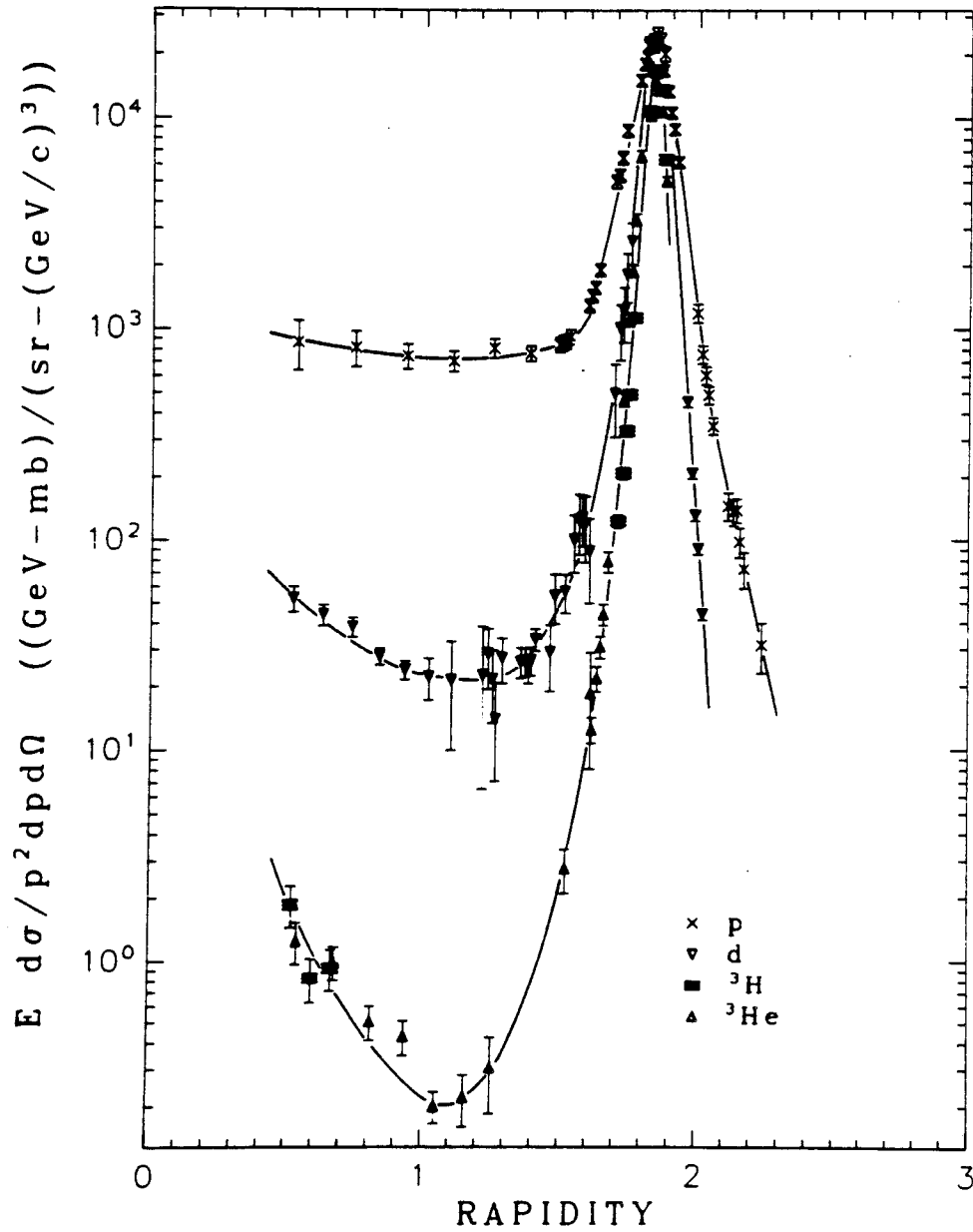
Fig. 7



XBL 753-453

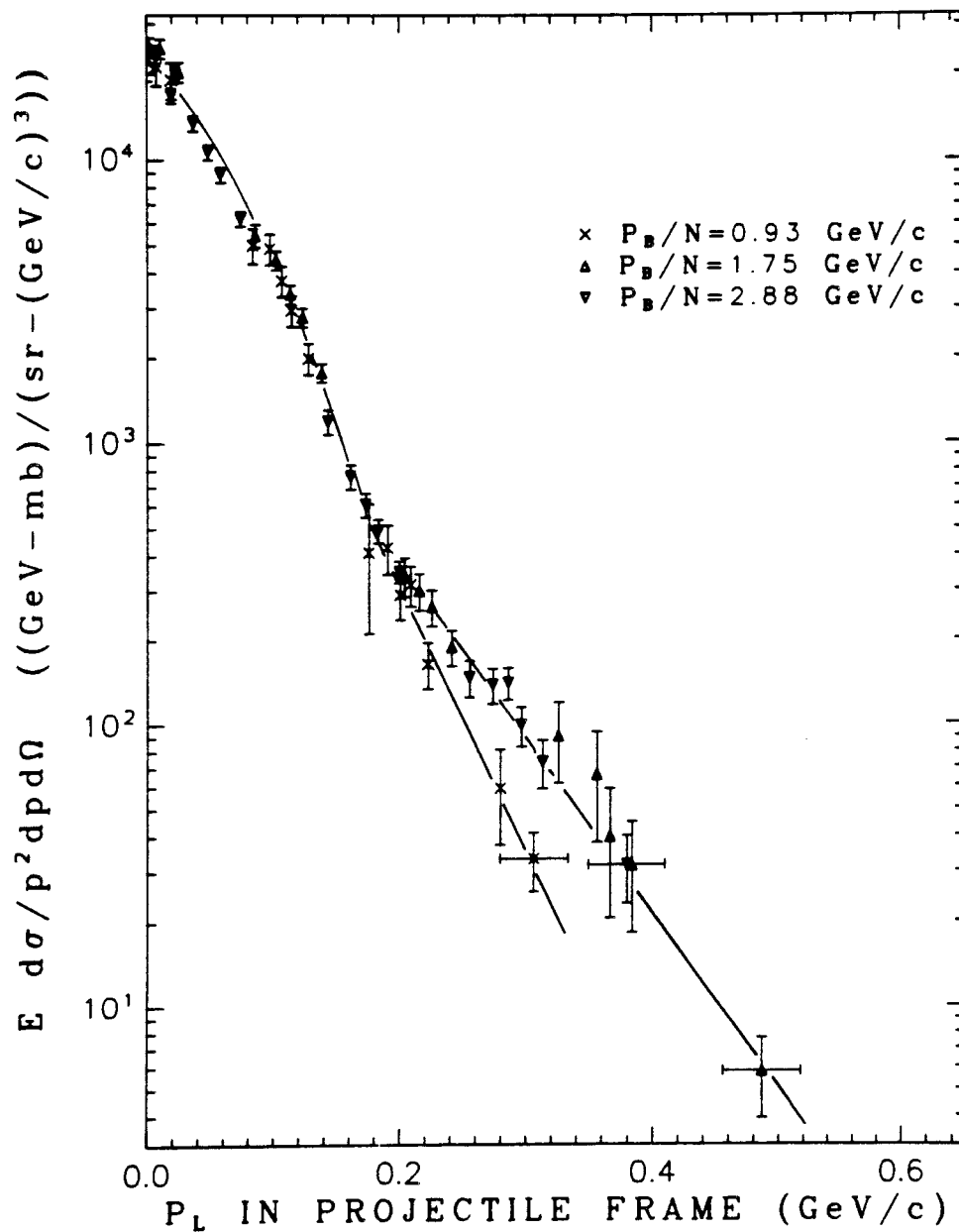
Fig. 8

2.88 GeV/c/N ALPHAS  
 $\alpha + C \rightarrow p, d, {}^3H, {}^3He + X$   
at  $\theta = 0$  deg



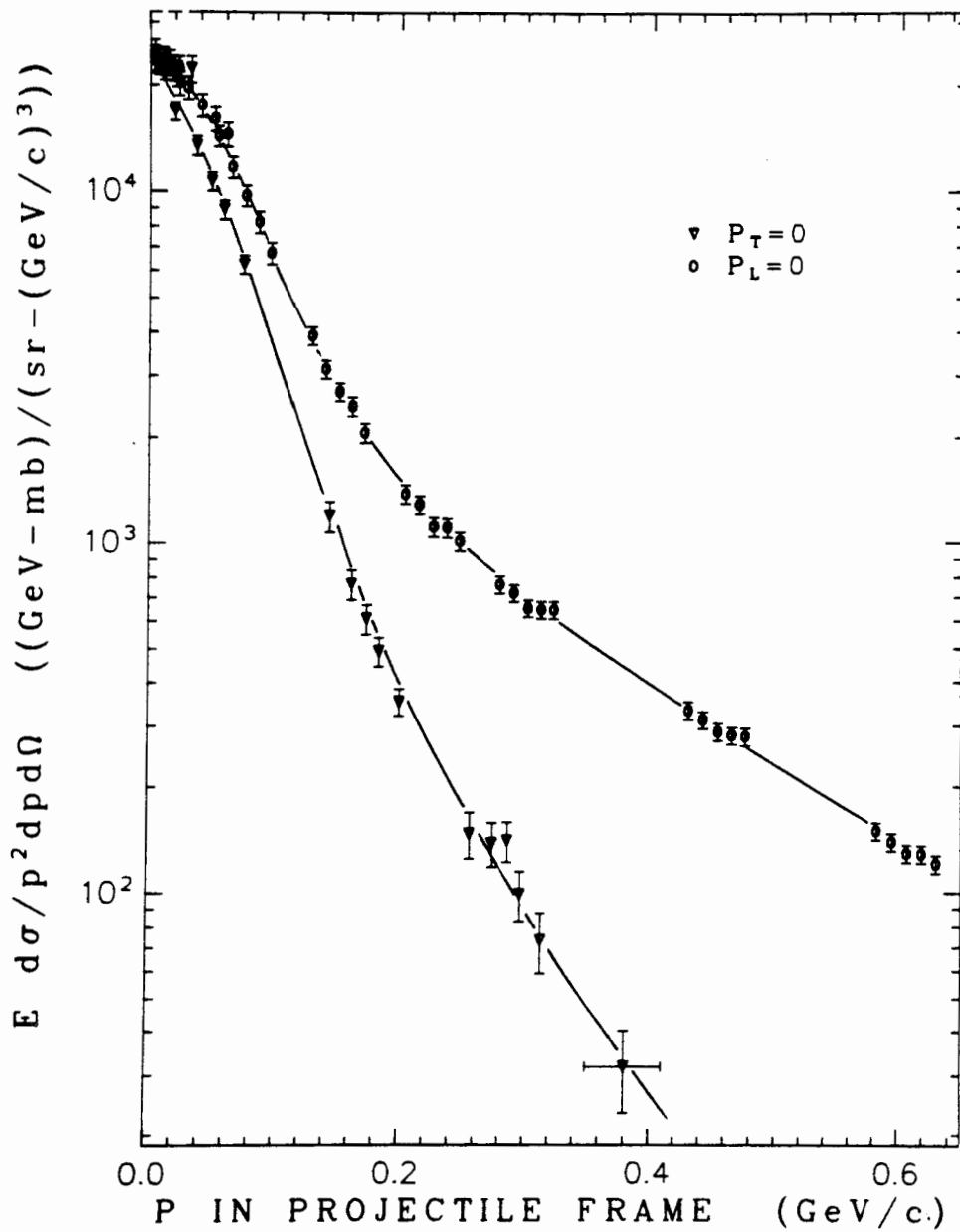
XBL 778-9786

Fig. 9



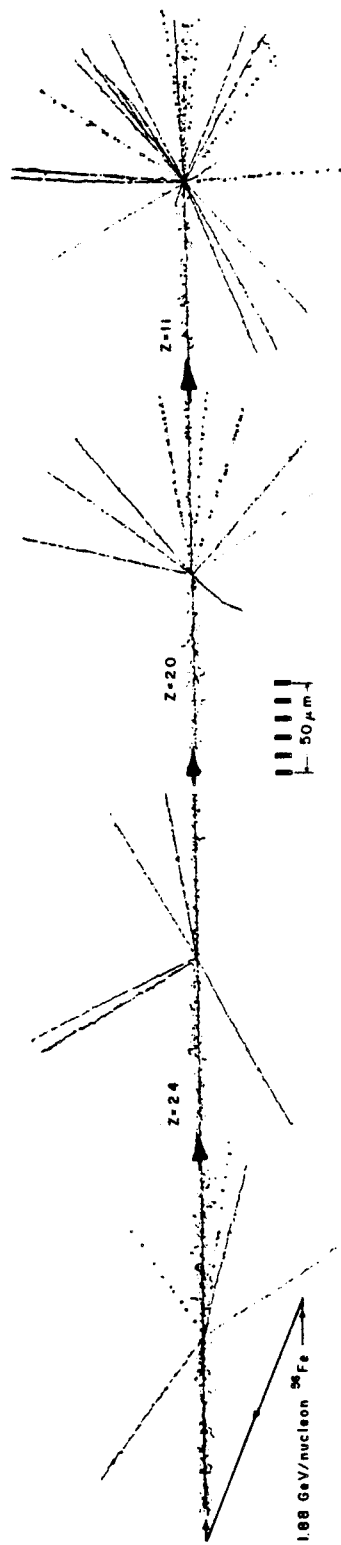
XBL 778-2603

Fig. 10



XBL 778-2601

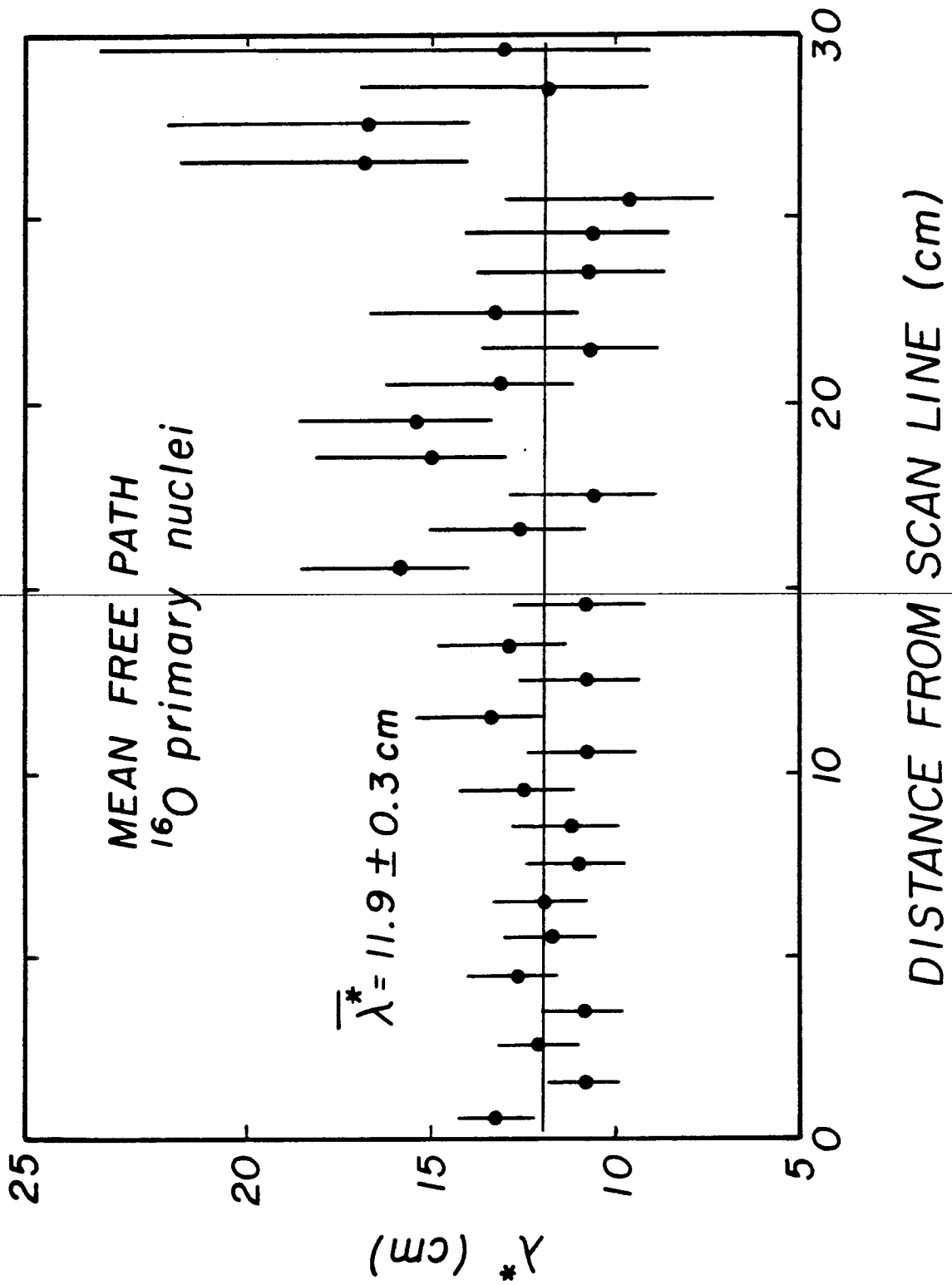
Fig. 11



XBL 794-9277

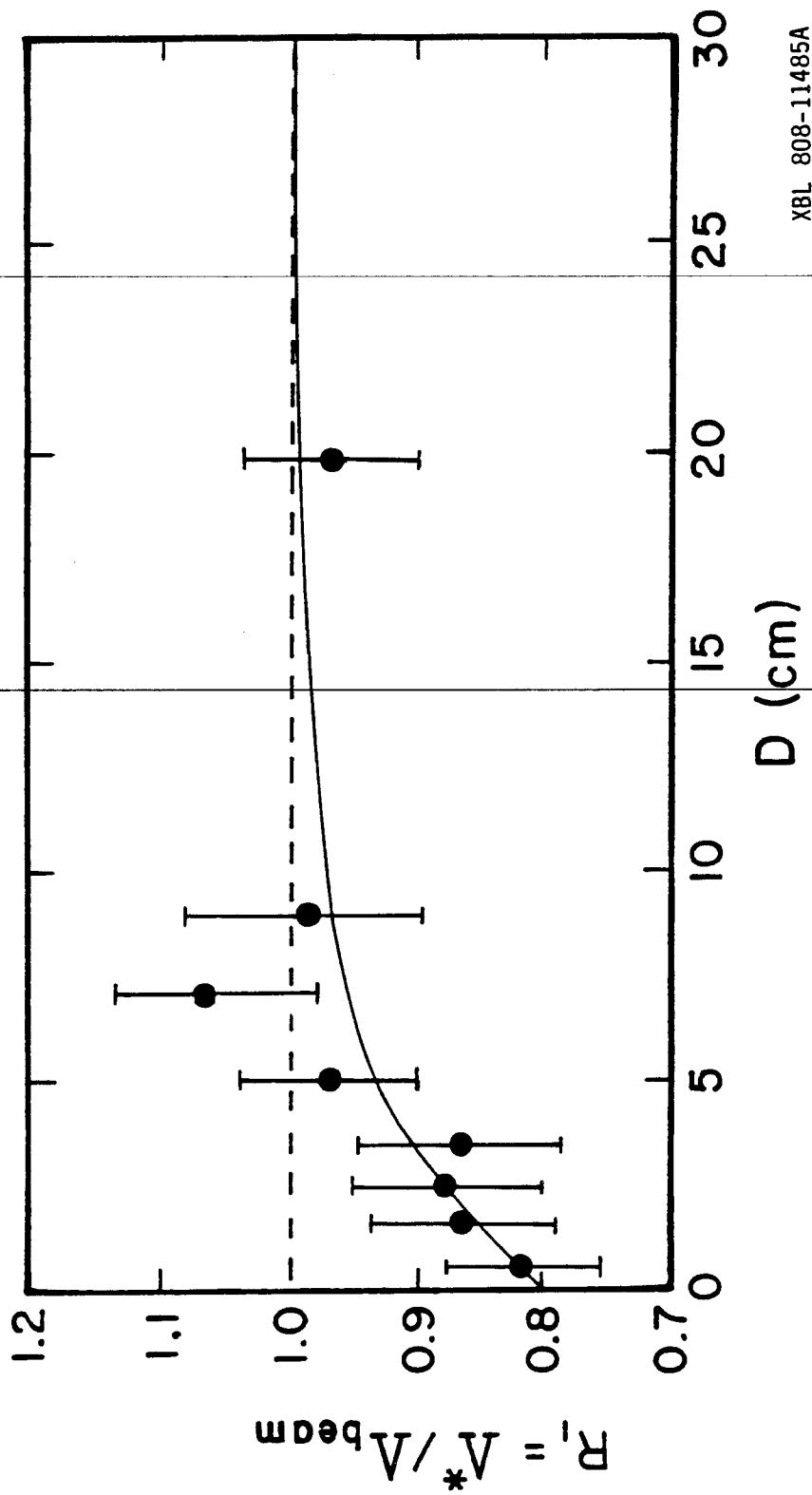
Fig. 12





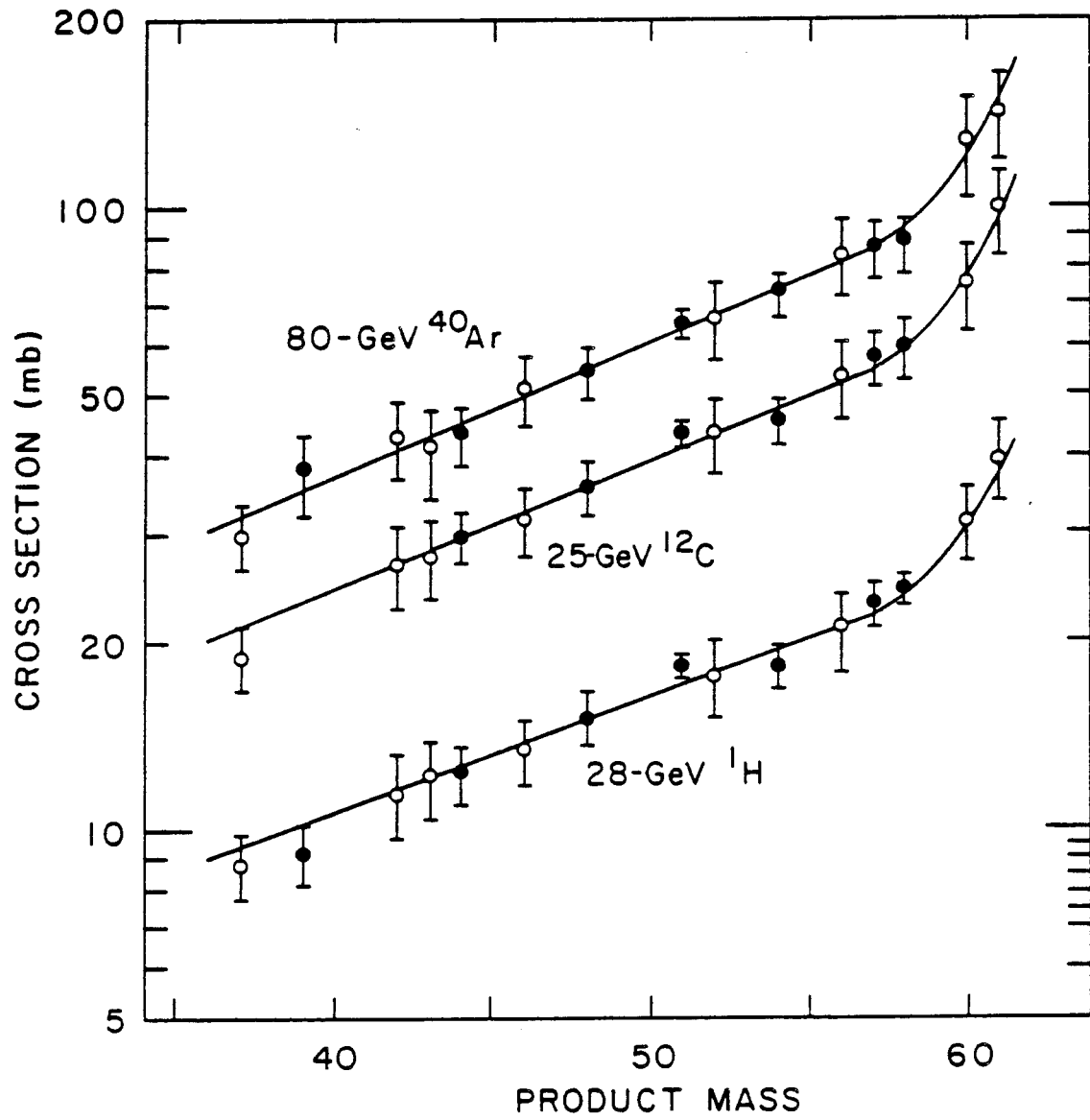
XBL 815-9835

Fig. 13



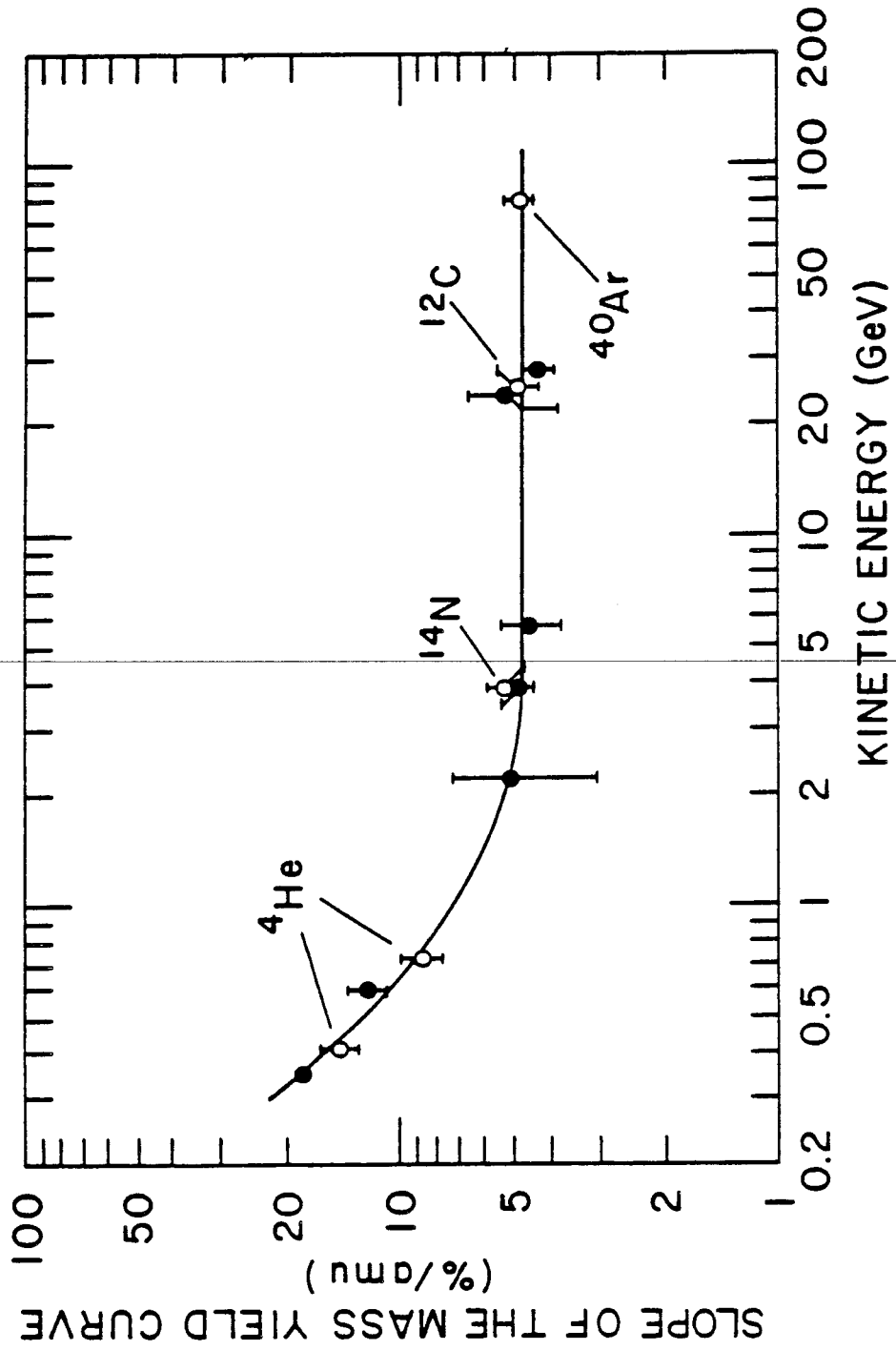
XBL 808-11485A

Fig. 14



XBL 815-9828

Fig. 15



XBL 815-9829

Fig. 16

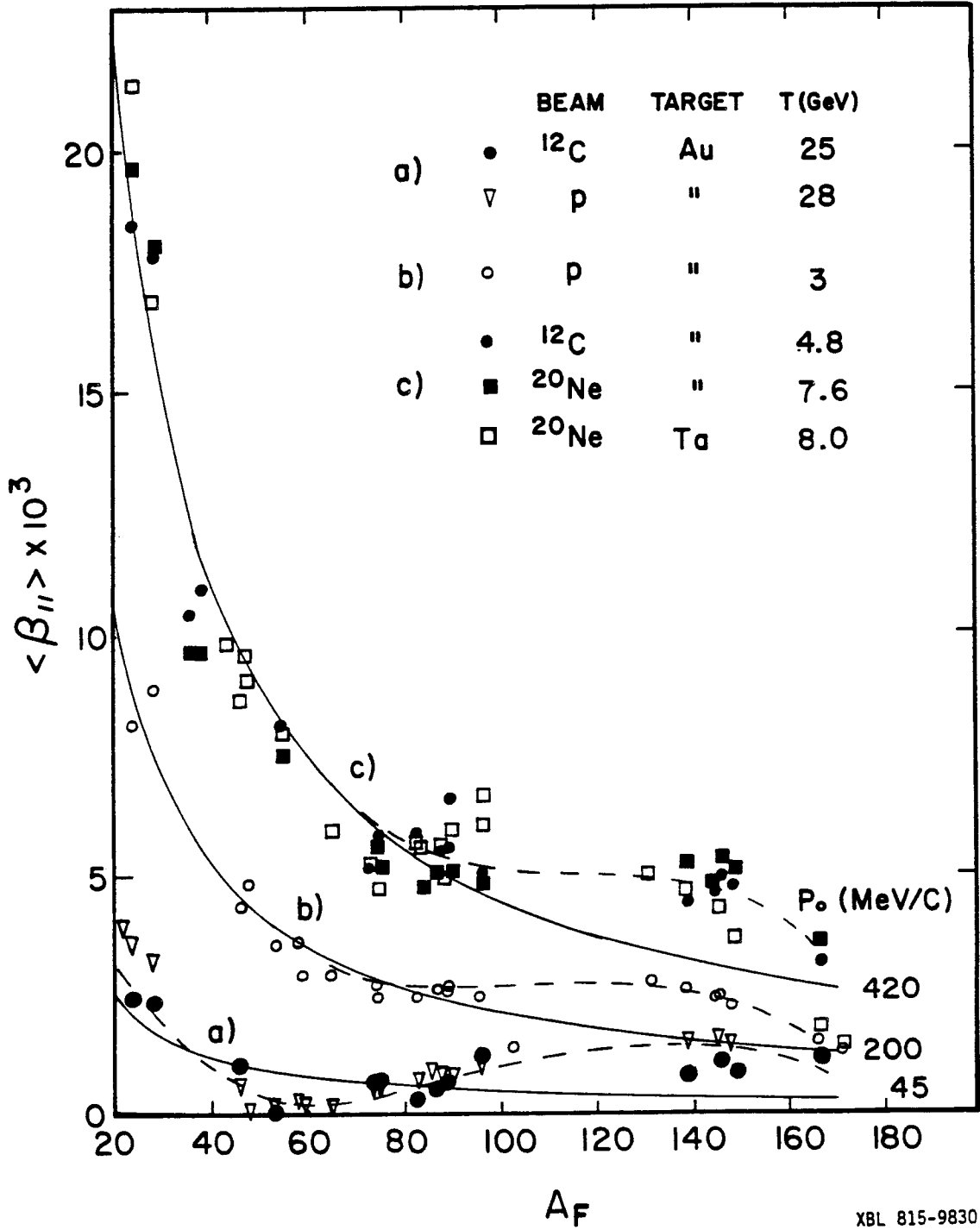
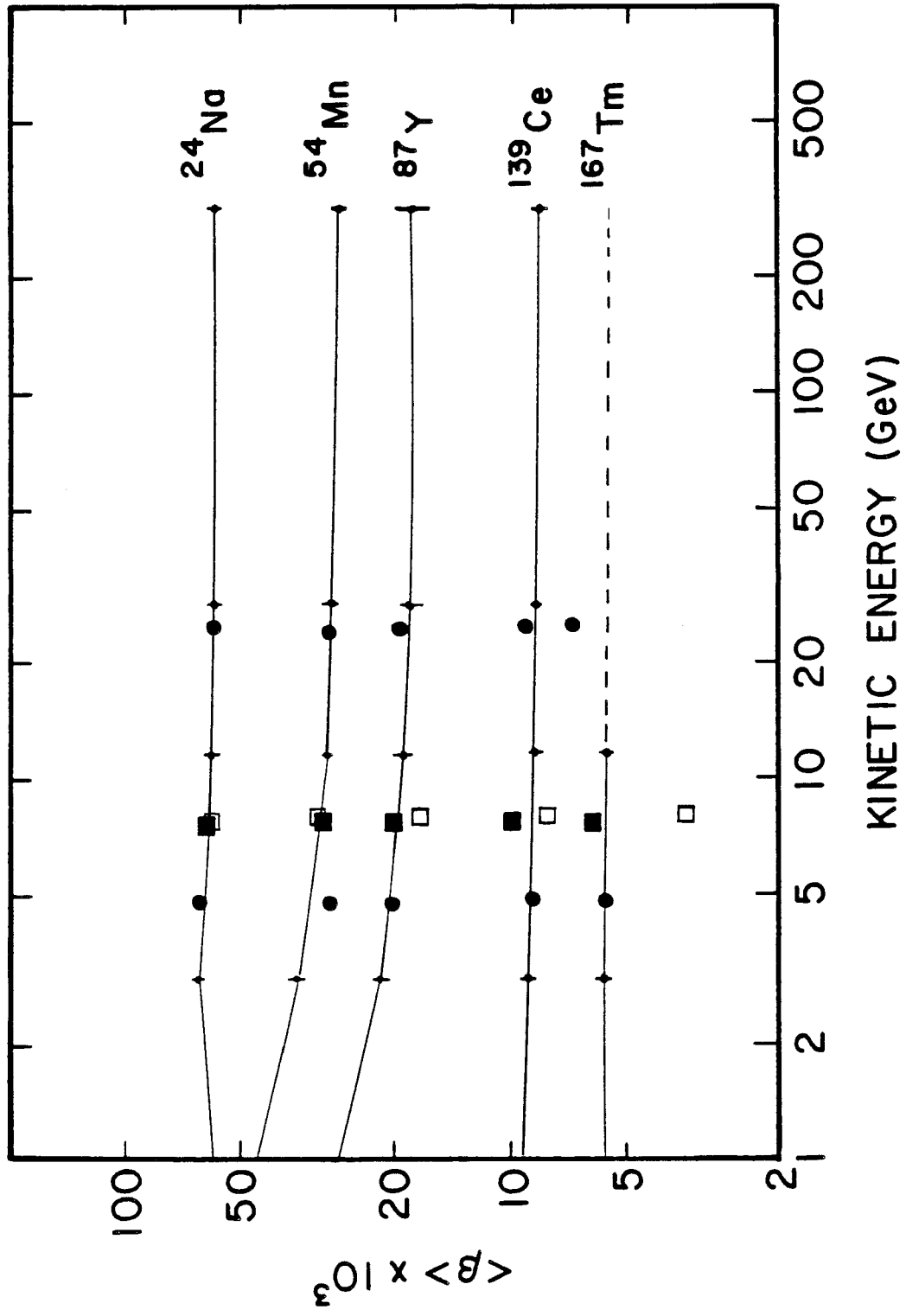


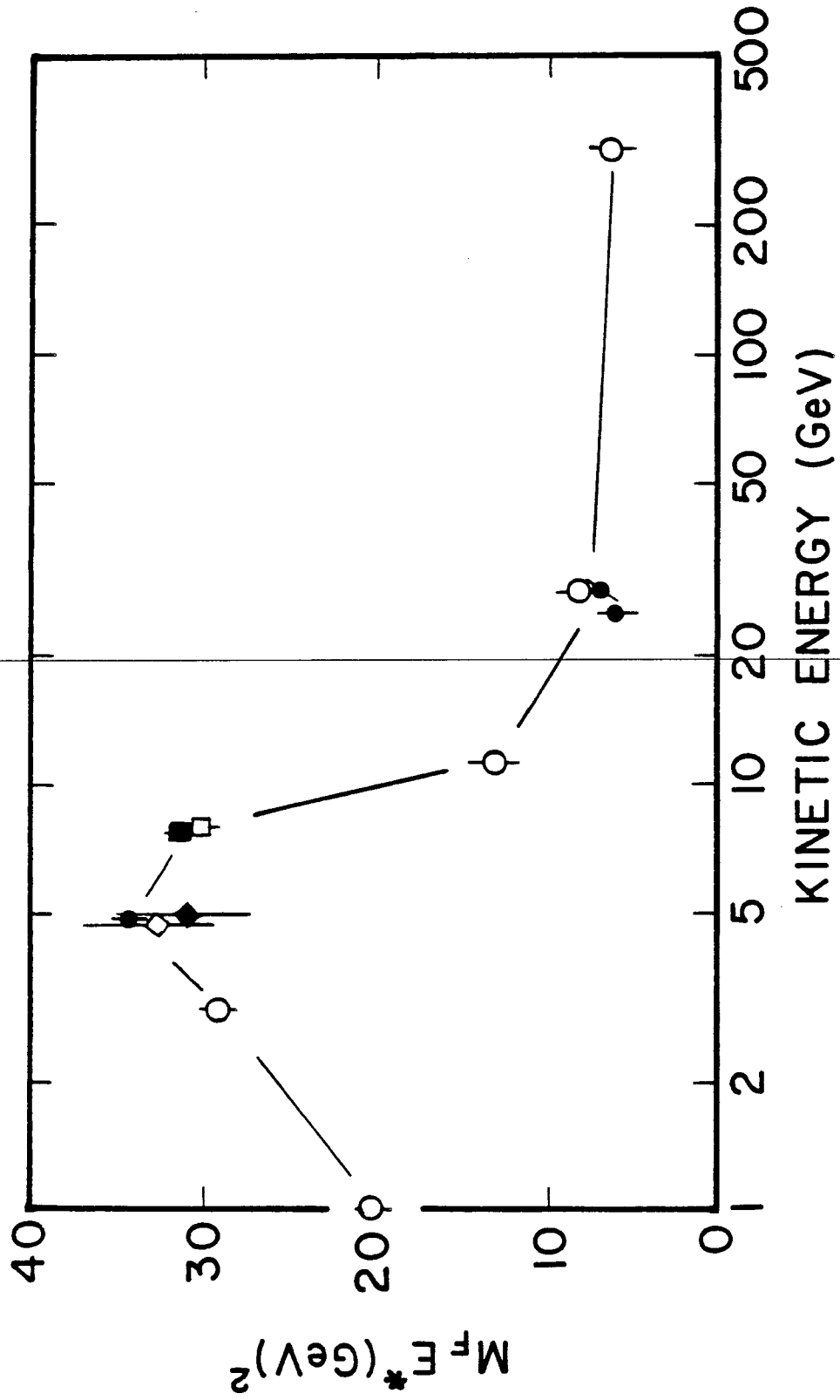
Fig. 17

XBL 815-9830



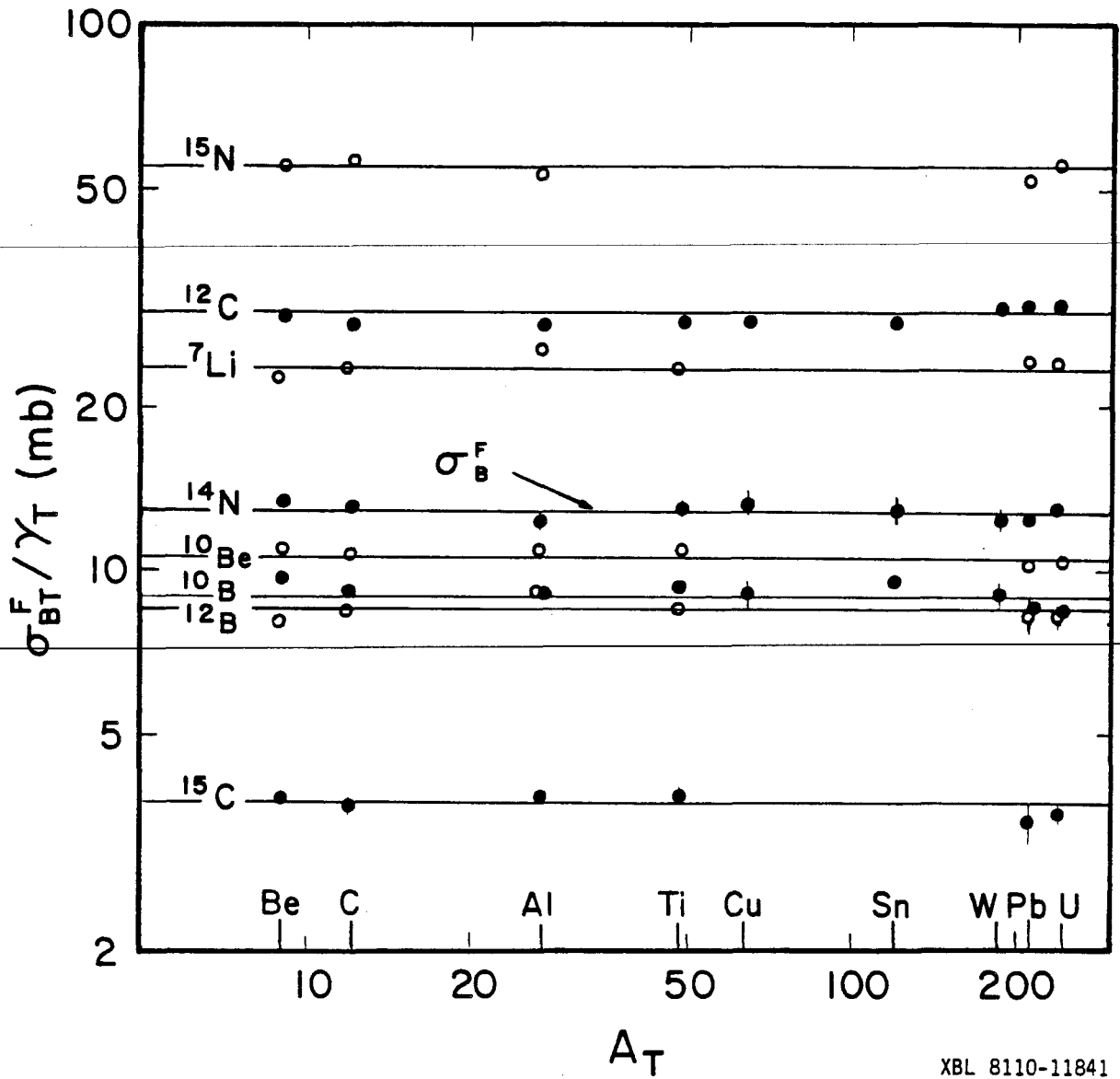
XBL 815-9831

Fig. 18



XBL 815-9832

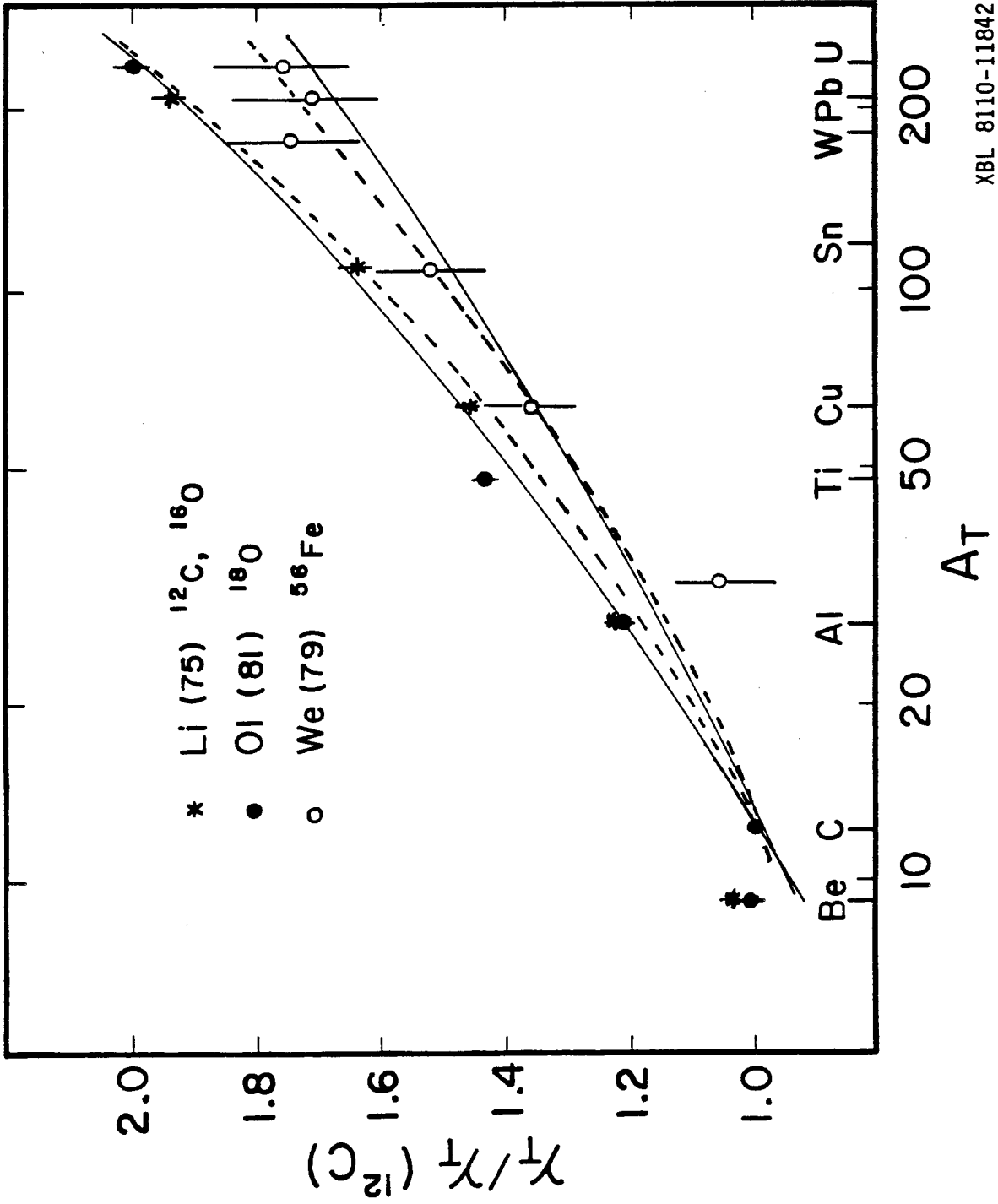
Fig. 19



XBL 8110-11841

Fig. 20





XBL 8110-11842

Fig. 21

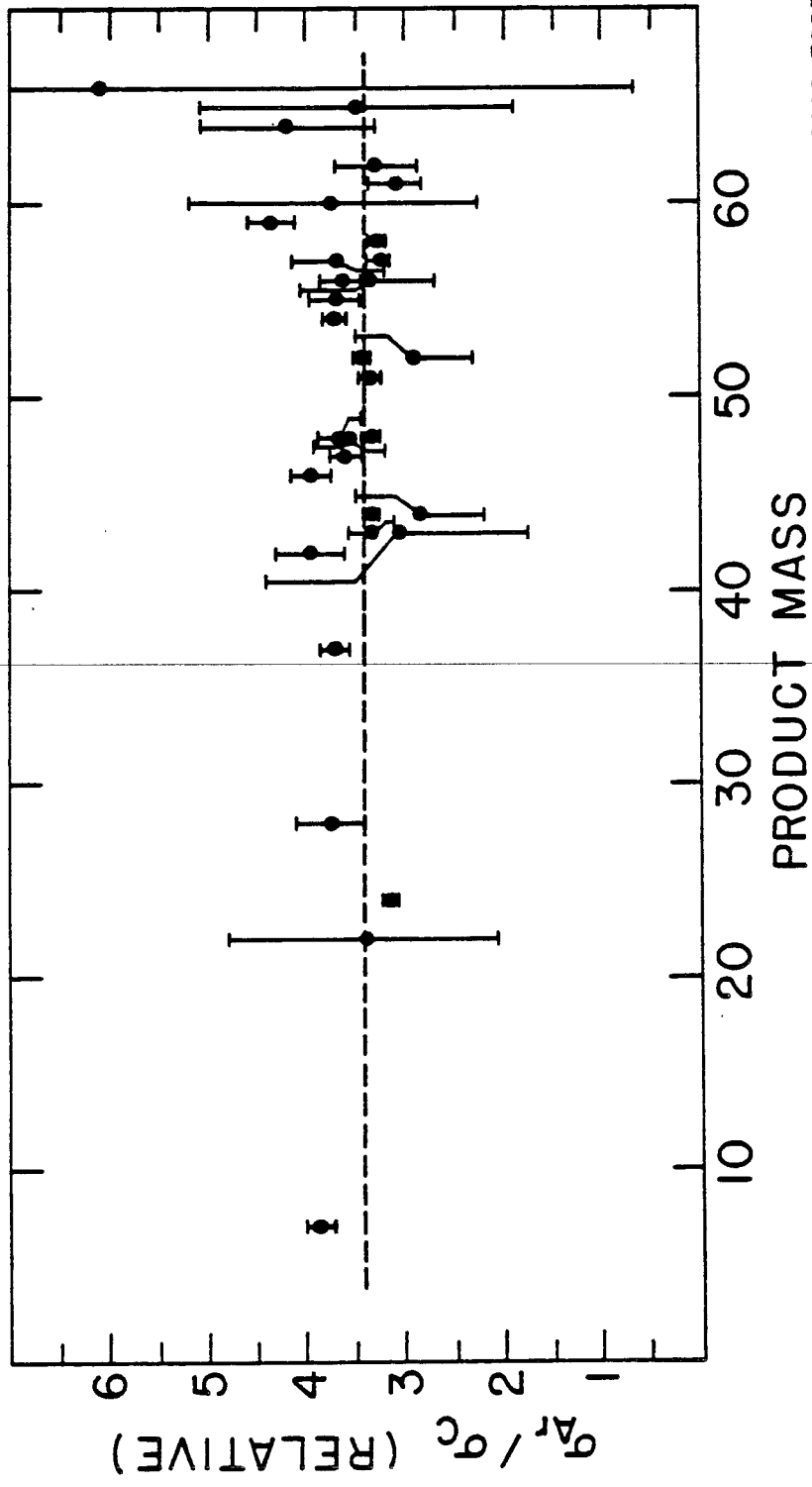


Fig. 22

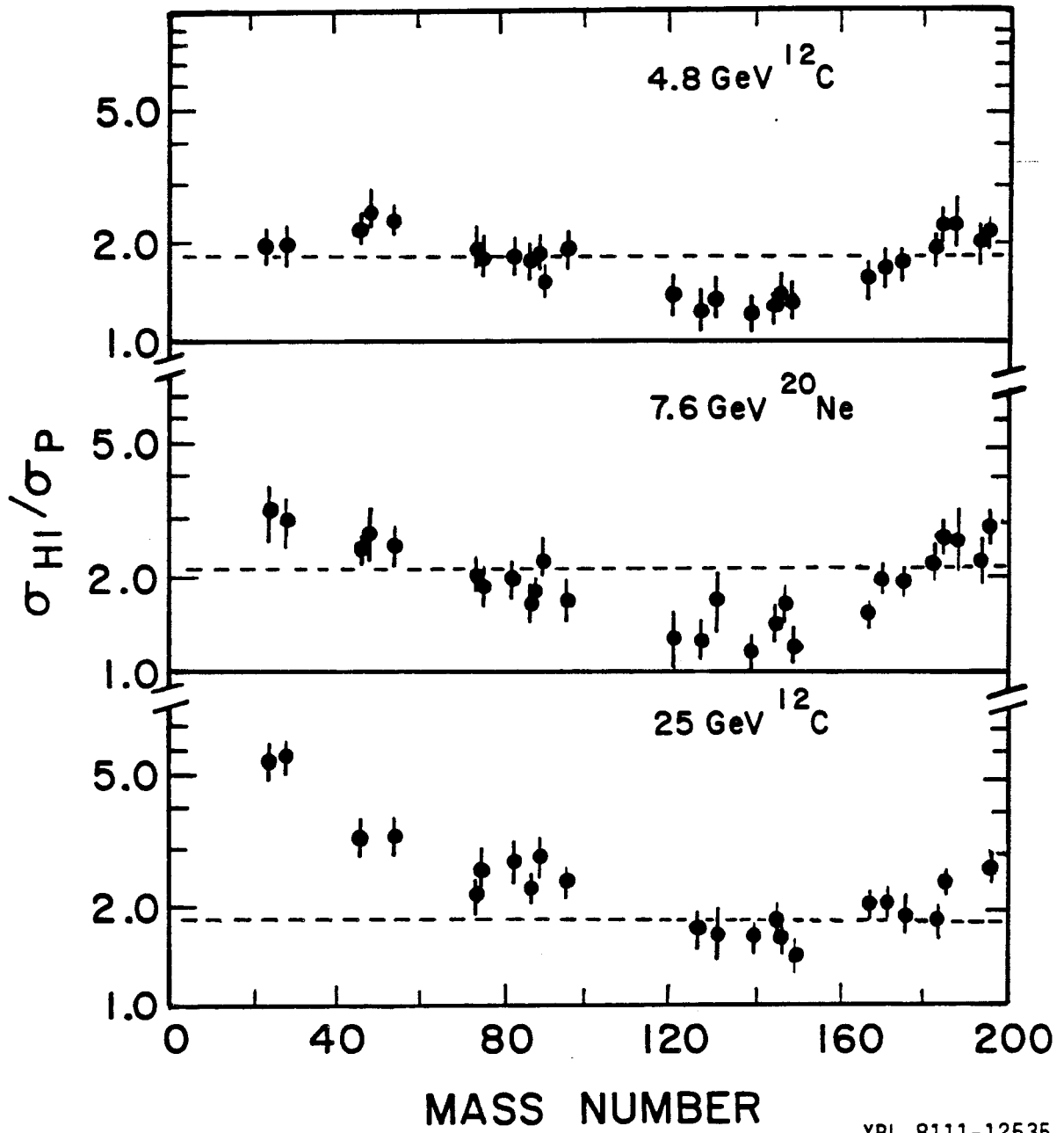


Fig. 23

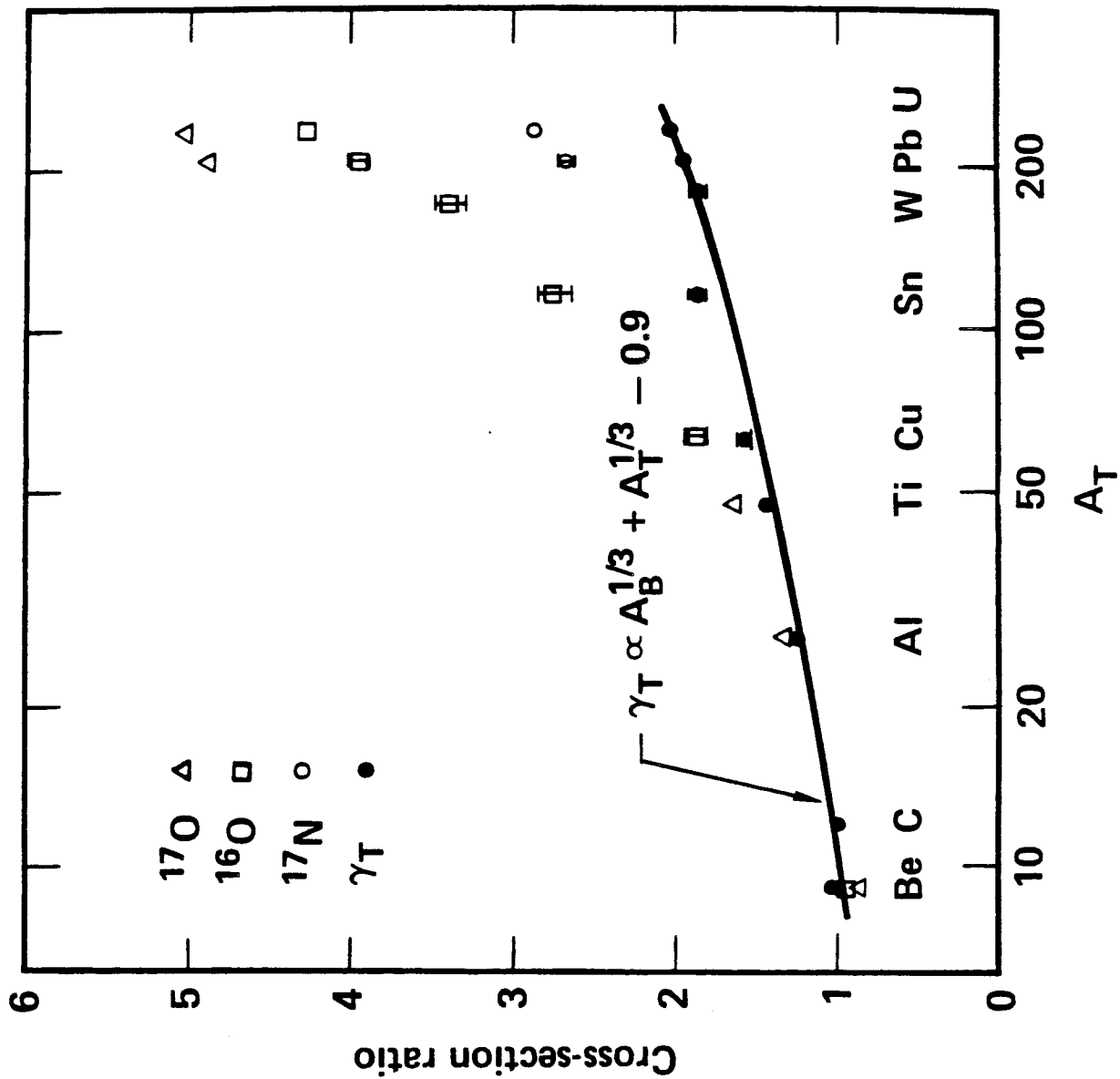
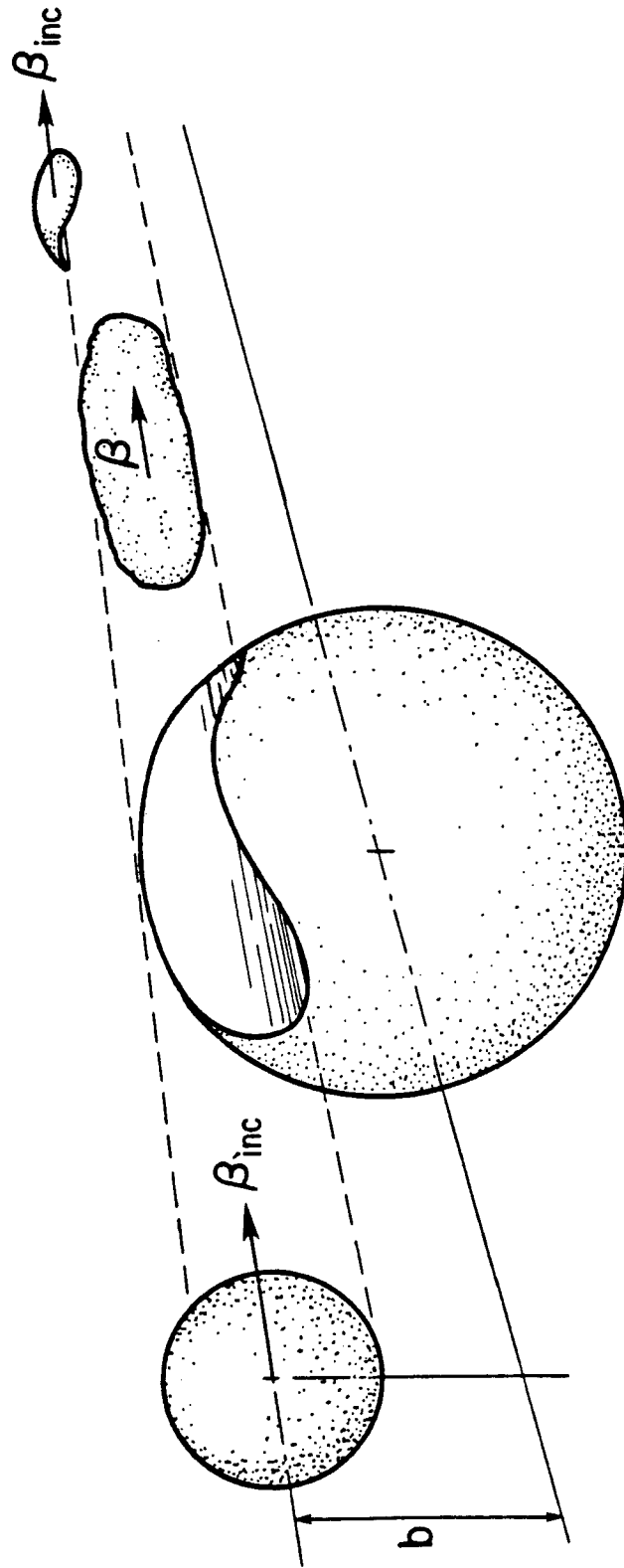
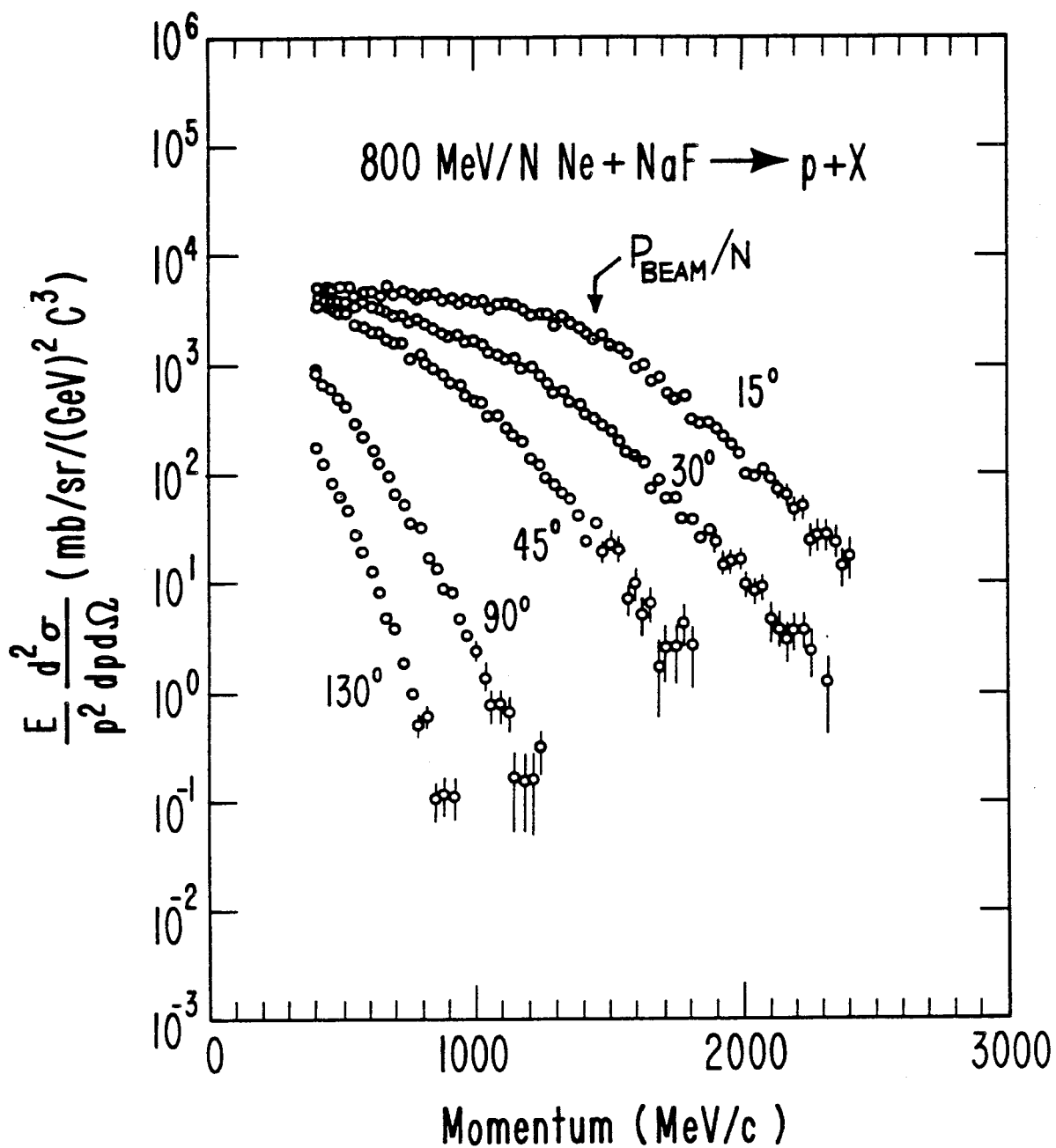


Fig. 24



XBL 768-3876

Fig. 25



XBL 779-1879

Fig. 26

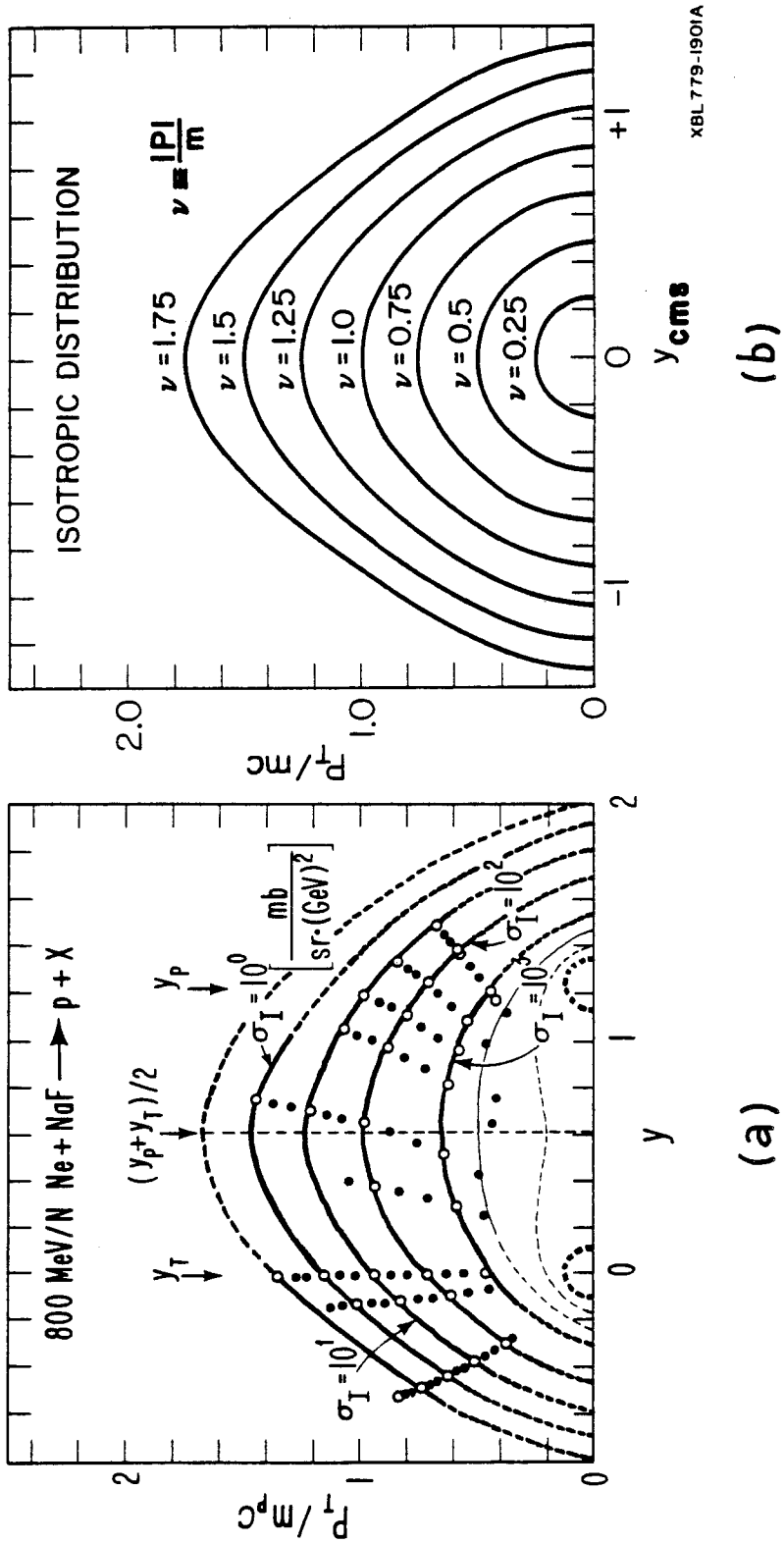
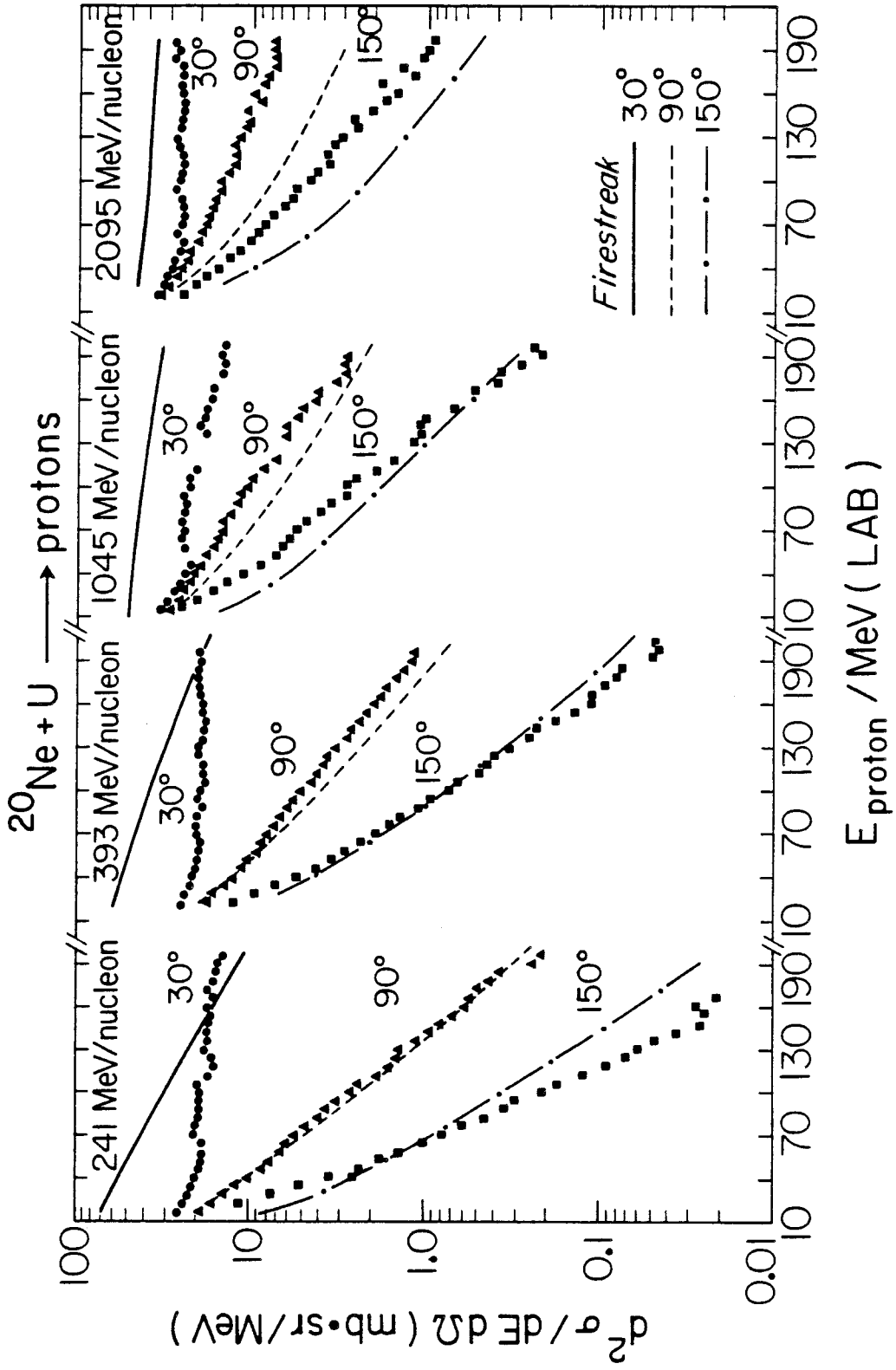


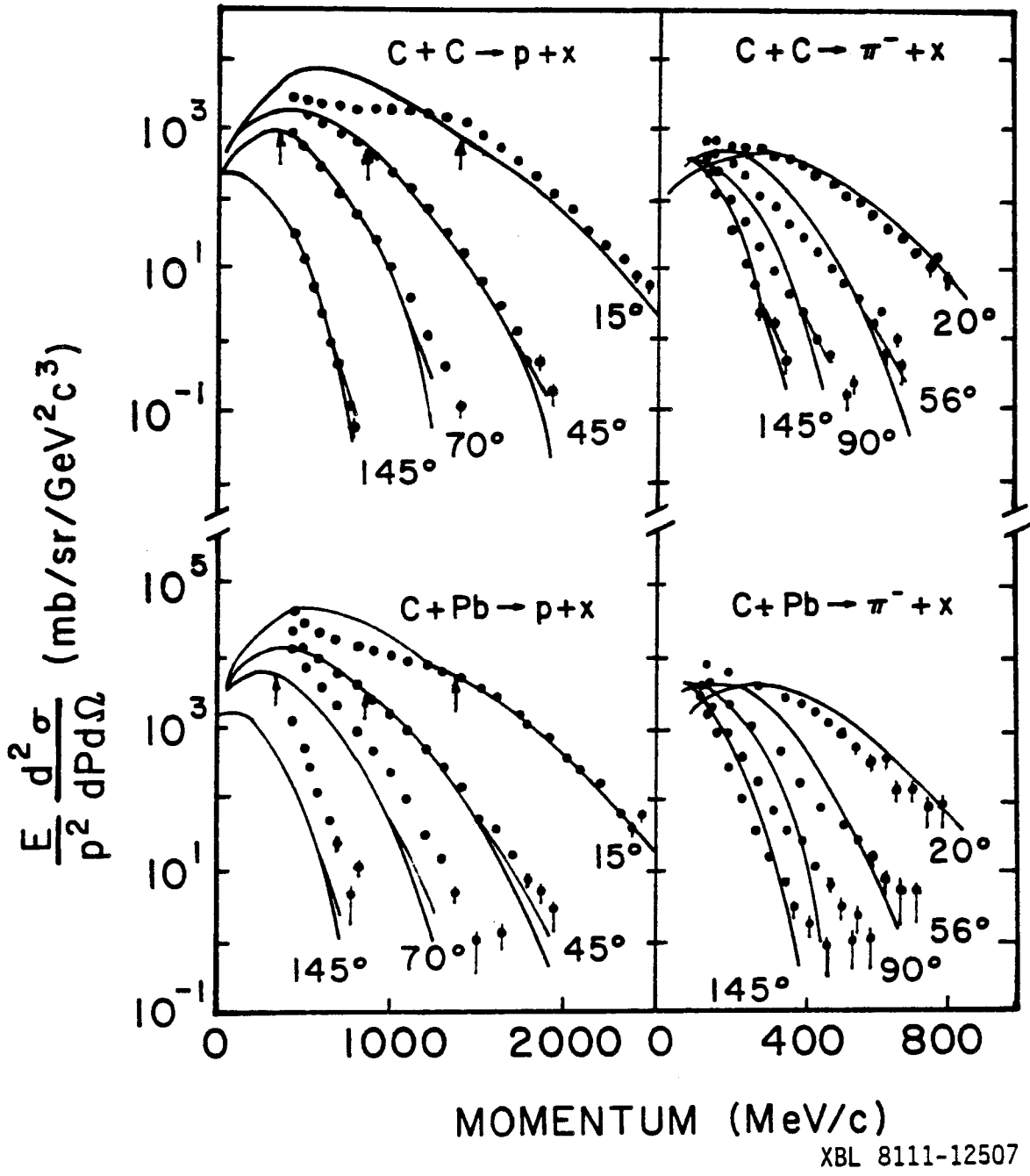
Fig. 27



XBL 7912-13547

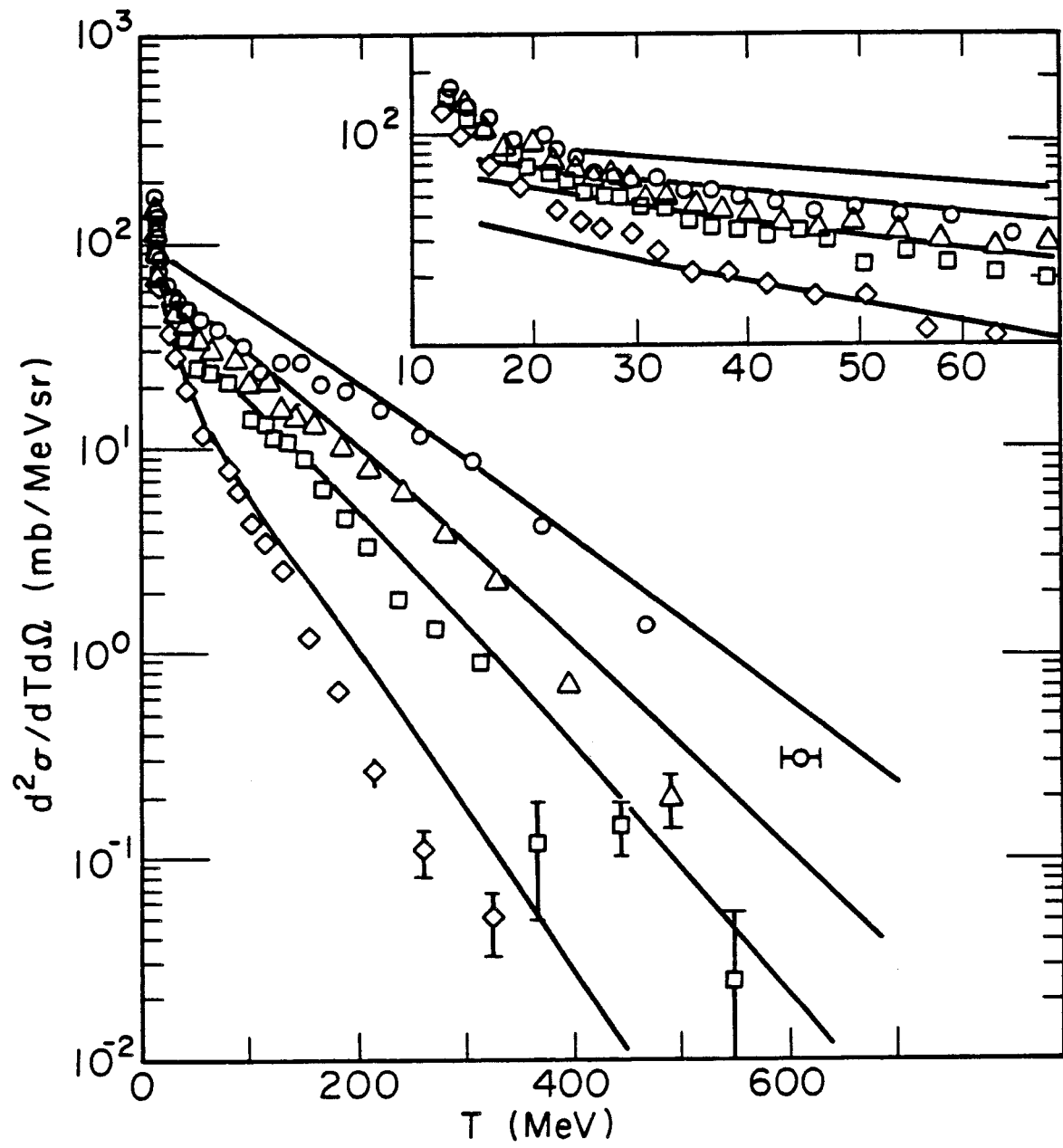
Fig. 28





XBL 8111-12507

Fig. 29



XBL7910-3833

Fig. 30

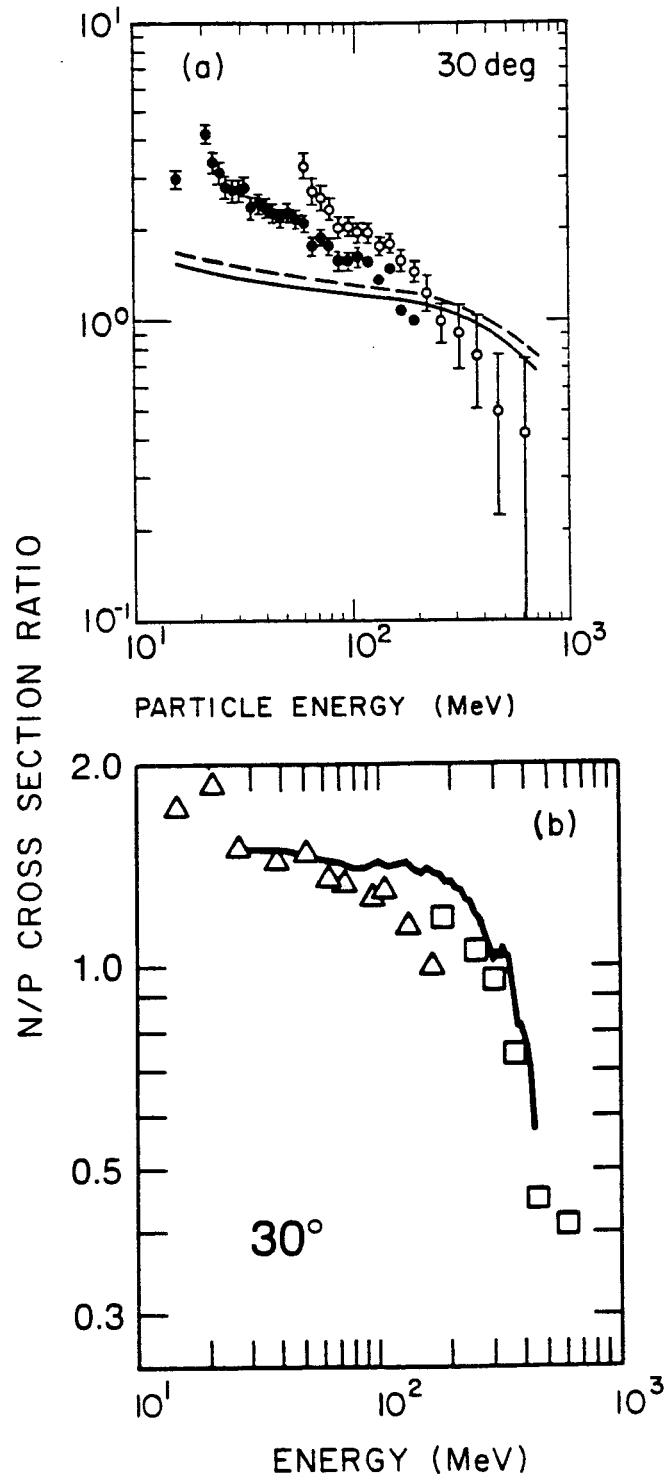


Fig. 31

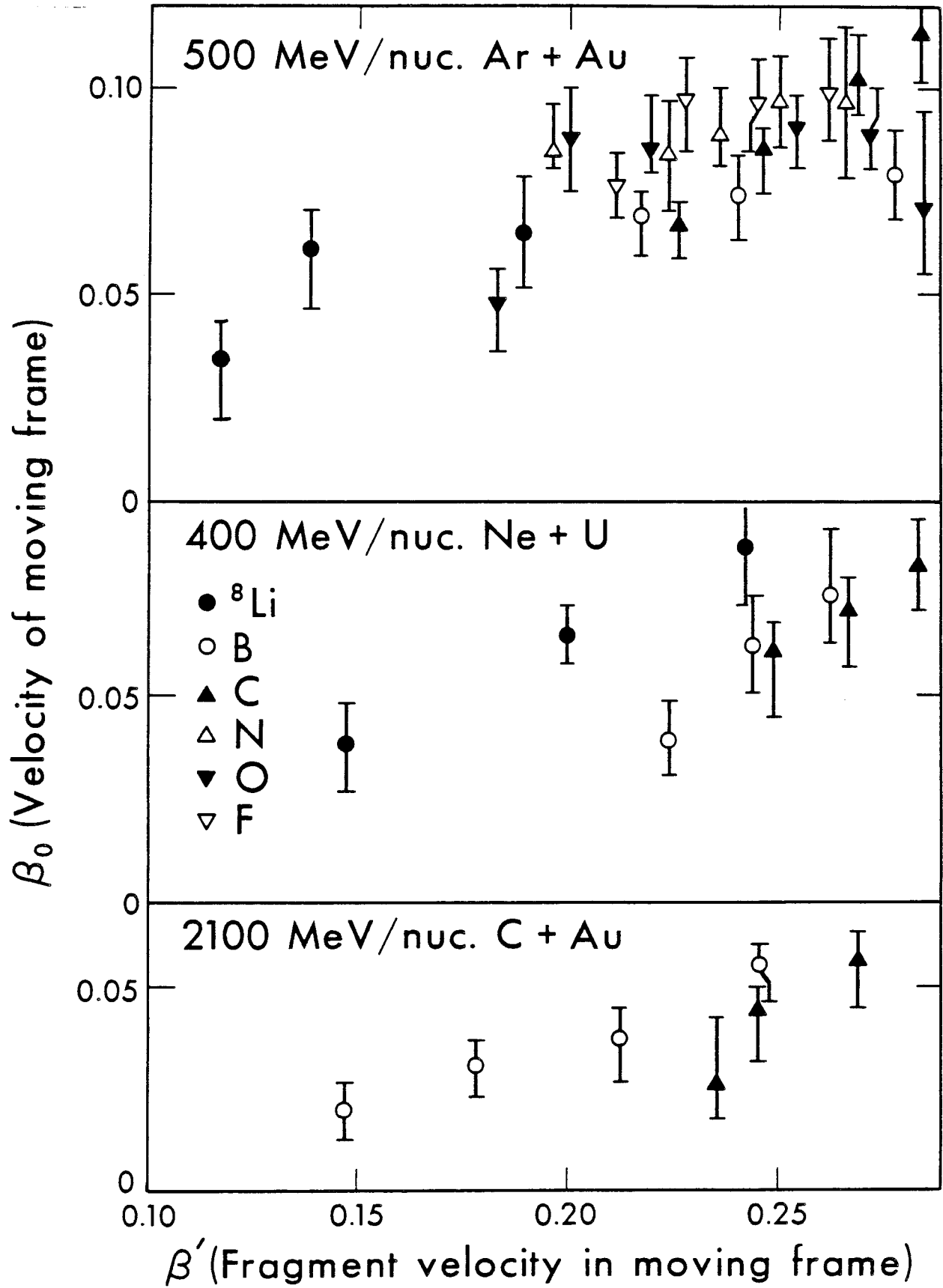
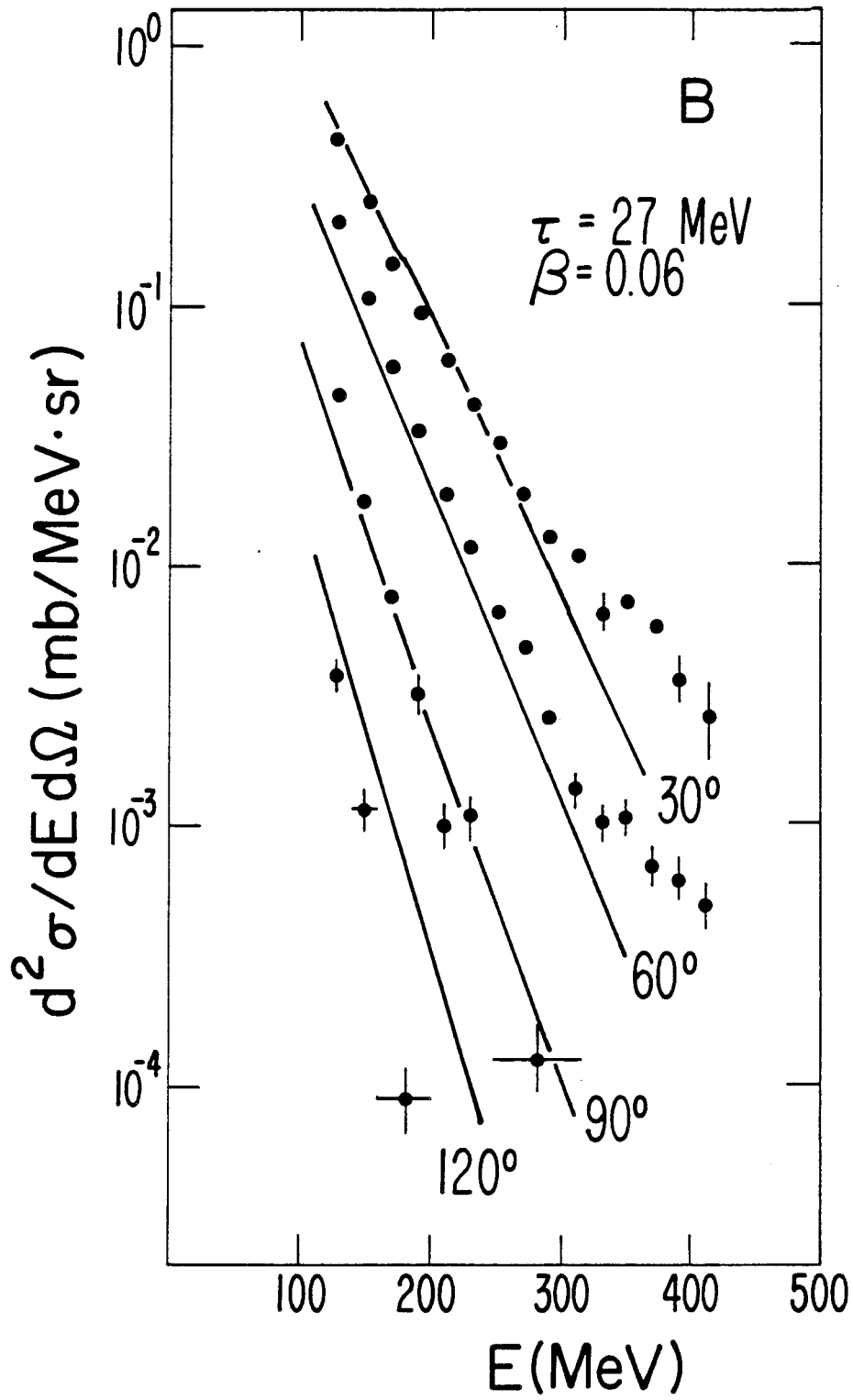


Fig. 32



XBL 774-891

Fig. 33

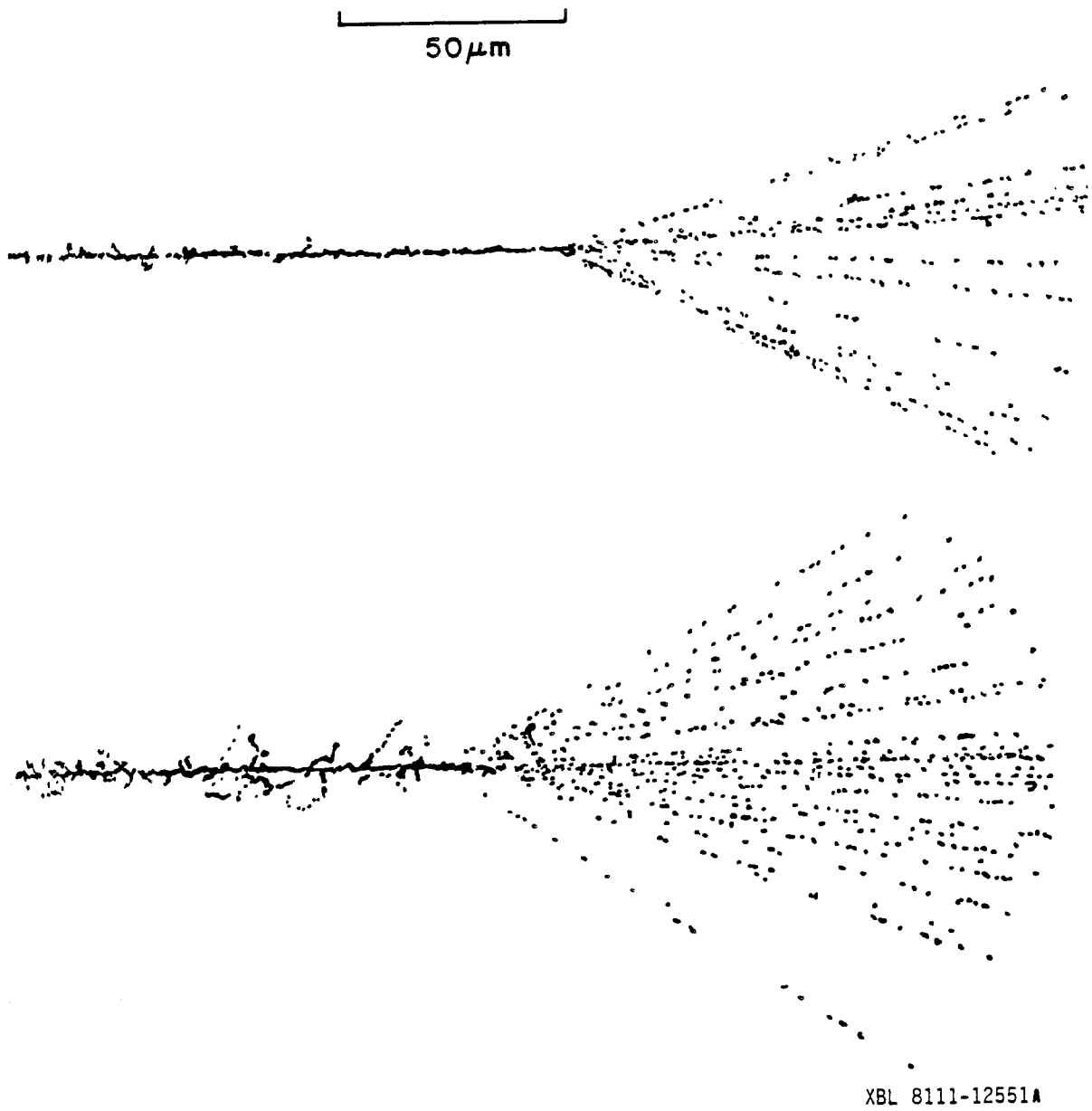


Fig. 34

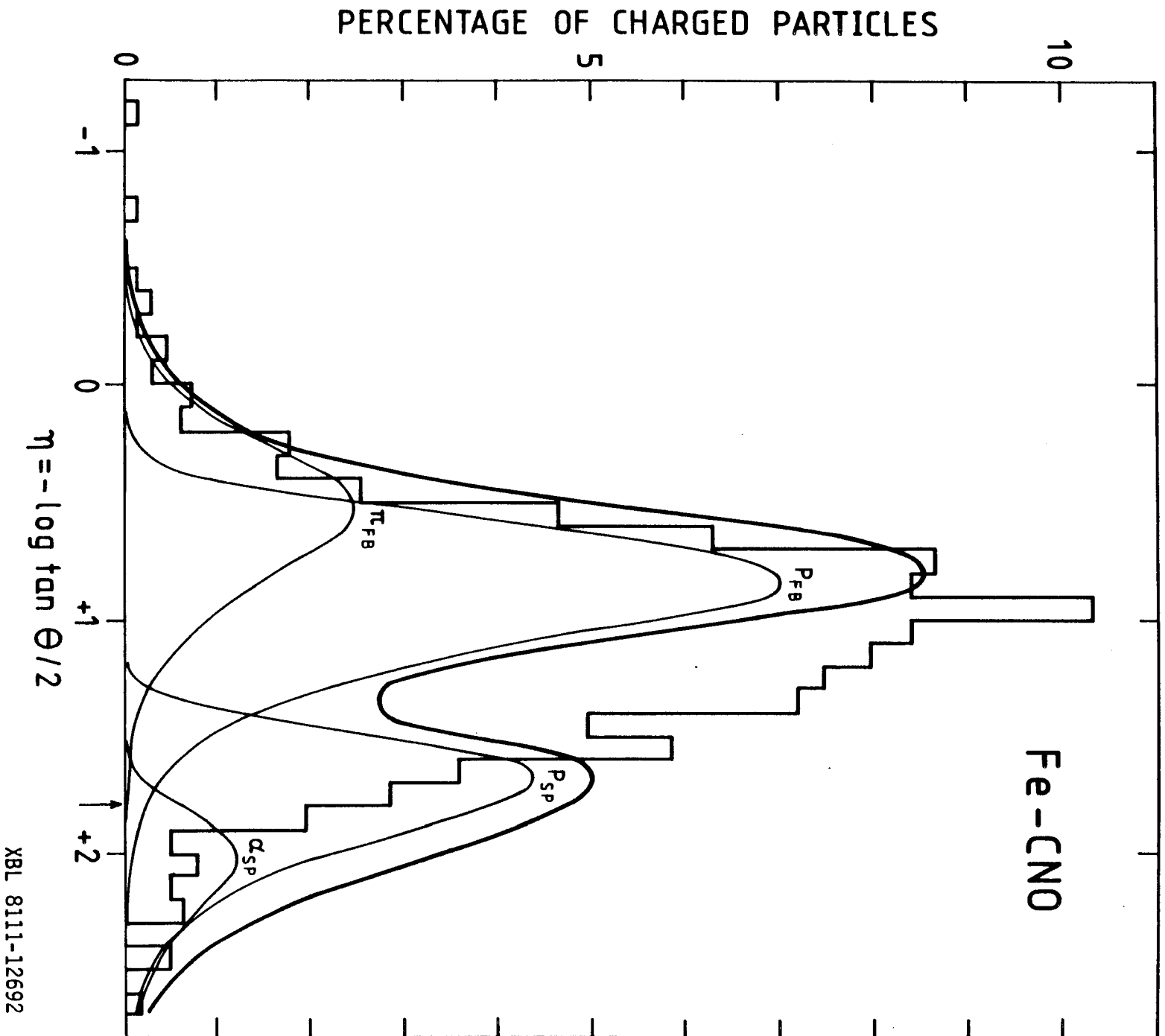
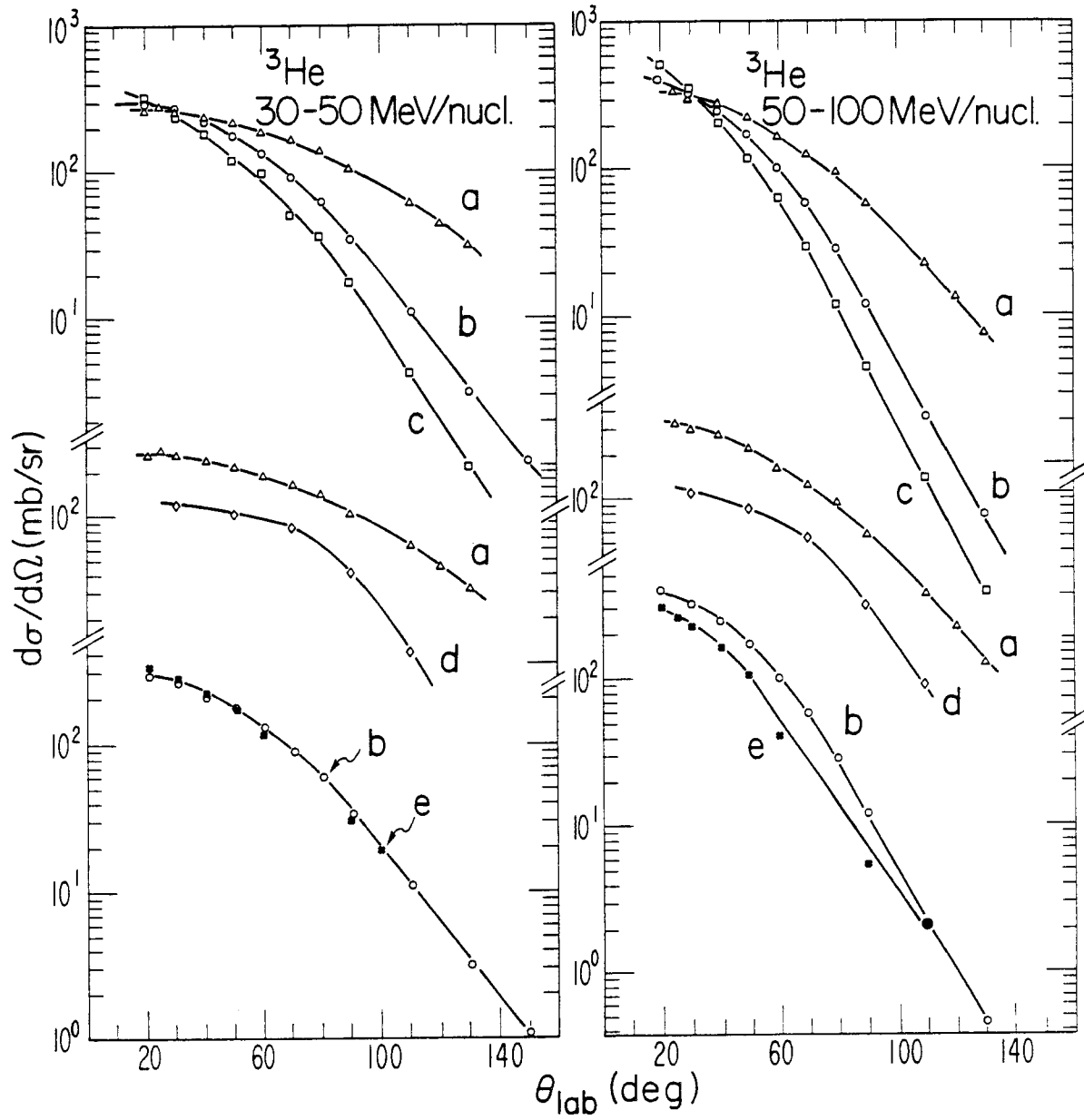


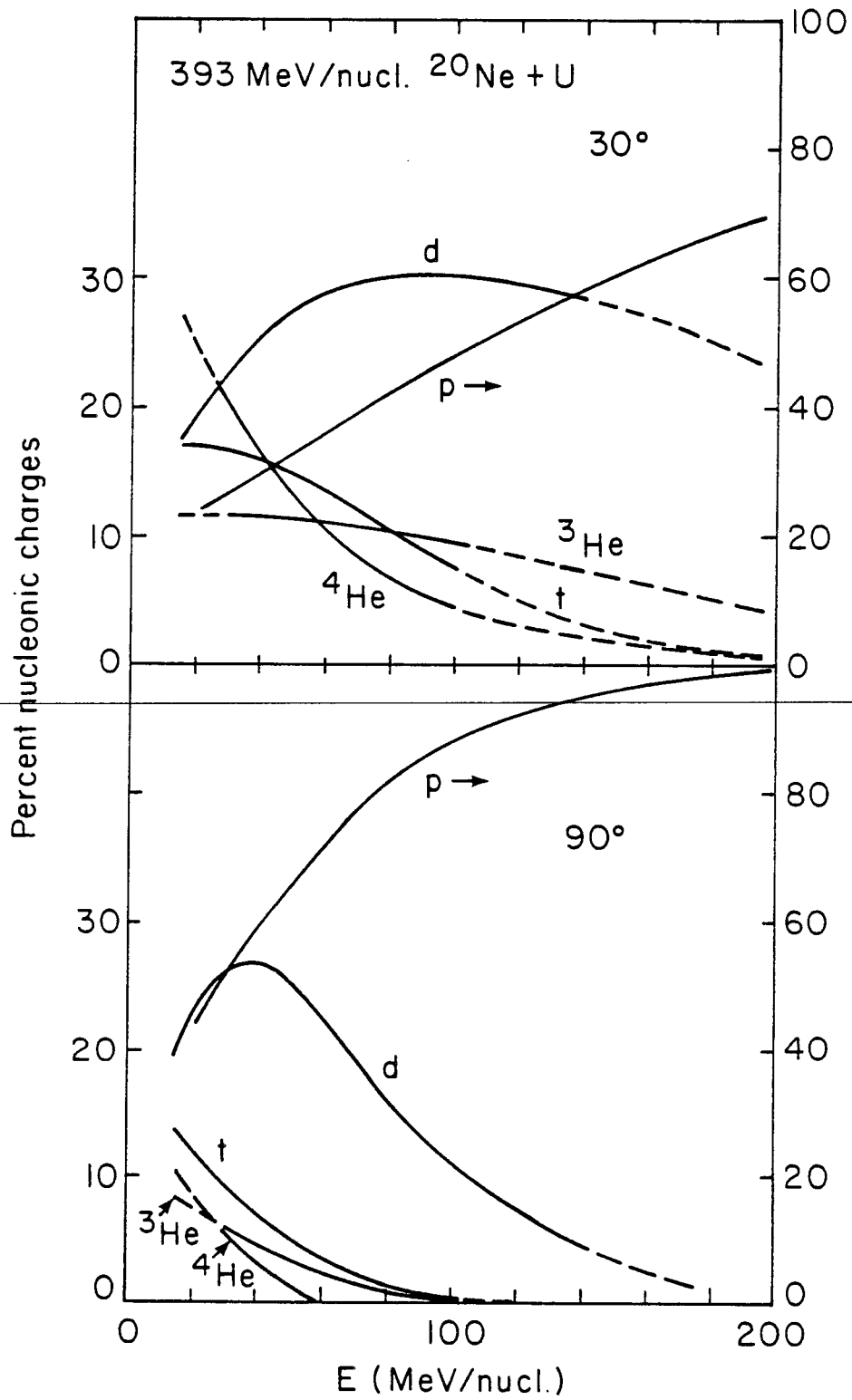
Fig. 35



XBL 774-890

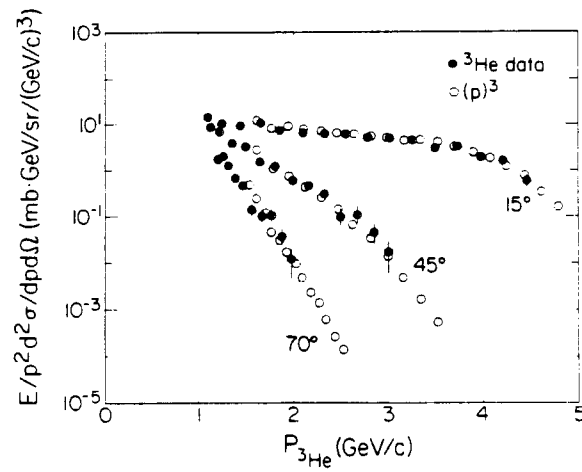
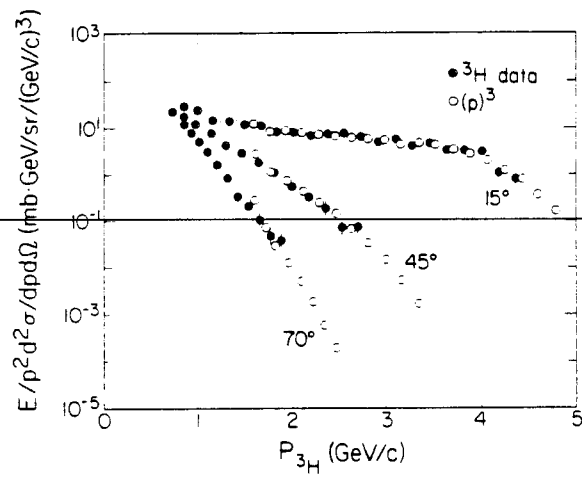
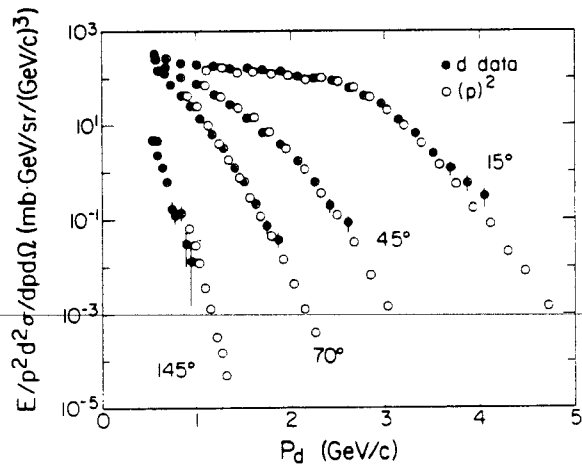
Fig. 36





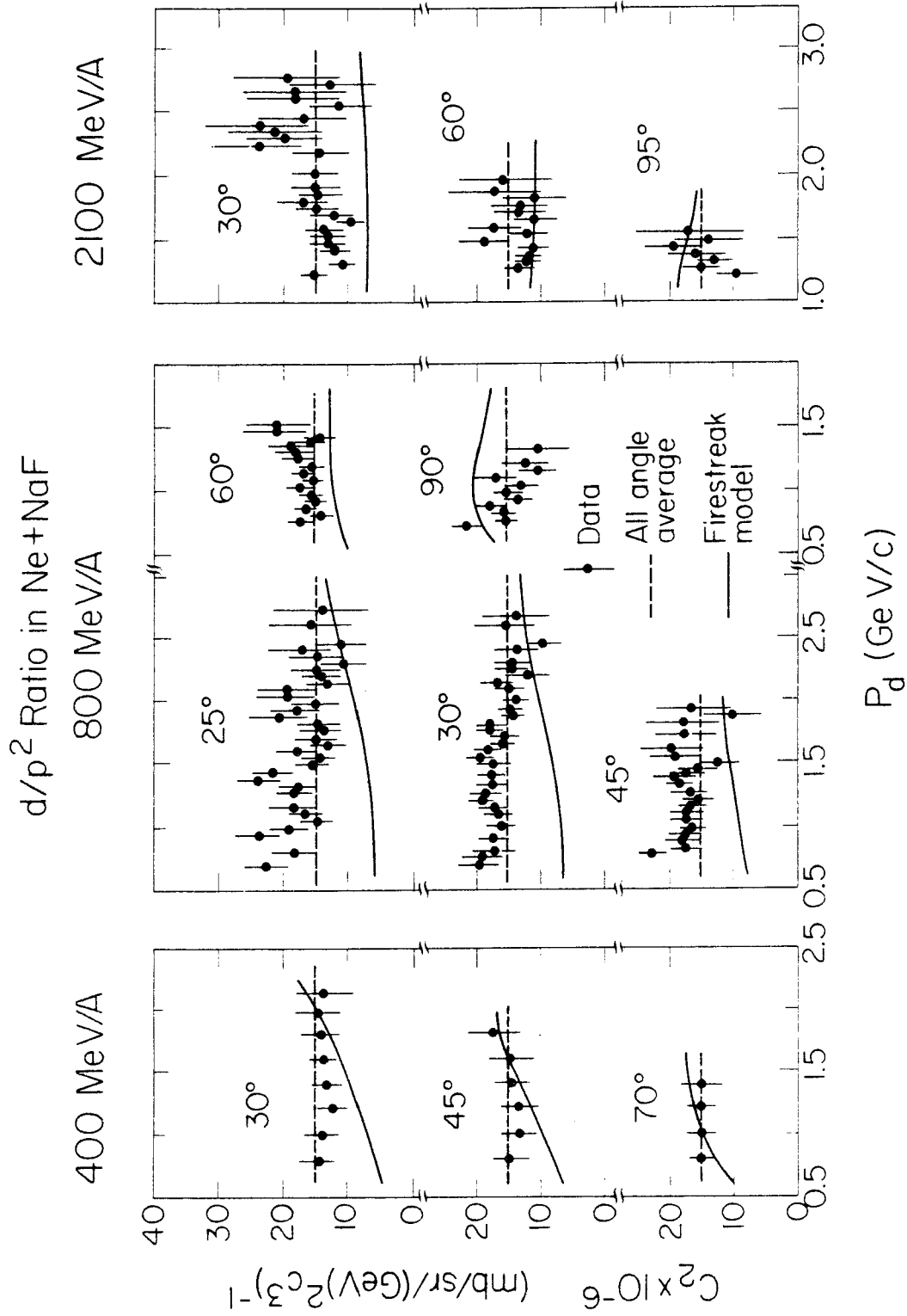
XBL 797-2268

Fig. 37



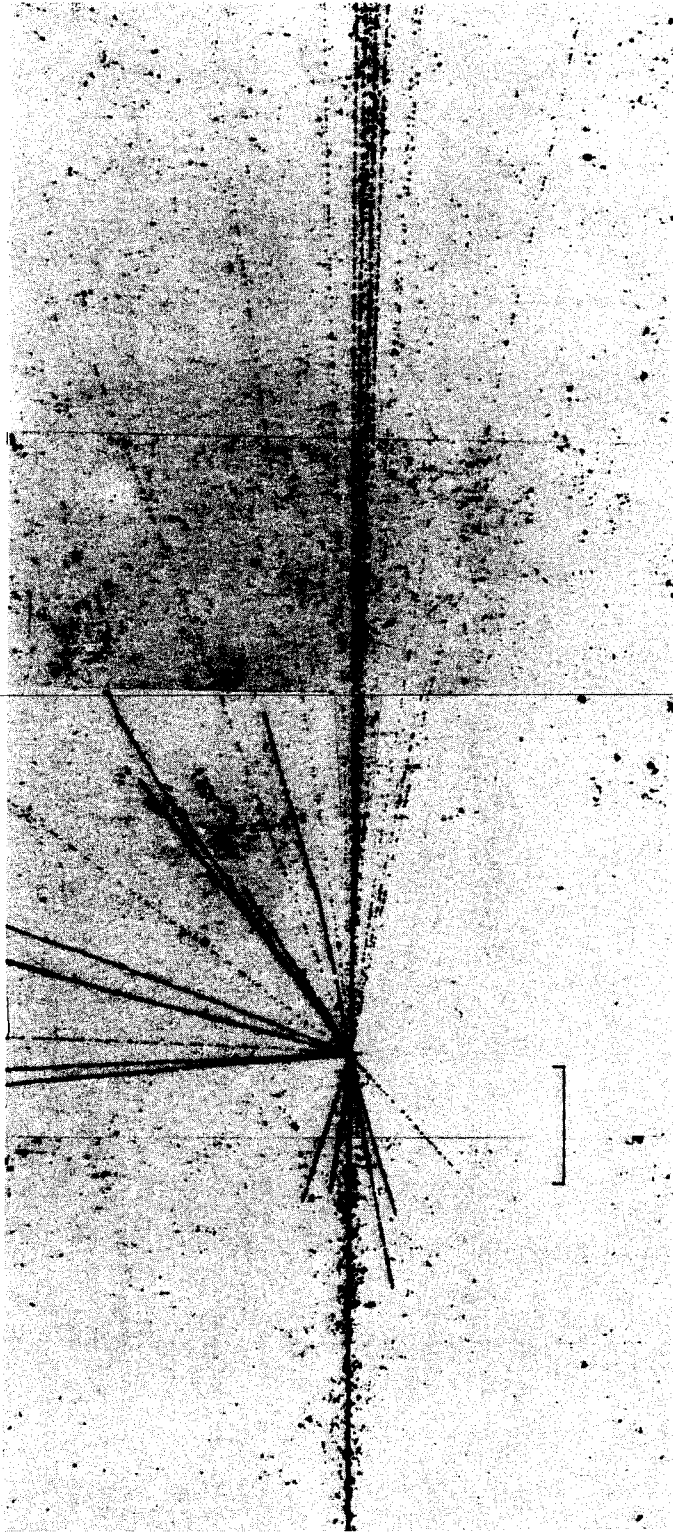
XBL 8012 2509 A

Fig. 38



XBL 8012-2517

Fig. 39



XBB802-1783

Fig. 40

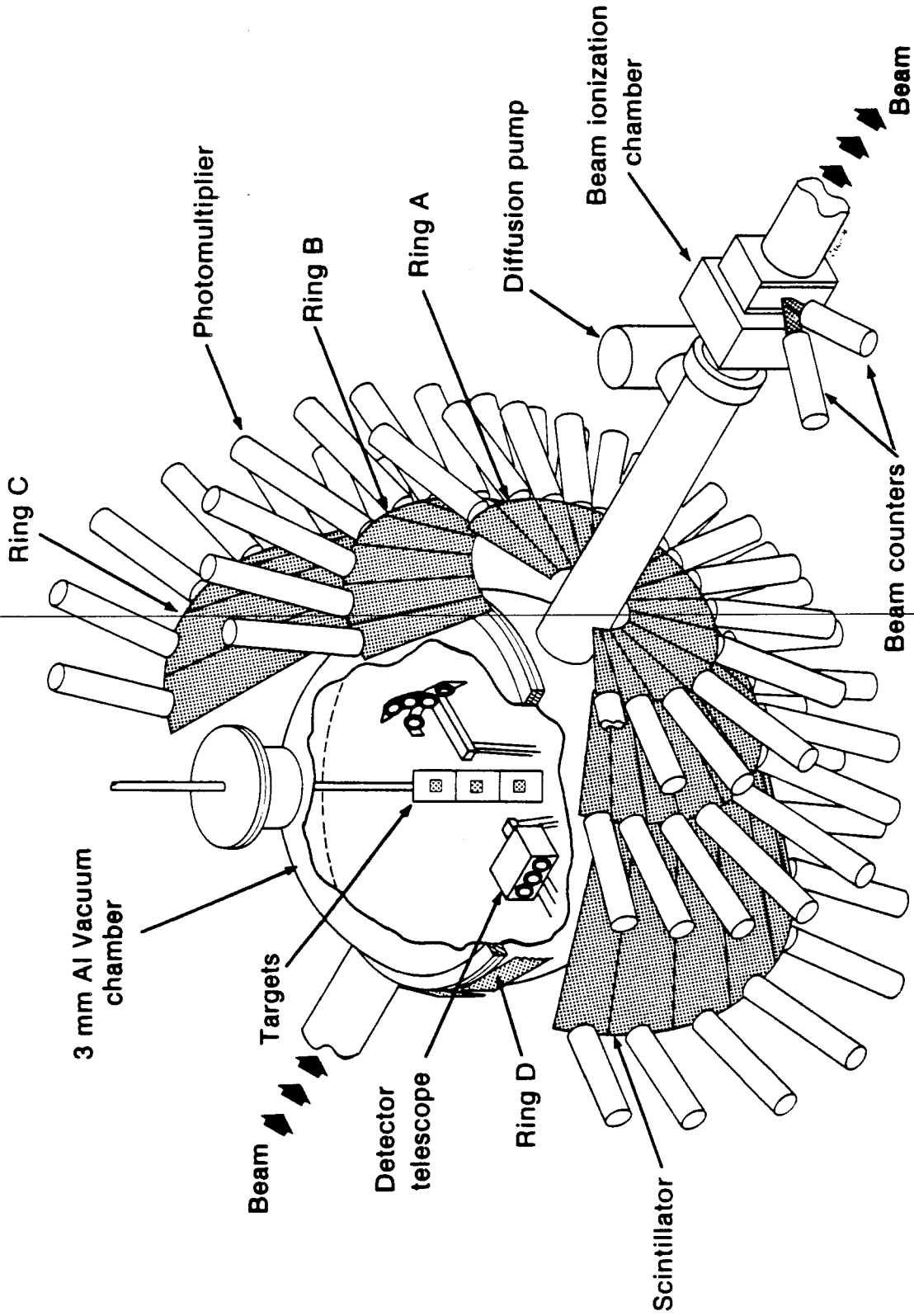
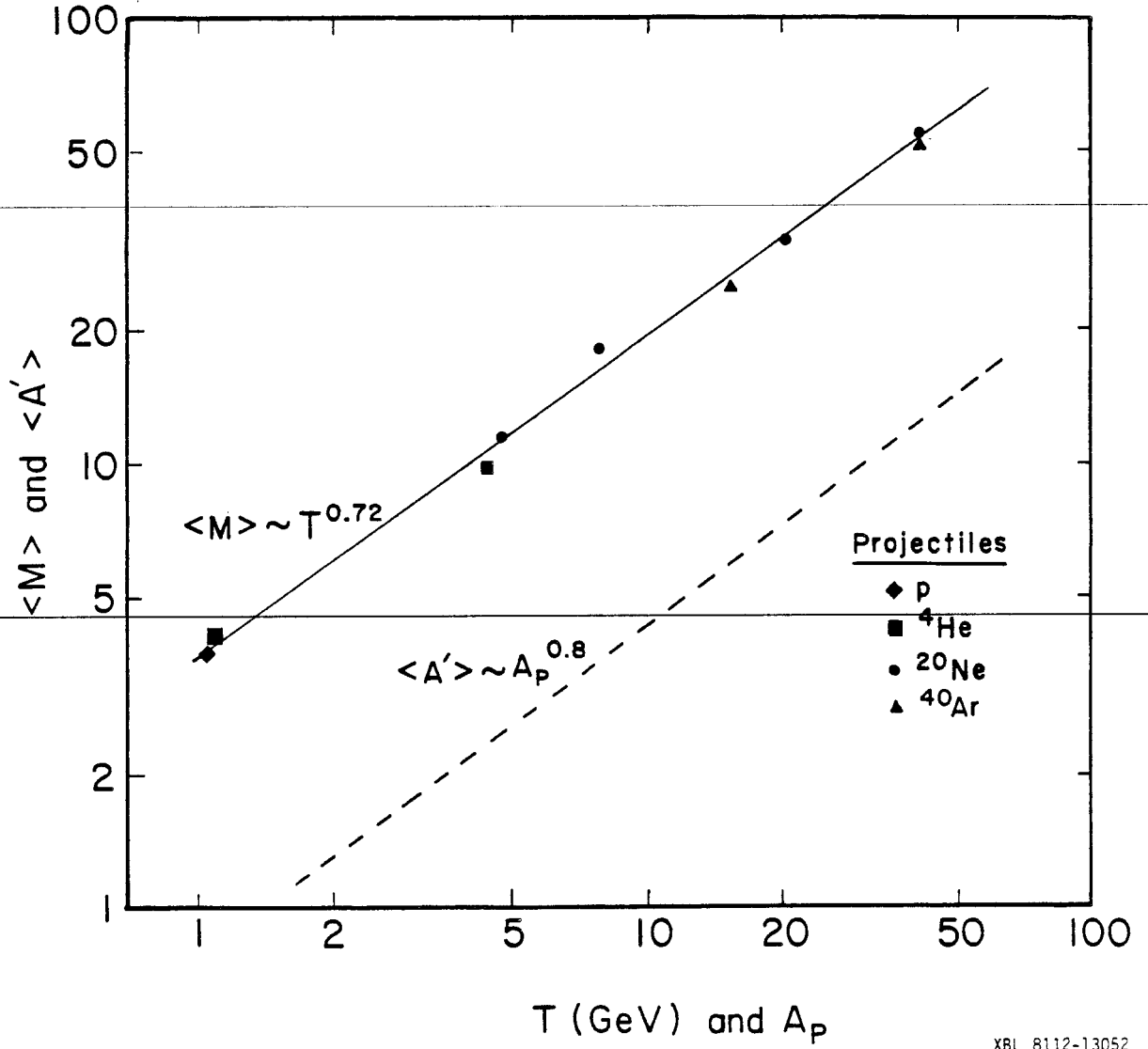


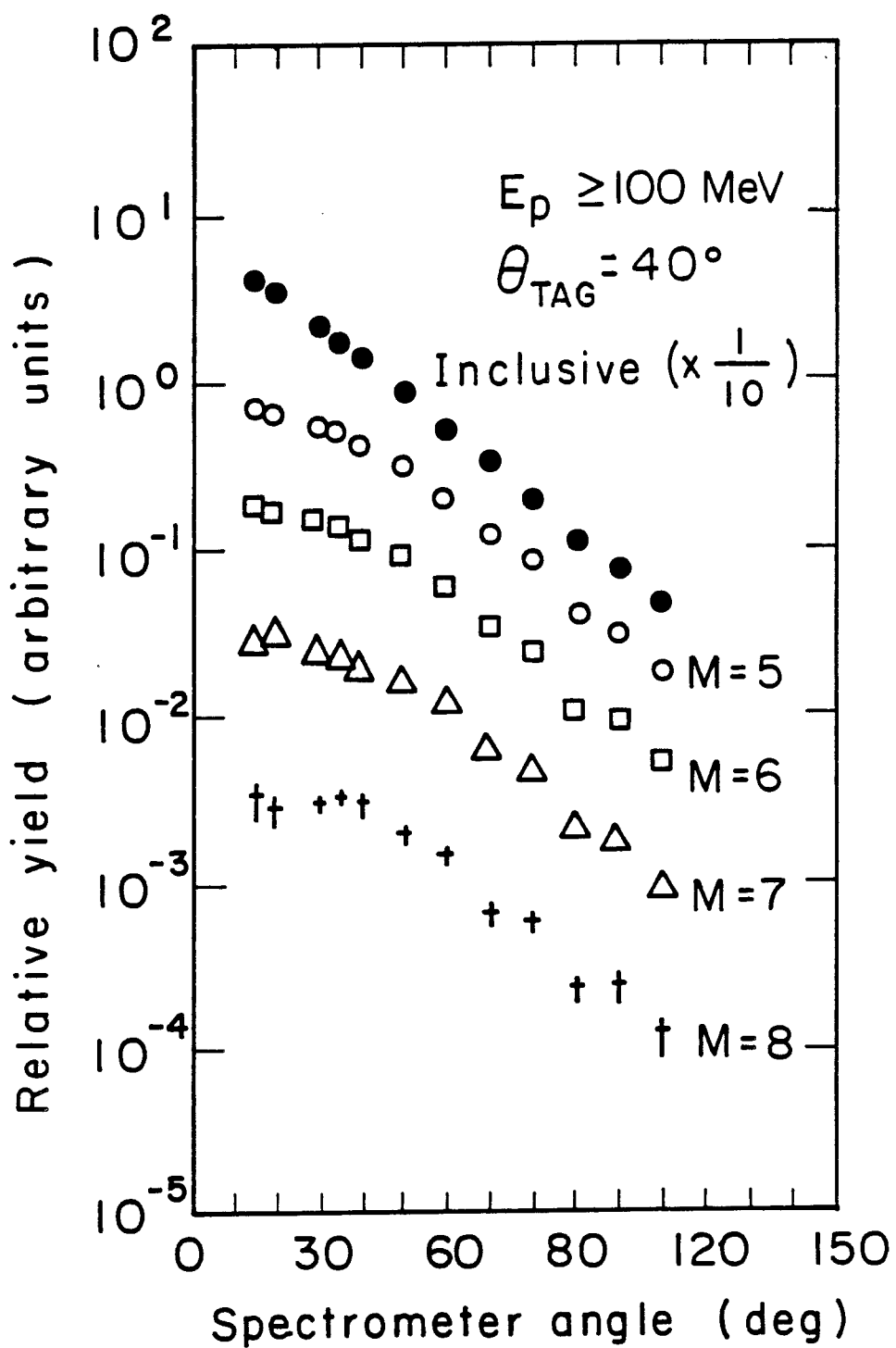
Fig. 41

XBL 782-7229 D



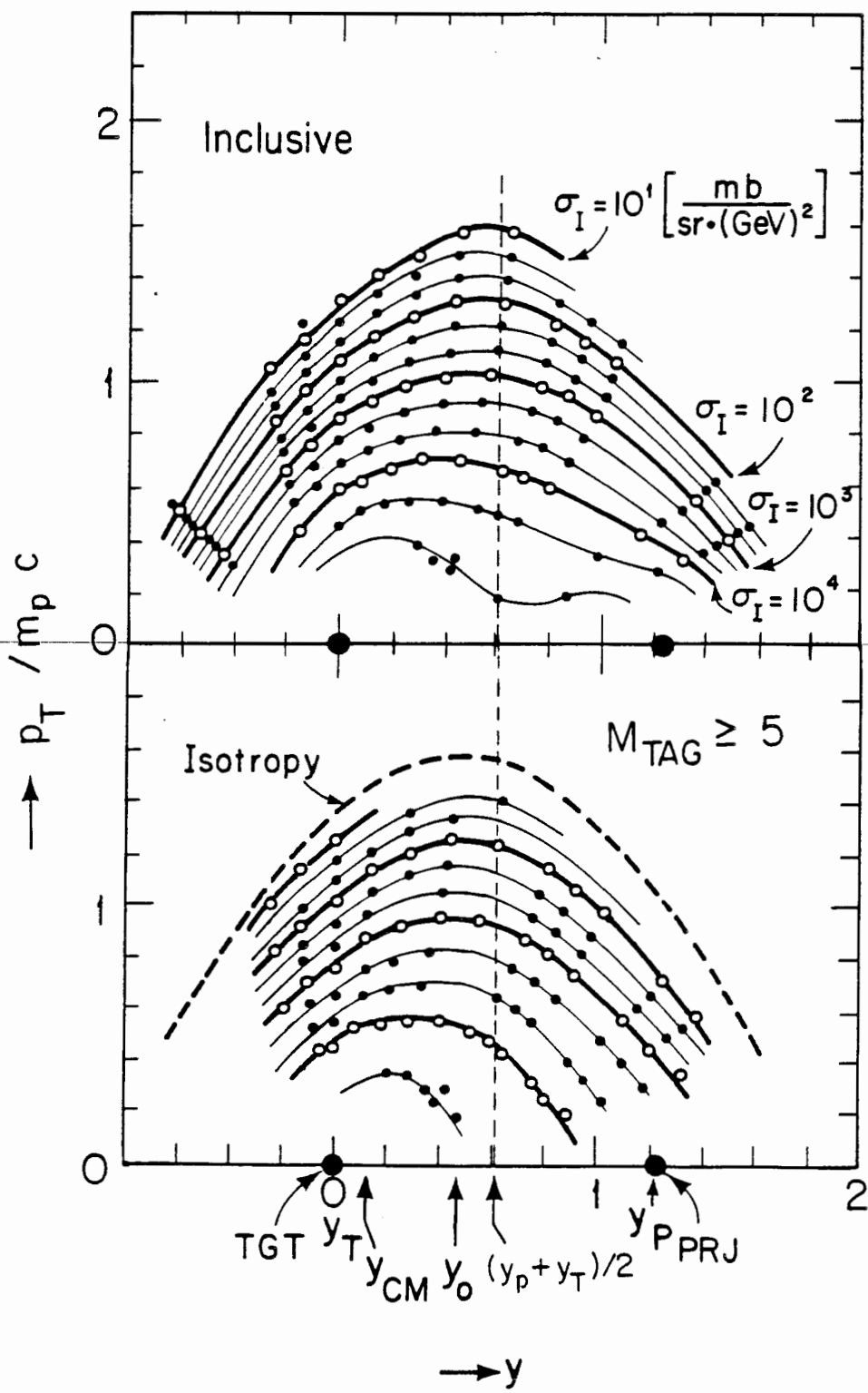
XBL 8112-13052

Fig. 42



XBL788-1586

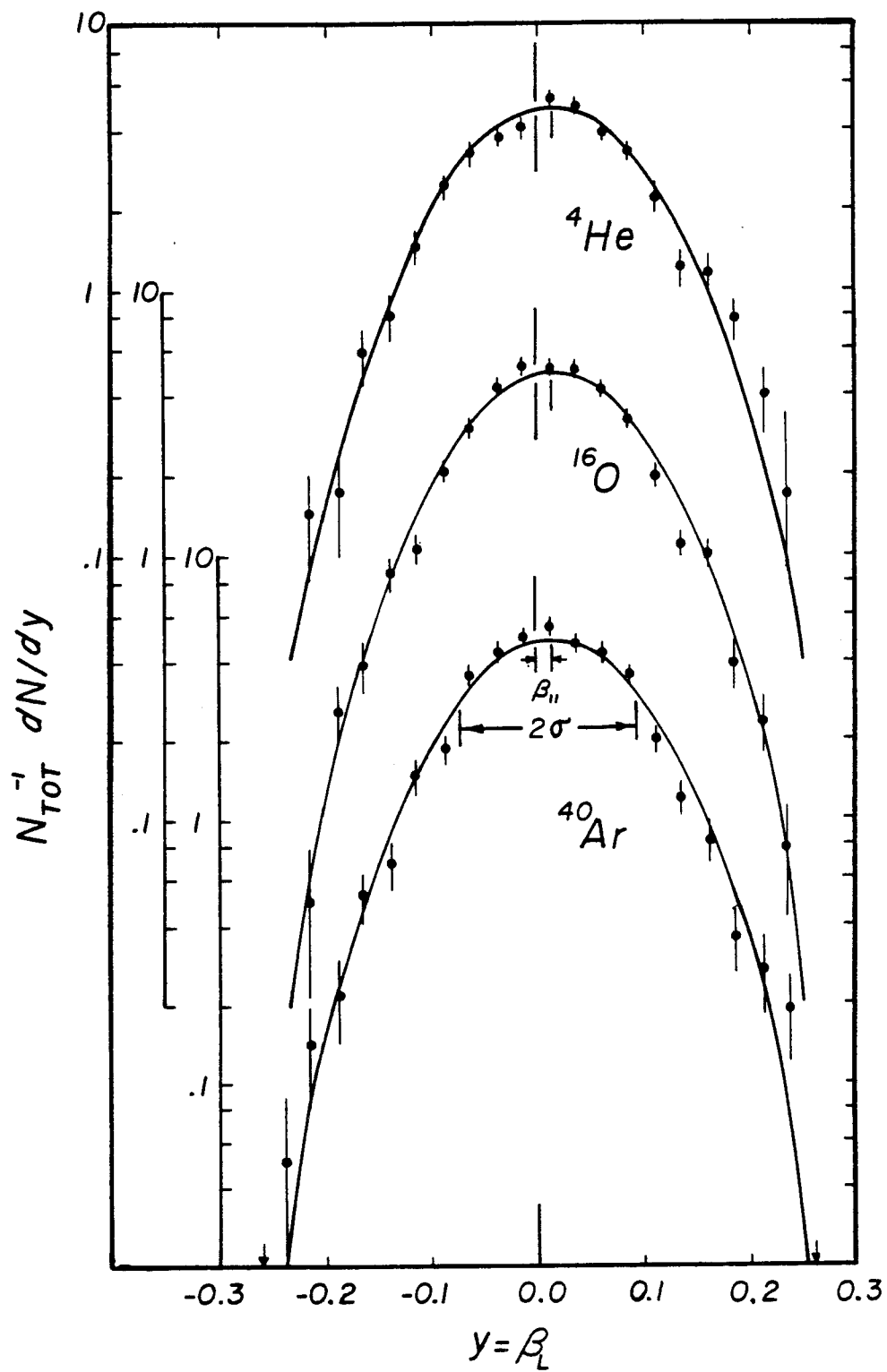
Fig. 43



XBL 797 · 2126

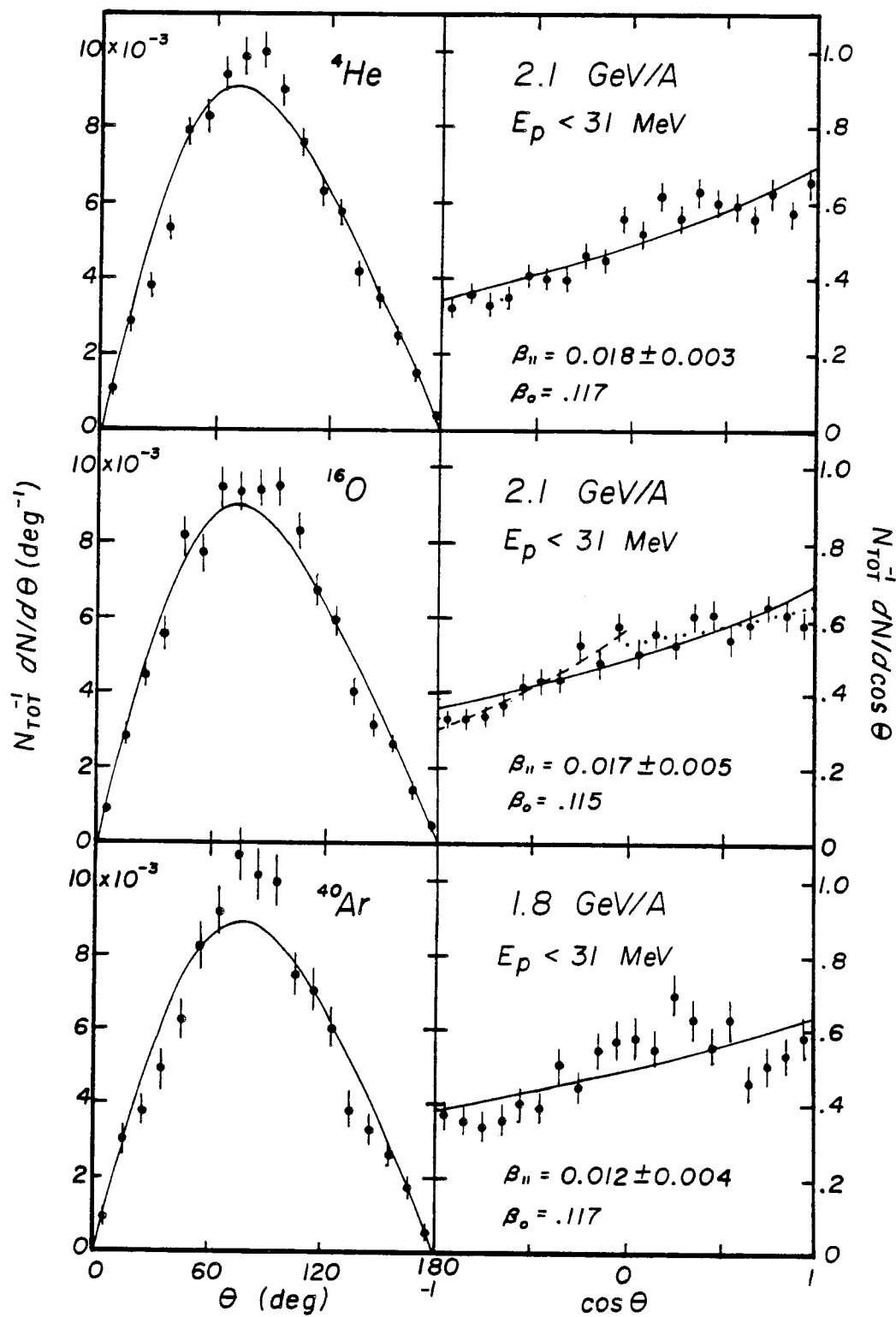
Fig. 44





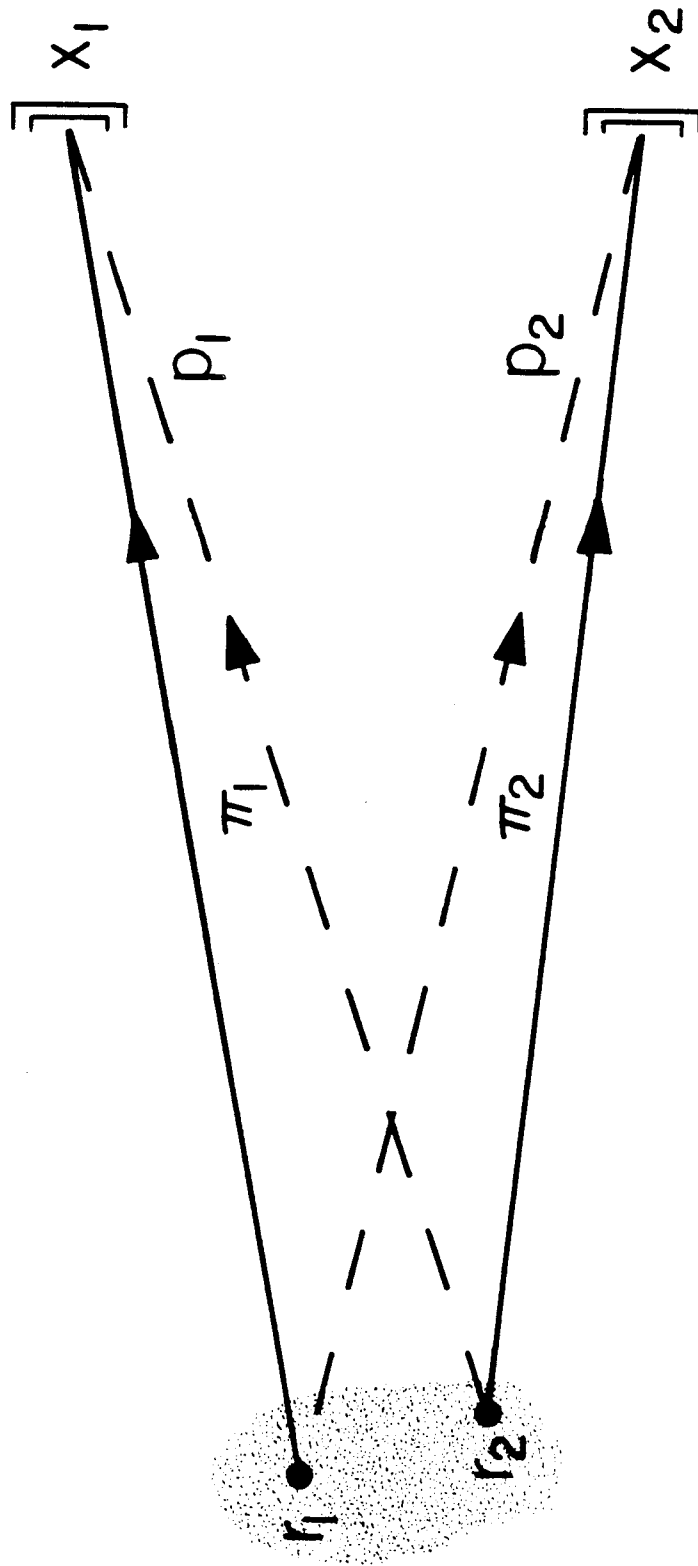
XBL 778-1645

Fig. 45



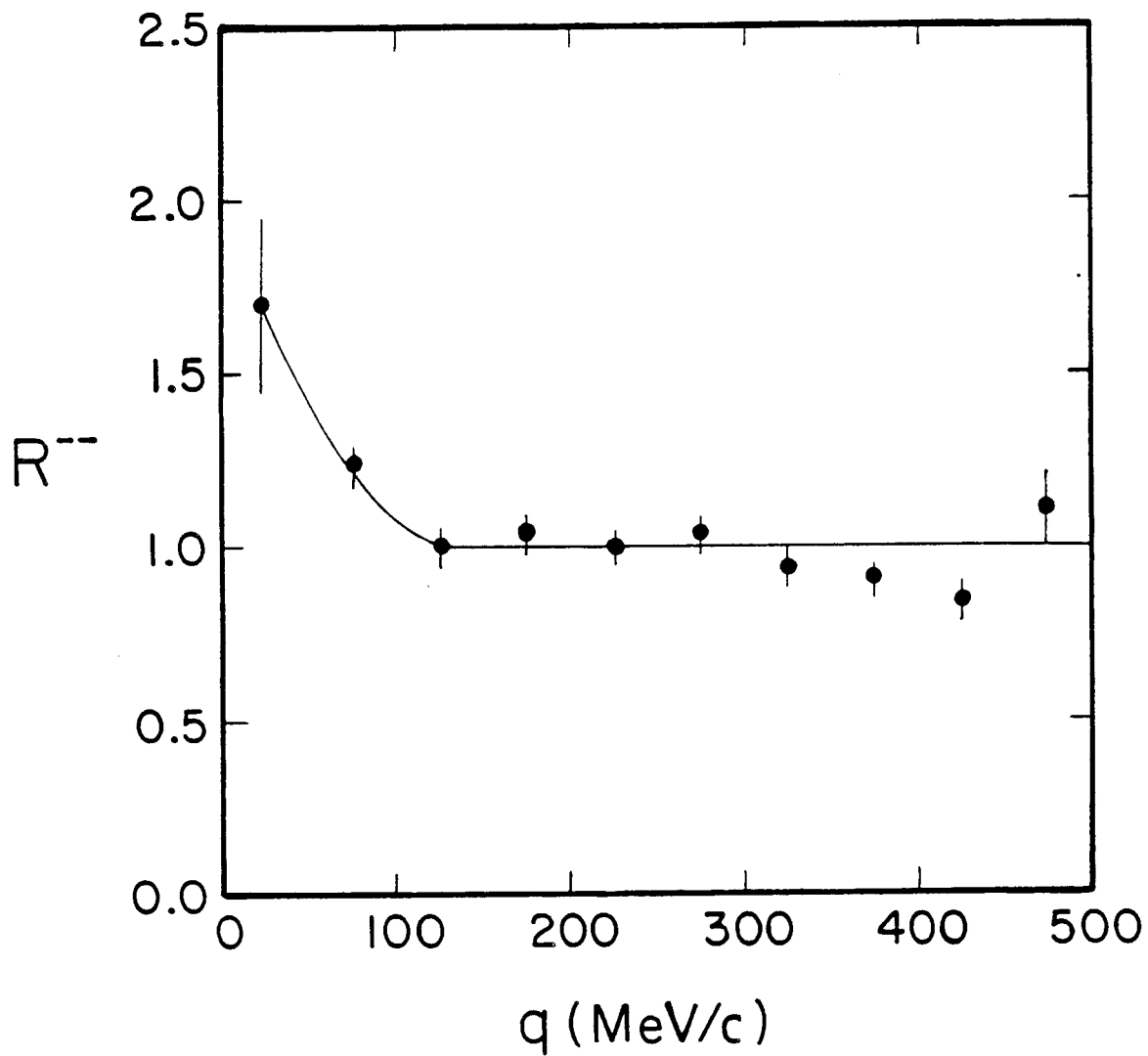
XBL 778-1646

Fig. 46



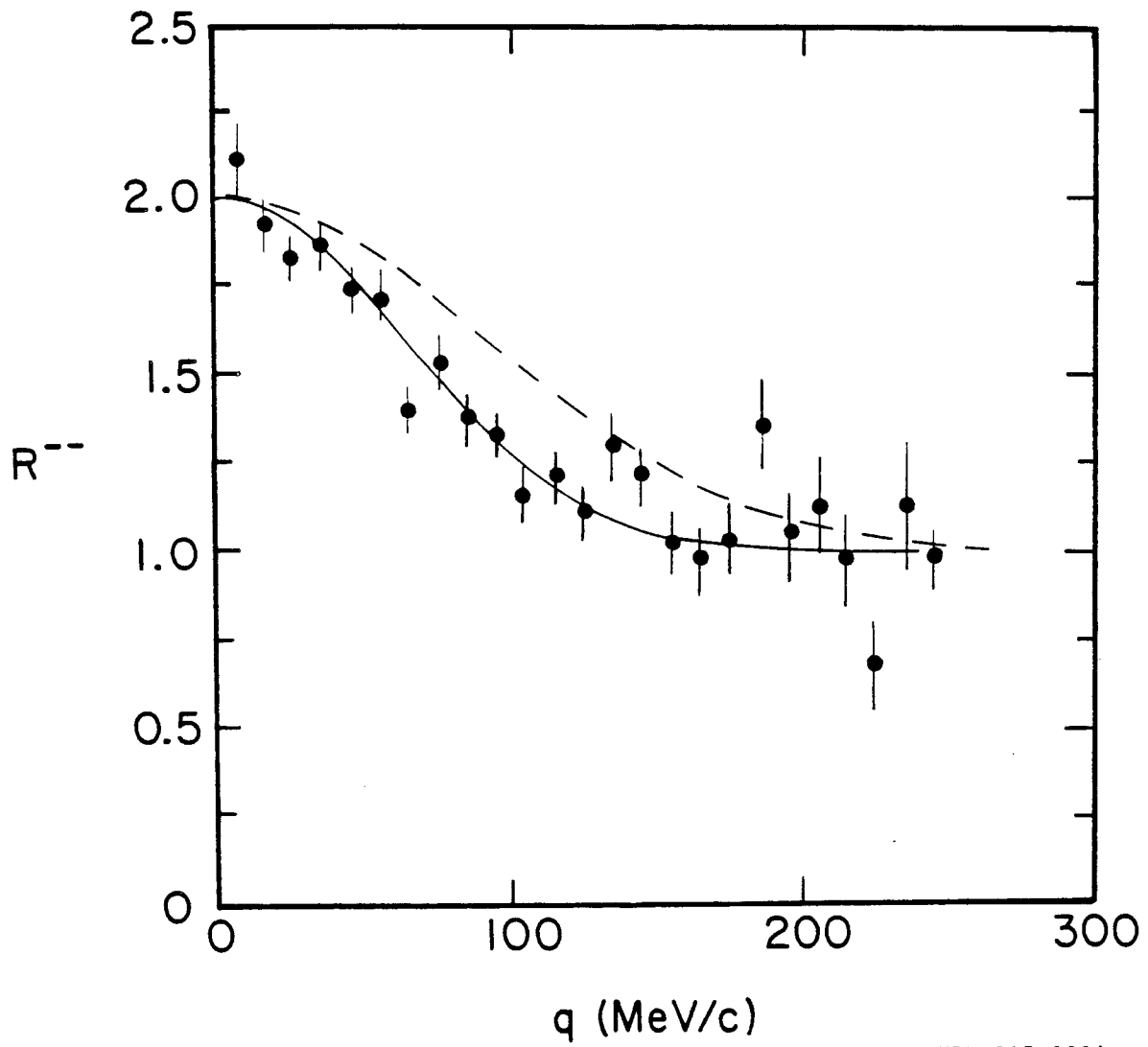
XBL 815-9836

Fig. 47



XBL 815-9833

Fig. 48



XBL 815-9834

Fig. 49

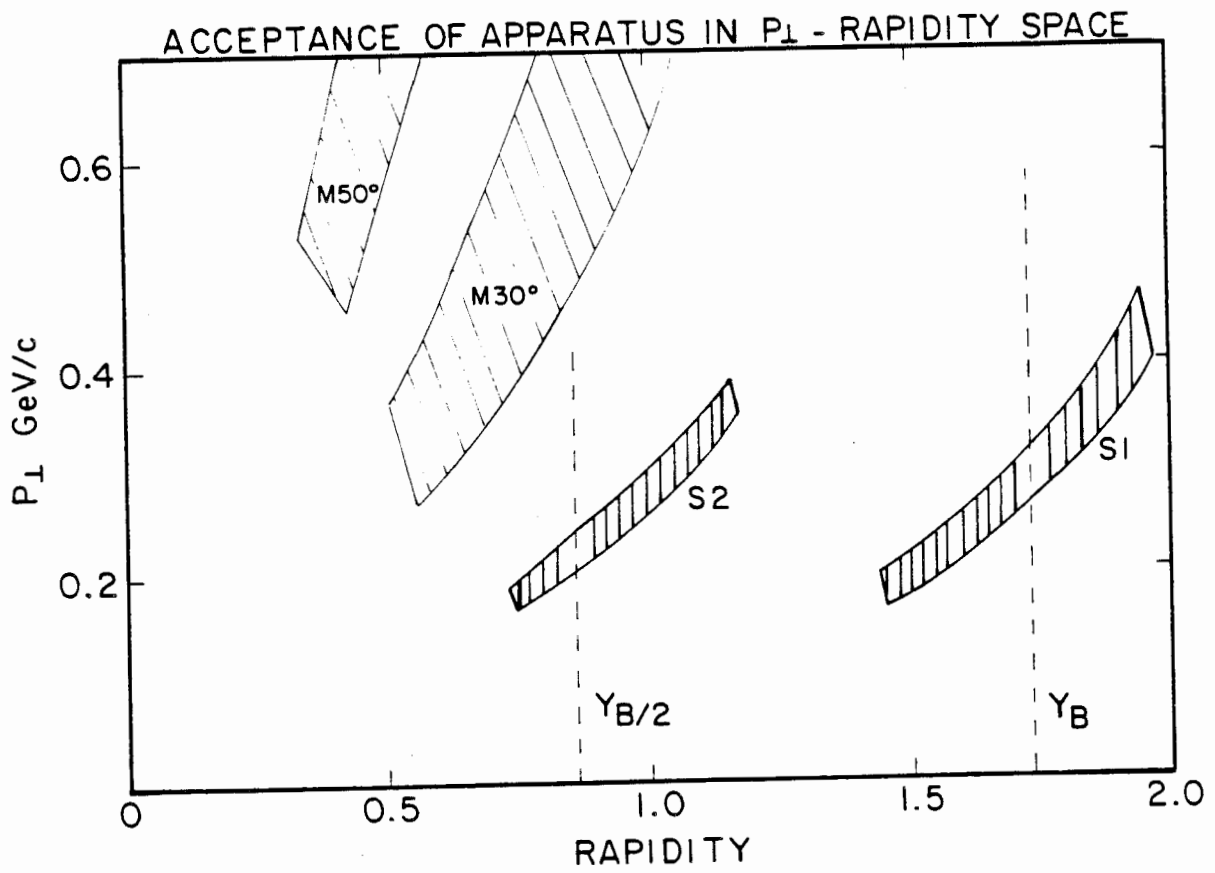


FIGURE 1

XBL 8010-12485

Fig. 50

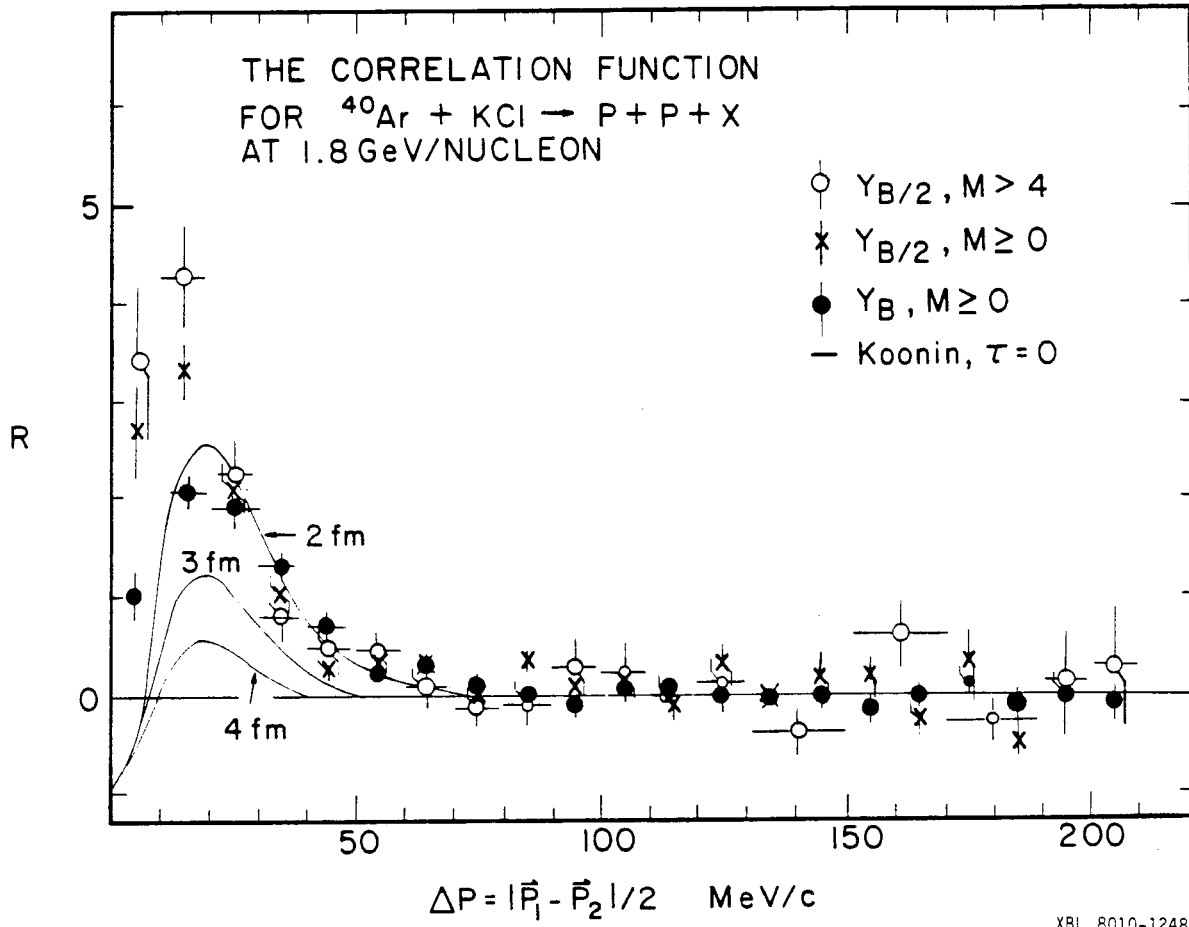


FIGURE 2

XBL 8010-12484

Fig. 51

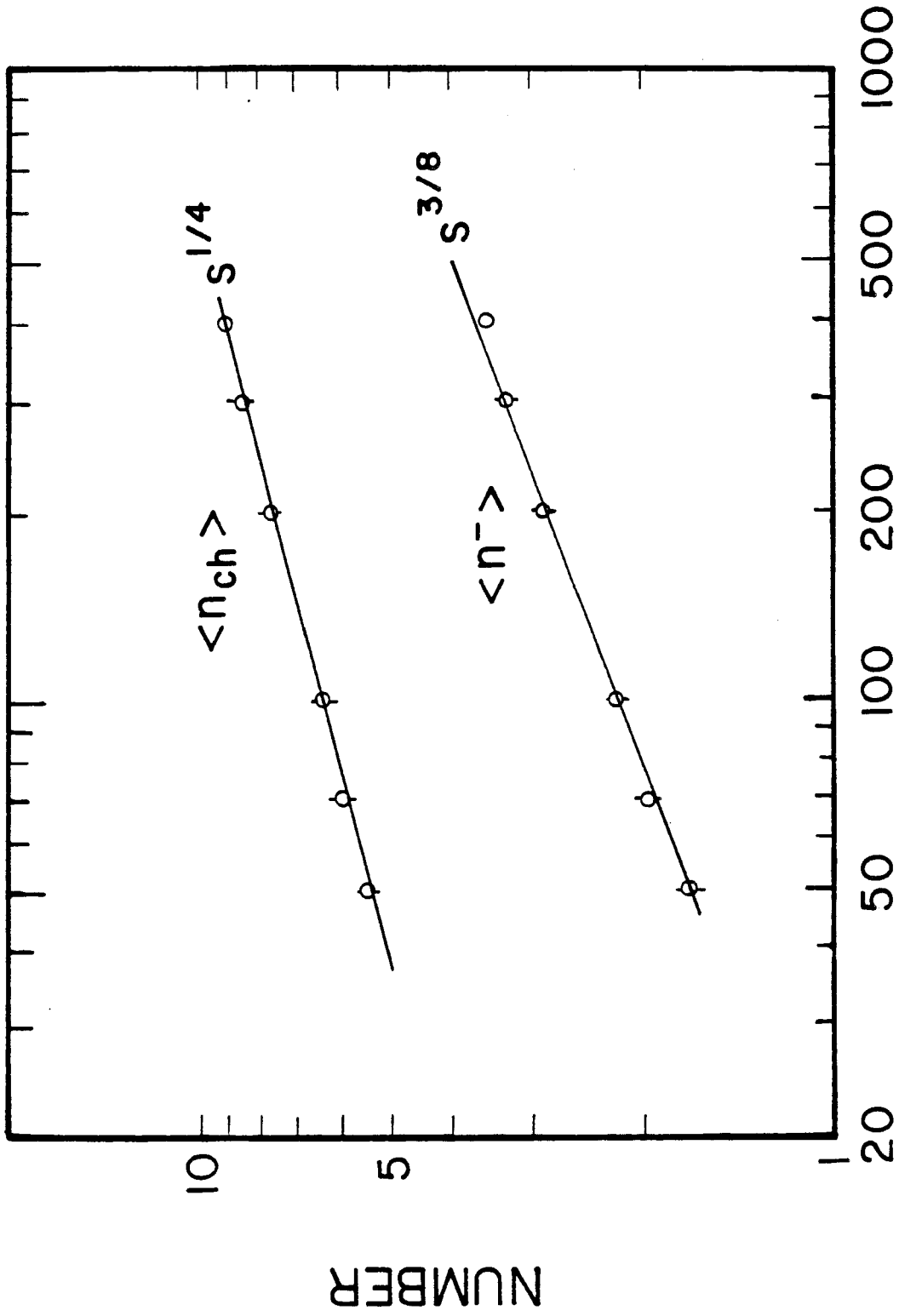
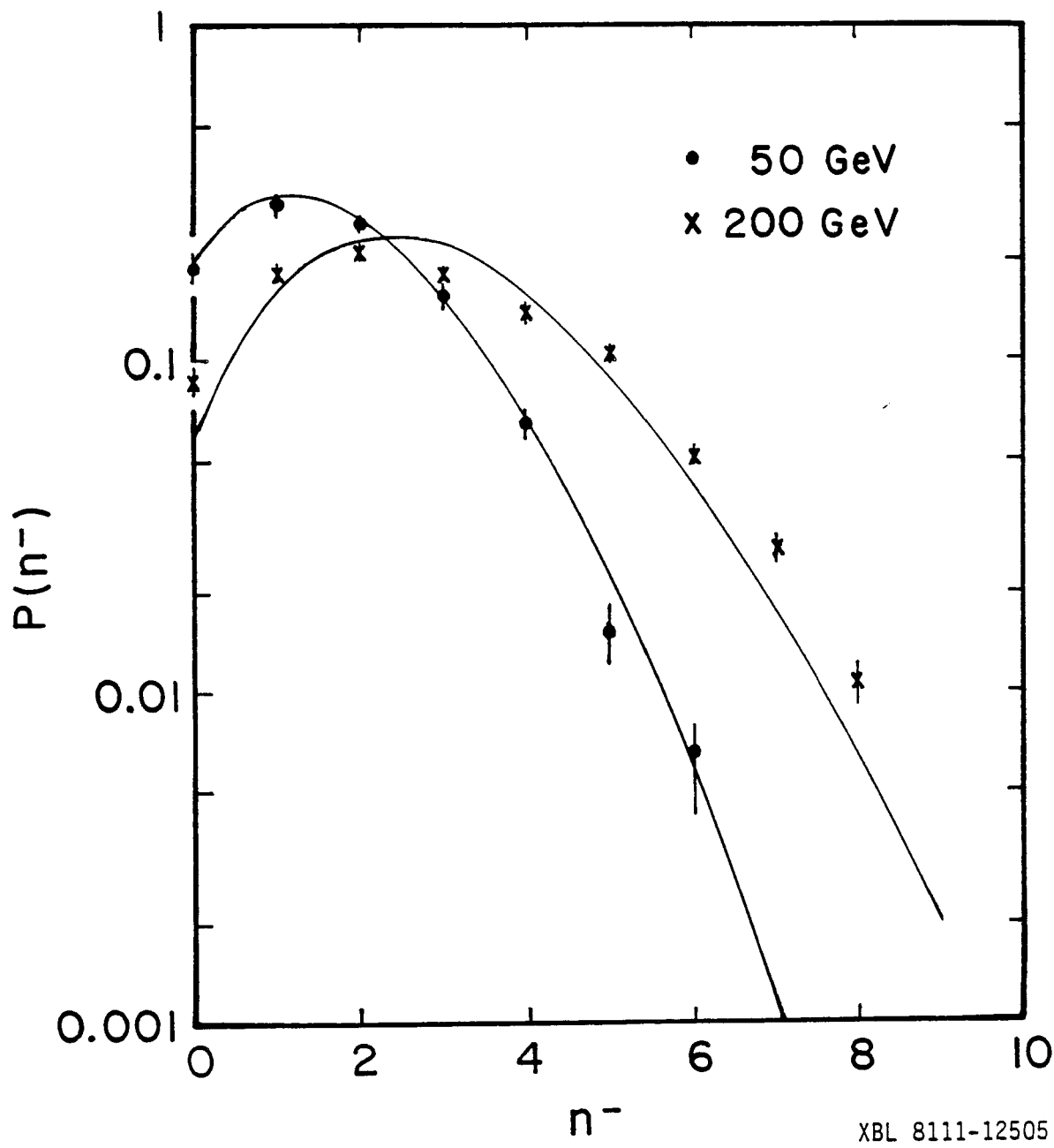


Fig. 52

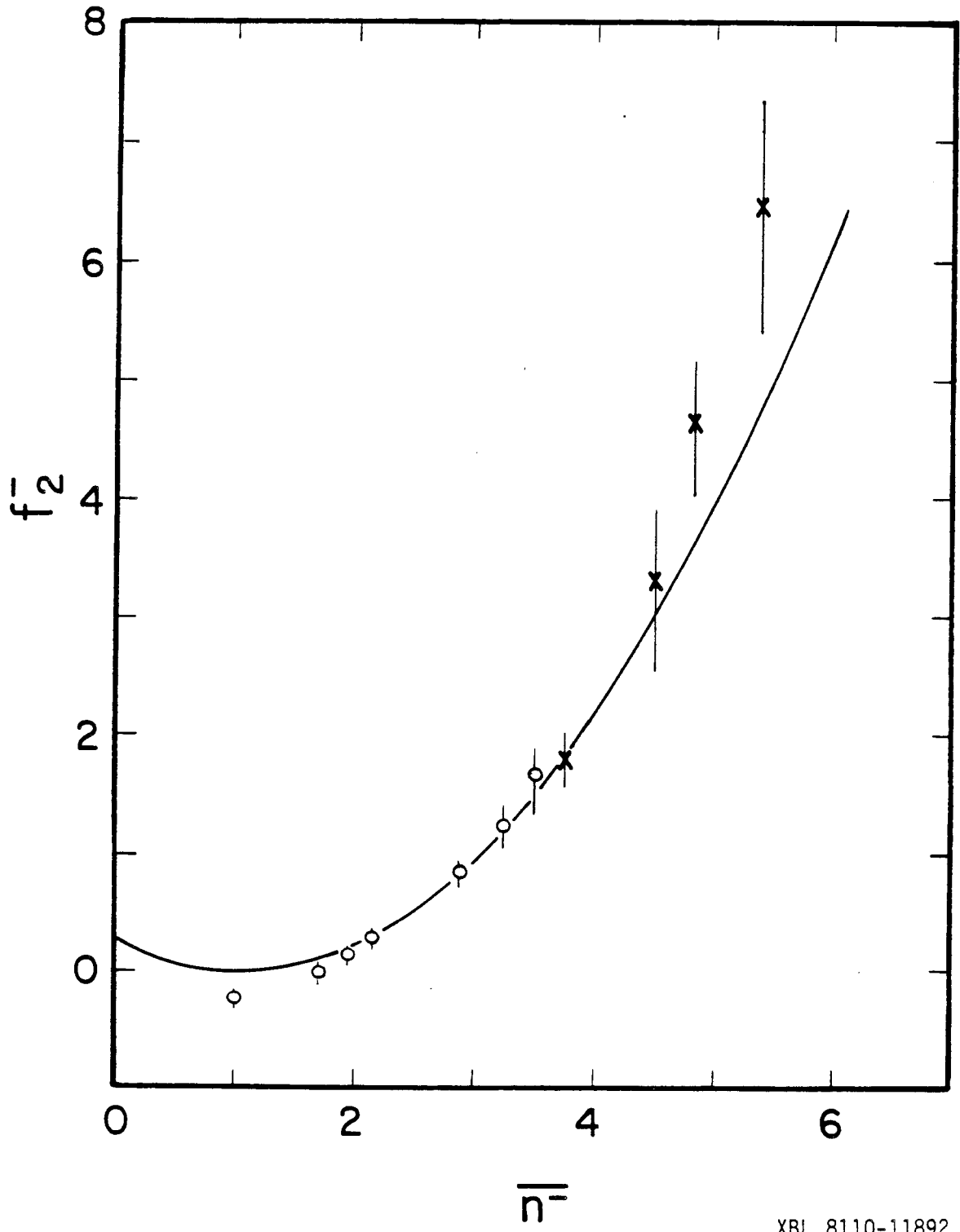
XBL 8111-12506





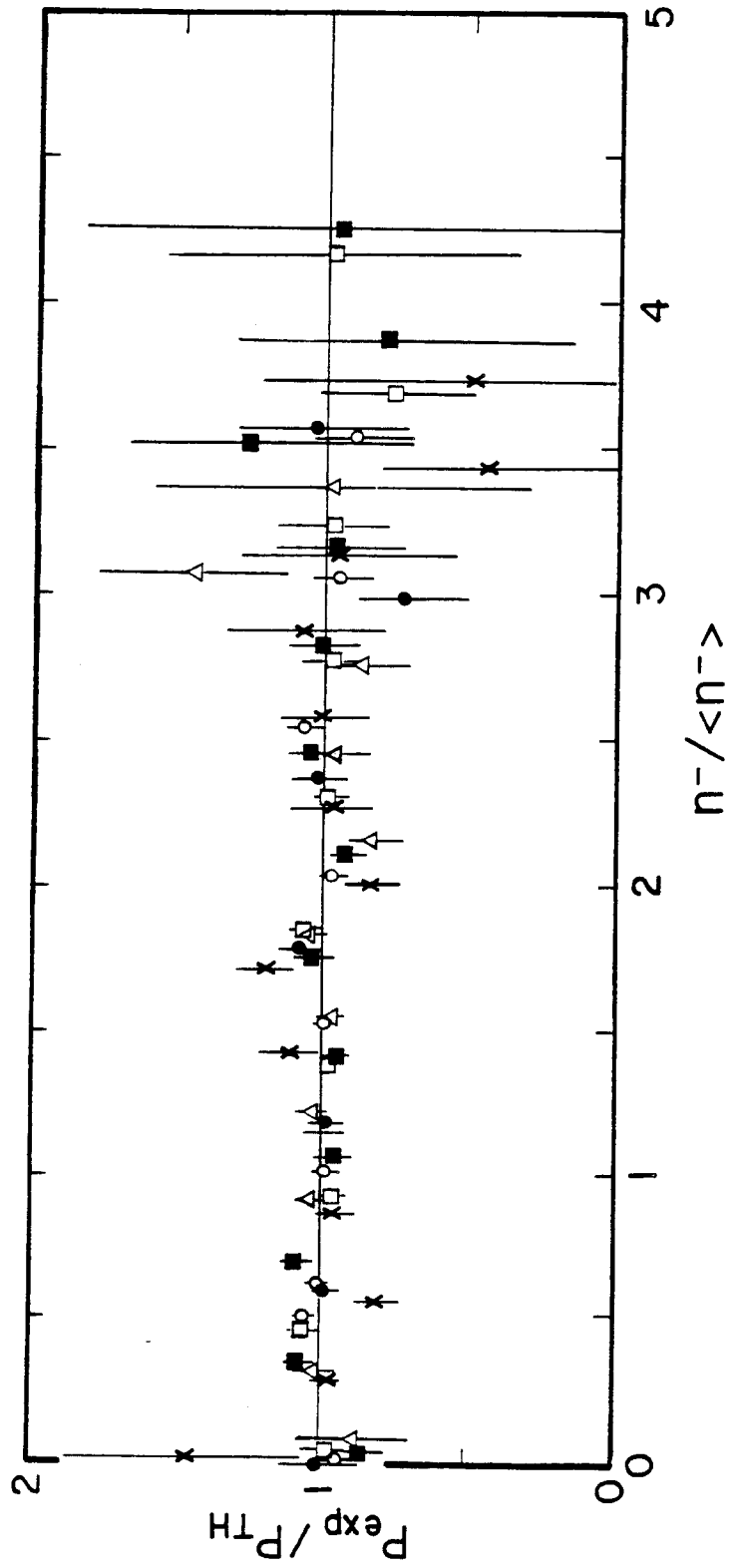
XBL 8111-12505

Fig. 53



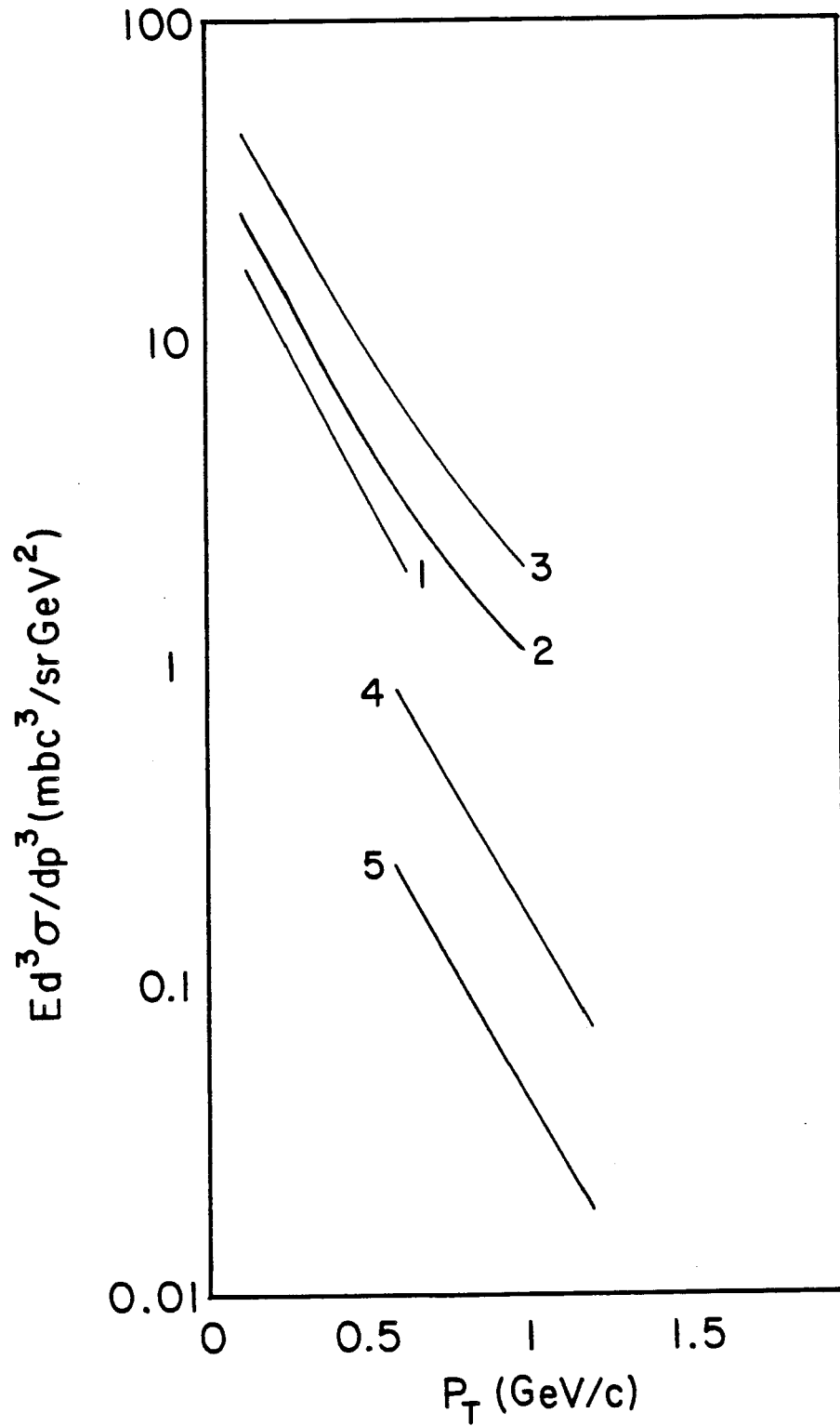
XBL 8110-11892

Fig. 54



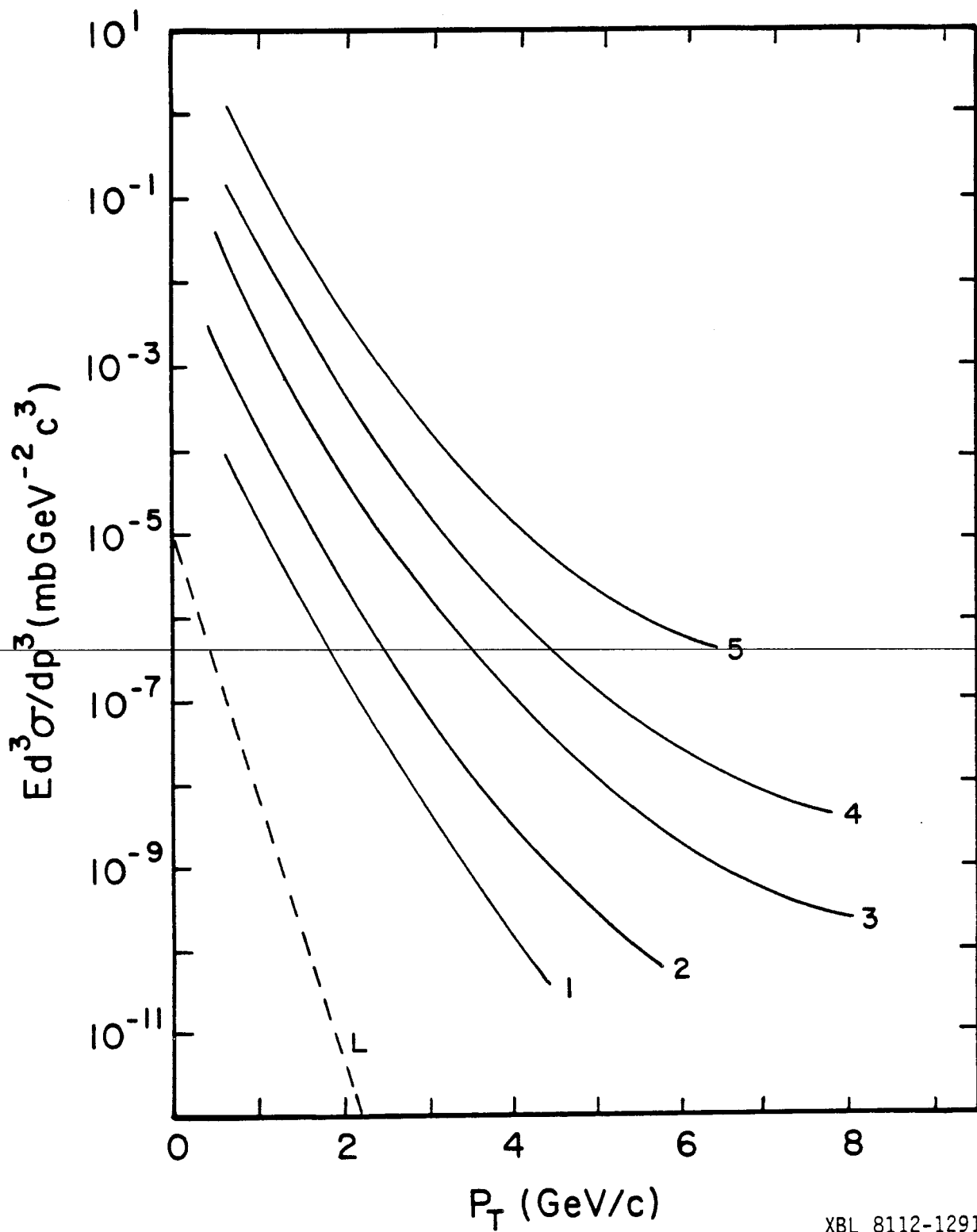
XBL 8111-12503

Fig. 55



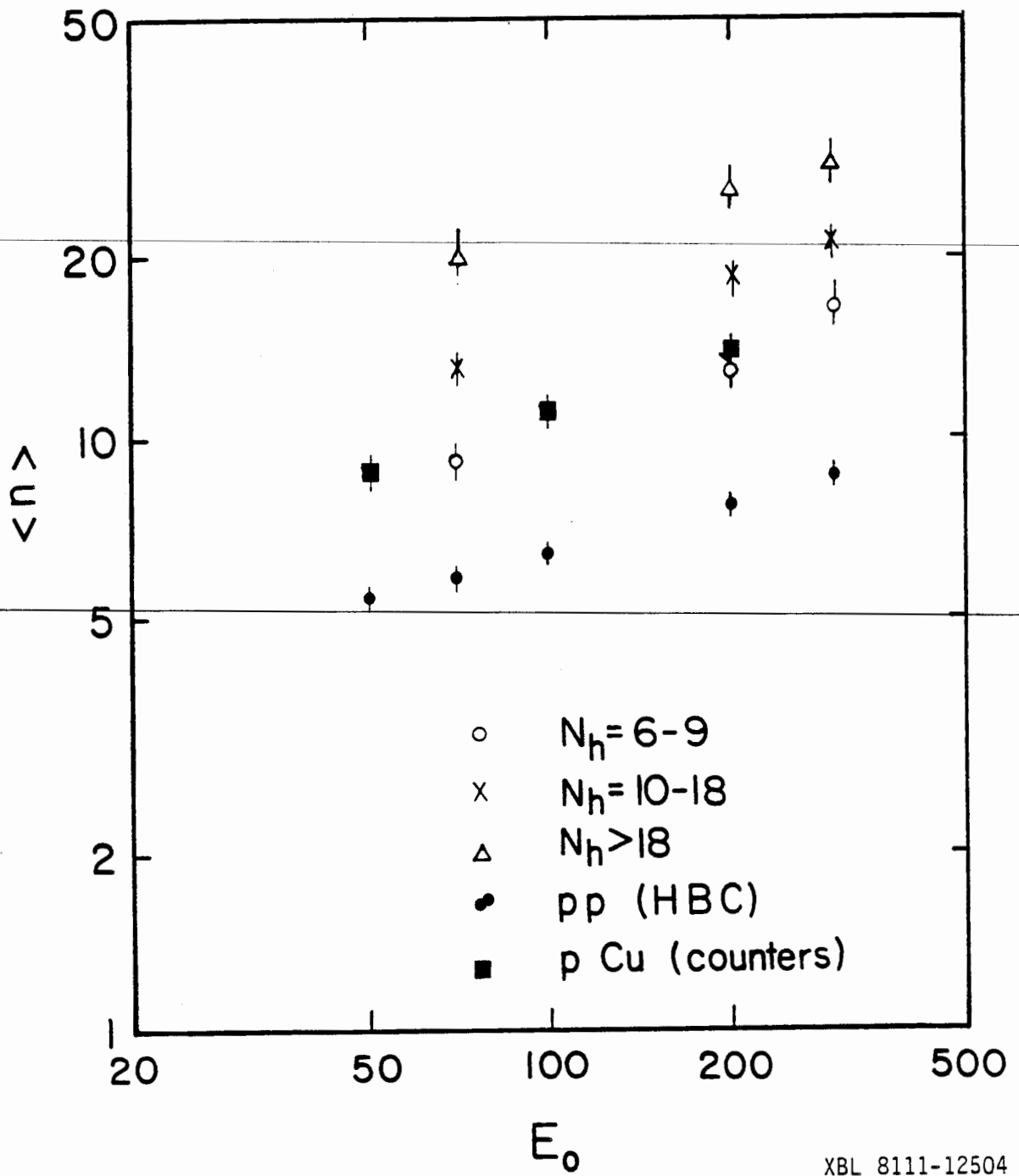
XBL 8112-12915

Fig. 56



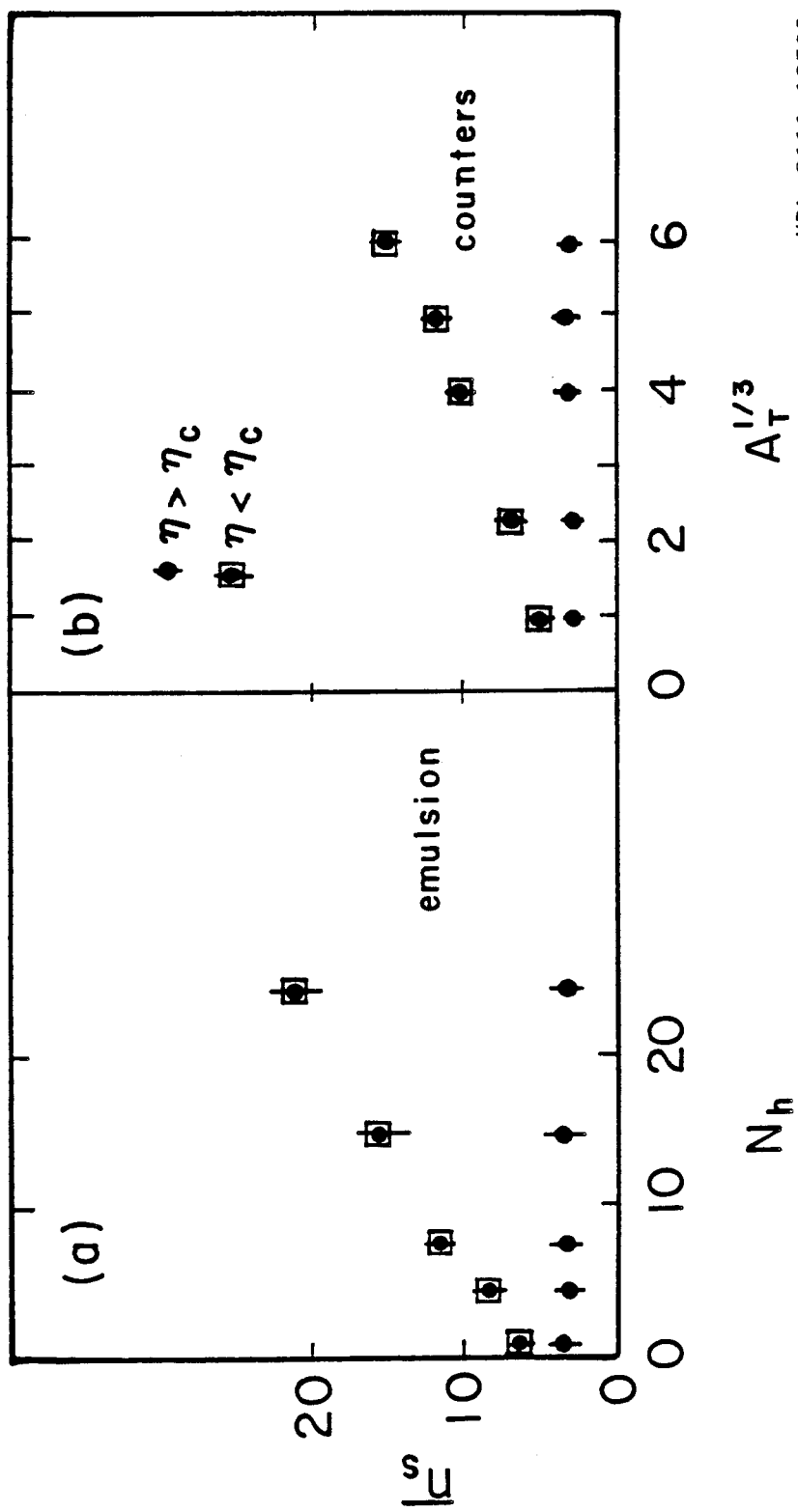
XBL 8112-12916

Fig. 57



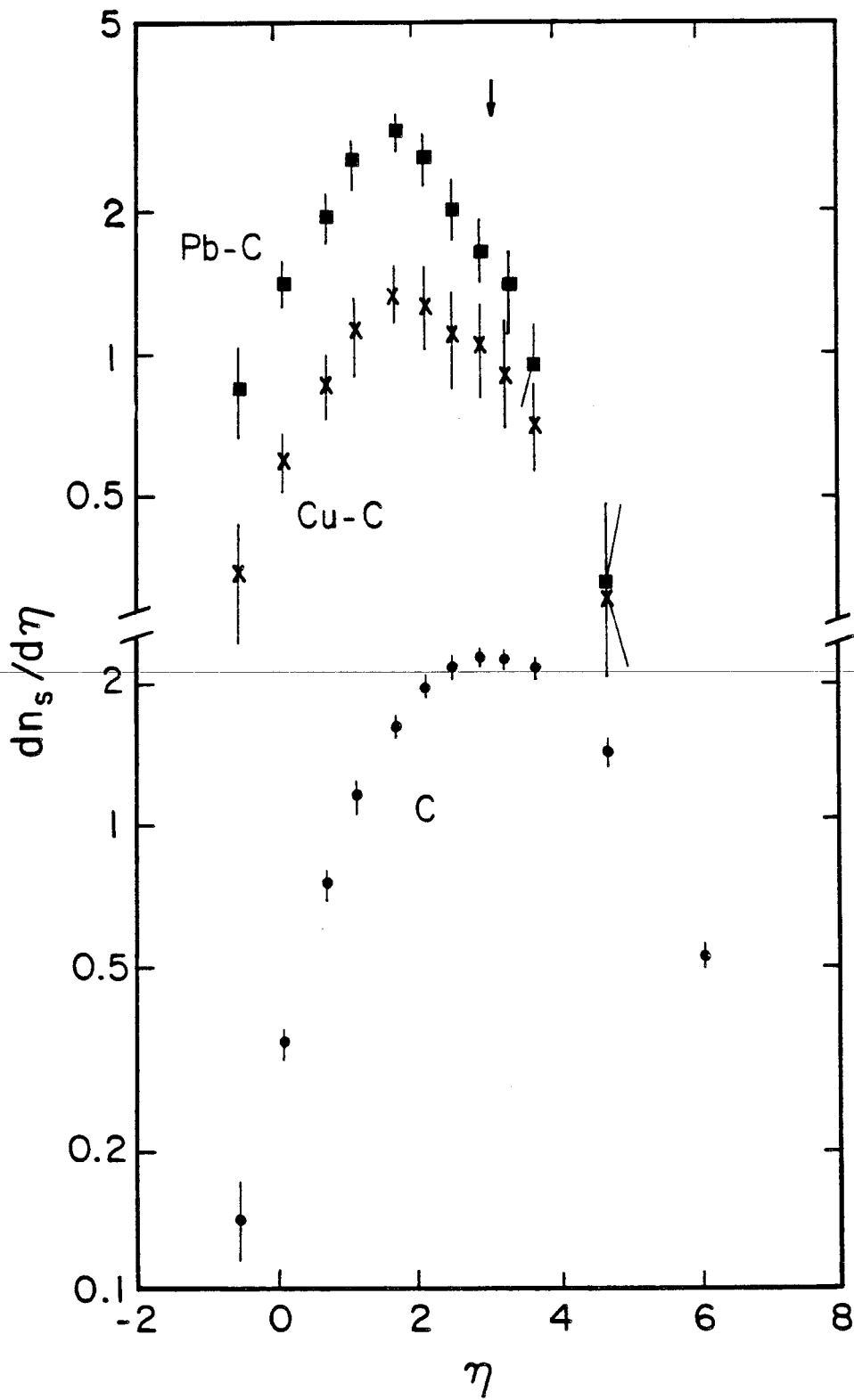
XBL 8111-12504

Fig. 58



XBL 8111-12502

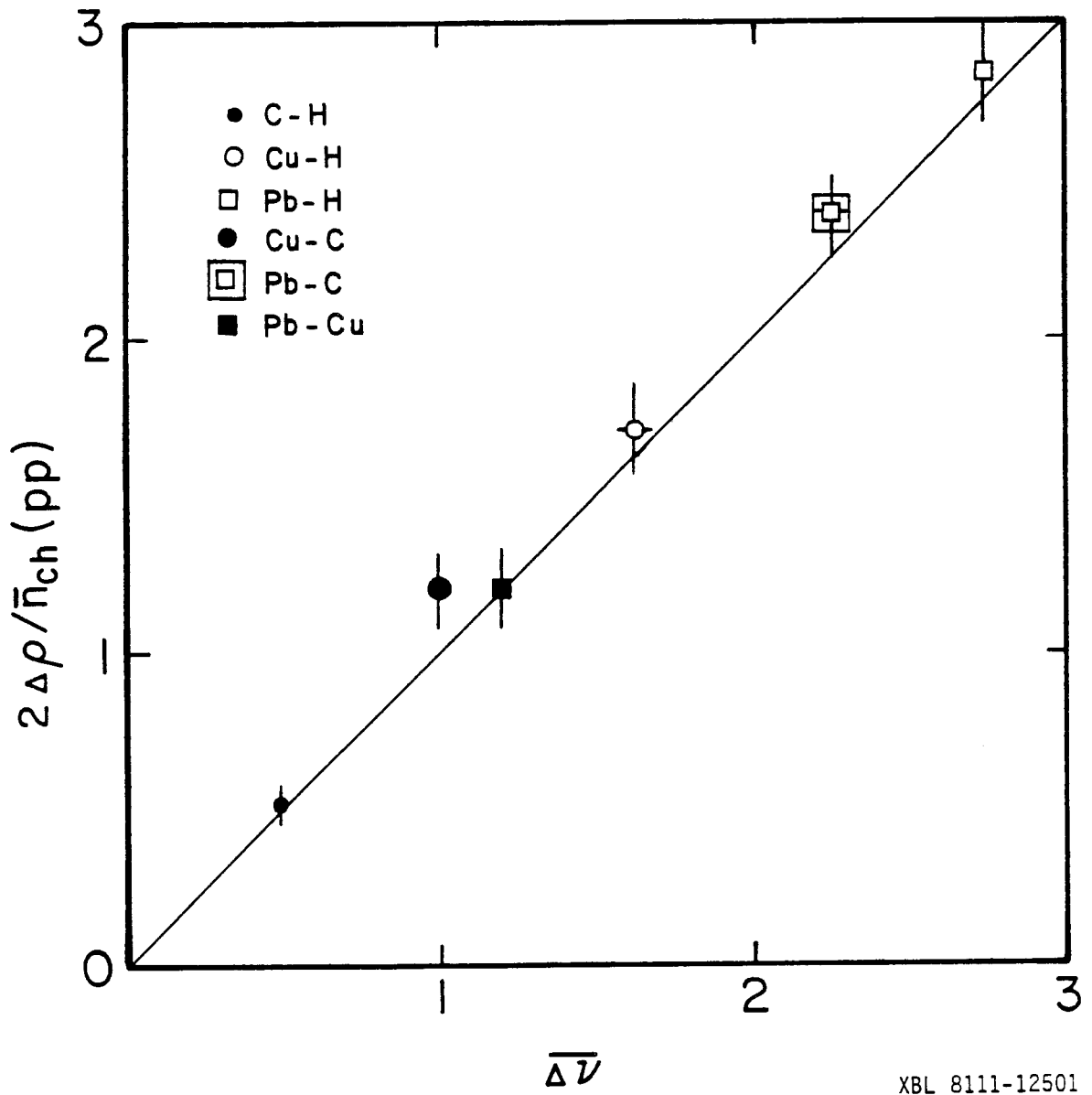
Fig. 59



XBL 8112-12761

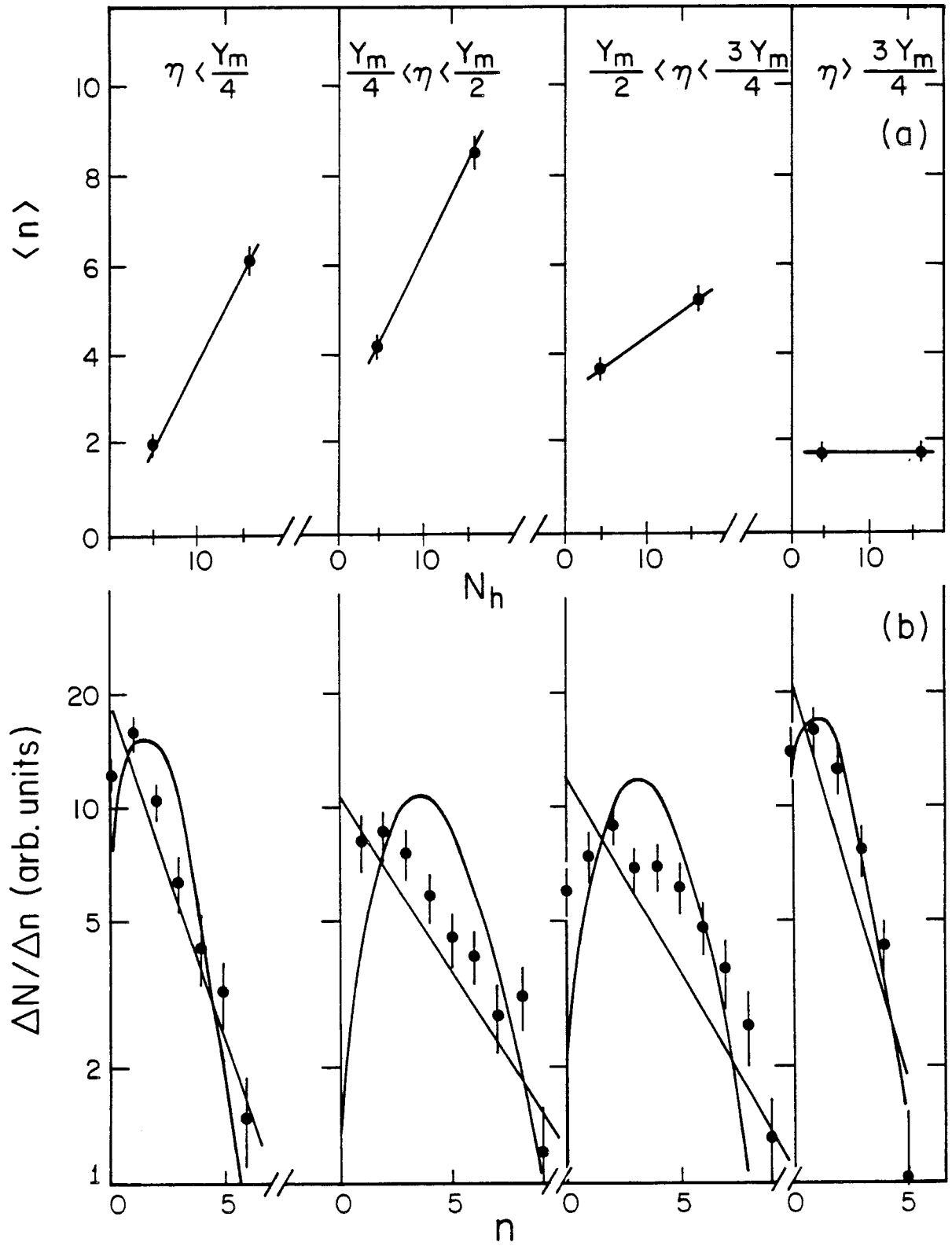
Fig. 60





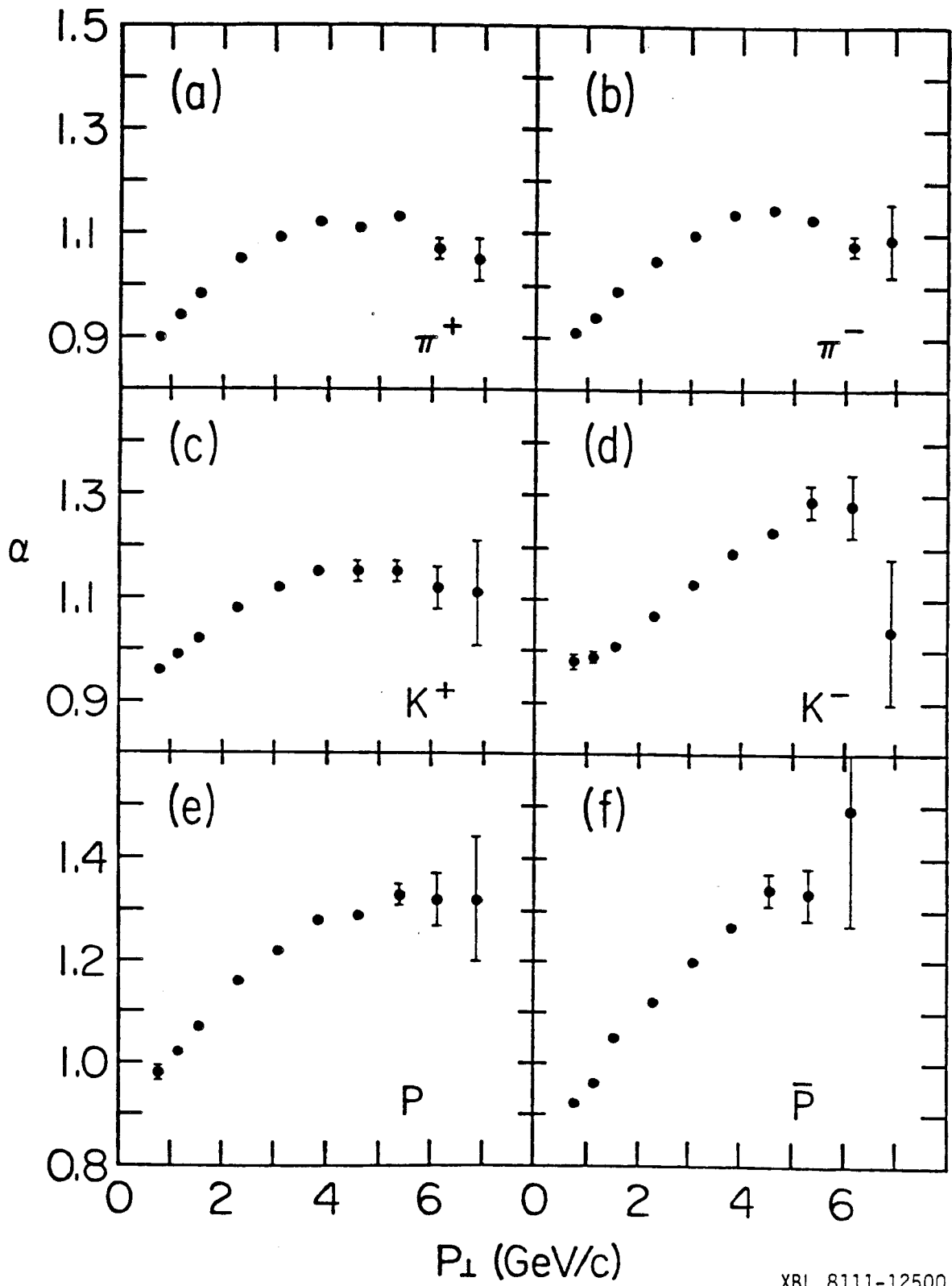
XBL 8111-12501

Fig. 61



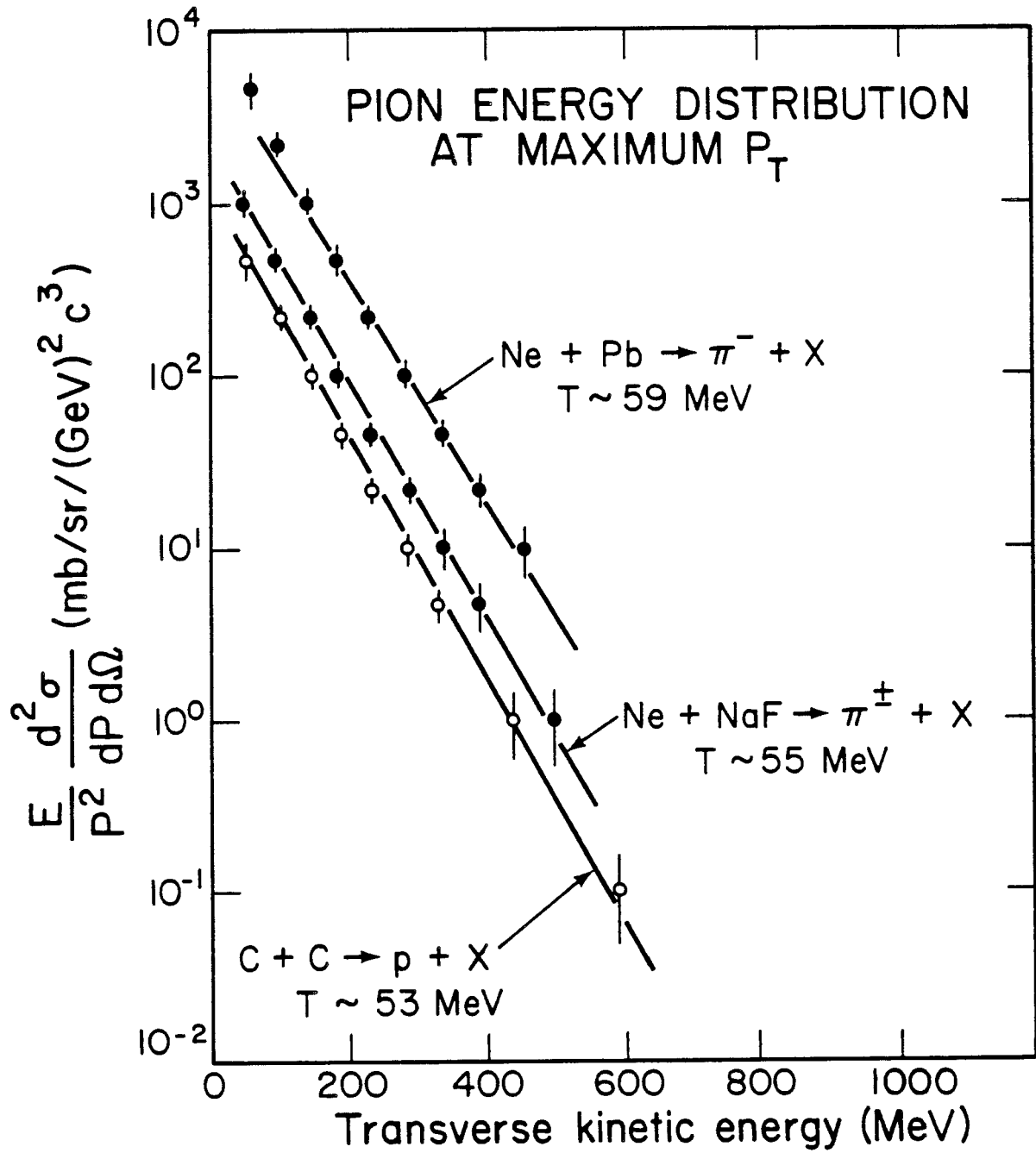
XBL816-936

Fig. 62



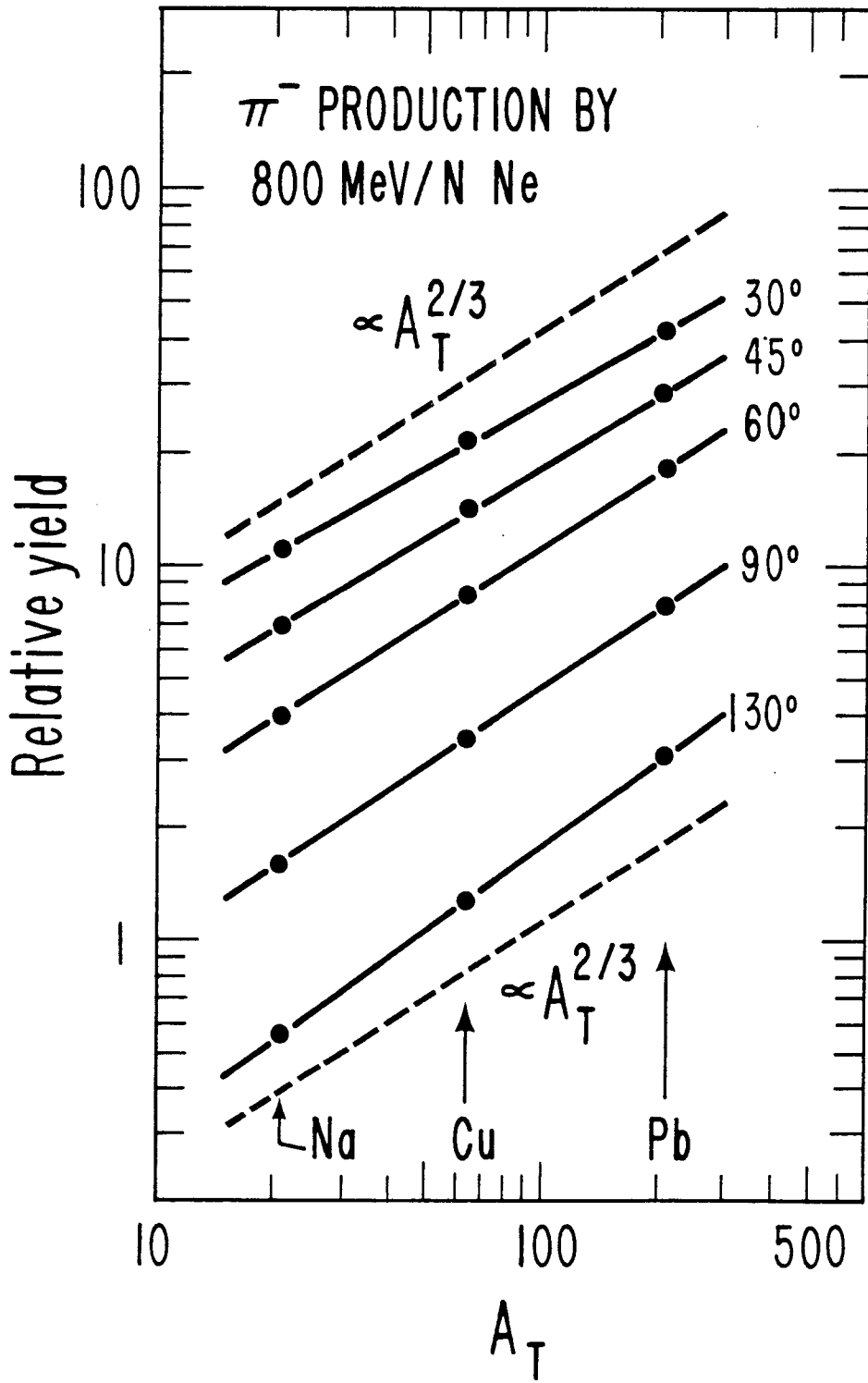
XBL 8111-12500

Fig. 63



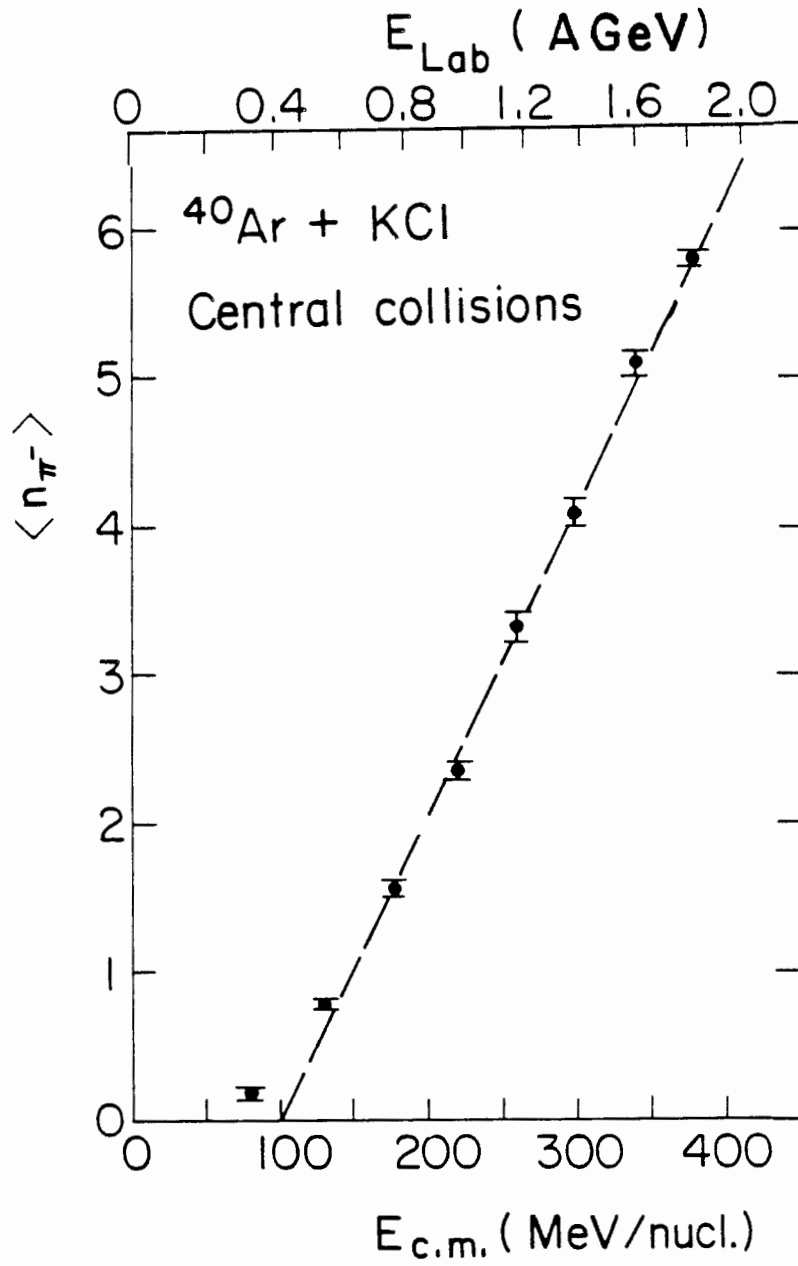
XBL 779-2017

Fig. 64



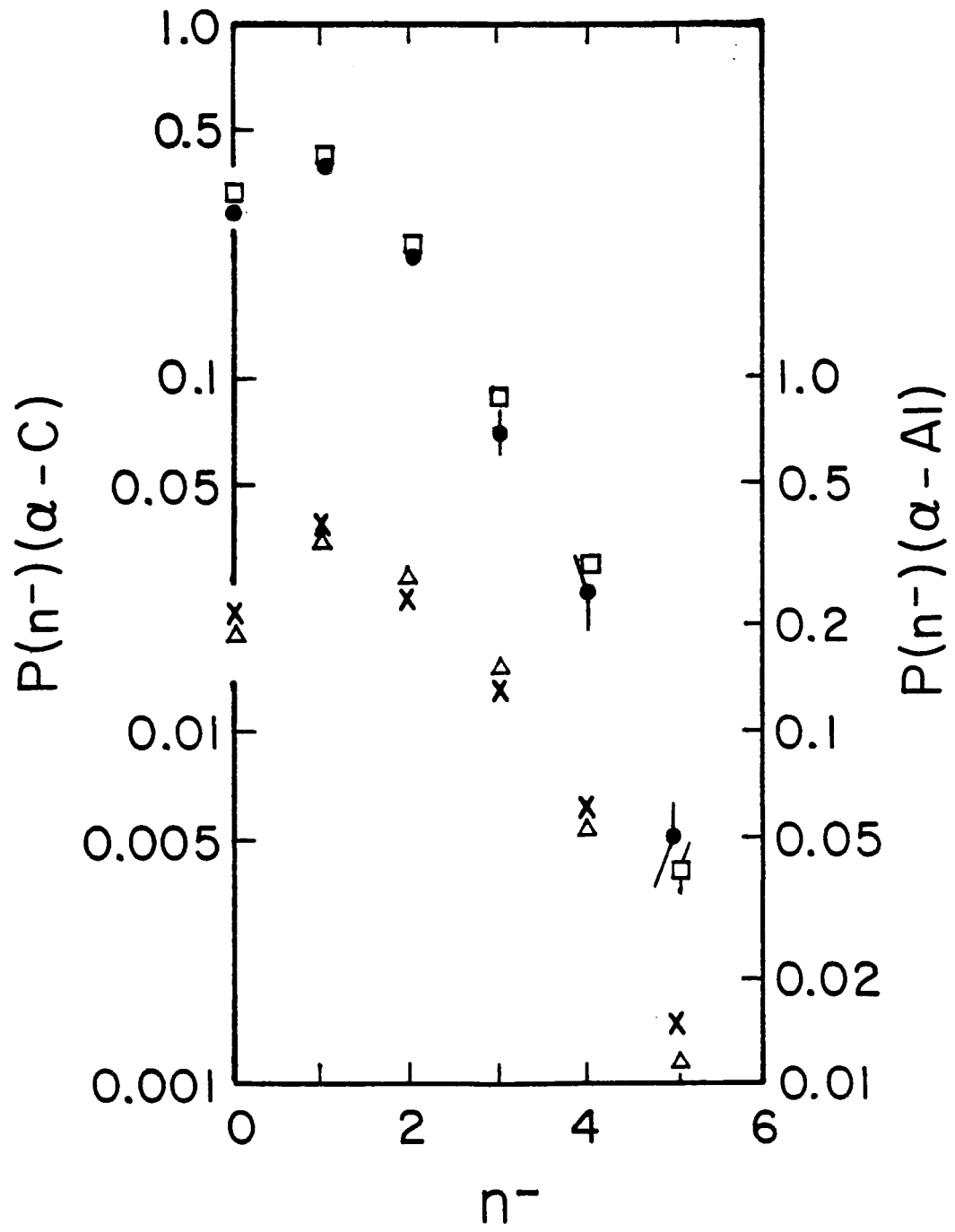
XBL779-1894

Fig. 65



XBL 804 - 701

Fig. 66



XBL 8112-12917

Fig. 67

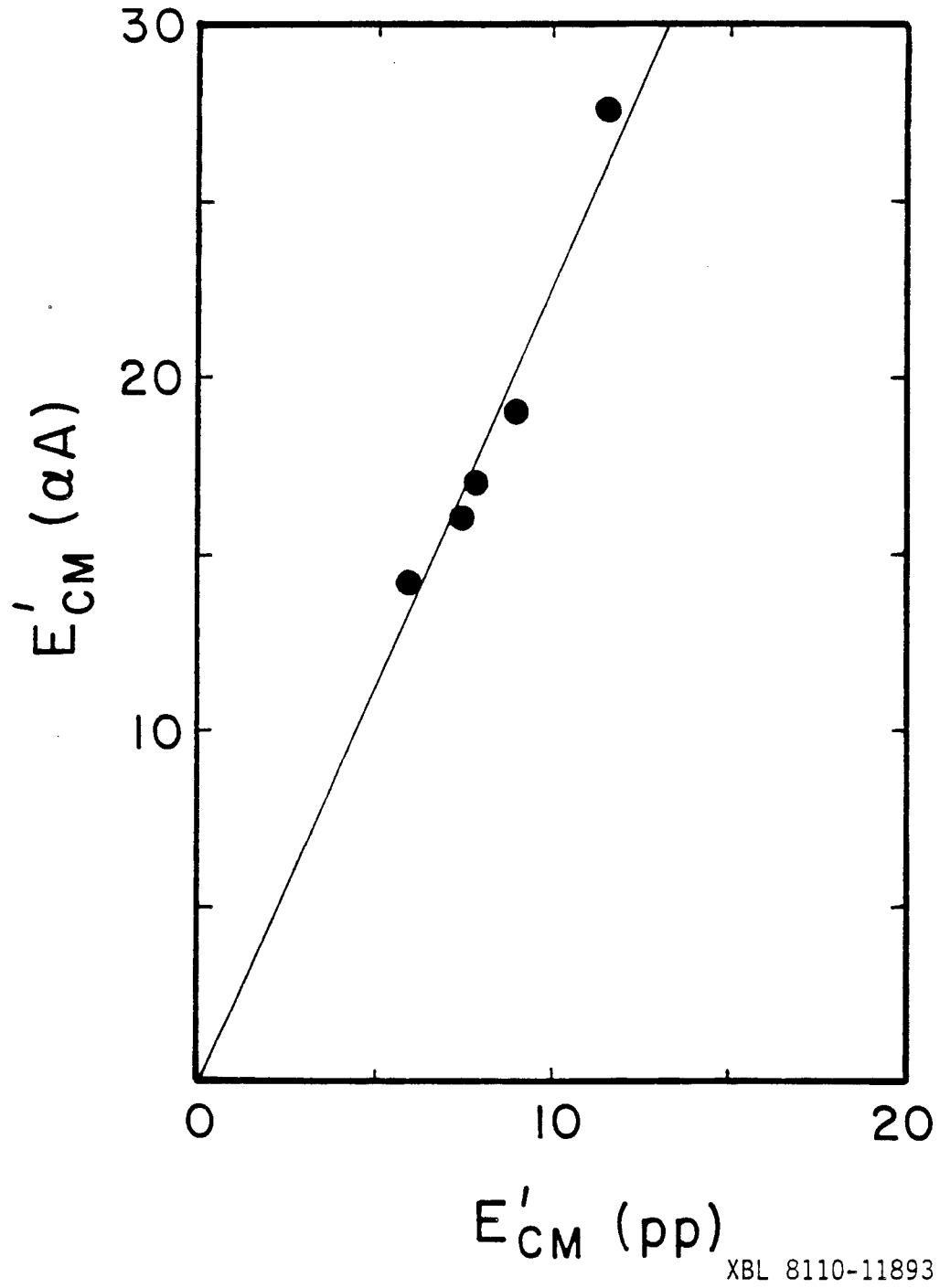


Fig. 68



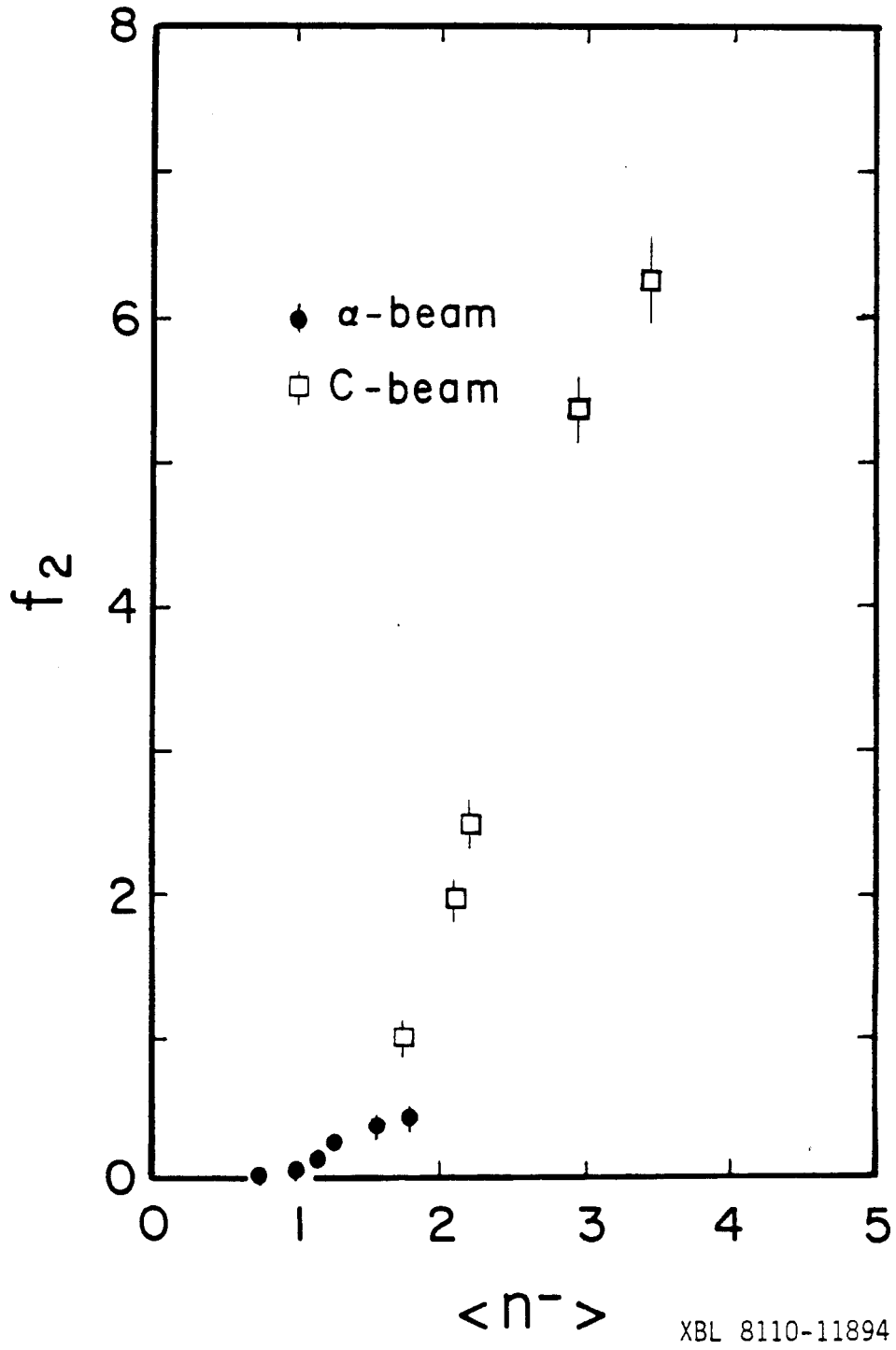
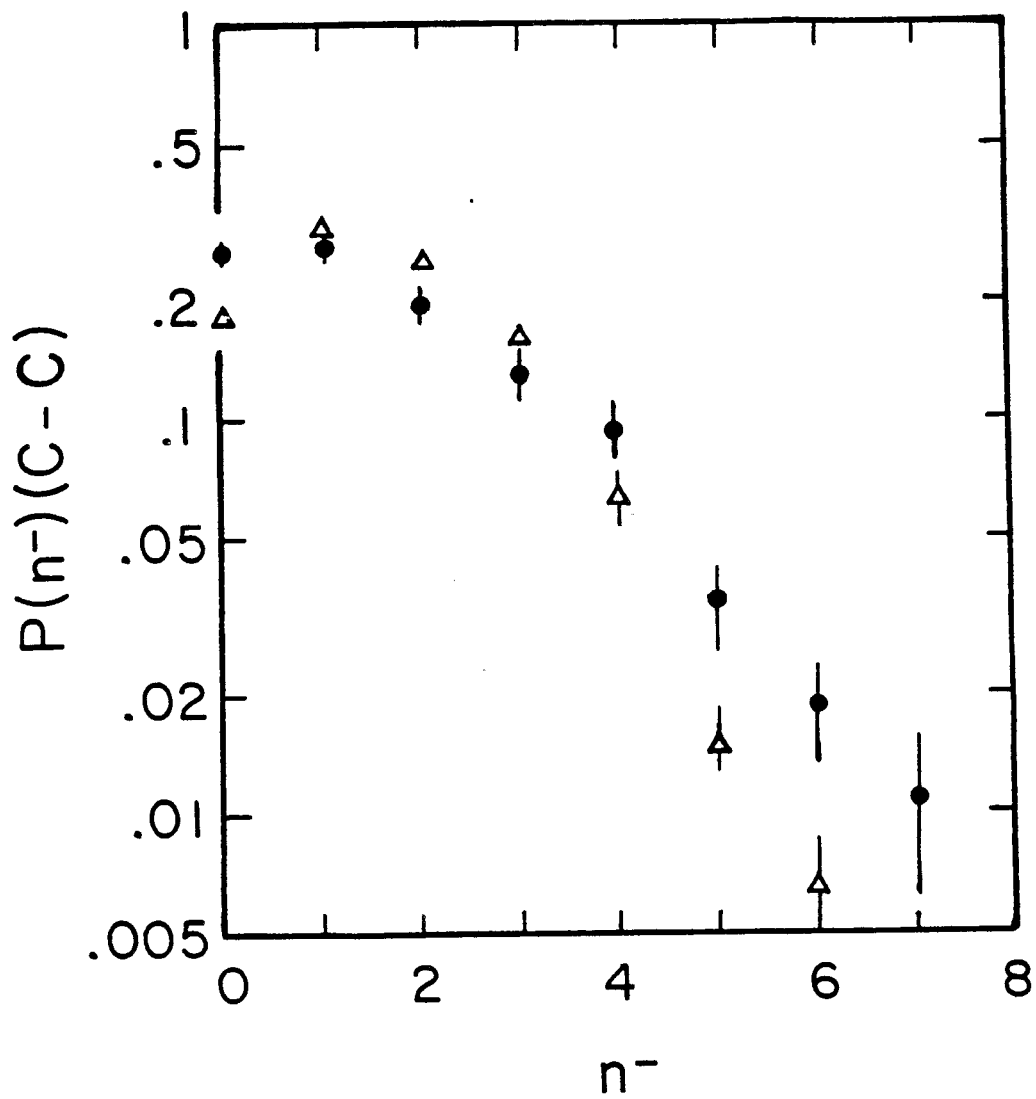


Fig. 69



XBL 8112-12918

Fig. 70

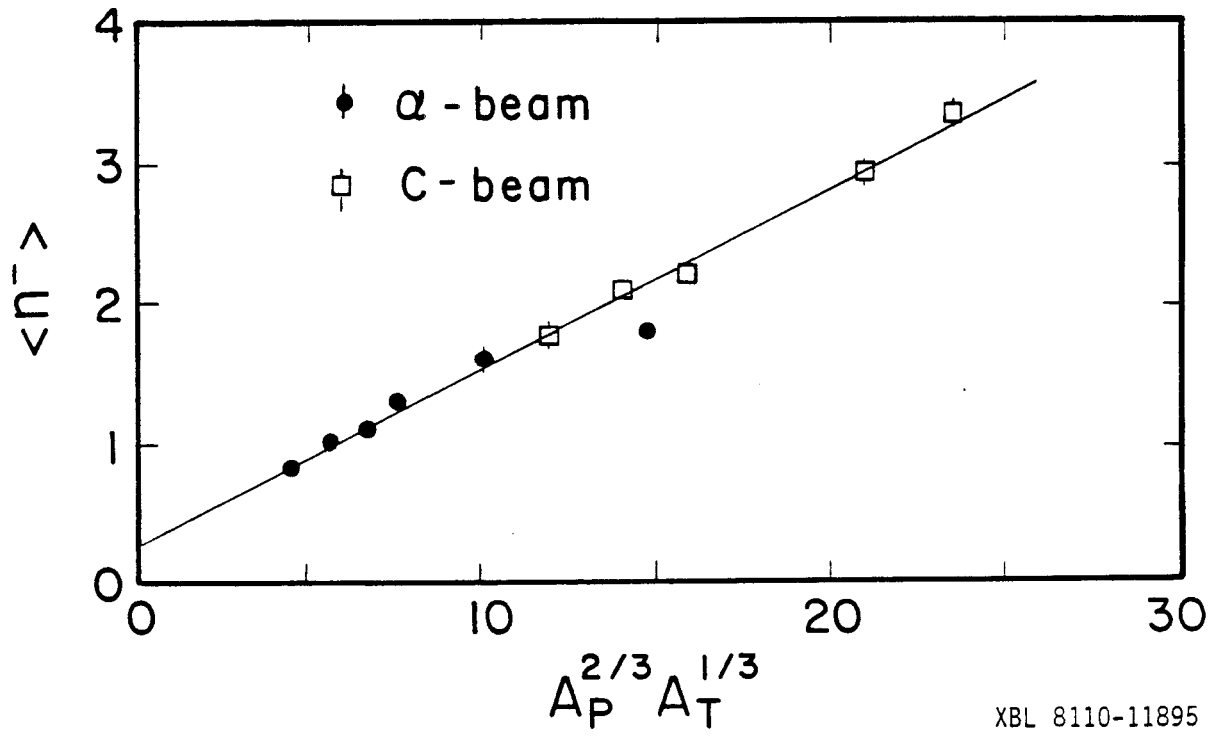


Fig. 71

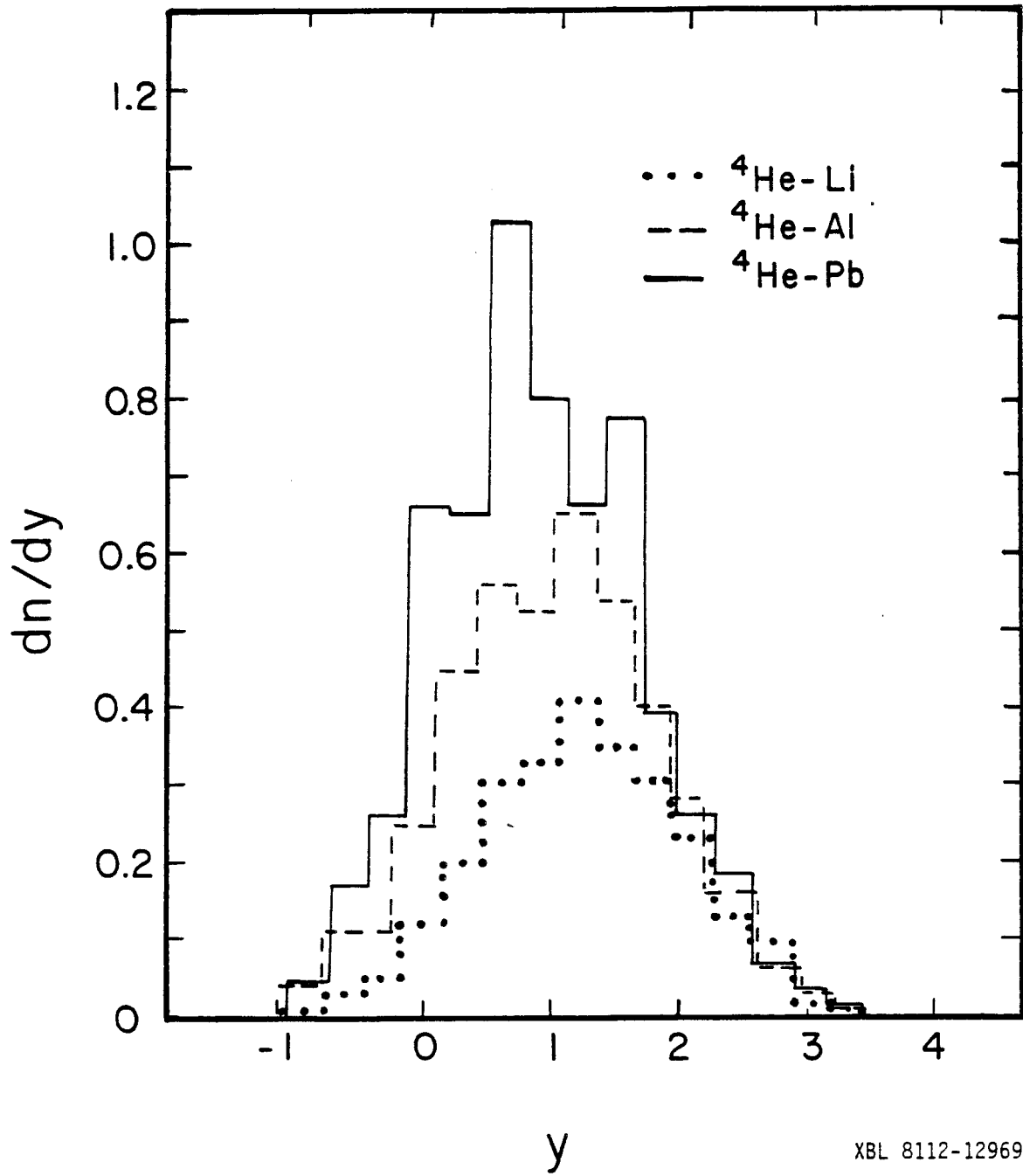
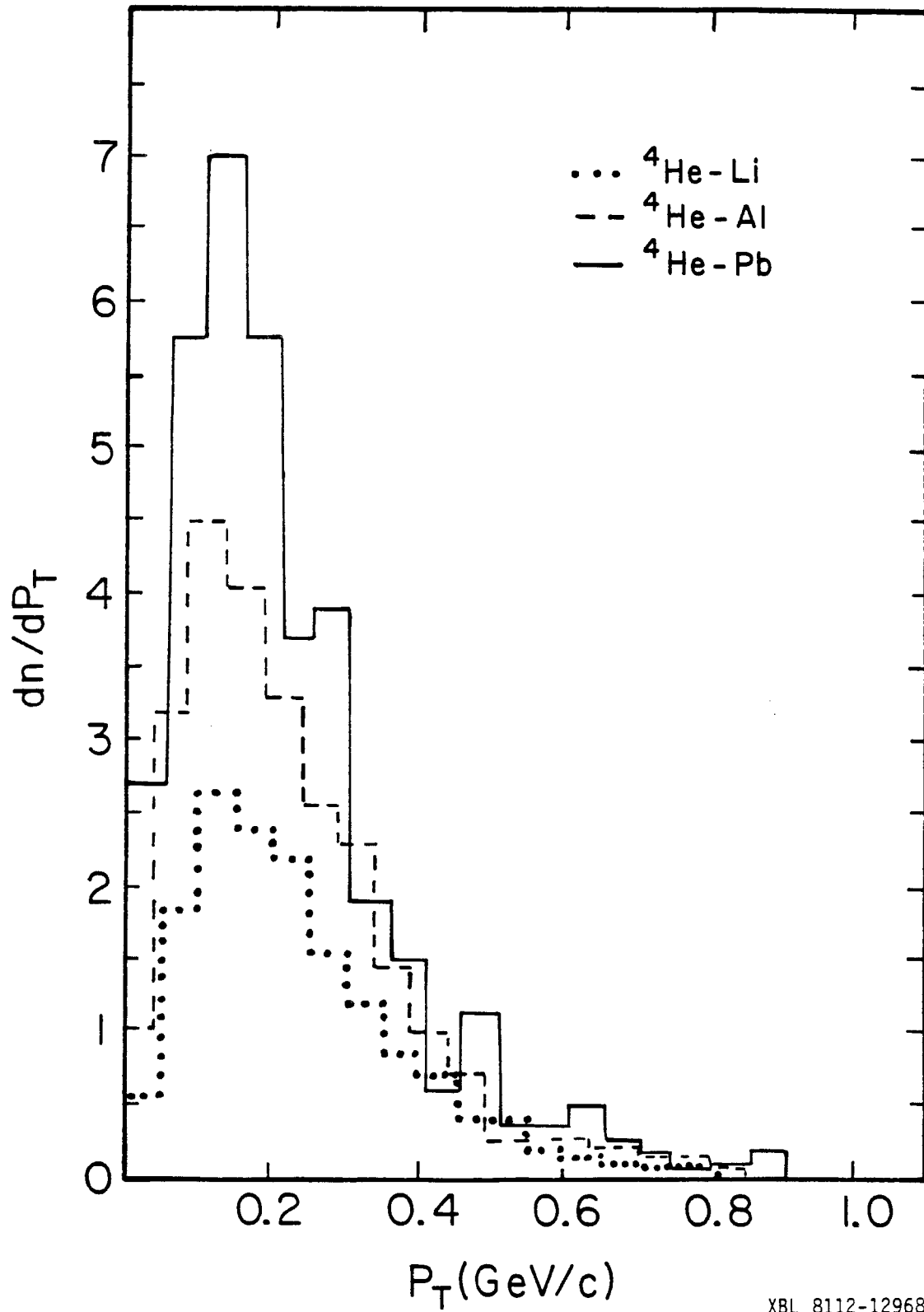
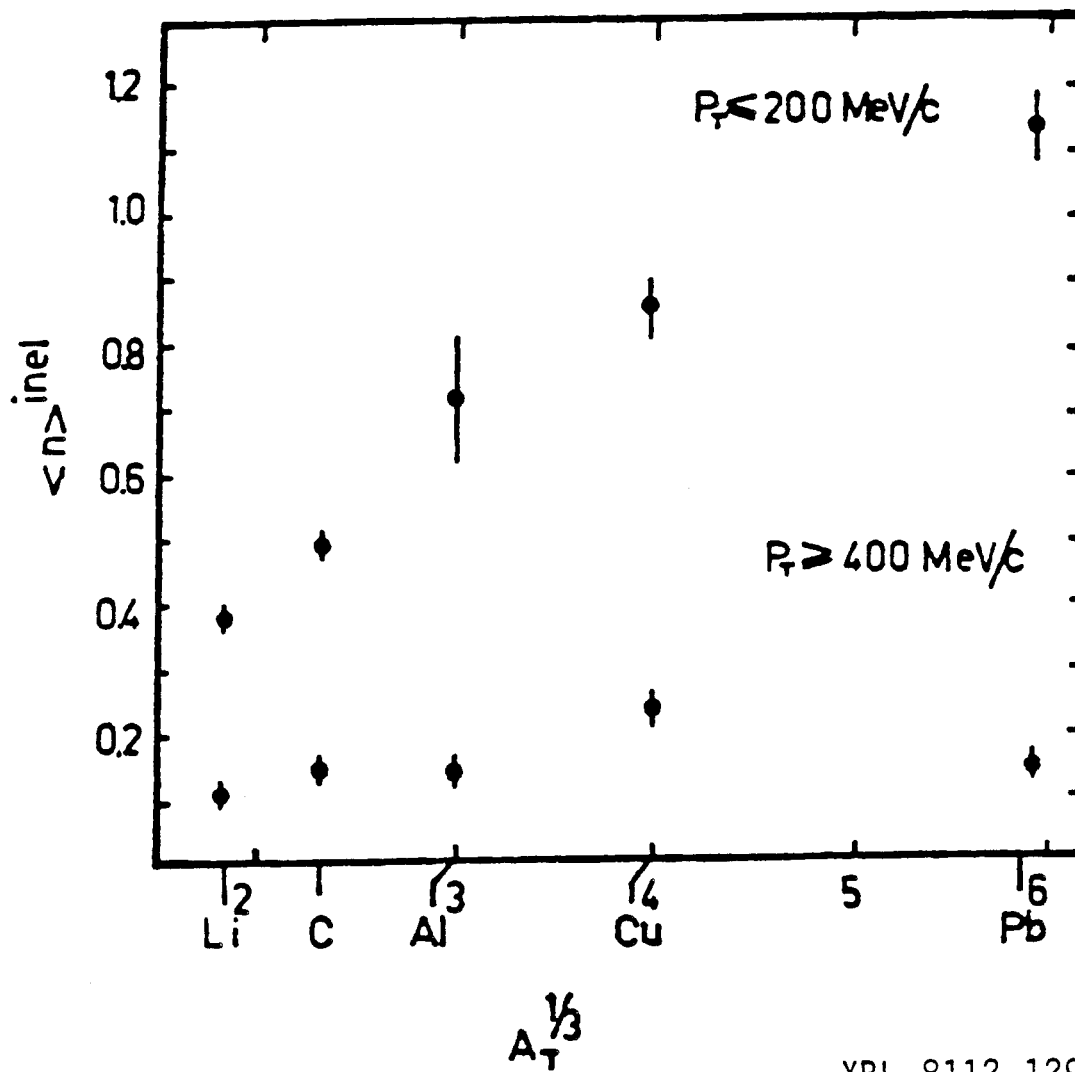


Fig. 72



XBL 8112-12968

Fig. 73



XBL 8112-12967

Fig. 74

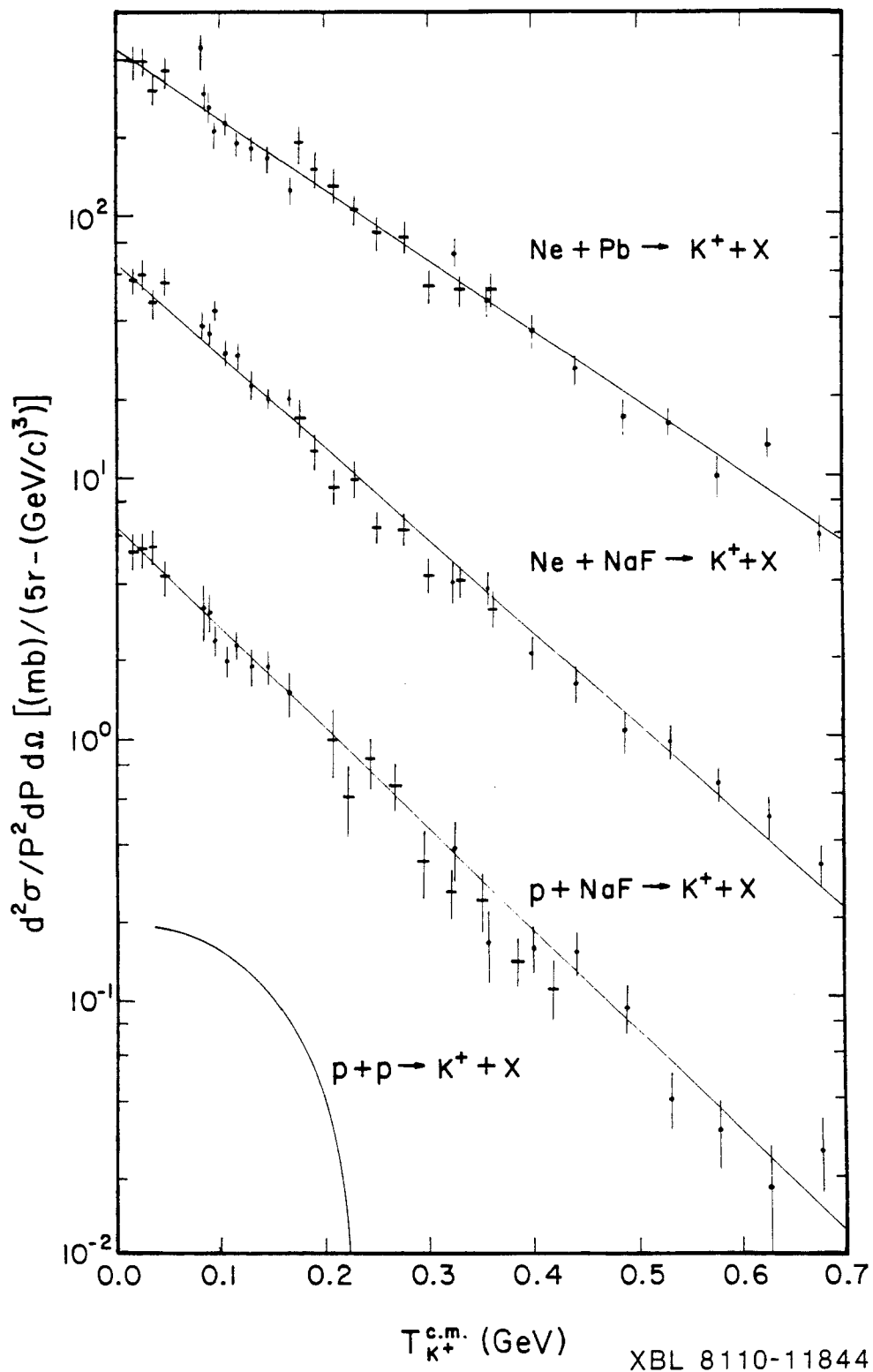
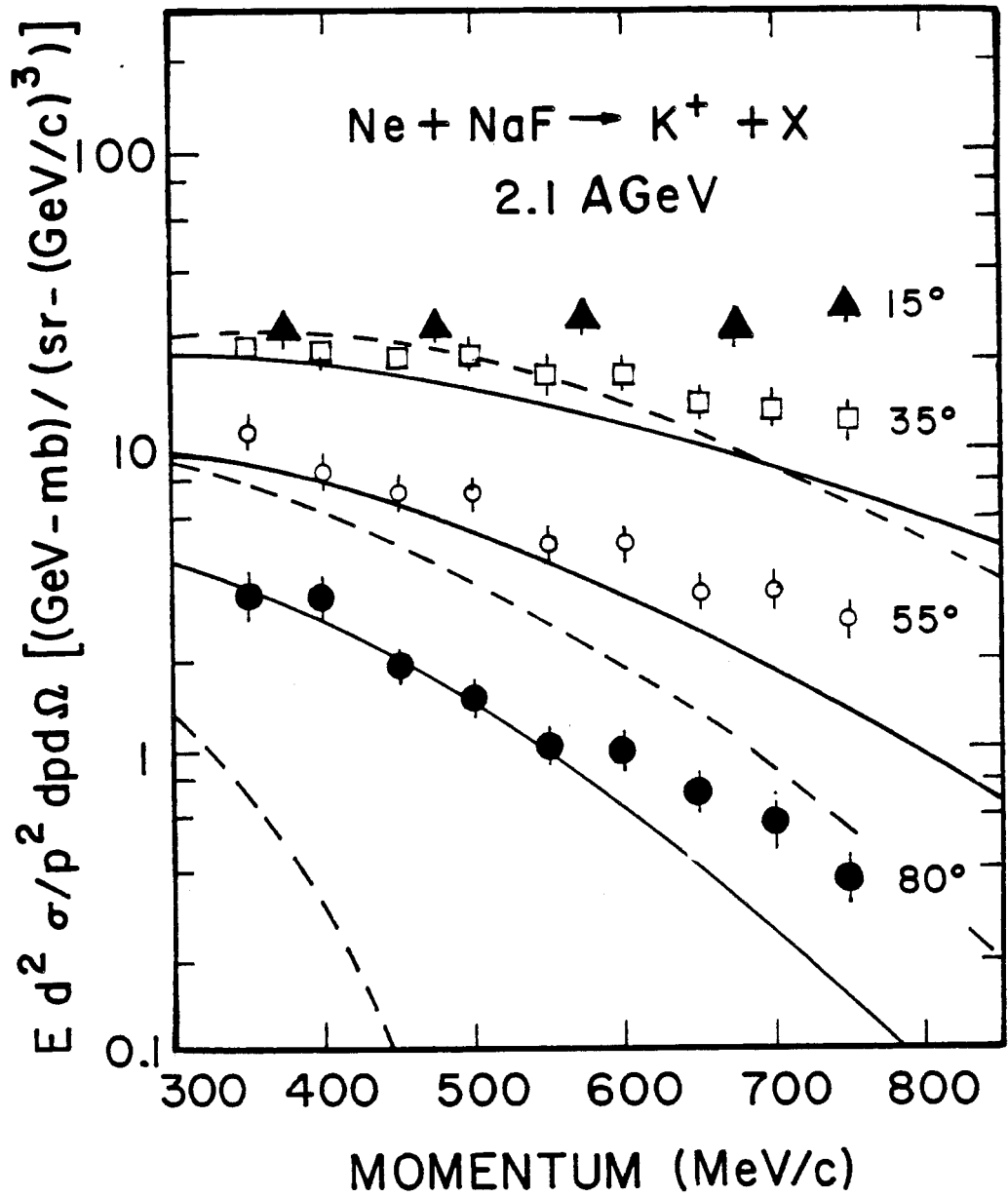


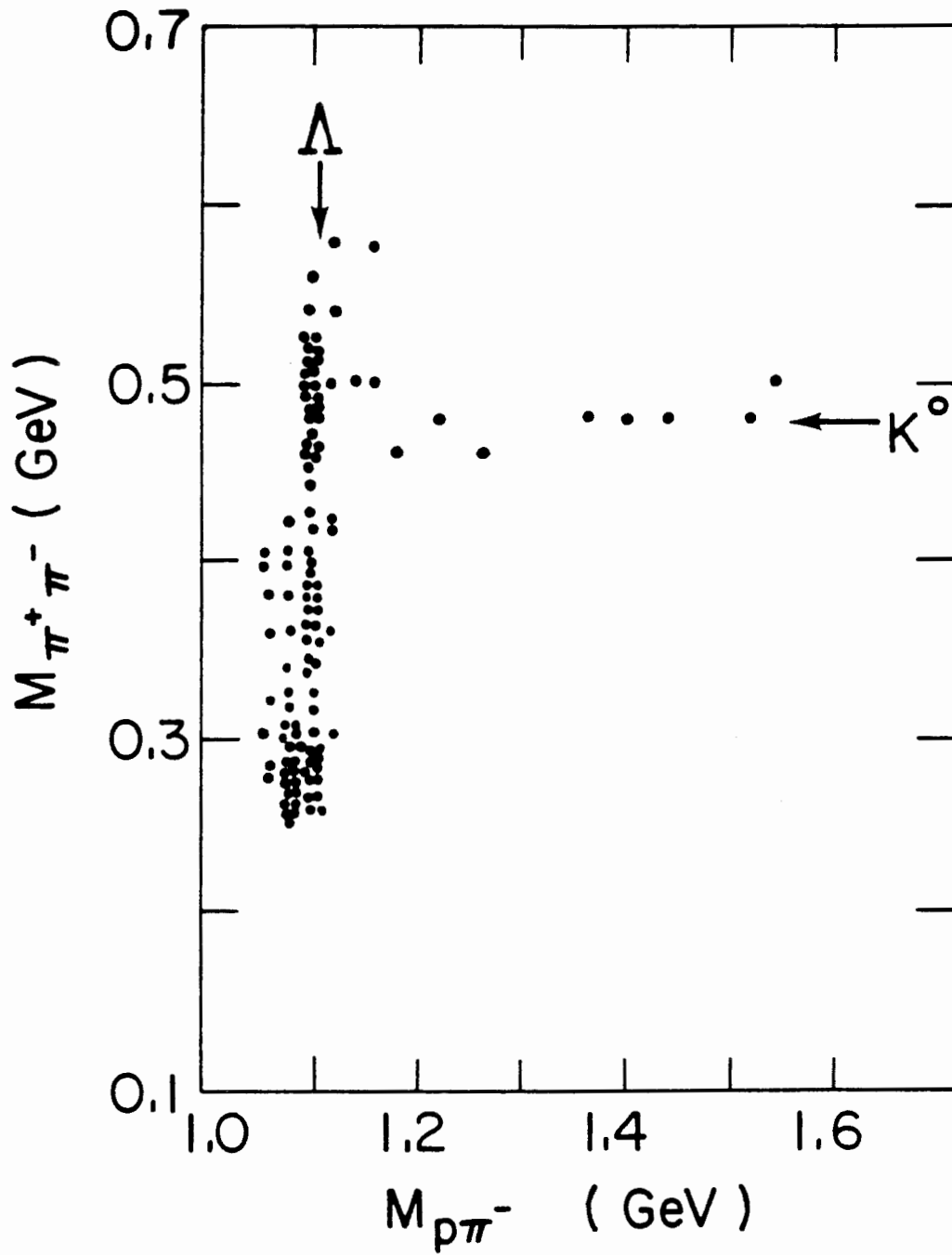
Fig. 75



XBL 8110-11843

Fig. 76

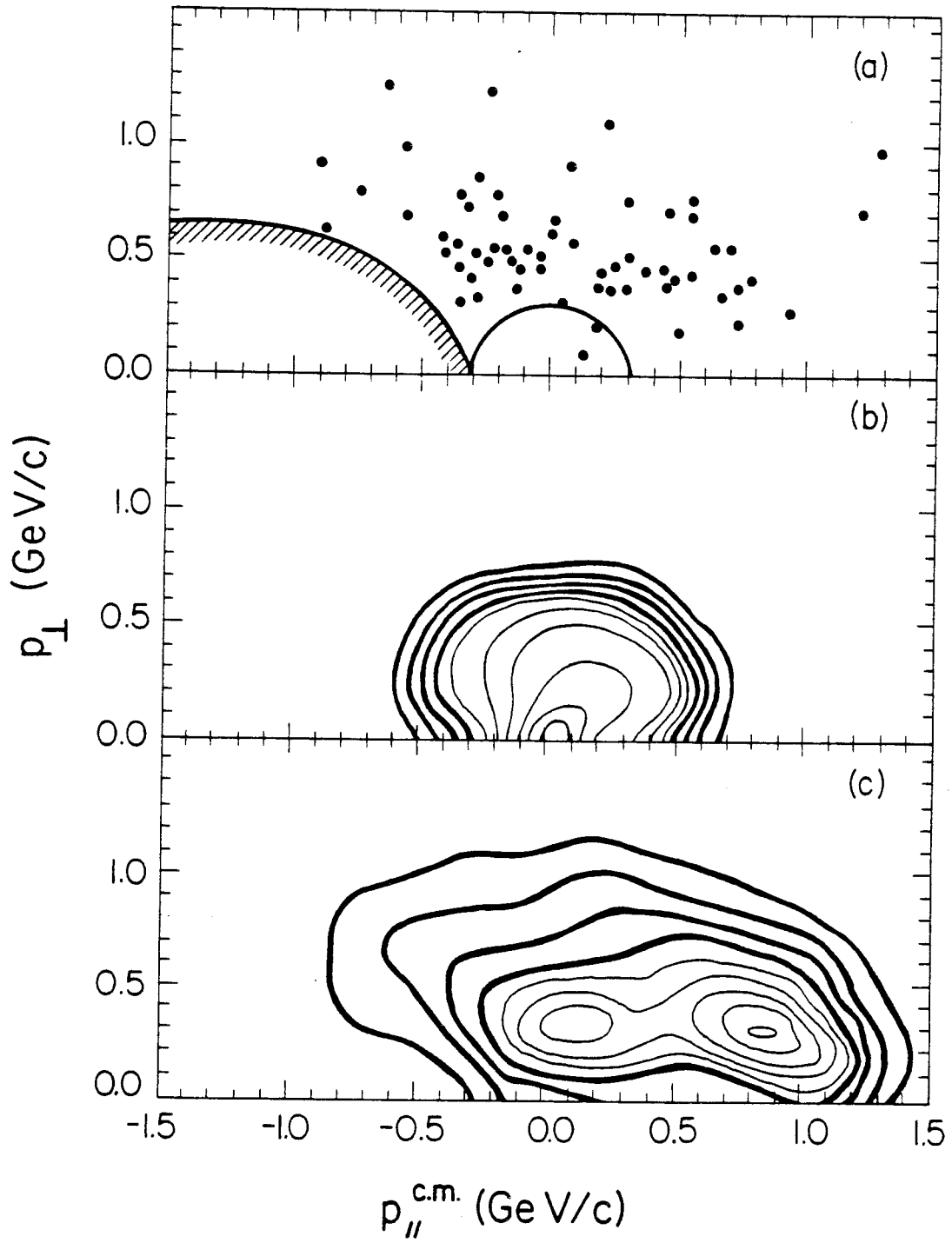




XBL 804-753

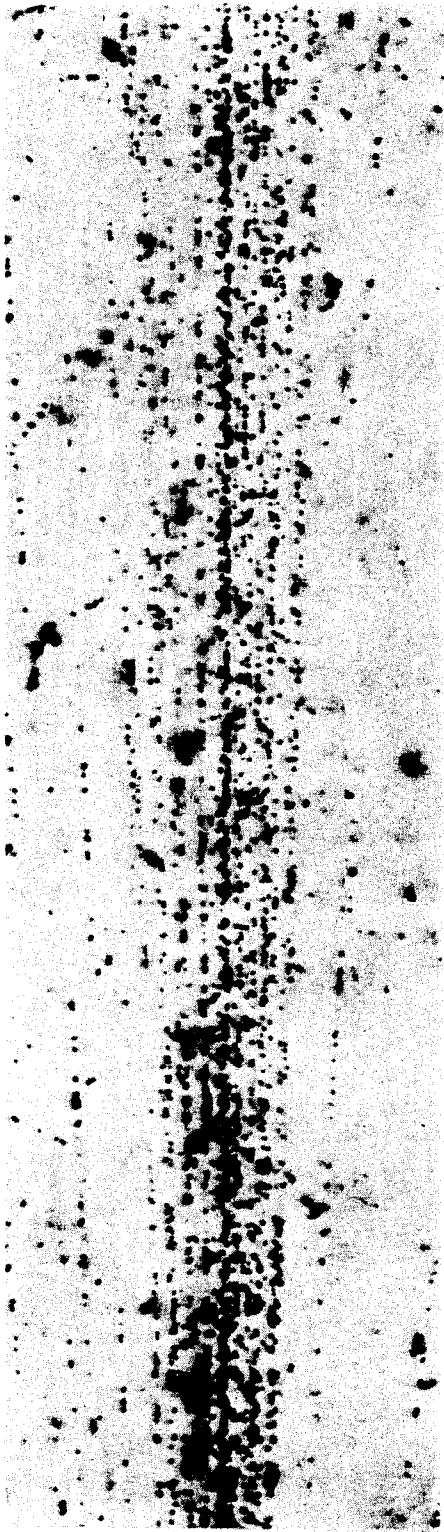
Fig. 77

$^{40}\text{Ar} + \text{KCl} \rightarrow \Lambda$       1.8 GeV/n



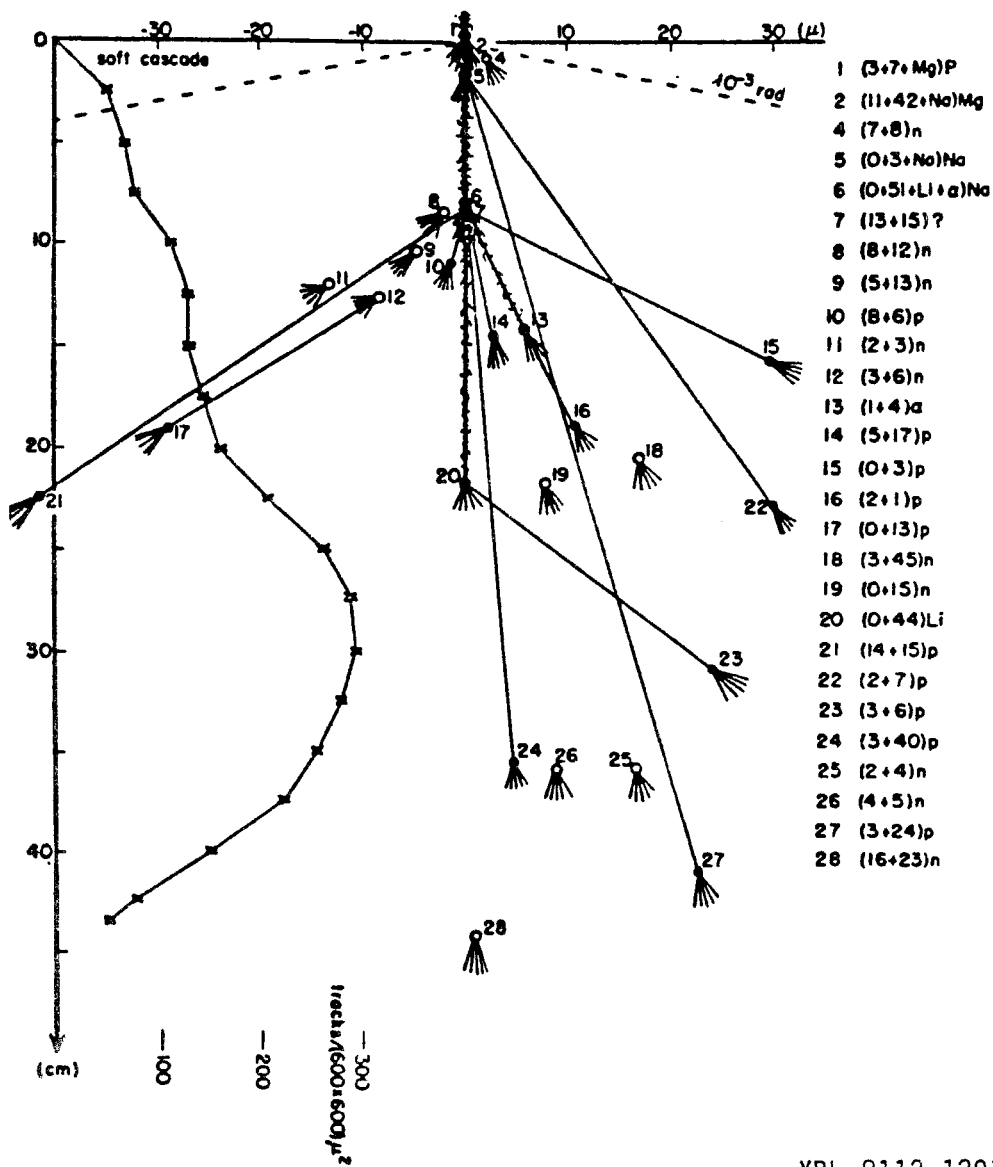
XBL 813-437

Fig. 78



XBB8112-11755

Fig. 79



XBL 8112-12913

Fig. 80

1300 GeV/NUCLEON

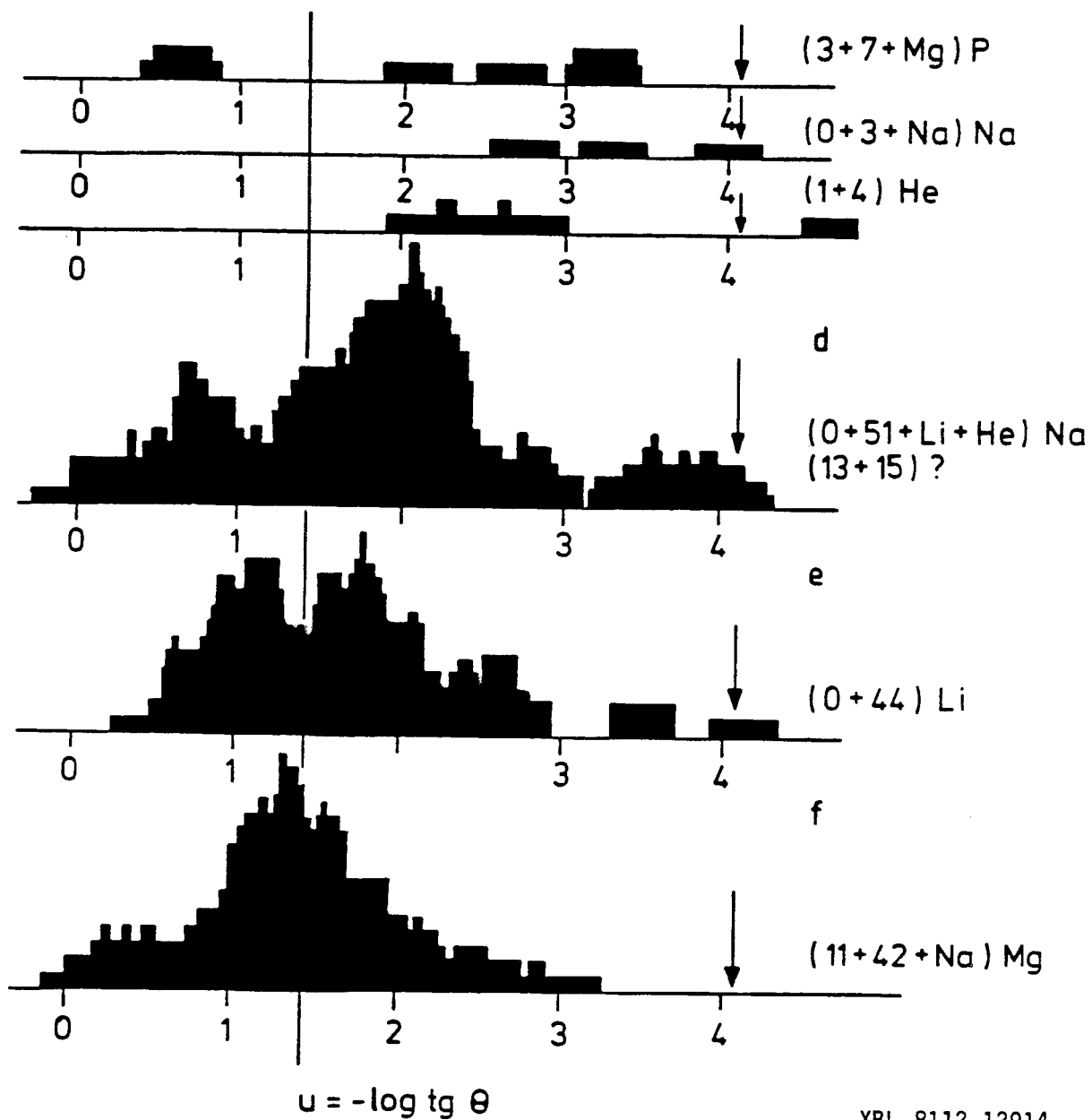


Fig. 81

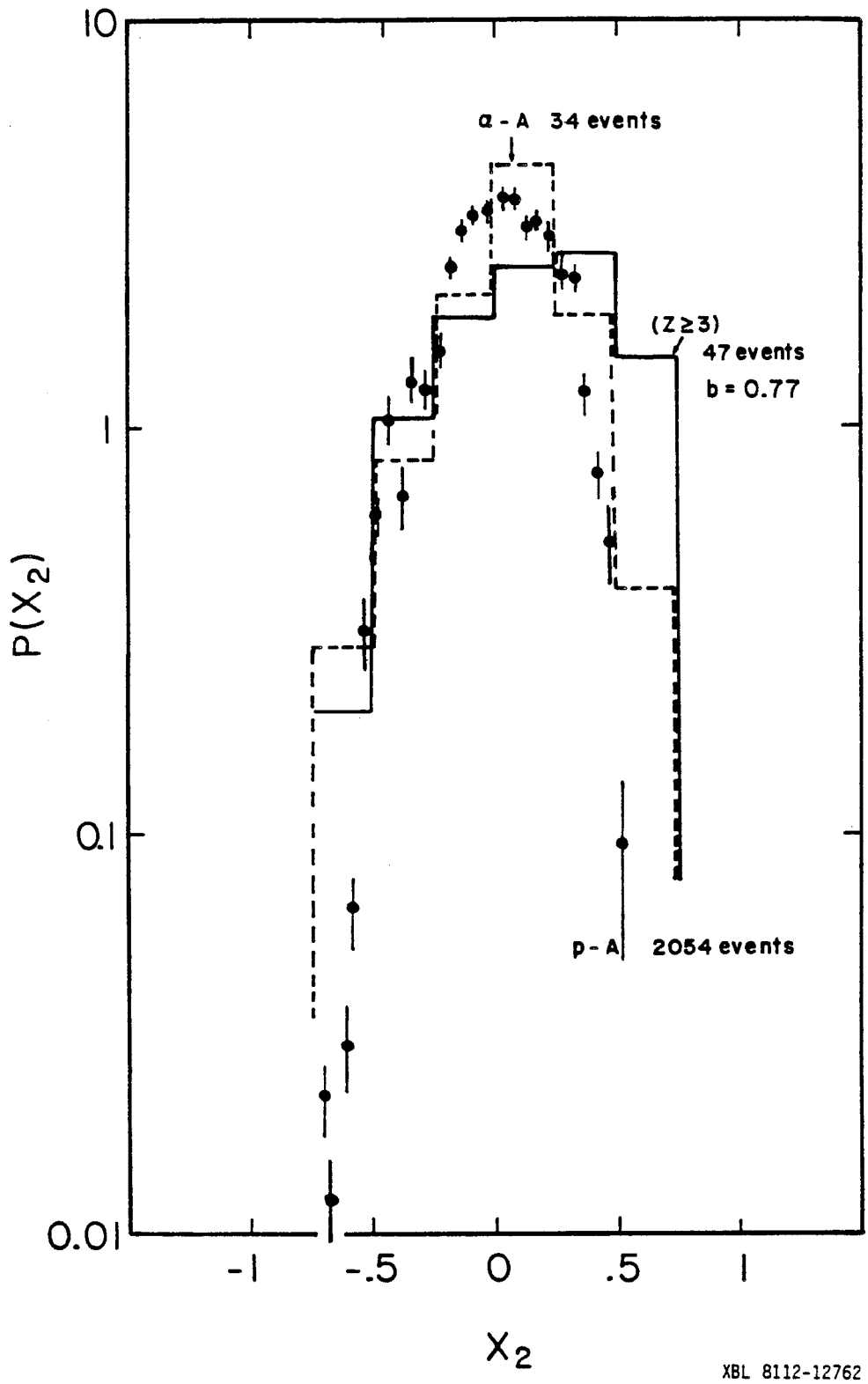
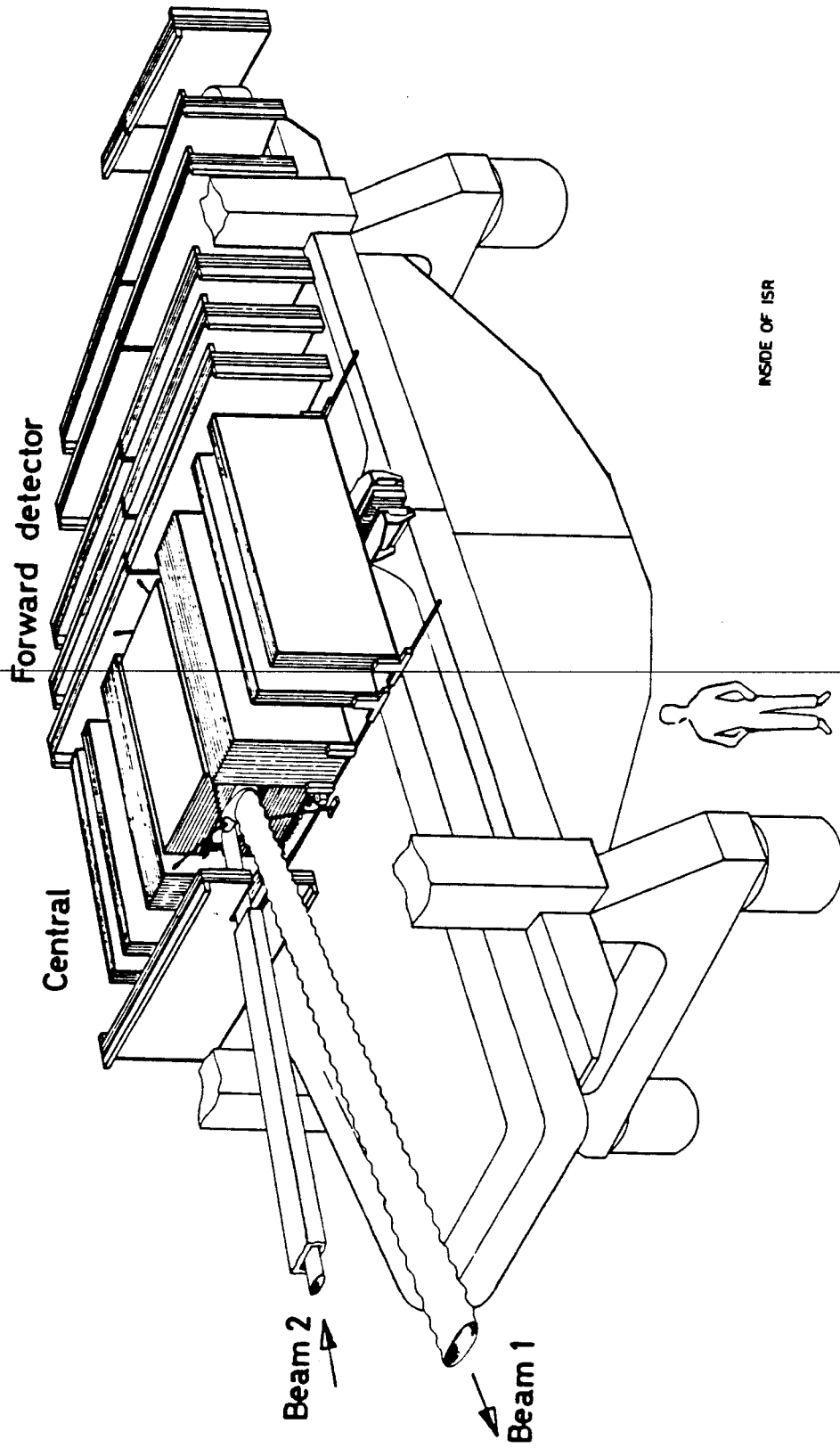


Fig. 82

XBL 8112-12762



XBL 8112-13013

Fig. 83

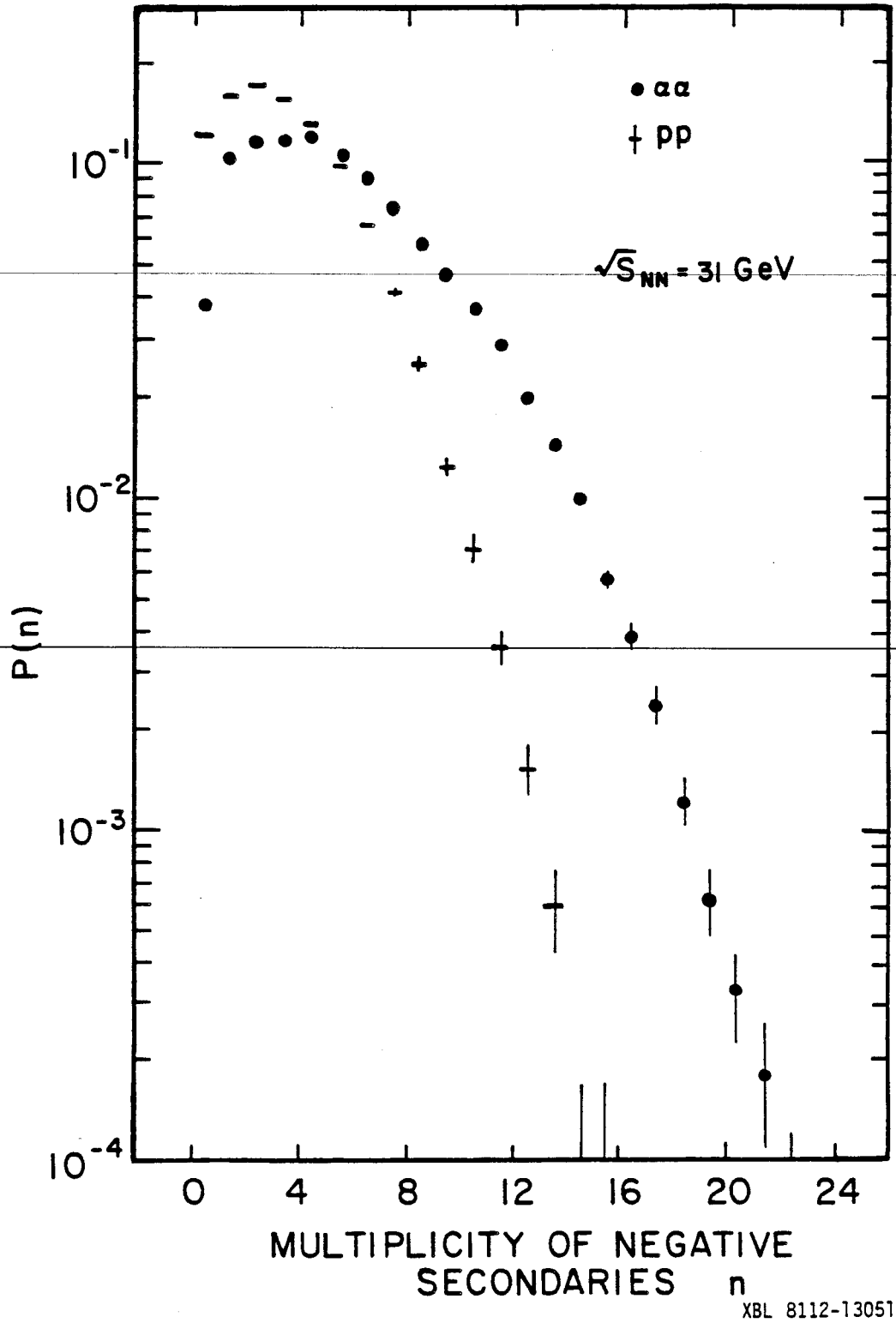
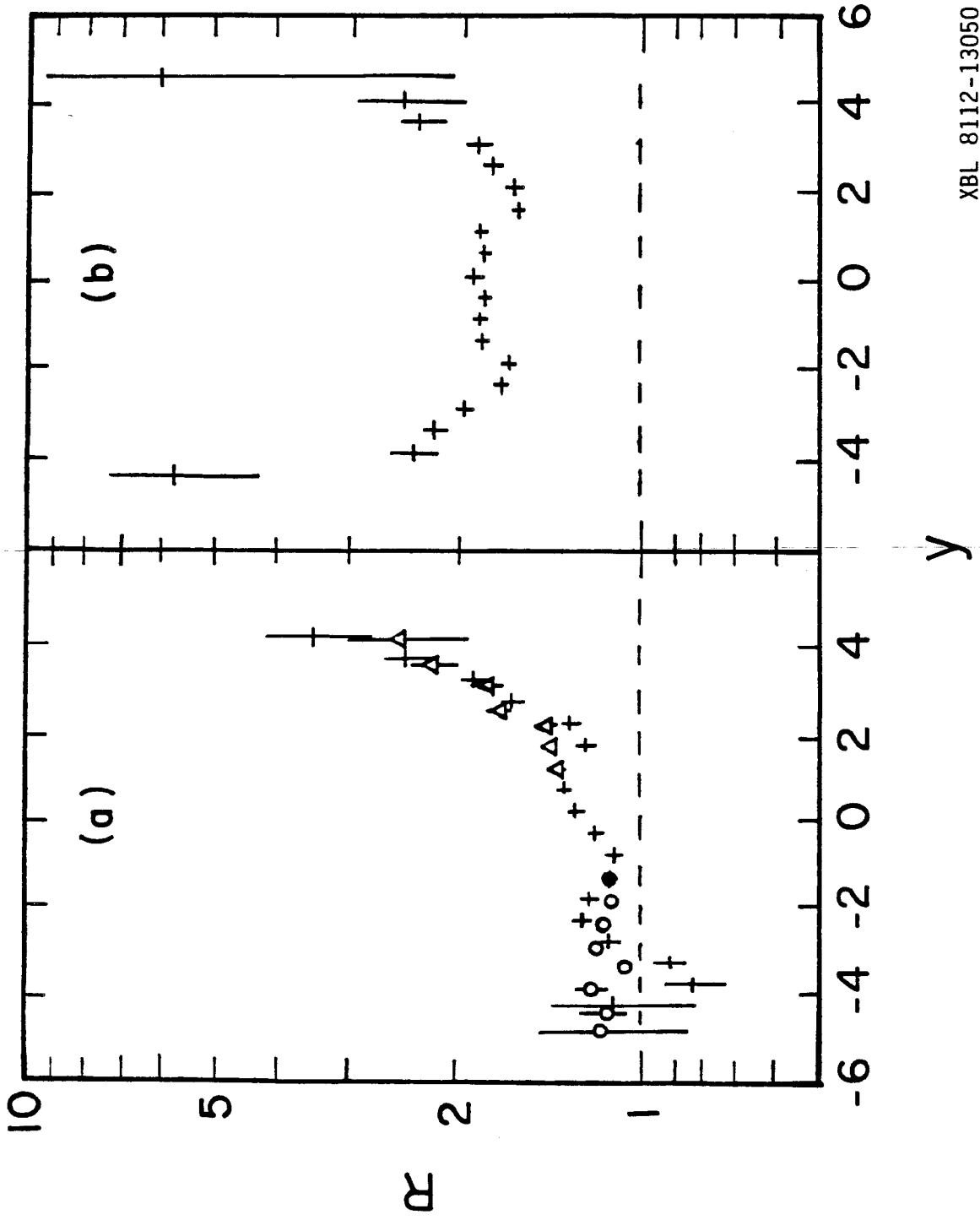


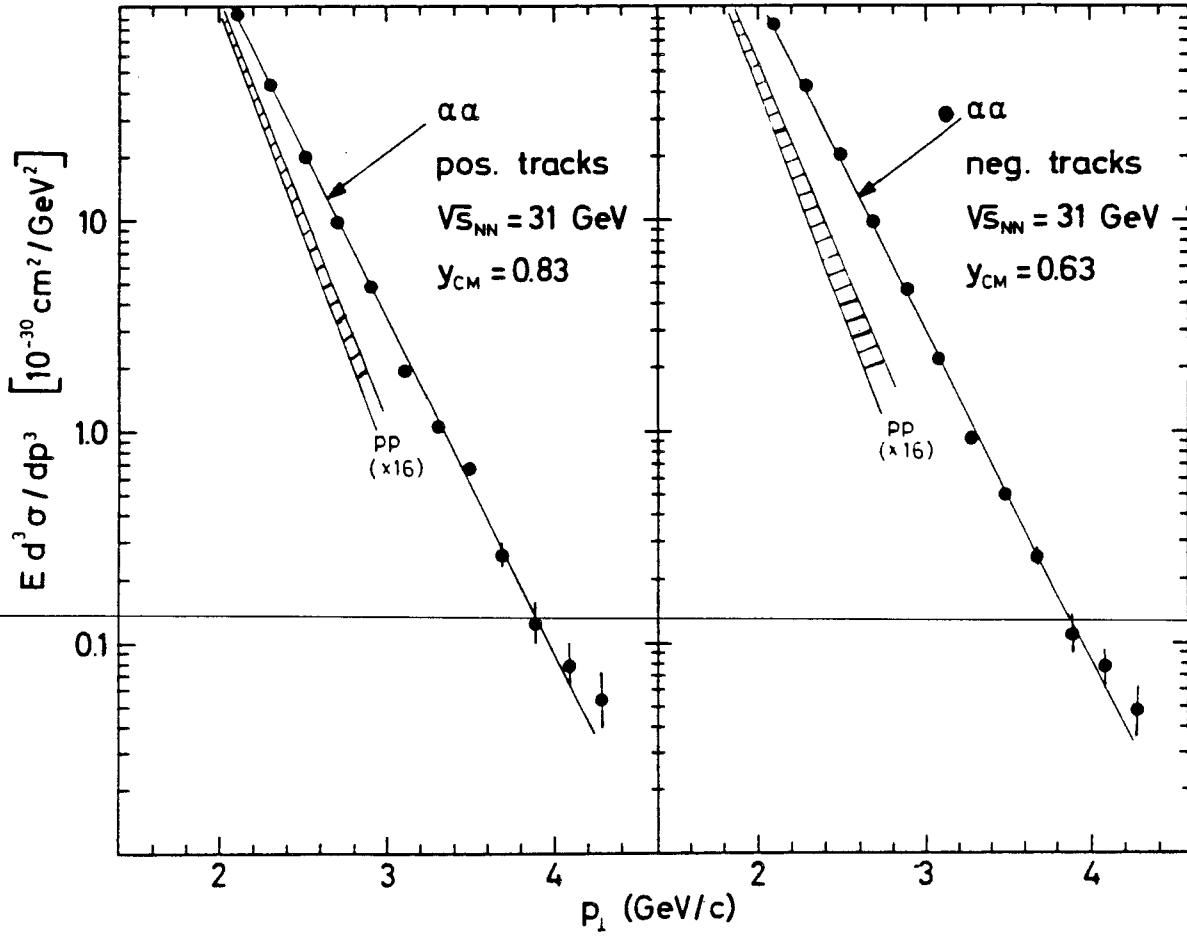
Fig. 84





XBL 8112-13050

Fig. 85



XBL 8112-13012

Fig. 86

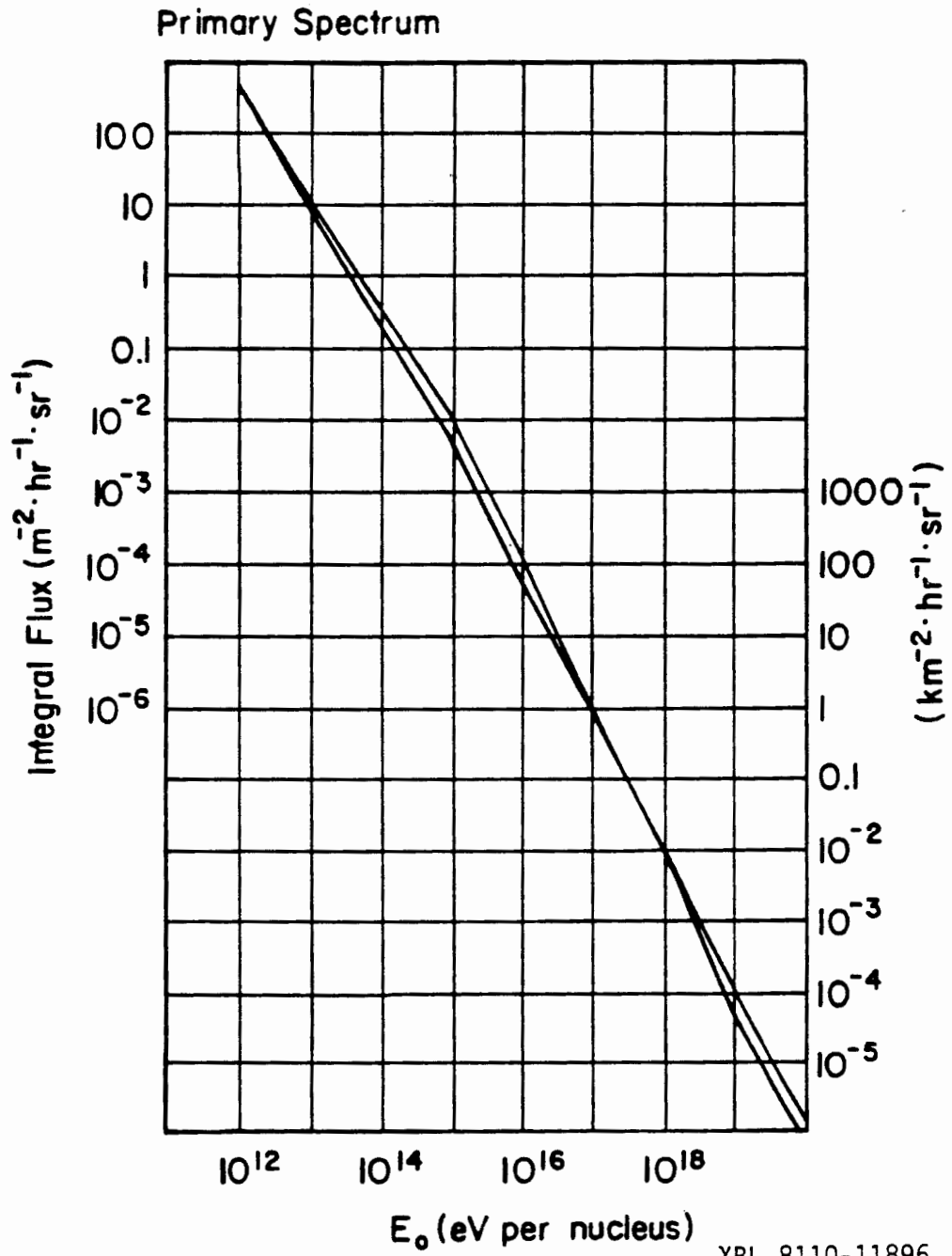


Fig. 87

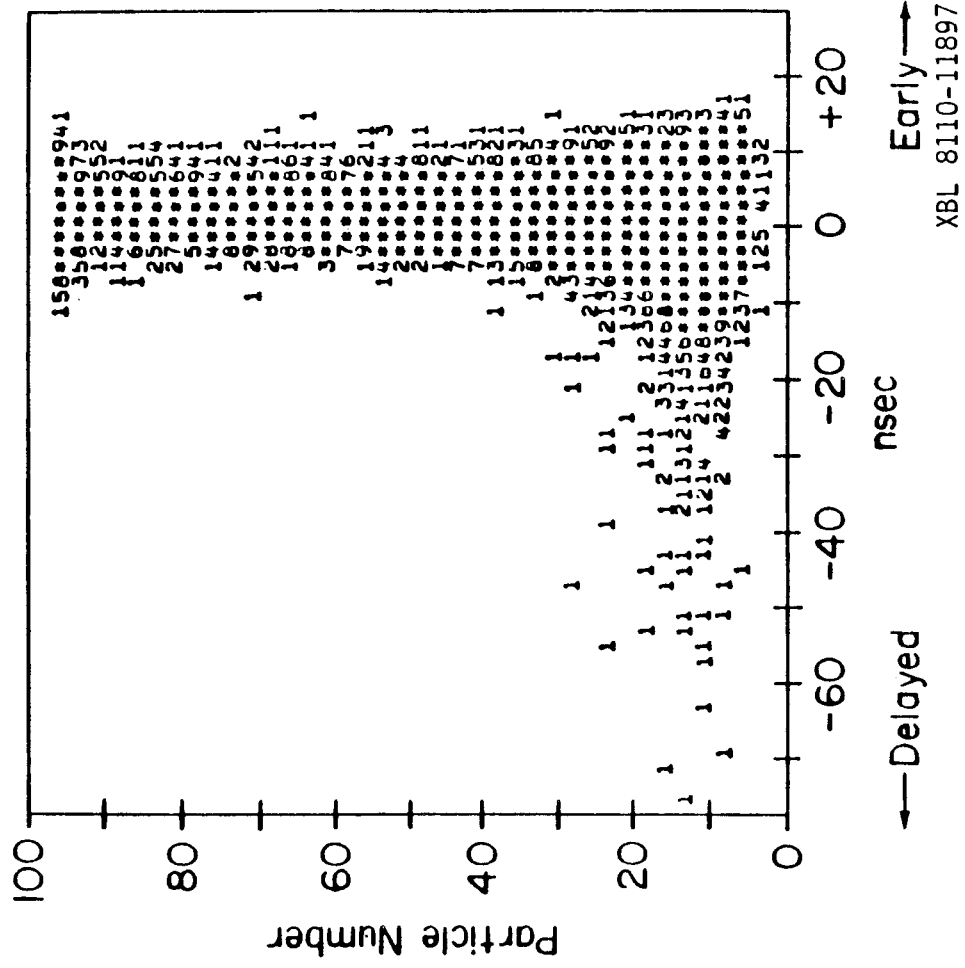


Fig. 88

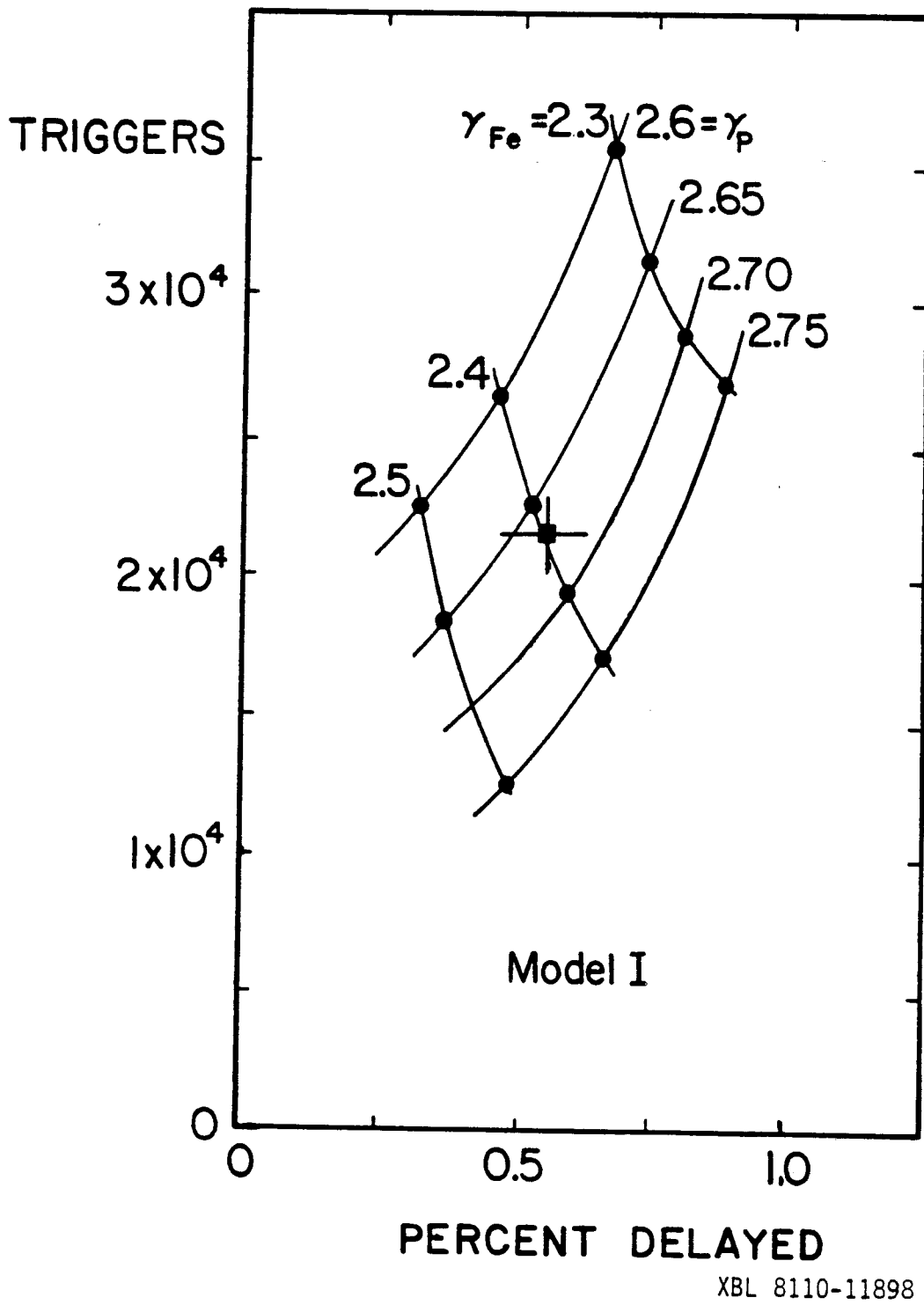
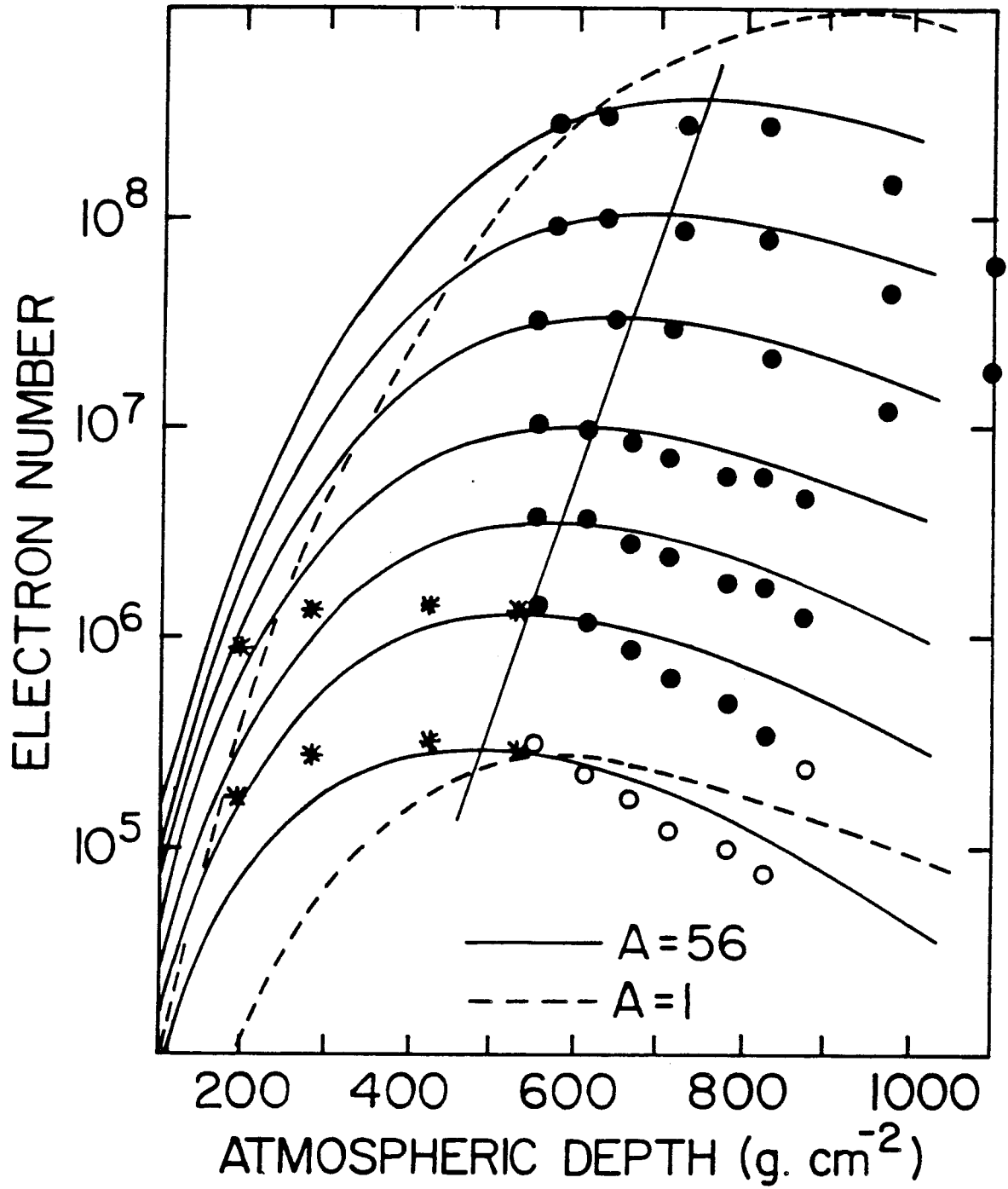


Fig. 89



XBL 8110-11899

Fig. 90

This report was done with support from the Department of Energy. Any conclusions or opinions expressed in this report represent solely those of the author(s) and not necessarily those of The Regents of the University of California, the Lawrence Berkeley Laboratory or the Department of Energy.

Reference to a company or product name does not imply approval or recommendation of the product by the University of California or the U.S. Department of Energy to the exclusion of others that may be suitable.

TECHNICAL INFORMATION DEPARTMENT  
LAWRENCE BERKELEY LABORATORY  
UNIVERSITY OF CALIFORNIA  
BERKELEY, CALIFORNIA 94720